Complex Organic Molecules In Solar Type Star Forming Regions

Ali Jaber Al-Edhari

To cite this version:

Ali Jaber Al-Edhari. Complex Organic Molecules In Solar Type Star Forming Regions . Solar and Stellar Astrophysics [astro-ph.SR]. Université Grenoble Alpes, 2016. English. NNT : . tel-01542982

HAL Id: tel-01542982
https://theses.hal.science/tel-01542982v1

Submitted on 20 Jun 2017

Communauté
UNIVERSITÉ Grenoble Alpes

THÈSE

Pour obtenir le grade de

DOCTEUR DE LA COMMUNAUTE UNIVERSITE GRENOBLE ALPES

Spécialité : **ASTROPHYSIQUE - PHYSIQUE & MILIEUX DILUES**

Arrêté ministériel : 7 août 2006

Présentée par

Ali Jaber Al-Edhari

Thèse dirigée par **Cecilia Ceccarelli**
et codirigée par **Claudine Kahane**

préparée au sein **de l'Institut d'Astrophysique et de Planétologie de Grenoble**
dans **l'École Doctorale Physique**

Complex Organic Molecules In Solar Type Star Forming Regions

Thèse soutenue publiquement le **19 Octobre 2016**,
devant le jury composé de :

M. Eric Quirico
Professeur, Université de Grenoble (France), Président
Mme Paola Caselli
Professeur, Max Planck Institute, MPE, Munich (Germany), Rapporteur
M. Francesco Fontani
Astronome, Osservatorio Astronomico d'Arcetri, Florence (Italy), Rapporteur
Mme Charlotte Vastel
Astronome, l'Institut de Recherche en Astrophysique et Planetologie, Toulouse (France), Examinateur
Mme Cecilia Ceccarelli
Astronome, Institut de Planétologie et d'Astrophysique de Grenoble (France), Directeur de thèse
Mme Claudine Kahane
Professeur, Université de Grenoble (France), Co-Directeur de thèse

To Martyr Major General ***Faisal Zamili****, martyr Lieutenant* ***Wissam al-Tikriti****, and to all the martyrs of Iraq, who Without them I could not complete my studies.*
To my family for their constant support over the years despite the distance, and to all those who get past this page..

Ali AL-EDHARI, Grenoble-France

Abstract

The present PhD thesis goal is the study of the molecular complexity in solar-type star forming regions. It specifically focuses on two classes of molecules with a prebiotic value, the complex organic molecules and the cyanopolyynes. At this scope, I analyzed data from single-dish spectral surveys by means of LTE or/and non-LTE radiative transfer codes in two sources, a solar-type protostar in an isolated and quiet environment (IRAS16293-2422) and a proto-cluster of solar-type protostars (OMC-2 FIR4). The ultimate goal is to find similarities and differences between these two cases.

I used data from two spectra surveys: TIMASSS (The IRAS16293-2422 Millimeter And Submillimeter Spectral Survey), which has been carried out in 2011 (Caux et al. 2011), and ASAI (Astrochemical Surveys At IRAM), which has been carried out in 2013-2015 (e.g. Lopez-Sepulcre et al. 2015). I extracted the lines (identification and integrated intensity) by means of the publicly available package CASSIS (Centre dAnalyse Scientifique de Spectres Infrarouges et Submillimtriques). Finally, I used the package GRAPES (GRenoble Analysis of Protostellar Envelope Spectra), which I helped to develop, to model the Spectral Line Energy Distribution (SLED) of the detected molecules, and to estimate their abundance across the envelope and hot corino of IRAS16293-2422 and OMC-2 FIR4, respectively.

The major results of the thesis are:

1. The first full census of complex organic molecules (COMs) in IRAS16293-2422;
2. The first detection of COMs in the cold envelope of a solar-type protostar (IRAS16293-2422), supporting the idea that a relatively efficient formation mechanism for the detected COMs must exist in the cold gas phase;
3. The discovery of a tight correlation between the dimethyl ether (DME) and methyl format (MF), suggesting a mother-daughter or sisters relationship;
4. The detection of formamide, a species with a high pre-biotic value, in several protostars, including IRAS16293-2422 and OMC-2 FIR4;
5. The full census of the cyanopolyynes in IRAS16293-2422 and OMC-2 FIR4, with the detection of HC_3N and HC_5N, DC_3N and, for OMC-2 FIR4, the ^{13}C isotopologue of HC_3N cyanopolyynes. Please note that the work on OMC-2 FIR4 is still on-going.

These results are the focus of two published articles (Jaber et al. 2014, ApJ; Lopez-Sepulcre, Jaber et al. 2015, MNRAS), one accepted article (Jaber et al., A&A) and a final article to be submitted (Jaber et al., A&A).

Resume

Le but de cette thèse est l'étude de la complexité moléculaire dans les régions de formation stellaire. Cette thèse est centrée sur deux classes de molécules importantes pour la chimie prébiotique : les molécules organiques complexes et les cyanopolyynes.

Pour ce faire, j'ai analysé les émissions moléculaires, dans le domaine radio millimétrique, de deux sources : une proto-étoile de type solaire, située dans un environnement calme (IRAS 16293-2422) et une proto-étoile de type solaire (OMC2-FIR4), située, elle, dans un proto-amas. Outre l'intérêt intrinsèque de l'étude de IRAS16293-2422, considérée comme le prototype des proto-étoiles de type solaire, l'objectif de mon travail était la recherche de similarités et de différences entre ces deux objets.

Pour ce faire, j'ai utilisé les données issues de deux grands relevés spectraux réalisés avec l'antenne de 30m de l'IRAM : TIMASSS (The IRAS16293-2422 Millimeter And Submilimeter Spectral Survey) réalisé entre 2004 et 2006 (Caux et al. 2011) et ASAI (Astrochemical Surveys At IRAM) réalisé pendant la période 2013-2015 (eg Lopez-Sepulcre et al. 2015).

L'identification et la détermination des paramètres des raies moléculaires ont été faites en utilisant un ensemble d'outils en accès libre, CASSIS (Centre d'Analyse Scientifique de Spectres Infrarouges et Sub- millimétrique). Afin d'estimer les propriétés physiques du gaz et les abondances moléculaires, j'ai modélisé la distribution spectrale d'énergie des raies moléculaires, dans les hypothèses de transfert radiatif à l'équilibre thermodynamique local et / ou hors d'équilibre, en utilisant les modèles et procédures constituant GRAPES (GRenoble Analysis of Protostellar Envelope Spectral) et les structures en densité et en température des deux sources déterminées antérieurement. CASSIS comme GRAPES utilisent les données de spectroscopie moléculaire issues des bases de données CDMS et JPL.

Les principaux résultats de la thèse sont les suivants :

1. Le premier recensement complet des molécules organiques complexes (COMs) dans le cœur chaud de IRAS16293-2422.

2. La première détection de COMs dans l'enveloppe froide de IRAS16293-2422, qui laisse à penser qu'un mécanisme de formation des COMS, relativement efficace, doit exister en phase gazeuse froide.

3. La découverte d'une forte corrélation entre les abondances du diméthyle-éther (DME) et du méthyle-formate (MF), qui suggère une relation mère-fille entre ces deux espèces.

4. La modélisation de l'abondance du formamide, molécule considérée comme prébiotique, récemment détectée dans plusieurs protoétoiles incluant IRAS16293-2422 et OMC2-FIR4.

5. Le recensement complet des cyanopolyynes et de leurs isotopes et leur modélisation dans IRAS16293-2422 et OMC2- FIR4.

Ces résultats ont conduit à la publications de 2 articles (Jaber et al. 2014, ApJ ; Lopez-Sepulcre, Jaber et al. 2015, MNRAS), à un article accepté (Jaber et al. 2016, A&A) et à un article en préparation (Jaber et al. 2016, A&A).

Acknowledgements

When it comes to writing acknowledgements, it becomes even more difficult than writing the whole thesis as the list is too long. No doubt, I was so worried and stressed when I started in Grenoble; different place, culture, people and language; 'Oh my God, what have I done to myself? Am I going to make it? and one day I will become Dr.! and realize my dream to revive astronomy in Mesopotamia'. I said to myself this sentence because my first week in IPAG there was a dinner party for all Ph.D. students in an Indian restaurant. After dinner, when I introduced myself, "Hey guys, I am Ali, a PhD student from Iraq" one of the students burst high laugh and said "Are you kidding me ! your country is torn by wars and you are here to study astrophysics?". Okey, to be frank, it was not the sentence that I expect to hear, but so what? do I give up? or do I continue? I select the tough answer. All of my worries were relieved the moment I joined the "Interstellaire" group, and was surrounded by the two angels, Cecilia & Claudine.

First and above all, I praise **God**, the almighty, for providing me this opportunity to be a graduate student of the honoured University Grenoble Alpes, UGA, and granting me the capability to proceed successfully. I still cannot believe that I made it, but I finally have. This thesis appears in its current form due to the assistance and guidance of several people. I would therefore like to offer my sincere thanks to all of them.

I want to express my gratitude to my esteemed supervisors, Professors **Cecilia Ceccarelli and Claudine Kahane**, thanks first of all for accepting me as a PhD student and for supporting me during my thesis. **Cecilia** is someone you will instantly love and never forget once you meet her. She's the funniest advisor and one of the smartest and modest people I know. I hope that I could be as lively, enthusiastic, and energetic as Cecilia and someday be able to guide an audience as well as she can. Thank you **Cecilia** for your warm encouragement, thoughtful guidance, critical comments, for being very patient teaching me several issues about coding and observations. **Claudine** has been supportive and provided insightful discussions about the research. I am also very grateful for her scientific advice and knowledge and many insightful discussions and suggestions.

It is a pleasure for me to thank **Paola Caselli** and **Francesco Fontani** for agreeing to be the referee of this thesis manuscript and **Eric Quirico** and **Charlotte Vastel** to be part of the referee of my thesis defence.

I would like to warmly thank the Institut de Planetologie et d'Astrophysique de Grenoble, where both the people and the scientific environment makes it a perfect place to do research. Thanks to all IPAG people. Special thank to two members of the lab who helped me in my everyday work and for their kindness: **Stephane Di Chiaro** and **Richard Mourey**.

I also want to thank many colleagues who have help me a lot during my thesis. **Jorge Morales, Nicola Astudillo-Defru, Vianney Taquet, Ana Lopez Sepulcre and Cecile Favre**.

Special thank to **Prof. Jean Gagnon**, for helping me to correct the English of my thesis.

I am indebted to my country **IRAQ** for the the financial support to complete my PhD study. I am also indebted to **FRANCE** for many things that provided me and my family, thank you France.

I would like to show my deepest gratitude to my parents for raising me the way I am, for giving me freedom deciding what to do and where to go, for their prayers and courage when I was fed up. To my brothers for always being there to help me when I need them. Thanks to all of you for being there all the time over the years, despite the distance.

The last words go to my wife, who has managed to support me during these years. I am really grateful for her support.

Thanks to all of those who should be acknowledged.

Contents

List of Figures

List of Tables

Chapter 1

Introduction

1.1 Overview

The major objective of this thesis is to study the complex organic molecules[1] in low mass star formation regions. To this end, in this introduction I will briefly summarize the physical and chemical evolution of these regions.

1.2 Low-mass star formation

The formation process of low-mass stars is thought to happen according to the following sequence: a protostar derived from a cold and dense prestellar core evolves through four principal stages represented by Class 0, I, II and III sources (Lada & Wilking 1984; Andre & Montmerle 1994). These are defined by their Spectral Energy Distribution (SED) and the characteristics of the SEDs are listed in Table 1.1. The SED of the system at different evolutionary stages and the corresponding system geometry are shown in the Figure 1.1.

Very briefly, the general idea is that large cold clouds with over density regions are where stars are born. These over density regions become more and more dense until the high density makes it collapse, because the internal pressure and rotation can no longer hold the cloud. At this stage we call this object Class 0 source. The density of the cloud becomes so large after $\sim 10^4$ to 10^5 years that radiation from cooling lines cannot get away and the temperature of the cloud becomes higher. Then the object moves to the next stage, namely Class I. The central object through this stage is heated up to several hundred degree K. A circumstellar disk is formed between the Class 0 and I phases, because of the conservation of the angular momentum. At the same time, the outflows work to eliminate the excess angular momentum.

When the bulk of the material has accreted onto the central object and only a thin circumstellar disk is left, the source become a Class II object. This comes after $\sim 10^6$ years. The embedded object becomes visible at optical and infrared wavelengths. When the accretion drops, then we can say that the object is in the Class III stage, which comes after $\sim 10^6$ to 10^8 years. At this stage, the majority of the primordial material in the disk is lost and the formation of a planet might start. The central protostar slowly contracts. Eventually, the star will enter the main sequence stage. When the density and temperature in the protostar are high enough to start hydrogen fusion, it is transformed in a "regular star".

---

[1] A complex organic molecule (COM) is defined as a molecule which contains carbon and consists of more than six atoms, following the literature (e.g. Herbst & van Dishoeck (2009)).

TABLE 1.1: The characteristic of SEDs for the four stages of low-mass star formation. Adopted from (Lada & Wilking 1984; Andre & Montmerle 1994)

Class	SED (Spectral Energy Distribution)
Class 0 sources	Their SEDs is fairly well described by a black body spectrum at a temperature below 30 K, peaking at sub-mm wavelengths ($\geq 100\mu$m). They have molecular outflows.
Class I sources	Their SEDs are broader than that of a black body and shift to far-IR wavelengths ($\leq 100\mu$m) as the temperature of the dust rises. Emission from both the accreting envelope and the thick disk are observed. The 10μm silicate absorption feature is often identified toward Class I sources, indicating that the envelope is optically thick. These sources are very deeply embedded and invisible in the optical. The SEDs are fitted by models of objects accreting mass from circumstellar matter. They often have molecular outflows.
Class II sources	Their SEDs are also broader than that of a black body, but they are flat or decreasing for wavelengths greater than $\sim 2\mu$m, corresponding to temperatures around 1000 to 2000 K. At longer wavelengths, an infrared excess is observed, originating from the dusty disk. They are visible in the optical and are mostly associated with T-Tauri stars with optically thick discs which are still accreting onto the young stellar object (YSO). This phase is also known as the classical T-Tauri phase (CTT). Their SEDs are well fitted by models of photospheres surrounded by a circumstellar disk and they often have molecular outflows.
Class III sources	Their SEDs can be modelled by reddened black bodies. They have little or no excess near infrared emission, but a slight excess in the mid infrared caused by the cool dust grains which are responsible for the extinction. Their SEDs are well modelled by reddened photospheres of stars very near to or on the zero age main sequence, with an optically thin disc and the envelope already dispersed. This phase is known as weak-line T-Tauri (WTT).

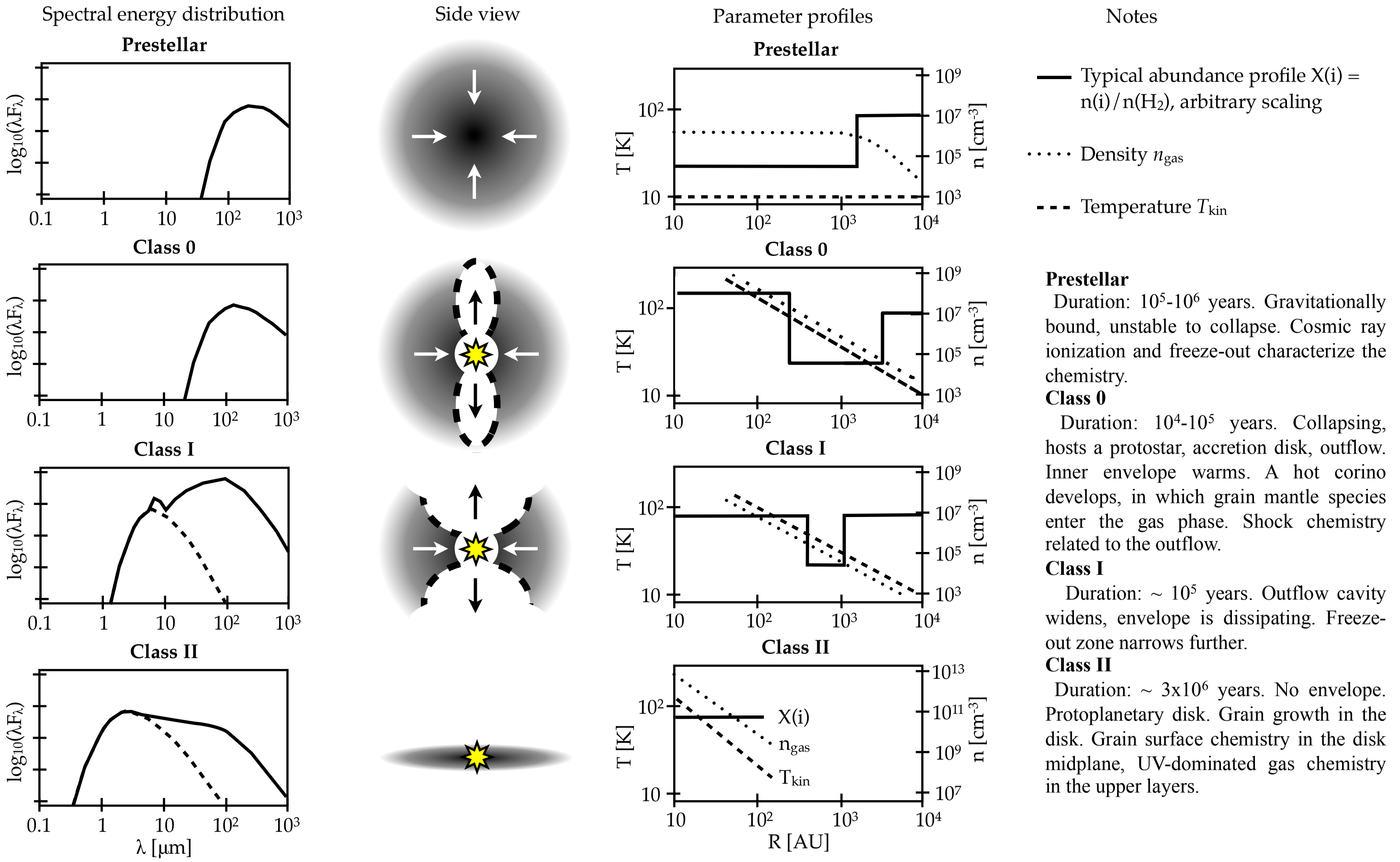

Typical abundance profile X(i) = n(i)/n(H$_2$), arbitrary scaling

Density n_{gas}

Temperature T_{kin}

Prestellar
Duration: 10^5-10^6 years. Gravitationally bound, unstable to collapse. Cosmic ray ionization and freeze-out characterize the chemistry.

Class 0
Duration: 10^4-10^5 years. Collapsing, hosts a protostar, accretion disk, outflow. Inner envelope warms. A hot corino develops, in which grain mantle species enter the gas phase. Shock chemistry related to the outflow.

Class I
Duration: ~ 10^5 years. Outflow cavity widens, envelope is dissipating. Freeze-out zone narrows further.

Class II
Duration: ~ 3x10^6 years. No envelope. Protoplanetary disk. Grain growth in the disk. Grain surface chemistry in the disk midplane, UV-dominated gas chemistry in the upper layers.

FIGURE 1.1: Schematic drawing of the different stages of low-mass star formation and their chemical characteristics (from Kama (2013)).

1.3 Chemical complexity evolution

Molecular complexity increases during the formation of low mass stars. It can be described by five stages, as suggested by Caselli & Ceccarelli (2012) (see Figure 1.2).

1. Pre-stellar cores: In the gas phase of a primordial cloud, atoms and simple molecules freeze out onto dust grains. At this stage, formation of molecules like water (H_2O), formaldehyde (H_2CO), methanol (CH_3OH) begins from surface hydrogenation of O and CO by the H atoms.

2. Protostellar envelopes: As the collapse continues, the temperature of the future star increases until it reached the mantle sublimation value (~ 100 K) in the so-called hot corino regions.

3. Protoplanetary disks: In time, a protoplanetary disk is formed and the envelope disappears. New and more complex molecules are synthesised in the hot regions close to the central object. In contrast molecules inside the cold equatorial plan freeze out again into grain mantle surfaces. At this stage, legacy and preservation starts.

4. Planetesimal formation: As dust grains coagulate into larger masses, namely planetesimals, icy grain mantles are also condensed within. Thus, these planetesimals, which will form future Solar System bodies, carry the history of their formation.

5. Planet formation: In the Solar System, during the formation of the early Earth, the planet is subjected to showers of comets and asteroids that contain ices trapped in the planetesimals. With the formation of oceans and atmosphere, life emerged about 2 billion years ago.

1.4 Census of molecules in the interstellar medium

The nature of molecules and estimation of their abundance in space has been obtained from spectroscopic observations. Many molecules have been discovered over several years of research. At first, simple molecules such as CH (Swings & Rosenfeld 1937), CN (McKellar 1940) and CH^+ (Douglas & Herzberg 1941) were identified. Much later, following the development of radioastronomy, more complex molecules like NH_3 were also discovered (Cheung et al. 1968). As detection technics improved, so did the number of identified molecules as well as their complexity. So far, this amounts to about 200 molecules according to CDMS databases (*https://www.astro.uni-koeln.de/cdms/molecules*). The number of identified molecules, sorted by increasing number of constituting atoms, are given in Figure 1.3a, while Figure 1.3b shows the numbers of molecules detected in the Orion nebula, and Figure 1.3c shows those detected in the solar type protostar IRAS16293-2422. As it is clear from these three figures, the most numerous molecules are the simplest ones, i.e., those with two or three atoms.

In Figure 1.4, the number of the detected molecules is plotted as a function of the molecular weight for five regions: ISM (Figure 1.4a), the Orion nebula (Figure 1.4b), IRAS16293-2422 (Figure 1.4c), OMC-2 FIR4 (Figure 1.4d) and extragalactic sources (Figure 1.4e). Interestingly, a similar peak at molecular weight around 40 to 49 is evidenced in these graphs, probably because the most abundant species in the universe are hydrogen, carbon, nitrogen and oxygen. Indeed, the simple combination of a few of these

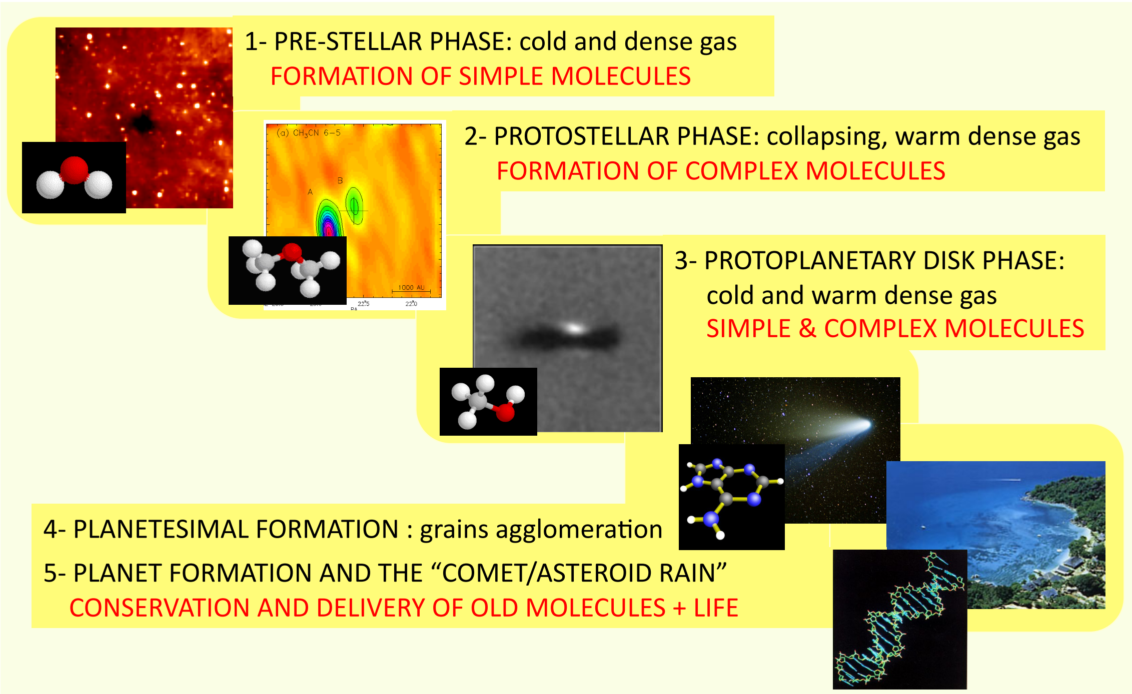

FIGURE 1.2: Chemical complexity and the formation of solar type stars. The sketch shows five main stages to form stars and planets as suggested by Caselli & Ceccarelli (2012)

atoms would easily result in species averaging 40-49 in molecular mass. Amongst the several combinational possibilities, we find for example HNCO and NH_2CHO which are important in the formation of more complex prebiotic species. This could indicate that the greater molecular abundance in the universe is formed from these atoms which being also the most abundant maybe not be surprising: Nature uses what is available. The majority of detected molecules are relatively simple, but several more complex polyatomic molecules have also been identified, albeit in low abundance. Many more are likely to be discovered in the near future. Thus, questions arised concerning their provenance: How did these molecules formed and can they be linked to the origin of terrestrial life?

1.5 Aims and structure of this thesis

This thesis aims to a better understanding of the chemistry in the early phases of low-mass star-forming regions. The thesis is separated into seven Chapters, as follows:

Chapter 1 presents a general brief review of the current knowledge on low-mass star formation and the chemical evolution.

Chapter 2 describes the two sources studied in detail in this thesis. For IRAS16293-2422, I describe in details the physical and chemical structure, along with outflow system. OMC-2 FIR 4 much less is known, so that the description is more concise.

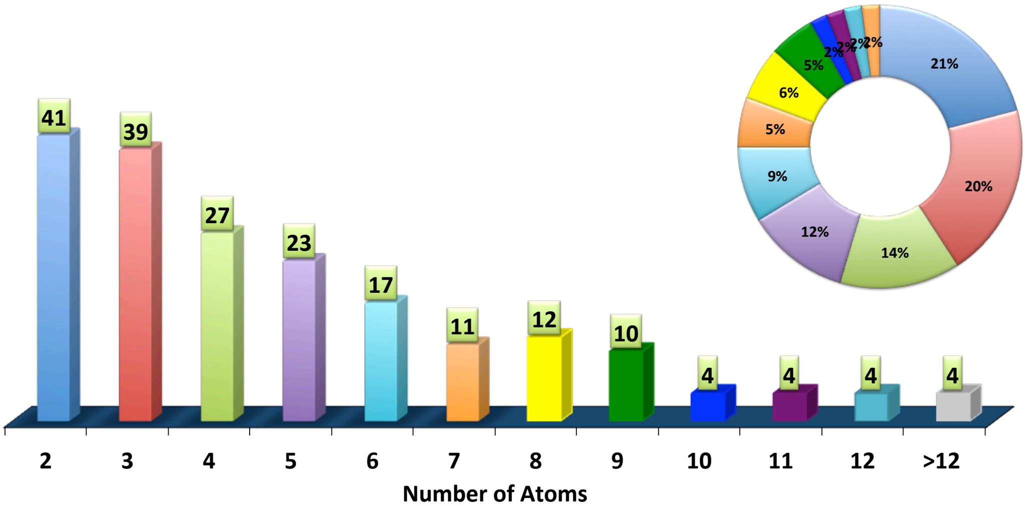

(A) Molecules detected in the ISM, from CDMS databases (*https://www.astro.uni-koeln.de/cdms/molecules*).

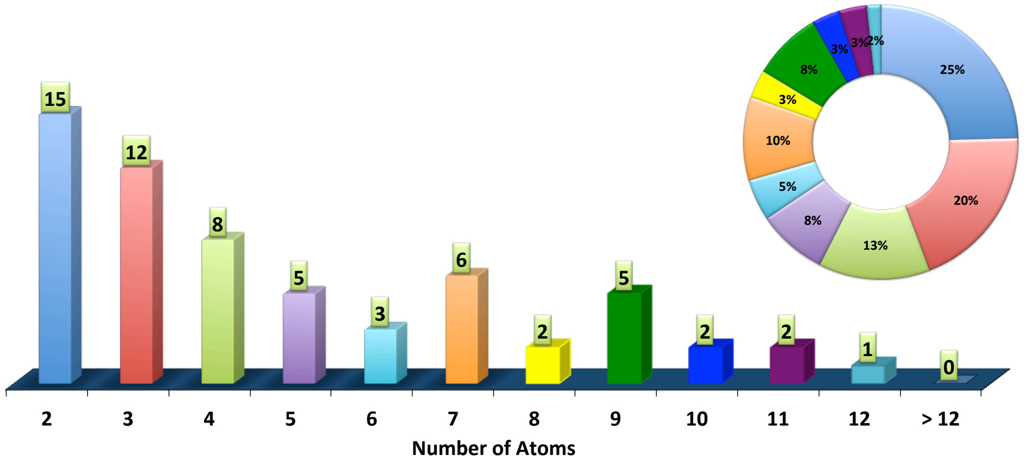

(B) Molecules detected in the Orion, from CDMS databases (*https://www.astro.uni-koeln.de/cdms/molecules*).

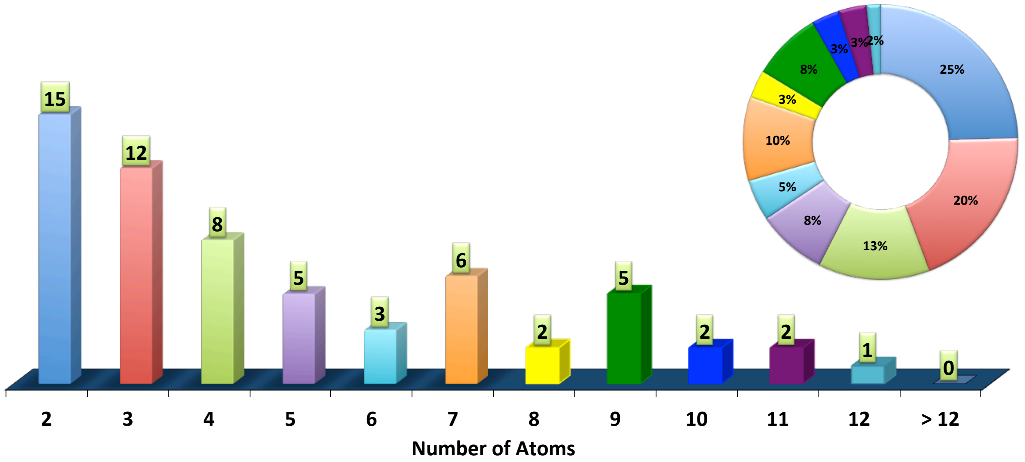

(C) Molecules detected in IRAS16293, from (Caux et al. (2011); Hily-Blant et al. (2010); Chandler et al. (2005); Coutens et al. (2012); Kahane et al. (2013); Cazaux et al. (2003); Jørgensen et al. (2012); Majumdar et al. (2016)).

FIGURE 1.3: Molecules detected in the ISM (upper panel), Orion (middle panel) and IRAS16293 (bottom panel) respectively with the percentage, sorted by increasing number of constituting atoms.

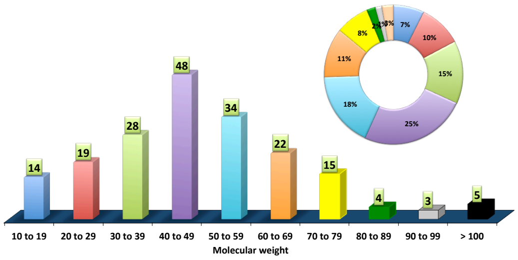

(A) Molecules detected in the ISM.

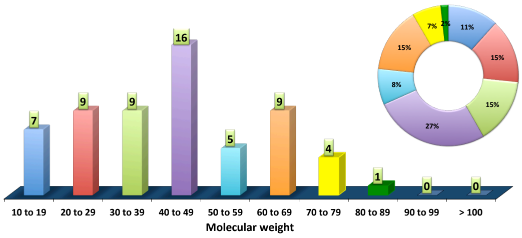

(B) Molecules detected in th Orion.

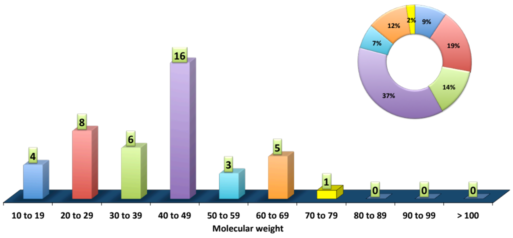

(C) Molecules detected in IRAS16293.

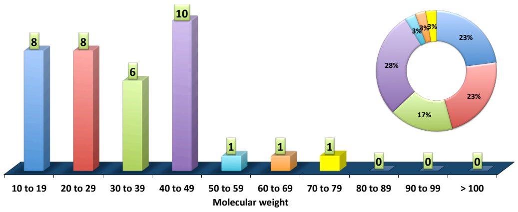

(D) Molecules detected in OMC-2FIR4, from Kama et al. (2013); Shimajiri et al. (2015); López-Sepulcre et al. (2015) and Jaber et.al. (in preparation).

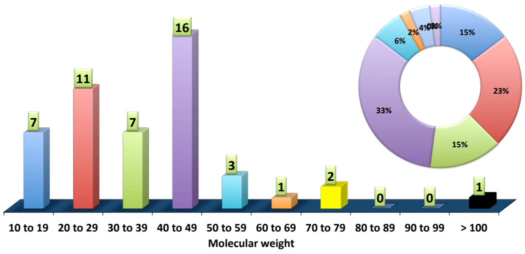

(E) Molecules detected in Extragalactic, from *https://www.astro.uni-koeln.de/cdms/molecules*) .

FIGURE 1.4: Molecules detected in the ISM, Orion, IRAS16293, OMC-2FIR4 and Extragalactic respectively with the percentage, sorted by molecular weight.

Chapter 3 introduces the tools that have been used in my work. This includes, spectral surveys, lines identification, lines parameters and SLED modeling tools.

Chapter 4 contains the census of complex organic molecules in the Solar type protostar IRAS16293-2422, and the article published in Astrophysical Journal in 2014, where I am first author.

Chapter 5 contains the census of cyanopolyynes in the solar type protostar IRAS16293-2422, and the article accepted to publish in Astronomy & Astrophysics journal, where I am first author.

Chapter 6 presents a study on the formamide abundance in low and intermediate mass protostars, including IRAS16293-2422 and OMC-2 FIR4, and the article published in Monthly Notes of Royal Astronomical Society in 2015, where I am second author.

Chapter 7 summarises the main conclusions of the thesis. I also address some of the future prospects arising from this thesis.

The bibliography is reported as a last Chapter.

Chapter 2

Description of IRAS16293-2422 and OMC-2 FIR 4

2.1 IRAS16293-2422

IRAS16293-2422 (hereinafter IRAS16293) was first detected by IRAS (Infrared Astronomical Satellite-1983) in the 25, 60, and 100μm bands, with color-corrected point source catalog fluxes of 1.59, 271, and 1062 Jy, respectively. The first radio continuum observations of this source were obtained at 1.3mm with NRAO (The National Radio Astronomy Observatory) 12m radio telescope in January 1986. IRAS16293 is a solar type Class 0 protostar in the eastern part of the ρ Ophiuchi star forming region, at a distance of 120 pc (Loinard et al. 2008). It has a bolometric luminosity of 22 $L_{\odot}$ (Crimier et al. 2010b). Given its proximity and brightness, it has been the target of numerous studies in all frequency ranges that have reconstructed its physical and chemical structure. IRAS16293 has a large envelope that extends up to ~6000 AU and that surrounds two sources, named I16293-A and I16293-B in the literature, separated by ~ 5" (~600 AU; Wootten (1989); Mundy et al. (1992)) as shown in Figure 2.1.

I16293-A itself is composed of two sources, A1 and A2, each one emitting a molecular outflow (Mizuno et al. 1990; Loinard et al. 2013). I16293-B possesses a very compact outflow Loinard et al. (2013) and is surrounded by infalling gas (Pineda et al. 2012; Zapata et al. 2013). The sizes of I16293-A are ~ 1", whereas that of I16293-B is unresolved at a scale of ~ 0.4" (Zapata et al. 2013). From a chemical point of view, IRAS16293 can be considered as composed of an outer envelope, characterised by low molecular abundances, and a hot corino, where the abundance of many molecules increases by orders of magnitude (Ceccarelli et al. 2000a; Schöier et al. 2002; Coutens et al. 2013a). The transition between the two regions occurs at ~100 K, the sublimation temperature of the icy grain mantles. In this chapter I will describe the physical and chemical structure in addition to the outflow system of IRAS16293.

2.1.1 The physical structure

The physical structure of IRAS16293, namely its dust and gas density and its temperature profiles, has been the goal of several studies, which I will describe briefly in the next paragraph.

In 2000, Ceccarelli et al. (2000a) used water and oxygen lines observations obtained with the Infrared Space Observatory (ISO) to derive the gas and dust density and the temperature profile. They assumed the semi-analytical solution described by Shu and coworkers (Shu 1977; Adams & Shu 1986) to fit the observational data.

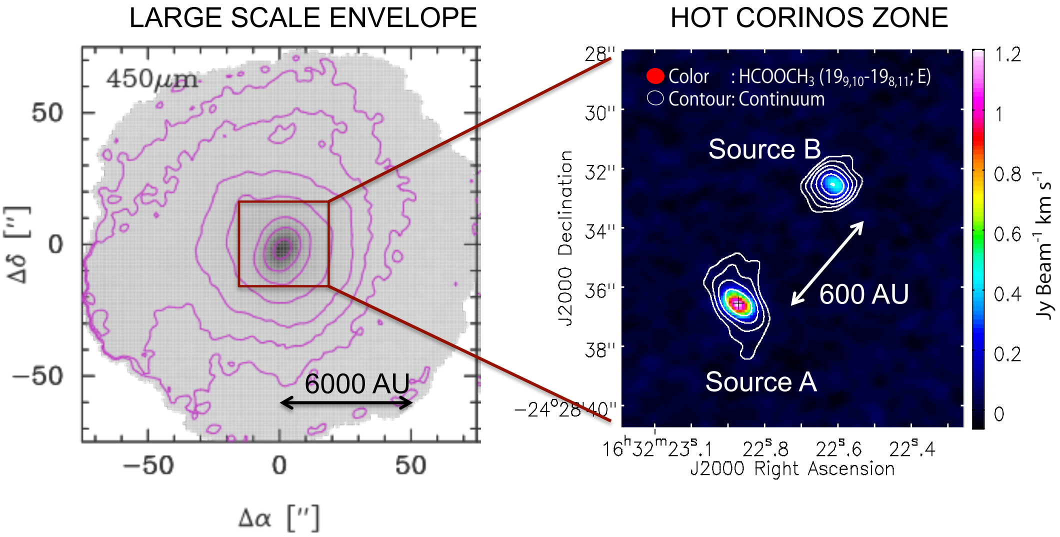

FIGURE 2.1: The IRAS16293-2224 structure. Adopted from Schöier et al. (2002); Oya et al. (2016)

In 2002, Schöier et al. (2002) used the dust continuum observations to derive the structure of the envelope and propose a single power law for the density distribution. Furthermore, they verified a posteriori that the Shu's solution also reproduced the observational data. These studies, by two different groups, gave two similar general results: *1)* the envelope of IRAS16293 is centrally peaked and has a density distribution in overall agreement with the inside-out collapse picture (Shu 1977); *2)*IRAS16293 has a hot corino region, about 200 AU in diameter, where the dust mantles sublimate.

In 2004, Schöier et al. (2004) published a study based on interferometric Owens Valley Millimeter Array at ∼2" resolution and the 1.37 mm continuum data revealed extended emission ; comparing their model predictions with these observations, they claimed that the envelope has a large central cavity, about 800 AU in diameter.

In 2005, Jørgensen et al. (2005) concluded that the envelope has an even larger central cavity, about 1200 AU in diameter. This large central cavity has a great impact on the whole interpretation of the hot corino of IRAS16293, because it predicts the absence of the mantle sublimation region. If the predicted cavity is real, the observed complex organic molecules must have an origin other than grain mantle sublimation from thermally heated dust. In addition to raising an important point in itself, Schöier et al. (2002) and Jørgensen et al. (2005) illustrated the paramount importance of correctly understanding the physical structure of the source in order to assess the chemical structure and all that follows.

In 2010, Crimier et al. (2010b) re-analyzed all available continuum data (single dish and interferometric, from millimeter to MIR) from scratch, in order to derive accurate density and dust temperature profiles. Using ISO observations of water, they also reconstructed the gas temperature profile, considering in addition the distance to this source estimated by Loinard et al. (2008) (120 pc instead of 160 pc, as assumed in (Ceccarelli et al. 2000a; Schöier et al. 2002; Jørgensen et al. 2005)). Their results show that an envelope of about 2$M_\odot$ surrounds the proto-binary system of IRAS16293. This envelope can be described with a Shu-like density distribution, corresponding to the gas collapsing towards a 2$M_\odot$ central star. Both the single dish and interferometric data have been able to be reproduced by an envelope with an inner radius between 20 and

30 AU, equivalent to about 0.4" and smaller than the radius at which the dust temperature reaches 100 K (the ice mantle sublimation temperature) namely 75 to 85 AU. Their analysis can reproduce the full SED, including the Spitzer MIR data, without the necessity of a central cavity of 800 AU radius, claimed by Jørgensen et al. (2005).

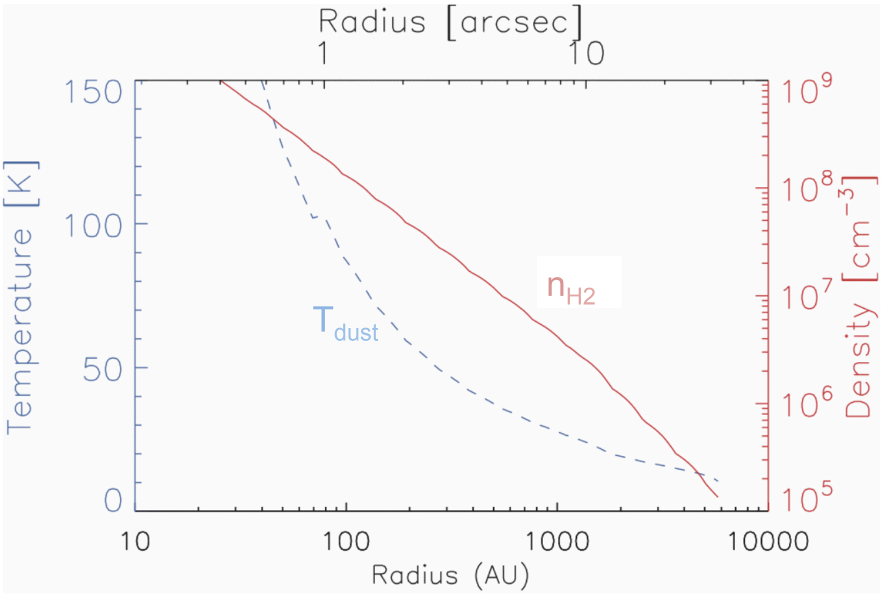

FIGURE 2.2: Temperature and density profile of IRAS16293. Adopted from Crimier et al. (2010b)

The structure of the IRAS16293 envelope, as derived by Crimier et al. (2010b) is shown in Figure 2.2. This Figure indicates that both density and temperature increase toward the center. Similarly the velocity of the infalling gas increases with decreasing distance from the center with an $r^{-1/2}$ power law, although part of the envelope may not be collapsing yet. The infall motion has proved difficult to disentangle from the outflow motions, but high spatial and spectral resolution observations obtained with ALMA have succeeded to probe it unmistakably by Pineda et al. (2012).

In 2012, Pineda et al. (2012), used a very high spectral resolution observation offered by ALMA to study the gas kinematics. They presented for the first time an unambiguously detected inverse P-Cygni profile in three molecular lines toward source B, as shown in Figure 2.3, which represents clear evidence for infall in source B. Also an absorption feature in SO (7_6–6_6) toward source B was reported by Chandler et al. (2005) as suggestive of infall.

2.1.2 The outflow system in the IRAS16293

To understand the IRAS16293 protostellar system, we need to understand when and where the energy is released back into the envelope. Indeed in the form of shocks driven by the protostellar outflow and jet, the injection of mechanical energy of the outflow can affect the overall evolution process of the source, as it allows accretion to proceed by removing angular momentum (Bodenheimer 1995). Furthermore, the outflow morphology can provide informations on the driving sources. For instance, the degree of collimation is believed to correlate with their age and mass (Machida et al. 2008; Arce et al. 2007), while multipolar outflows can often indicate a multiple system (e.g. Carrasco-González et al. (2008)).

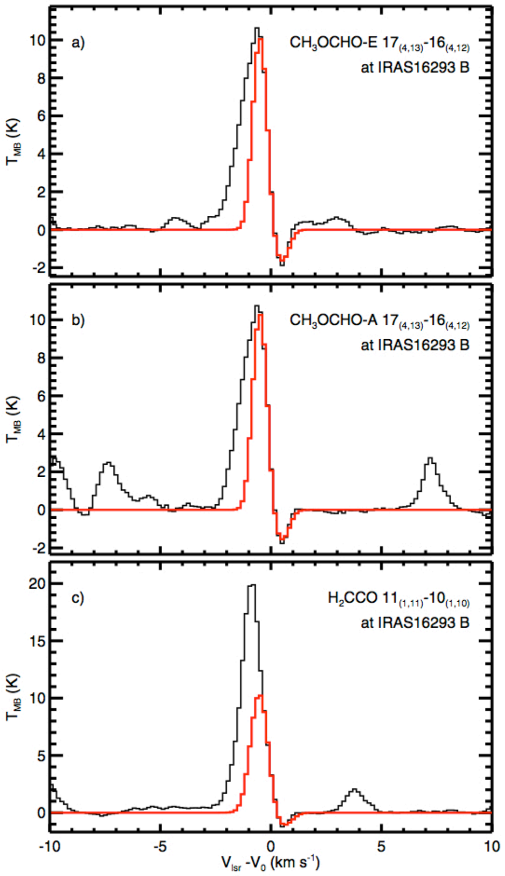

FIGURE 2.3: Molecular line spectra from the ALMA data toward the continuum peak of IRAS16293B. In each panel, a red line shows the best two- layer model of infall fit for each spectrum. From (Pineda et al. 2012)

In 1986, Walker et al. (1986) introduced the first evidence of an outflow in IRAS16293. Then, Mizuno et al. (1990) found that this source contains two bipolar outflow structures. One is oriented in the north-east–south-west direction (hereafter called the NE-SW flow), while the other is oriented nearly east-west (hereafter the EW flow). While sources A1 and A2 appear active and drive two outflows, source B is more quiescent, as shown in Figure 2.4.

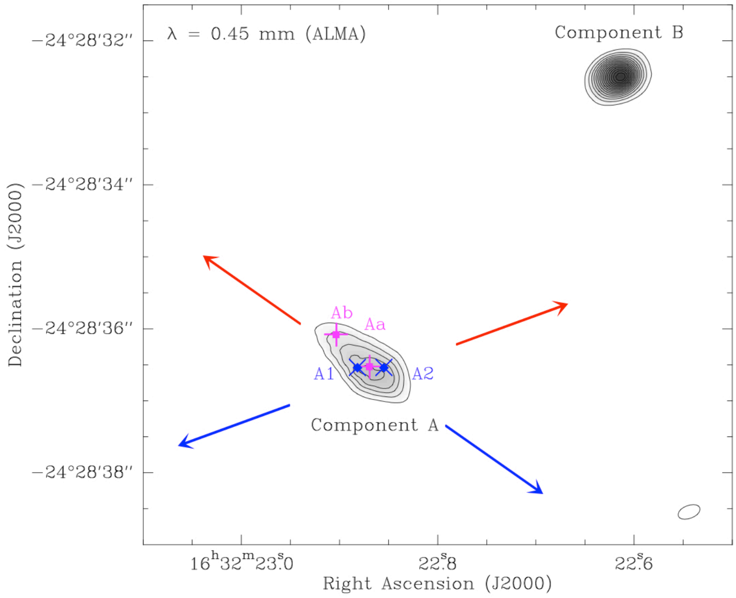

FIGURE 2.4: Sub-millimeter continuum image of the IRAS16293 system from ALMA. The contours run from 0.2 to 4 Jy beam^{-1} by steps of 0.2 Jy beam^{-1} ; the synthesized beam (0".32 × 0".18; -69°) is shown at the bottom-right. The noise level is 0.02 mJy beam^{-1}. The two main components (A and B) are labelled, and the direction of the two outflows driven from component A are indicated from Mizuno et al. (1990). The sub- millimeter peaks Aa and Ab from Chandler et al. (2005) and the centimeter sources A1 and A2 are shown. From (Loinard et al. 2013).

Loinard et al. (2013) used combined VLA and ALMA CO(6-5) observations to check the outflow activity in the IRAS16293. They confirmed that the NE-SW and E-W large-scale molecular flows are driven from component A. They also reported an outflow toward source B. From its unusual properties, highly asymmetric, slow (10 km s^{-1}), with a dynamical age of about 200 years, they concluded to the extreme youth of source B.

Soon after in the same year, IRAS16293 was targeted by Kristensen et al. (2013) to examine the origin of CO molecular emission, using ALMA science verification data of the CO(6-5) transition, see Figure 2.5. The very high angular resolution of these data reveal an infall associated with source B and that a bow shock from source A coincides, in the plane of the sky, with the position of source B.

In the 2014, Girart et al. (2014) presented CO 3–2, SiO 8–7, C^{34}S 7–6, and 878 μm dust continuum sub-arcsecond angular resolution observations with the SMA (Submillimeter Array), see Figure 2.6. These authors also concluded that the E-W and NW-SE outflow are both driven by the protostars of source A, which are embedded in a circumbinary disk traced by the 878μm continuum and the C^{34}S 7–6 emission. They also claimed that, according to the SiO(8-7) emission, the NW-SE outflow seems to be impacting on I16293B. In conclusion, all these results show that most (if not all) of the

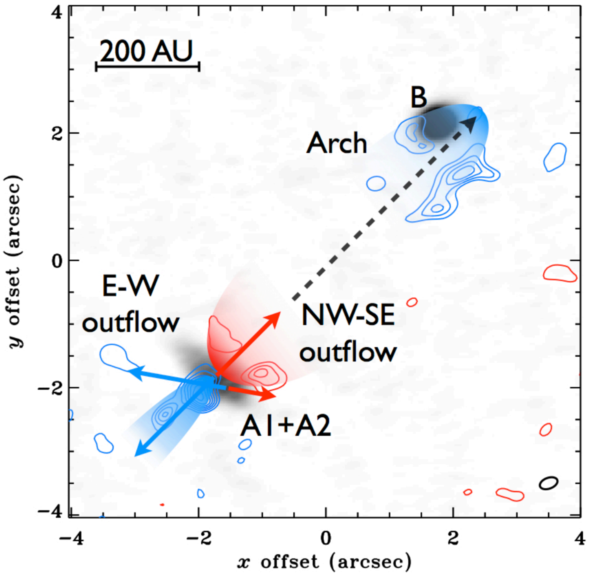

FIGURE 2.5: The CO J=6-5 emission integrated over the highest velocities. The different features are highlighted by arrows and are labeled. The black dashed arrow is an extrapolation of the red lobe of the NW-SE outflow (Kristensen et al. 2013).

outflows come from the A sources, while source B shows only little, if any, outflow activity.

2.1.3 The chemical structure

One can ask, what is remarkable in the chemistry of IRAS16293 and star formation regions in general? The answer needs to consider the following points:

1. The chemistry controls important physical parameters such as the level of ionization and the cooling of the gas.
2. Molecules formed trace the gas in more or less optically thick regions.
3. Gas-dust interactions lead to freeze-out during the core collapse and desorption during the warm-up phase.
4. The desorption is a thermometer of gas during the warm-up phase.
5. Astrochemistry is time-dependent, so the chemistry defines an evolutionary age.

In Table 2.1 and Figure 2.7, I summarized all the species detected in IRAS16293 so far. This source has been the subject of numerous far-infrared, millimetre and centimetre wavelength observations, just as Orion KL has done for high mass protostars, which have revealed its rich chemistry and its exceptional high deuterium fractionation (Ceccarelli et al. 2007). In the following I will briefly summarize the history of the chemistry studies in IRAS16293.

The story of IRAS16293 chemistry started in the mid-nineties of the last century with the first unbiased survey observations by (Blake et al. 1994; van Dishoeck et al. 1995). Ceccarelli et al. (1996) developed the first model of the thermal structure of

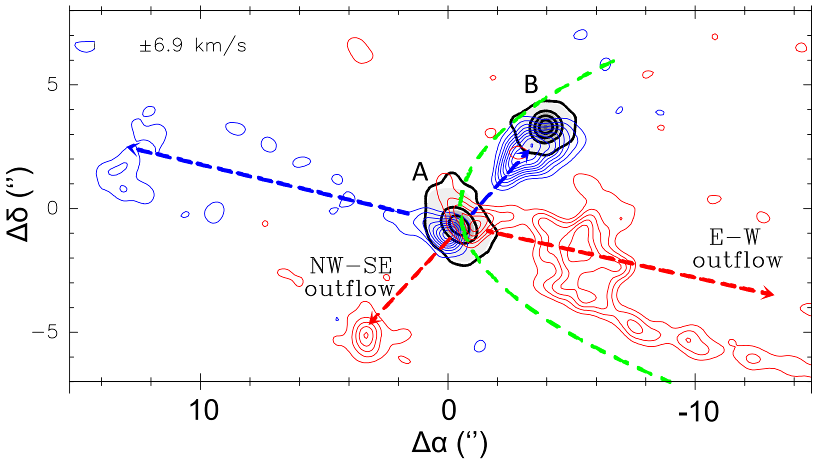

FIGURE 2.6: Map of the CO 3-2 for the blue-shifted (blue contours) and redshifted (red contours) emission, overlapped with the 878 μm dust emission (black contours and grey scale), the outflow velocity is indicated in the top left corner of panel (Girart et al. 2014).

TABLE 2.1: Species detected in the protostar IRAS16293-2422.

Species	Name	Species	Name
$^{(1)}$NH	Nitrogen monohydride	$^{(2)}H_2CO$	Formaldehyde
$^{(2)}$CN	Cyanogen	$^{(2)}C_3H$	Propynylidyne
$^{(1)}N_2$	Nitrogen	$^{(2)}$HNCO	Isocyanic acid
$^{(2)}$CO	Carbon monoxide	$^{(3)}H_2CS$	Thioformaldehyde
$^{(2)}$NO	Nitric oxide	$^{(2)}C_3H_2$	Cyclopropenylidene
$^{(2)}$CS	Carbon monosulfide	$^{(2)}H_2CCO$	Ketene
$^{(3)}$SiO	Silicon monoxide	$^{(6)}$HCOOH	Formic acid
$^{(4)}$NS	Nitrogen monosulfide	$^{(2)}C_4H$	Hydrogen tetracarbon
$^{(2)}$SO	Sulfur monoxide	$^{(2)}HC_3N$	Cyanoacetylene
$^{(1)}NH_2$	Amidogen	$^{(7)}NH_2CHO$	Formamide
$^{(5)}H_2O$	Water	$^{(2)}CH_3OH$	Methanol
$^{(2)}C_2H$	Ethynyl	$^{(2)}CH_3CN$	Methyl cyanide
$^{(2)}$HCN	Hydrogen cyanide	$^{(8)}CH_3SH$	Methanethiol
$^{(2)}$HNC	Hydrogen isocyanide	$^{(2)}CH_3CCH$	Methyl acetylene
$^{(2)}HCO^+$	Formyl ion	$^{(6)}CH_3CHO$	Acetaldehyde
$^{(3)}H_2S$	Hydrogen sulfide	$^{(9)}HC_5N$	Cyanodiacetylene
$^{(3)}HCS^+$	Thioformyl ion	$^{(6)}HCOOCH_3$	Methyl formate
$^{(2)}C_2S$	Dicarbon sulfide	$^{(10)}HCOCH_2OH$	Glycolaldehyde
$^{(3)}$OCS	Carbonyl sulfide	$^{(6)}CH_3OCH_3$	Dimethyl ether
$^{(2)}SO_2$	Sulfur dioxide	$^{(6)}C_2H_5CN$	Ethyl cyanide
$^{(1)}NH_3$	Ammonia	$^{(11)}(CH_2OH)_2$	Ethylene glycol

(1) Hily-Blant et al. (2010); (2) van Dishoeck et al. (1995); (3) Blake et al. (1994); (4) Chandler et al. (2005); (5) Coutens et al. (2012); (6) Cazaux et al. (2003); (7) Kahane et al. (2013); (8) Majumdar et al. (2016); (9) Parise et al. (2004); (10) Jørgensen et al. (2012); (11) Jørgensen et al. (2016).

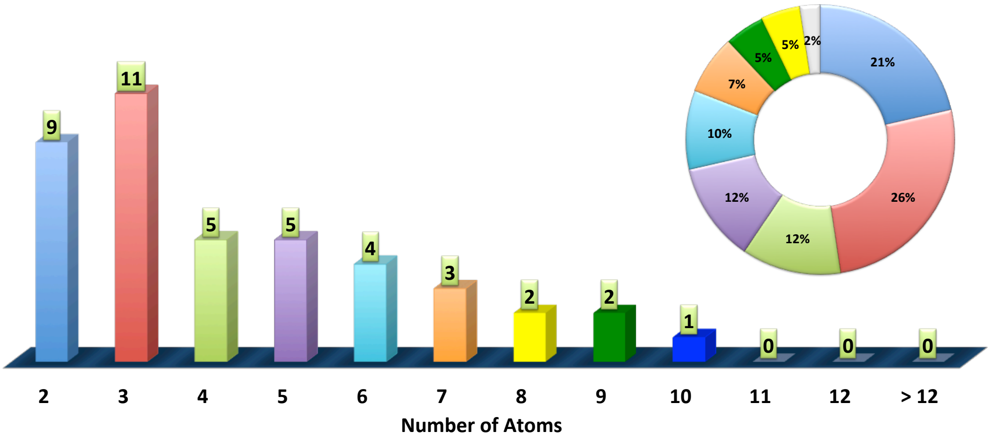

FIGURE 2.7: Number of detected molecules in IRAS16293 as a function of their number of atoms and the corresponding percentage.

this low-mass protostellar envelope. For this, they considered an inside-out collapse model where the physical conditions and the chemical content were defined to scales of $\sim$ 10 AU, in order to compute the resulting line emission. In this model, the gas temperature in the innermost regions of the envelope increases over $\sim$ 100 K, resulting in a sublimation of H_2O from grain mantles.

Ceccarelli et al. (1998b), using the Mid-IR (MIR) observations obtained with the low wavelength spectrometer (LWS) on board of the Infrared Space Observatory (ISO) satellite, revealed a rich molecular spectrum dominated by the OI (63μm) line and the CO, H_2O and OH rotational lines. These observations also showed the presence of weak, diffuse and uniform CII (157μm) emission, interpreted as the result of the illumination of the cloud by a faint UV-field. Ceccarelli et al. (1998b) also concluded that the narrow profile of the CI (609μm) line indicates that this species probes the quiescent material around the source. Combining the high CO J_{up} = 14 to 25 observed emissions with the CO J_{up}= 6 measurements, these authors obtained limits on the density, temperature and column density of the emitting gas of 3 x $10^4 cm^{-3}$,$\sim$ 1500 K, and 1.5 x $10^{16} cm^{-2}$, respectively. They conclude that the relatively low H_2O abundance ($\sim$ 2 x $10^{-5} H_2$) reflects either that most of O is locked into grains, or that the time scale required to convert gaseous O to H_2O is larger than the outflow dynamical scale, or both (Ceccarelli et al. 1998b).

In 2000 a modelling by Ceccarelli et al. (2000a) for the H_2O, O, SiO emission lines showed that they come from an envelope collapsing towards a protostar of mass 0.8 $M_\odot$ at a rate of 3.5 x 10^{-5} $M_\odot yr^{-1}$.

The same year, Ceccarelli et al. (2000b) reported the detection of the H_2CO and $H_2^{13}CO$ line emissions. They developed a model in which H_2CO lines were found to be emitted by two components: a cold H_2CO-poor outer envelope and a warm H_2CO-rich core. Their model calculations showed a dramatic increase in the abundances of H_2CO, H_2O, and SiO in the inner, warmer and denser region of the envelope, the so-called "hot corino". This change occurs when the dust temperature exceeds 100 K, corresponding to the grain mantles evaporation and injection of their mantle species in the gas-phase.

In 2003, Cazaux et al. (2003) revealed the presence of abundant complex organic molecules, COMs, in IRAS16293. More generally, when compared to massive hot cores, hot corinos seem to possess larger quantities of COMs, by about a factor of 10. An example of the detected COMs in the studied hot corinos sources, is given in Ceccarelli (2007) and Taquet et al. (2015), while a complete up-to-date list of all observed COMs in the Universe is given in CDMS (Müller et al. 2005) databases (*http://www.astro.uni-koeln.de/cdms/molecules*).

In 2013 Kahane et al. (2013), reported the first detection of formamide in the hot corino of IRAS16293. This COM is the simplest possible amide, and it could play a central role in the synthesis of metabolic and genetic molecules, the chemical basis of life. The abundance of formamide with respect to H_2 is $\sim 1.3\times10^{-10}$, which is similar to that found in the massive star-forming regions SgrB2 and Orion-KL, where this species has previously been detected.

Recently, several lines of the complex sulphur species CH_3SH were detected by Majumdar et al. (2016). Observed abundances were compared with simulations using the NAUTILUS[1] gas-grain chemical model. Modelling results suggest that CH_3SH has an abundance of 4×10^{-9} for radii lower than 200 AU and is mostly formed on the grain surface. From this identification of CH_3SH, the authors suggest that several new families of S-bearing molecules, starting from CH_3SH, should be looked for in IRAS16293.

As we stated previously, IRAS16293 is divided into two regions, warm inner part and cold outer envelope, each region having its own chemical properties (see for example Caux et al. (2011); Jørgensen et al. (2011), and reference therein). To clarify this point I show in Figure 2.8, adapted from (Caselli & Ceccarelli 2012), a sketch of the distribution for detected chemical species of IRAS16293, based on the analysis of the single-dish unbiased spectral millimeter and sub-millimeter survey carried out by Caux et al. (2011) and confirmed by the submillimeter interferometric unbiased survey of Bottinelli et al. (2004), Chandler et al. (2005) and Jørgensen et al. (2011). Four groups of species are identified:

1. Group I : Millimeter lines from simple molecules, like CN and HCO^+, are dominate in the cold envelope. Also, emission from simple carbon-chains are associated with the cold envelope.

2. Group II : Source A is rich in N- and S- bearing molecules.

3. Group III : Source B is rich in O-bearing COMs.

4. Group IV : Molecules like CH_3OH, H_2CO, CH_3CCH and OCS emit low-lying lines in the cold envelope and high-lying lines in the two sources A and B.

An obvious question is: why are source A and B so chemically different? A similar composition would be expected as they are formed from the same parent cloud. The difference is probably originating from the different evolutionary status caused by the difference in mass of the two objects (Bottinelli et al. 2004; Caux et al. 2011; Pineda et al. 2012). However, so far no attempt has appeared in the literature to theoretically model the two sources separately to understand what exactly causes the observed chemical differences.

---

[1] NAUTILUS: chemical code which computes the abundances of species (e.g. atoms, ions, radicals, molecules) as a function of time in the gas phase and at the surface of the interstellar grains. All the equations and physicochemical processes included in the model were discussed in detail in Reboussin et al. (2014) and in Ruaud et al. (2015).

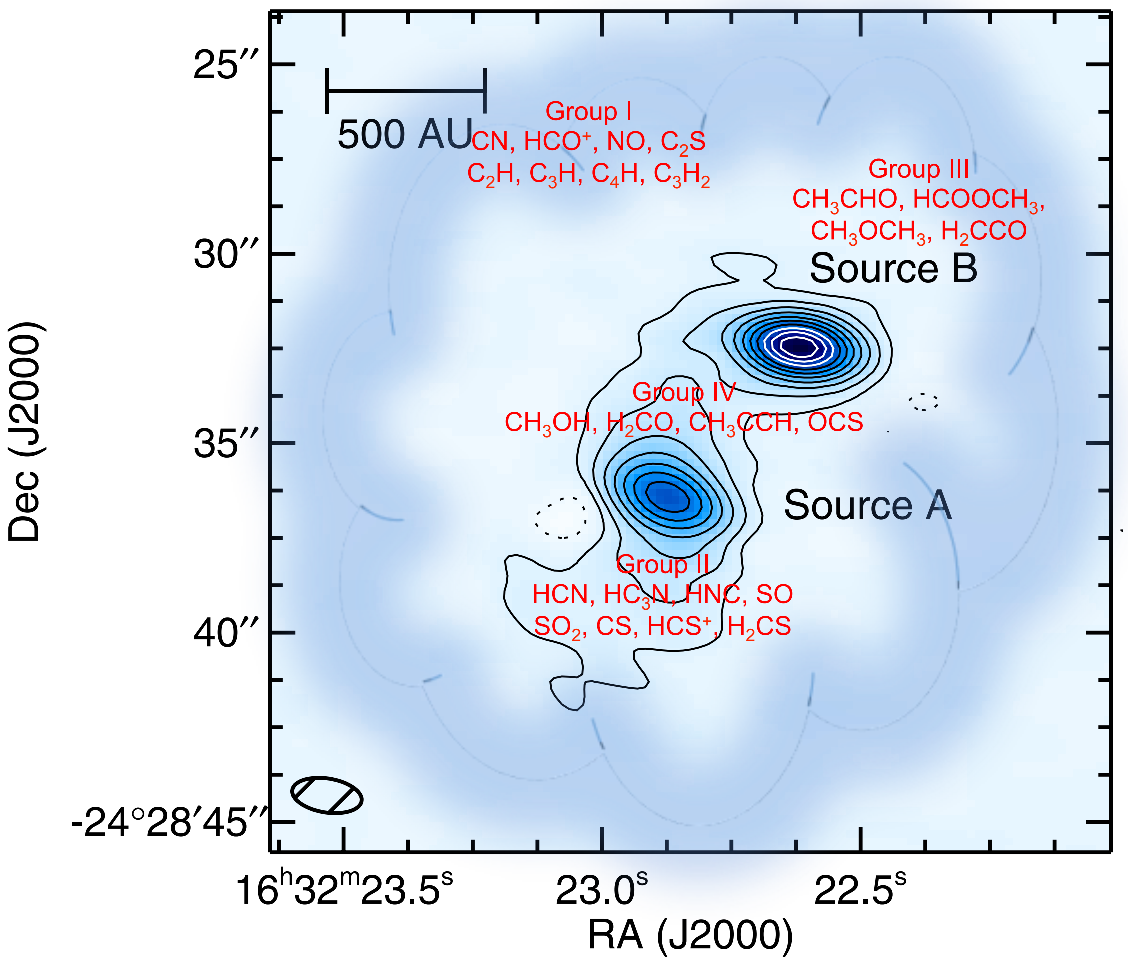

FIGURE 2.8: Chemical composition of the IRAS16293, a protobinary system composed of two sources, A and B, as marked. The four groups list the species in the different components of the system: species in Group I are associated with the cold envelope surrounding A and B; species in Group II are associated with source A and in Group III with source B; species in Group IV are present in the cold envelope and the two sources. Map from (Pineda et al. 2012).

2.1.4 Deuteration in IRAS16293

Deuterium (D) is an isotope of hydrogen. As a large number of molecules and reactions are hydrogen-dominated, the importance of deuterium chemistry is clear. It mainly involves the study of the relative abundances between the deuterated and the undeuterated analogue (hence on referred to as D/H ratio). There is an observed elemental D/H ratio $\sim 1.5\times10^{-5}$ (Linsky et al. 2006). However, many deuterated molecules with high abundances are detected in star forming regions. The first deuterated molecule DCN, was discovered by Jefferts et al. (1973) in the Orion cloud. Since then, many mono-deuterated molecules were discovered: HD, HDO, DCO^+, DNC, NH_2D, HDCO, etc. The first detection of the doubly deuterated molecule D_2CO in Orion cloud by Turner (1990) represents an important step.
van Dishoeck et al. (1995) observed several deuterated species towards IRAS16293, namely, DCO^+, DCN, C_2D, HDS, HDCO, NH_2D, detected in the different regions around this source. The first region is the warm and dense inner core (T$\geq$80 K, nH $\sim 10^7$ cm^{-3}) found to be rich with organic molecules, the second is the circumbinary envelope with T$\sim$ 40 K and nH$\sim 10^6$ - 10^7 cm^{-3}, where molecules such as DCO^+ and HDCO where found, and the third is the colder, low-density outer part of the envelope with T$\sim$ 10-20 K and nH$\sim 10^4$ - 10^5 cm^{-3} with radicals such as CN, C_2H, C_3H_2.
Ceccarelli et al. (1998a) gave a new boost to the deuteration studies when they reported the first doubly deuterated species, D_2CO, in the vicinity of IRAS16293. This discover showed that IRAS16293 is a true gold mine for studies of deuterated molecules, with ratios of deuterated species relative to the normal ones orders of magnitude higher than the overall [D]/[H] ratio of $\sim 1.5\times\ 10^{-5}$ and motivate the search for new multi deuterated molecules. Two triply deuterated molecules have been detected: ND_3 (Lis et al. 2002) and CD_3OH (Parise et al. 2004), with a D/H of about 10^{-3} for ammonia and 10^{-2} for methanol, or about 11-12 orders of magnitude above the elemental D/H. This deuterium fraction can be increased up to a factor of 10^{9-13} for doubly and triply deuterated species like D_2CO and CD_3OH (Ceccarelli et al. 2007).
In 2004, Stark et al. (2004) observed H_2D^+, DCO^+, HCO^+, HDO and H_2O toward IRAS16293. They measured the H_2D^+ abundance to be 2×10^{-9} in the cold outer envelope with $nH_2 = 10^4$ -10^5 cm^{-3} and T < 20 K. While DCO^+ and HCO^+ were observed with abundances 2×10^{-11} and $< 1\times10^{-9}$ respectively. HDO was observed with abundance 3×10^{-10}, finally, the observed abundance of H_2O is 4×10^{-9} in the cold regions of the envelope and 3×10^{-7} in warmer regions. The [HDO]/[H_2O] abundance in the warm inner envelope of IRAS16293 ($\sim 2\times10^{-4}$) is close to the value that has been measured in the Solar Systems.
In 2012, Coutens et al. (2012) have observed multiple lines of HDO and $H_2^{18}O$ towards IRAS16293A with an estimated D/H $\sim$ 0.034 in the hot corino region and D/H $\sim$ 0.005 in the outer envelope, utilizing a standard isotopic ratio of $H_2^{18}O/\ H_2^{16}O = 500$.
In the same year, Parise et al. (2012) observed for the first time the OD radical outside the Solar System in IRAS16293, by using the GREAT instrument[2] receiver on board SOFIA(Stratospheric Observatory for Infrared Astronomy), they observed the ground-state OD transition at 1391.5 GHz. They also present the detection of the HDO 1_{11} - 0_{00} line using the APEX(Atacama Pathfinder EXperiment) telescope and they found a high OD/HDO ratio of $\sim$ 10 - 100.

---

[2] GREAT is a development by the MPI fur Radioastronomie and the KOSMA/Universitat zu Koln, in cooperation with the MPI fur Sonnensystemforschung and the DLR Institut fur Planetenforschung.

TABLE 2.2: Deuterated species detected in the interstellar medium from Tielens (2005).

Mono-deuterated			Doubly deuterated		Triply deuterated
HD	H_2D^+	CH_3OD	D_2H^+	CHD_2OH	ND_3
OD	HDO	CH_2DOH	D_2O	CH_2DCCD	CD_3OH
ND	NH_2D	CH_3CCD	NHD_2	CHD_2CCH	
HDS	HDCS	CH_2DCCH	D_2S	D_2CO	
CCD	C_4D	HDCO	D_2CS		
DNC	DCN	CH_2DCN			
DC_3N	DC_5N				
N_2D^+	DCO^+				

In 2013, Coutens et al. (2013b) used the Herschel/HIFI[3] to observe ortho–D_2O at 607 GHz and para–D_2O at 898 GHz. They show that the component seen in absorption in the D_2O lines requires a D_2O/H_2O ratio of about 0.5%. At a 3σ uncertainty, upper limits of 0.03% and 0.2% were obtained for this ratio in the hot corino and the colder envelope respectively. Recently, deuterated formamide has been reported in IRAS16293 by Coutens et al. (2016), measured from ALMA observations, unbiased, high angular resolution and sensitivity spectral survey. Authors reported three singly deuterated forms of NH_2CHO (NH_2CDO, cis- and trans-NHDCHO), besides DNCO towards the IRAS16293-B. Similar deuterium fractionation for the three different forms with a value of $\sim$ 0.02, and $\sim$ 0.01 for DNCO/HNCO ratio, have been stated in this study. The different deuterated molecules detected in the interstellar medium are listed in Table 2.2. In IRAS16293, (18) mono-deuterated, (3) doubly-deuterated and (1) triply-deuterated molecules, distributed between hot corino and cold outer envelope have been detected ; they are listed in Table 2.3. The high deuteration ratios and the various ratios observed for a given molecule (e.g., CDH_2OH versus CH_3OD) may provide important clues on the chemical pathways toward the formation of the complex organics in IRAS16293. They are shown in Figure 2.9.

This summary of the COMs and deuterated species detected so far in IRAS16293 shows that it is a very chemically rich source. In addition, IRAS16293 shows a complex structure : two protostellar sources A and B (A itself is composed of two sources, each one emitting a molecular outflow) embedded in a circumbinary envelope, and at least two outflow traversing the envelope.

In the next chapters I shall present additional observations, which still enrich this molecular content. To interpret these molecular emissions, I shall use a model which assumes a simplified IRAS16293 structure, composed of an inner hot corino and outer cold envelope.

2.2 OMC-2 FIR4

The Orion Molecular Cloud is the nearest giant complex molecular cloud, located at a distance of ~420 pc (Menten et al. 2007; Hirota et al. 2007). This young (~ 10 Myr old) complex is divided into two fragments : Orion A and B. In addition, Orion A is formed by three sub-clouds OMC-1, OMC-2 and OMC-3, each containing numerous Class 0 protostars (Shimajiri et al. 2008). The sub-cloud OMC-2 was observed for the first time

---

[3] Herschel is an ESA space observatory with scientific instruments provided by European-led principal Investigator consortia and with important participation from NASA.

TABLE 2.3: Deuterated species detected towards the line of sight of IRAS16293 with abundance ratios.

Species	D/H Ratio		References
	Hot corino	Outer envelope	
ND	-	0.065±0.035	Bacmann et al. (2010)
OD	-	-	Parise et al. (2012)
HDO	0.028	0.009	Coutens et al. (2013a)
D_2O	≤ 0.0003	≤ 0.002	Coutens et al. (2013b)
C_2D	-	0.18±0.09	van Dishoeck et al. (1995)
DCN	-	0.013±0.0065	van Dishoeck et al. (1995)
DNC	-	0.03±0.015	van Dishoeck et al. (1995)
DCO^+	-	0.0086±0.0043	van Dishoeck et al. (1995)
HDS	-	0.1±0.05	van Dishoeck et al. (1995)
NH_2D	-	0.1±0.05	van Dishoeck et al. (1995)
HDCO	0.15±0.07	-	Loinard et al. (2000)
D_2CO	0.05±0.025	-	Loinard et al. (2000)
HDCS	-	0.1±0.05	van Dishoeck et al. (1995)
DNCO	~0.01	-	Coutens et al. (2016)
c-C_3HD	-	-	Caux et al. (2011)
DC_3N	≤ 0.05	0.5±0.2	Chapter 5 in this thesis
CH_2DOH	$0.37^{+0.38}_{-0.19}$	-	Parise et al. (2004)
CH_3OD	$0.018^{+0.022}_{-0.012}$	-	Parise et al. (2004)
CHD_2OH	$0.074^{+0.084}_{-0.044}$	-	Parise et al. (2004)
CD_3OH	1.4±0.014	-	Parise et al. (2004)
NH_2CDO	~0.02		Coutens et al. (2016)
CH_2DCCH	-	-	Caux et al. (2011)

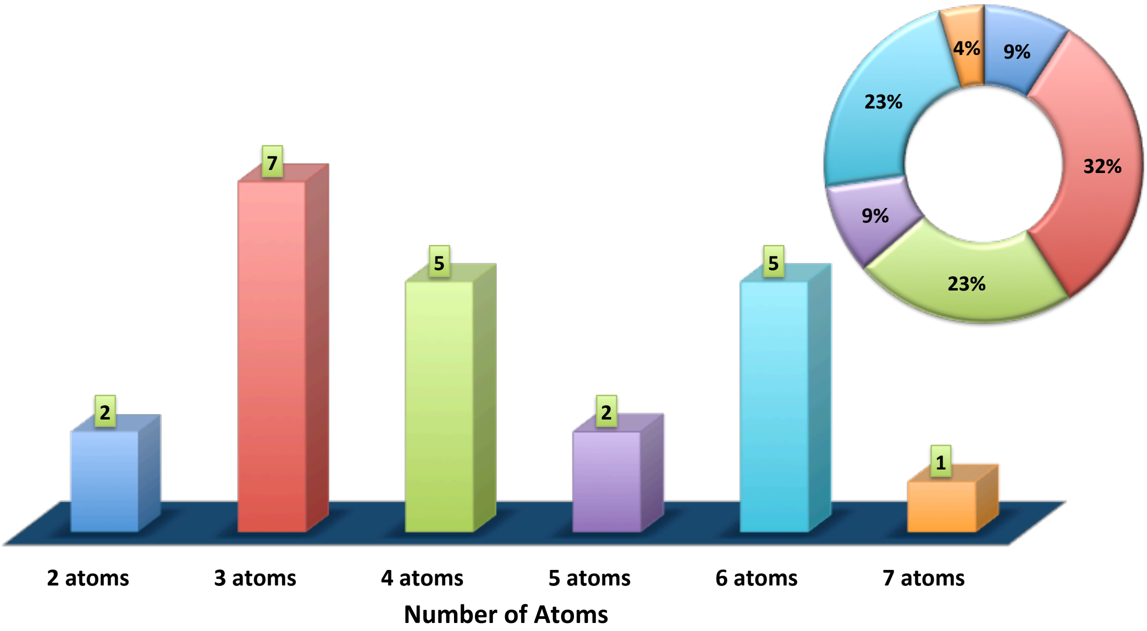

(A) Number (and corresponding percentages) of deuterated species, sorted by increasing number of constituting atoms.

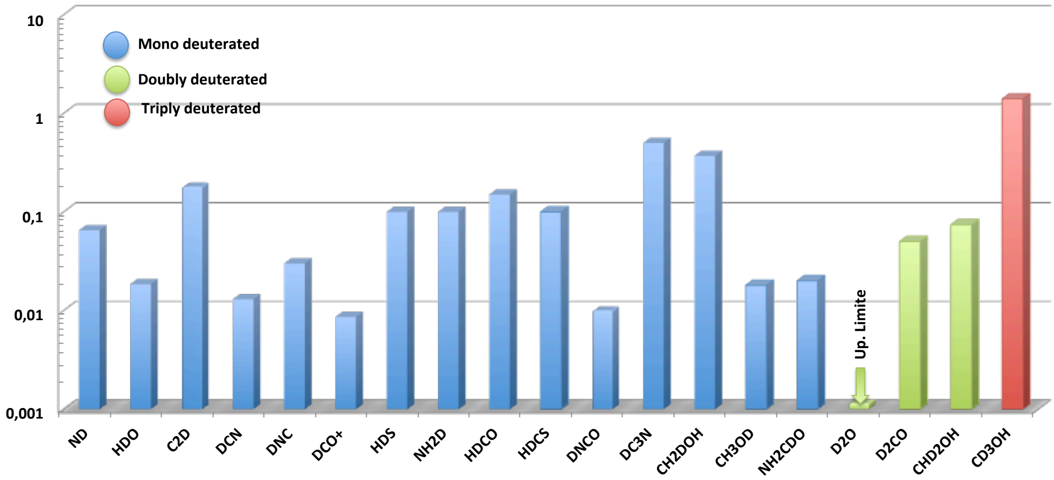

(B) Deuteration ratios.

FIGURE 2.9: Deuterated species detected in the IRAS16293 and inferred D/H ratios.

in the near-IR by Gatley et al. (1974). It lies about 2 pc north of the Trapezium, its mass is $\sim$ 102 $M_\odot$ (Bally et al. 1987), its luminosity $\sim$ 2000 $L_\odot$ (Thronson et al. 1978).
The brightest submillimeter (350-1300μm) source in the OMC-2 region is FIR 4. This source has a mass between 30 and 60 $M_\odot$. Figure 2.10 shows the position of OMC-2 FIR 4 relative to our Solar System (All dimensions are in parsecs relative to the center of Gould's belt[4]). OMC-2 FIR 4 is indeed a protocluster of intermediate-mass young stellar objects, where the near-infrared, mid-infrared and millimetre-wavelength emission peaks are all offset from one-another by $\sim$ 5″. Interferometric continuum observations at 2 and 3.3 mm showed a clumpy substructure at the 5″ scale, with the presence of at least three cores (Shimajiri et al. 2008; López-Sepulcre et al. 2013), see Figure 2.11.

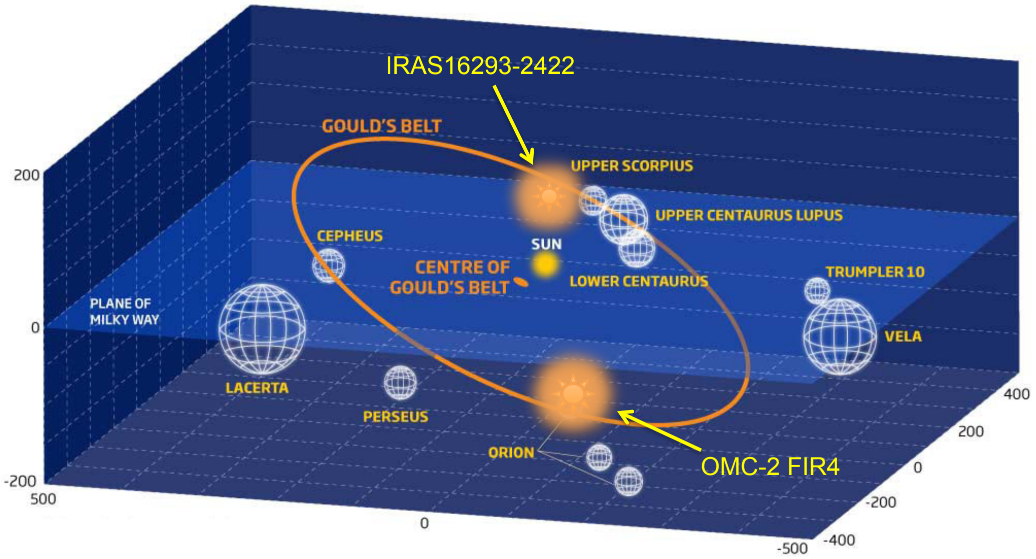

FIGURE 2.10: Plane of milky way showing position of OMC-2 FIR4 and IRAS16293 relative to our Solar System. Adapted from new scientist-website (2016).

OMC-2 FIR 4 is kinematically and chemically complex. Castets & Langer (1995) used the observations of $C^{32}S$ J=5-4 to report the outflows in OMC-2. Several studies followed this paper (e.g. Jørgensen et al. (2006); Shimajiri et al. (2008); Crimier et al. (2009); Kama et al. (2010)). These studies suggested that OMC-2 FIR 4 contains three main components. *1)*: Cool Envelope: large-scale cool envelope about 10000 AU (i.e. 0.05 pc) across. *2)*: Hot Core: An inner hot region, with kinetic temperatures above 100 K and around 400 AU in size. *3)*: Shock Region: produced by the interaction of an external bipolar outflow driven by the nearby OMC-2 FIR 3, which lies to the north-east of FIR 4. In addition Shimajiri et al. (2008) suggested the presence of 11 cores, seen at 3 mm inside this region, and speculated that such fragmentation has been externally triggered by the FIR 3 outflow. Successive observations with IRAM PdBI only detected 3 sources (López-Sepulcre et al. 2013).
Many evidence have been reported from kinematical and excitation considerations suggesting that FIR 4 hosts a compact outflow. Note that the detection of such an

---

[4] Gould's belt: our solar system is close to the center of a ring of OB stars, that is tilted with respect to the Milky Way's plan. Several giant molecular clouds, where star formation is going on, are also associated with this ring.

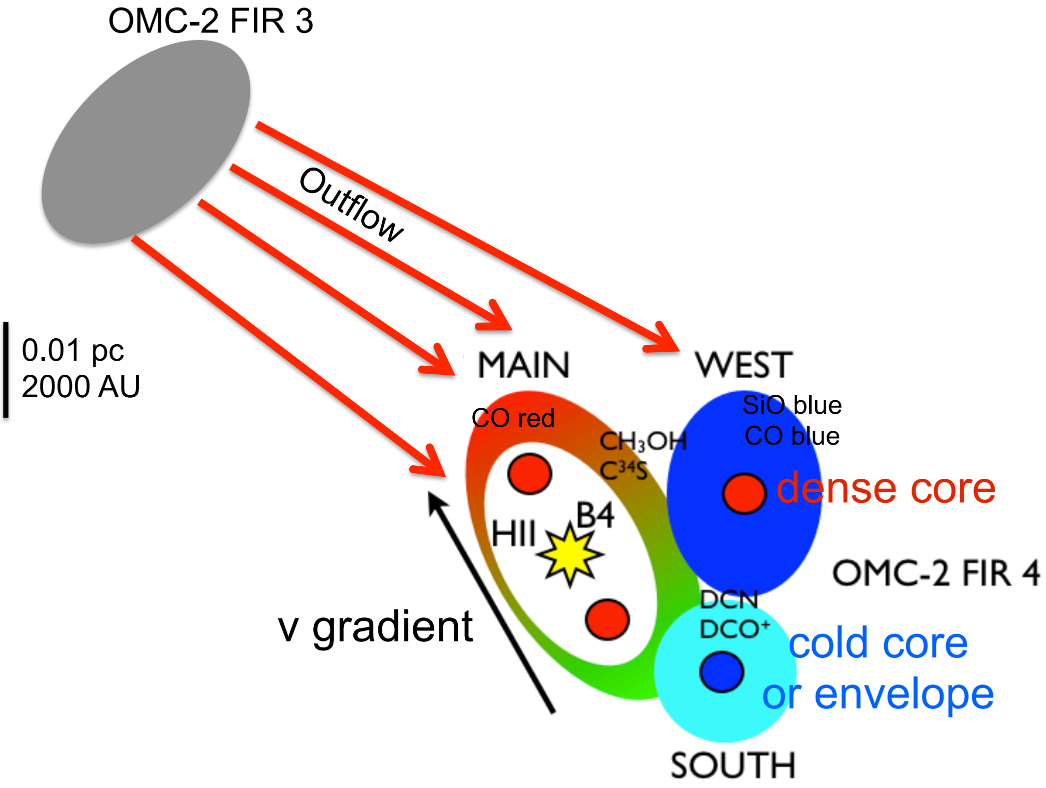

FIGURE 2.11: Schema of OMC-2 FIR 4 and the nearby OMC-2 FIR 3, summarising all the physical elements in the region. The white ellipse inside the main source depicts the ionised region powered by a B4 young star. The colours of the main, west, and south sources represent their systemic velocities with respect to the nominal value for OMC-2 FIR 4 (V_{LSR} = 11.4 km s^{-1}), marked in green. The small red and blue circles within the three sources represent the possibility that they harbour smaller unresolved molecular condensations, with the colour blue denoting a colder temperature than red. Adapted from López-Sepulcre et al. (2013).

outflow would be a key piece of evidence to support the interpretation of OMC-2 FIR 4 as a young protostar (Shimajiri et al. 2008). Recently, Furlan et al. (2014) find that the position of OMC-2 FIR 4, measured with the IRAC 4.5 μm image, is offset with respect to the position measured at 8-70 μm, but matches that of the radio continuum source detected at 3.6 cm by Reipurth et al. (1999). Both could be interpreted as emission from shocked gas in an outflow. Furthermore, there is evidence in favor of an outflow from far-IR line spectra (Manoj et al. 2013; Kama et al. 2013) based on velocity profiles, temperatures, and densities derived from CO lines. Note however that the CO emission although they may contain a contribution from an outflow driven by the nearby protostar OMC-2 FIR 3. In summary, these data support the idea that FIR 4 is indeed a protocluster, driving a compact outflow. In addition, its centimeter flux is consistent with that observed in outflows from other protostars with luminosities <100 $L_\odot$ (Anglada 1995). Finally, Shimajiri et al. (2015) reported the first line-survey observations at 82–106 GHz and 335–355 GHz toward FIR 4, using the Nobeyama 45 m and ASTE(Atacama Submillimeter Telescope Experiment) telescopes. They find that broad components of $C^{34}S$, SO, SiO, $H^{13}CN$, $HC^{15}N$, $H_2^{13}CO$, H_2CS, HC_3N, and CH_3OH are detected only towards FIR 4. Again, this is in favour of an outflow-shocked gas origin. Finally, recent Herschel observations have discovered the presence of a source of energetic (> 10 MeV) particles inside the OMC-2 FIR complex (Ceccarelli et al. 2014b).
OMC-2 FIR 4 is one of intermediate-mass chemically rich objects. In Table 2.4 I list all the detected molecules so far, and Figure 2.12 shows the number of detected molecules in OMC-2 FIR 4 as a function of their number of atoms. The origins of the chemical enrichment in this source is still under discussions.

TABLE 2.4: Species detected in the OMC-2 FIR 4. From Kama et al. (2013); Shimajiri et al. (2015); López-Sepulcre et al. (2015) and Jaber et.al. (in preparation).

Species	Name
NH	Nitrogen monohydride
CH	Methylidyne
CH^+	Methylidyne cation
CN	Cyanogen
CO	Carbon monoxide
CS	Carbon monosulfide
SiO	Silicon monoxide
SO	Sulfur monoxide
OH	Hydroxide radical
OH^+	Hydroxyl cation
SH^+	Mercapto radical
HF	Hydrogen fluoride
HCl	Hydrogen chloride
H_2O	Water
H_2O^+	Oxidaniumyl
C_2H	Ethynyl
HCN	Hydrogen cyanide
HNC	Hydrogen isocyanide
HCO^+	Formyl cation
H_2S	Hydrogen sulfide
HCS^+	Thioformyl ion
SO_2	Sulfur dioxide
N_2H^+	Diazenylium
NH_3	Ammonia
H_2CO	Formaldehyde
HNCO	Isocyanic acid
H_2CS	Thioformaldehyde
c-C_3H_2	Cyclopropenylidene
HC_3N	Cyanoacetylene
CH_3OH	Methanol
CH_3CN	Methyl cyanide
NH_2CHO	Formamide
CH_3CCH	Methyl acetylene
CH_3CHO	Acetaldehyde
HC_5N	Cyanodiacetylene

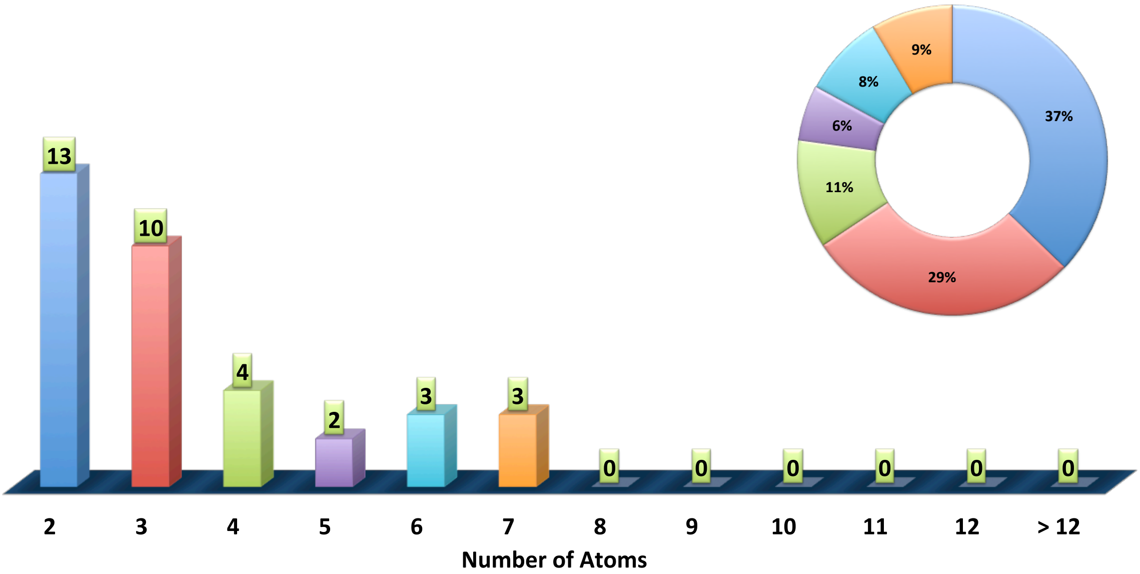

(A) Detected molecules with the percentage, sorted by increasing number of constituting atoms.

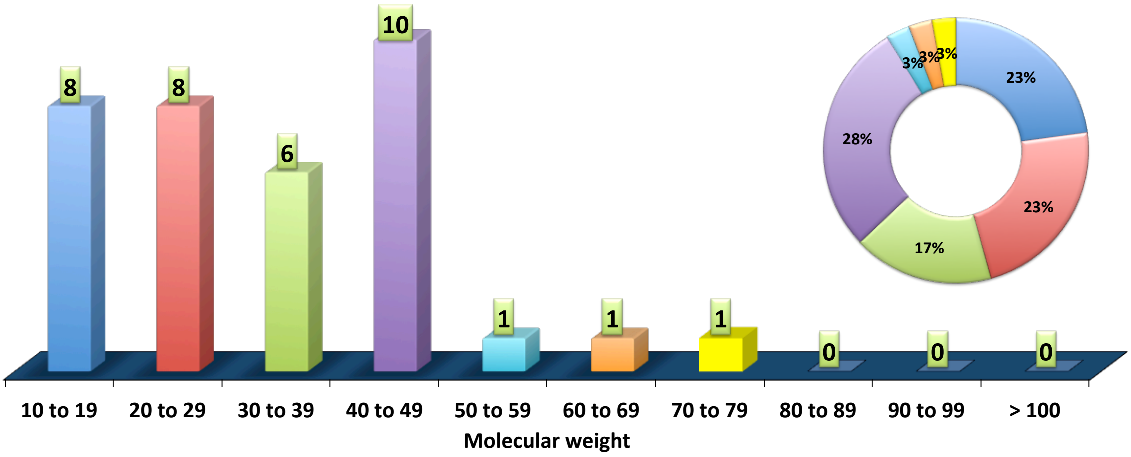

(B) Detected molecules with the percentage, sorted by molecular weight.

FIGURE 2.12: Molecules detected in the OMC-2 FIR 4. From Kama et al. (2013); Shimajiri et al. (2015); López-Sepulcre et al. (2015) and Jaber et.al. (in preparation).

Chapter 3

Used Tools

3.1 Overview

Limitations of available tools is one of the obstacles to overcome in order to explore and study the complex organic molecules (COMs) in the star formation regions. Since the beginning of astronomical science, observations at different wavelength has been the main approach, where, high spatial and spectral resolution observations, with high sensitivity, are generally sought after. To peer into the deep interior of the early stages of star formation we need to observe using radio telescopes, because these objects emit at long wavelengths roughly from 10 μm to a few mm and cm.

For my research project, I used radio observations from surveys performed with the IRAM 30m telescope, namely TIMASSS (The IRAS16293 Millimeter And Submillimeter Spectral Survey) and ASAI (Astrochemical Surveys at IRAM). The publicly available package CASSIS (Centre d'Analyse Scientifique de Spectres Instrumentaux et Synthétiques) has been used as a second tool for lines identification and to determine the observed line emission of molecules. The radiative transfer model GRAPES (GRenoble Analysis of Protostellar Envelope Spectra) is the third tool used to interpret them. Figure 3.1 represents this three tools and the sequence of utilisation.

FIGURE 3.1: The tools used in this thesis.

3.2 Spectral surveys

3.2.1 Context

Molecular content in star forming regions can be determined precisely from spectral surveys. Study of excitation and line shapes of individual species can be used to analyse physical and chemical conditions in regions where these species are coming from, thus allowing us to understand the complex chemistry in these regions.

From different viewpoints, unbiased spectral surveys studies are valuable tools to investigate the star formation process. They give access to different lines from the same molecule, permitting multi-frequency analysis and modelling. Since lines corresponding to different upper level energies and Einstein coefficients are excited at different

TABLE 3.1: TIMASSS Parameters of the observations at IRAM-30 m and JCMT-15 m telescopes. Adapted from Caux et al. (2011).

Telescope	Frequency	Resolution		Backend$^{(1)}$	rms$^{(2)}$	Tsys	HPBW
	(GHz)	(MHz)	(Km.s^{-1})		(mK)	(K)	(arcsec)
IRAM	80-115.5	0.32	0.81-1.17	VESPA	2-8	90-400	30-21
IRAM	129-177	0.32	0.53-0.72	VESPA	5-14	200-1000	19-14
IRAM		1.0	1.65-2.25	1 MHz FB			
IRAM	197-265	1.0	1.13-1.52	1 MHz FB	7-13	180-1200	12-9
IRAM		1.25	1.41-1.90	VESPA			
IRAM	265-280	1.25	1.34-1.41	VESPA	9-17	470-4200	9
JCMT	328-366	0.625	0.51-0.57	ACSIS	4-9	90-400	14

(1) In the 2mm band, each frequency setting is observed twice, i.e., once at each of the two spectral resolutions (0.32 and 1 MHz), while in the 197-265 GHz band, each frequency setting is observed only one time, at a slightly different spectral resolution (1 or 1.25 MHz), (2) rms is given in 1.5km.s^{-1} bins.

temperatures and densities, they can probe several regions in the line of sight. Therefore, a careful analysis can distinguish between the various physical components in the beam even without the spatial resolution, in some cases . If one adds also the kinematic information provided by the line profiles, the method can be so powerful that it can identify sub-structures in the line of sight, even if the spatial resolution of the observations is too low to solve them. Because of this diagnostic power, several unbiased spectral surveys have been obtained in the past in the millimeter and sub-millimeter bands accessible from ground in the direction of star forming regions. List of these surveys can be found in Herbst & van Dishoeck (2009) and Caselli & Ceccarelli (2012). For my work, I used the following spectral survey projects:

3.2.2 TIMASSS

The observational data from The IRAS16293 Millimeter And Submillimeter Spectral Survey (**TIMASSS**: *http://www-laog.obs.ujf-grenoble.fr/heberges/timasss/*; Caux et al. (2011)) were used for this project. Briefly, the survey covers the 80-280 and 328-366 GHz frequency intervals and it was obtained at the IRAM-30m and JCMT-15m telescopes during the period from January 2004 to August 2006. Overall, the observations required a total of about 300 hours (∼ 200hr at IRAM and ∼100hr at JCMT) of observing time. Details on the data reduction and calibration can be found in Caux et al. (2011). Observations are centered on IRAS16293B at α(2000.0) = $16^h\ 32^m\ 22^s.6$, δ(2000.0)= $-24^o\ 28'\ 33''$. The A and B components are both inside the beam of observations at all frequencies. Parameters of the observations are listed in Table (3.1).

3.2.3 ASAI

The Large Program (**ASAI**:**A**strochemical **S**urveys at **I**RAM), carried out at the IRAM 30m telescope joins the efforts of several groups in astrochemistry in Spain and France, to address the question of our "chemical origins". ASAI goal is to obtain a complete census of the gas chemical composition, its evolution along the main stages of the star formation process, from prestellar cores and protostars to protoplanetary disks, in order to understand the processes which govern the emergence of molecular complexity,

TABLE 3.2: ASAI: Source sample and their properties. Adapted from López-Sepulcre et al. (2015).

Source	R.A.(J2000)	Dec.(J2000)	V_{lsr} (km s^{-1})	d (pc)	M ($M_\odot$)	L_{bol} ($L_\odot$)	Type*
L1544	05:04:17.21	+25:10:42.8	+7.3	140	2.7	1.0	PSC
TMC1	04:41:41.90	+25:41:27.1	+6.0	140	21	-	PSC
B1	03:33:20.80	+31:07:34.0	+6.5	200	1.9	1.9	Class 0
L1527	04:39:53.89	+26:03:11.0	+5.9	140	0.9	1.9	Class 0,WCCC
L1157-mm	20:39:06.30	+68:02:15.8	+2.6	325	1.5	4.7	Class 0
IRAS 4A	03:29:10.42	+31:13:32.2	+7.2	235	5.6	9.1	Class 0, HC
SVS13A	03:29:03.73	+31:16:03.8	+6.0	235	0.34	21	Class 0/1
OMC-2 FIR 4	05:35:26.97	05:09:54.5	+11.4	420	30	100	IM proto-cluster
Cep E	23:03:12.80	+61:42:26.0	-10.9	730	35	100	IM protostar

*PSC: pre-stellar core; HC: hot corino; WCCC: warm carbon-chain chemistry; IM: intermediate-mass.

and the formation of pre-biotic molecules. This is achieved through highly sensitive and systematic spectral line surveys of a sample of sources illustrative of the various stages of protostellar evolution. Observations and data reduction procedures are presented in detail in López-Sepulcre et al. (2015). Briefly, the spectral data were obtained in several observing runs between 2011 and 2014 using the EMIR receivers at 3 mm (80–116 GHz), 2 mm (129–173 GHz), and 1.3 mm (200– 276 GHz), see Table 3.2.

3.3 Lines identification

This step uses the CASSIS tools package (see §3.3.2). Figure 3.2 shows a snapshot of the CASSIS screen used for line identification. For the analysis of the molecular line emission presented in my thesis, I only consider lines identified according to the criteria discussed in the next sub-section.

3.3.1 Criteria for identification

This point will again be discussed in detail in Chapter 5. Briefly, to secure my modelling, I take into account only the lines identified according to the following criteria:

1. The line is included in the JPL (Pickett et al. 1998) or / and CDMS (Müller et al. 2005) databases.
2. The line is detected with a S/N ratio larger than 3σ in terms of integrated line intensity derived from a gaussian fit to the line. Figure 3.3 shows such gaussian fits to the spectral lines of HC_5N, one of the molecules studied in Chapter 5.
3. The line is not severely blended with an other molecular line.
4. The line integrated intensity is compatible with the general behaviour of the molecule Spectral Line Energy Distribution (SLED) (see the upper panel of Figure 3.4).
5. The line shows a V_{LRS} central velocity, derived from the gaussian fit, compatible with the general behaviour of the V_{LRS} of the other lines, as shown in figure 3.4, middle pannel.

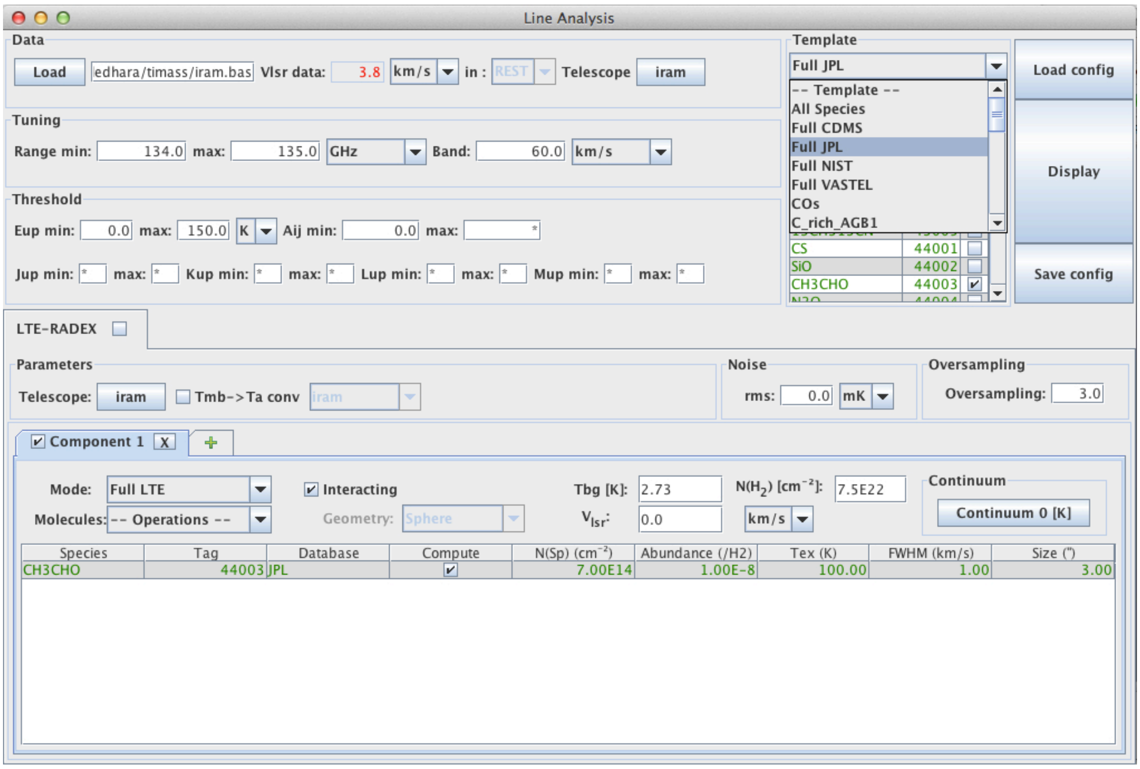

Data

Load | edhara/timass/iram.bas | Vlsr data: 3.8 km/s | in : REST | Telescope iram

Tuning

Range min: 134.0 max: 135.0 GHz Band: 60.0 km/s

Threshold

Eup min: 0.0 max: 150.0 K Aij min: 0.0 max: *

Jup min: * max: * Kup min: * max: * Lup min: * max: * Mup min: * max: *

Template

Full JPL

- -- Template --
- All Species
- Full CDMS
- Full JPL
- Full NIST
- Full VASTEL
- COs
- C_rich_AGB1

CS	44001	☐
SiO	44002	☐
CH3CHO	44003	☑

Parameters

Telescope: iram ☐ Tmb->Ta conv iram

Noise

rms: 0.0 mK

Oversampling

Oversampling: 3.0

☑ Component 1 X

Mode: Full LTE ☑ Interacting Tbg [K]: 2.73 N(H_2) [cm^{-2}]: 7.5E22

Molecules: -- Operations -- Geometry: Sphere V_{lsr}: 0.0 km/s

Continuum

Continuum 0 [K]

Species	Tag	Database	Compute	N(Sp) (cm^{-2})	Abundance (/H2)	Tex (K)	FWHM (km/s)	Size (")
CH3CHO	44003	JPL	☑	7.00E14	1.00E-8	100.00	1.00	3.00

FIGURE 3.2: Snapshot of the CASSIS panel showing some available databases, among them, the CDMS and JPL databases.

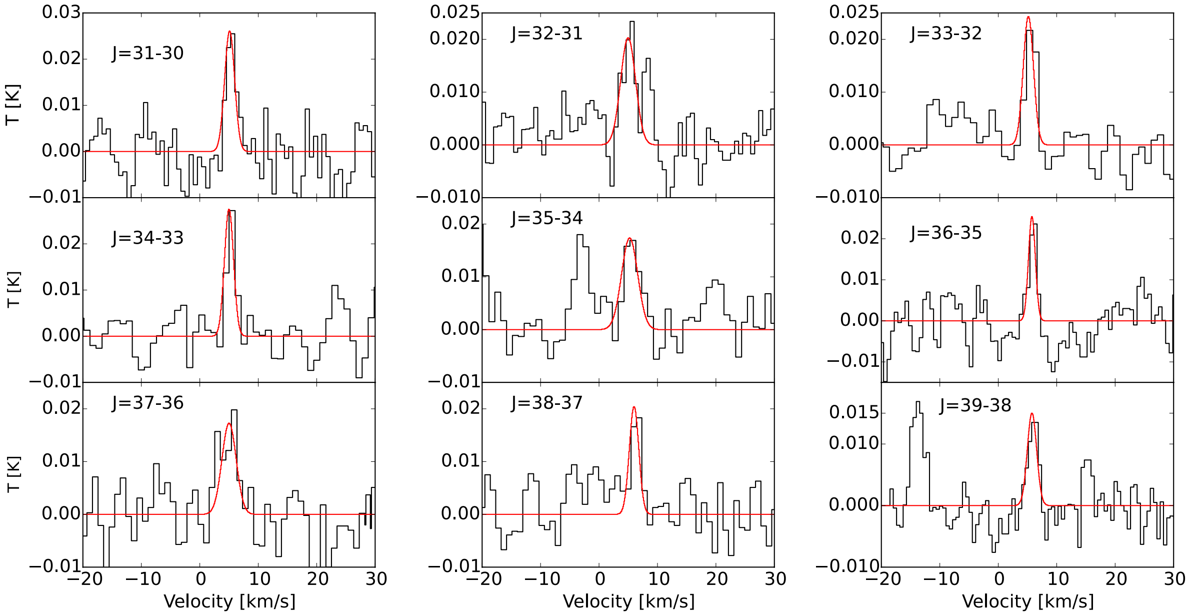

FIGURE 3.3: Spectral lines of HC_5N in IRAS16293-2422, as an example of the molecules studied in my thesis. The red curves show the Gaussian fits computed with the CASSIS tool.

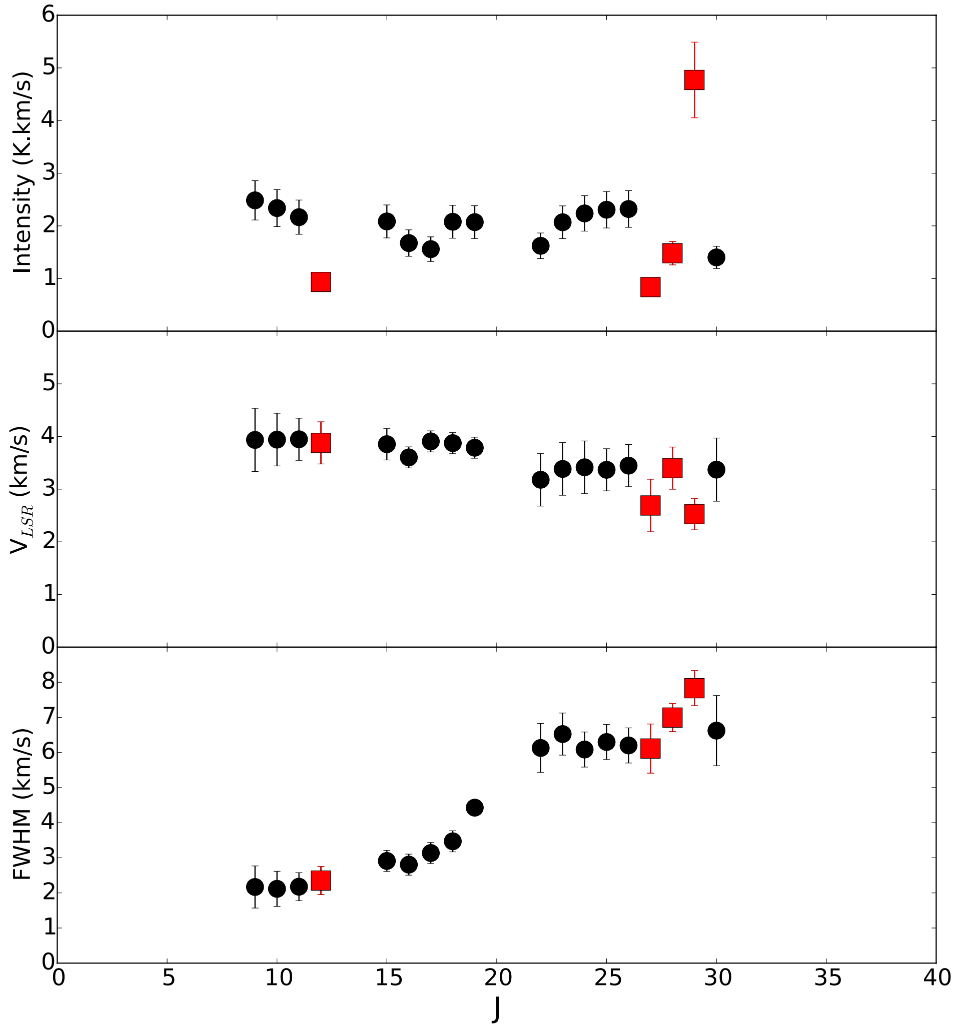

FIGURE 3.4: IRAS16293-2422 observation. HC$_3$N integrated line intensity (upper panel), rest velocity V$_{LSR}$ (middle panel) and FWHM (bottom panel) derived from a gaussian fit to the lines, as a function of the upper J of the transition. The red square points show the lines that have been discarded because they do not satisfy at least to one of the criteria 4 to 6 of (§3.3.1) (see text).

6. The line shows a FWHM line width, derived from the gaussian fit, compatible with the general behaviour of the FWHM of the other lines, as shown in Figure 3.4, bottom pannel.

Application of these criteria has led me to rule out some lines showing abnormal values of intensity, velocity and/or FWHM, as shown in Figure 3.4 for HC_3N towards IRAS16293-2422 as an example.

3.3.2 Tool: CASSIS

CASSIS (**C**entre d'**A**nalyse **S**cientifique de **S**pectres **I**nstrumentaux et **S**ynthétiques) software has been developed by IRAP-UPS/CNRS (*http://cassis.irap.omp.eu*) since 2005. I have used this software to explore the TIMASSS (Caux et al. 2011) and ASAI (López-Sepulcre et al. 2015) spectral survey files, in order to search for complex organic and cyanopolyynes molecules in IRAS16293 and OMC2-FIR4 respectively. This tool reads the spectra file header and displays in the graphical interface the portions of spectra corresponding to the lines of the selected species. In addition, to help to look for contamination by nearby lines, the lines of other species included in the database can be shown in the same spectral window. Figure 3.5 shows an example of such a plot. During my thesis, I used CASSIS for the following tasks:

1. Line identification.
2. Gaussian fit.
3. Derivation of the upper limit to the abundance for undetected species.

In this section I only describe the first point. The second & third steps will be described in the next section (§3.4)

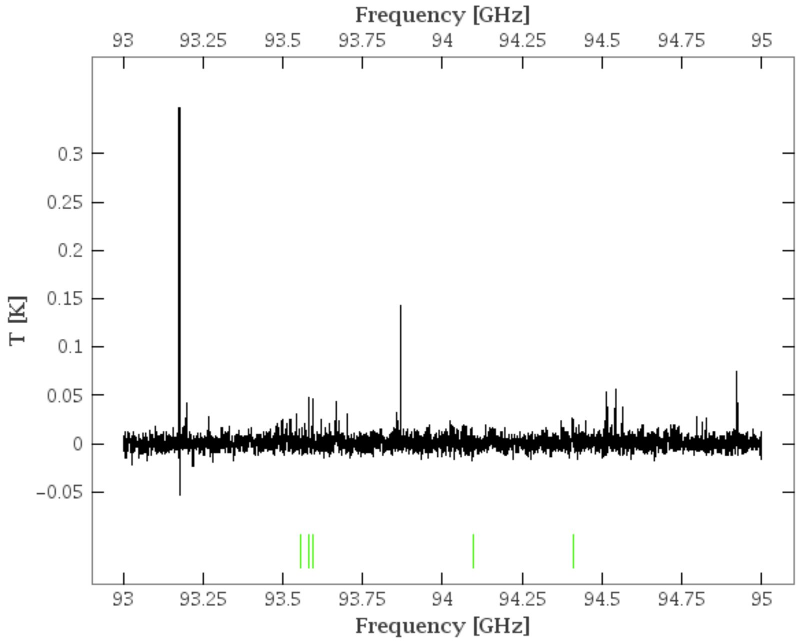

FIGURE 3.5: On this spectrum observed towards IRAS16293, the lines belonging to CH_3CHO, with upper energy levels lower than 150 K, are indicated by the small green ticks.

Here is a brief summary of the successive steps I follow. First, I select the data file; CASSIS can read various formats (.bur, .class, .30m, etc...), provided that the header contains the LO frequency and the telescope IF frequency.
After that, I select a species belonging to the available databases within the "template" section. Then CASSIS will find and display all lines present in the data file that match the tuning range and the line parameters thresholds (frequency, upper energy, Einstein coefficient...). Lines are displayed in a mosaic of panels. Figure 3.6 shows, as an example, the result of the display for HC_3N, one of the molecules studied in my thesis.

To be sure that the detected line is clean (i.e., not suffering from misidentification or severe blending), CASSIS allows to view the transitions belonging to other species found in the database present in the signal and image (if it applies) bands. An example is given in Figure 3.6b.

3.4 Lines parameters

3.4.1 Gaussian fit

CASSIS has been used to do a Gaussian fit to derive the line V_{LSR}, FWHM and integrated intensity, for each of the lines, for all detected molecules as follow: From "Manage Components", I select "Add Line" then "Gaussian" ; the parameters appear with blue fields for the initial guesses (which CASSIS automatically fills in with the next step). Grey fields are non editable and will show the statistical errors once the fit is done, as shown in Figure 3.7a; then I select the domain to be fitted by "Alt" key + click, Figure 3.7b; in final step, I choose "Fit current" ; the fit is in red, the residuals are in orange, Figure 3.7c. That is for normal cases i.e, one peak and one Gaussian fit. But in some cases I do two-Gaussians fit for lines blended with a nearby species as shown in Figure 3.8a. In some rare cases, I also select "Add Baseline" then "Polynomial" and "Degree 3" (Figure 3.8b the gaussian fits). Then I select the first peak and use the line box to fix the first gaussian parameters (Figure 3.8c); after that I follow the same steps for the second peak (Figure 3.8d) and finally I release all the gaussian parameters and choose "Fit Current", as shown in Figure 3.8e. Then I save the file which contains the following parameters:

- **#:** Value corresponding to the order in which the component was added in the "Manage Components" panel.
- **Transition:** Name and quantum numbers of the transition from the database.
- **Frequency(Mhz):** Frequency in MHz from the database.
- **Eup(K):** Energy of the upper level in K from the database.
- **Aij:** Einstein A-coefficient (in s^{-1}) from the database.
- **FitFreq.(xunit):** Fitted frequency.
- **DeltaFitFreq.:** Associated 1-sigma error.
- **Vo(km/s):** Fitted velocity in km/s.
- **DeltaVo :** Associated 1-sigma error.

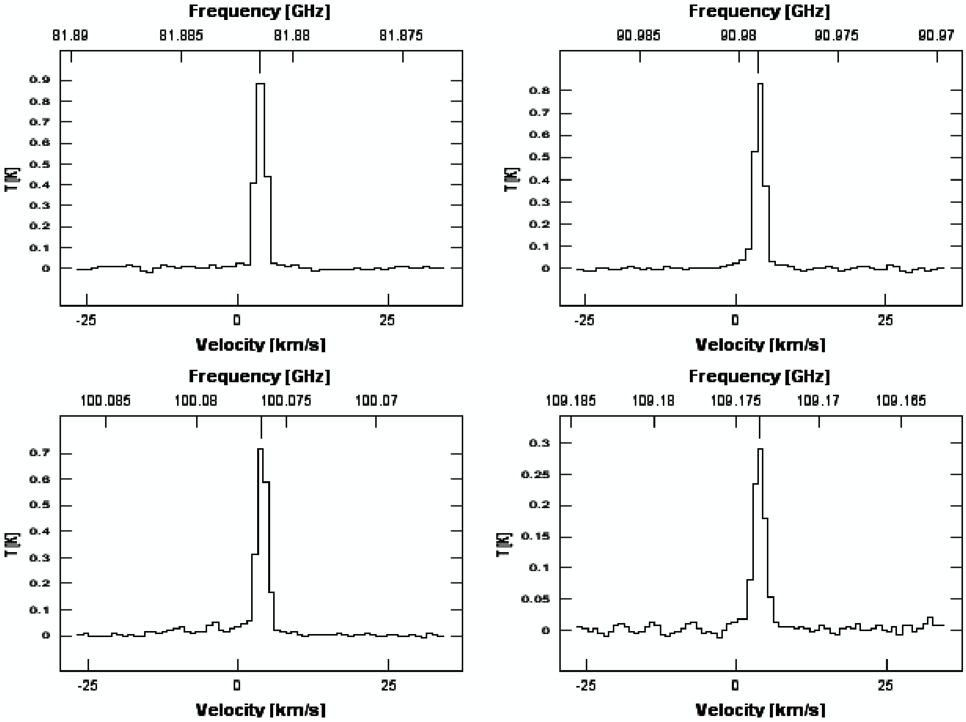

(A) without information on other species.

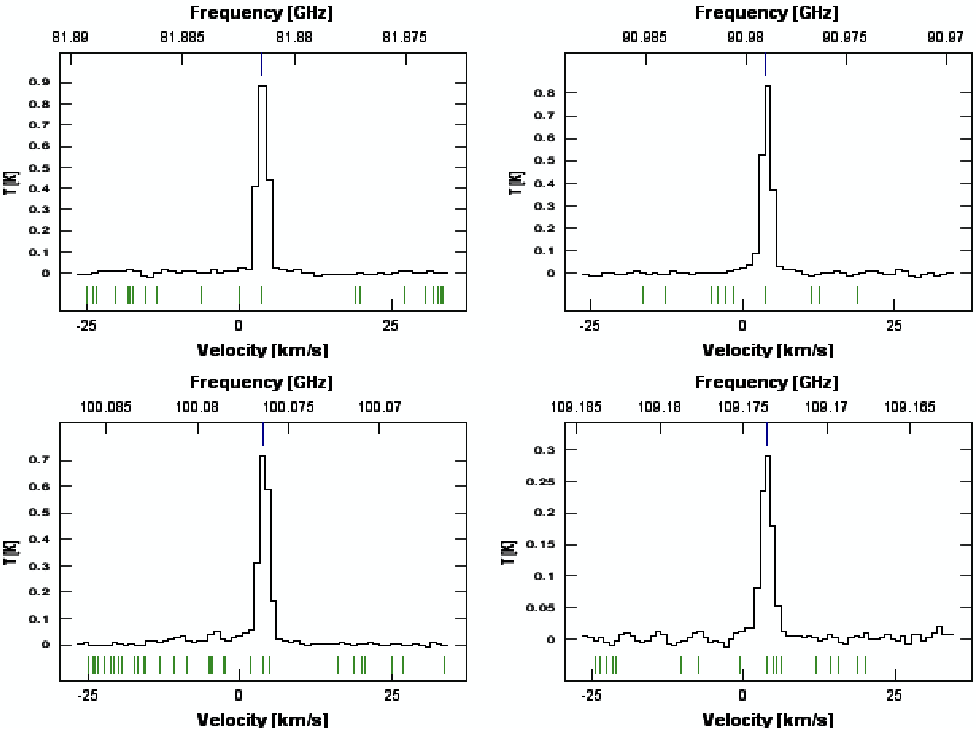

(B) showing the signal band lines with an upper energy level of less than 150 K for all the species present in the JPL database.

FIGURE 3.6: Display from CASSIS of the HC_3N lines in the range 80 GHz – 110 GHz

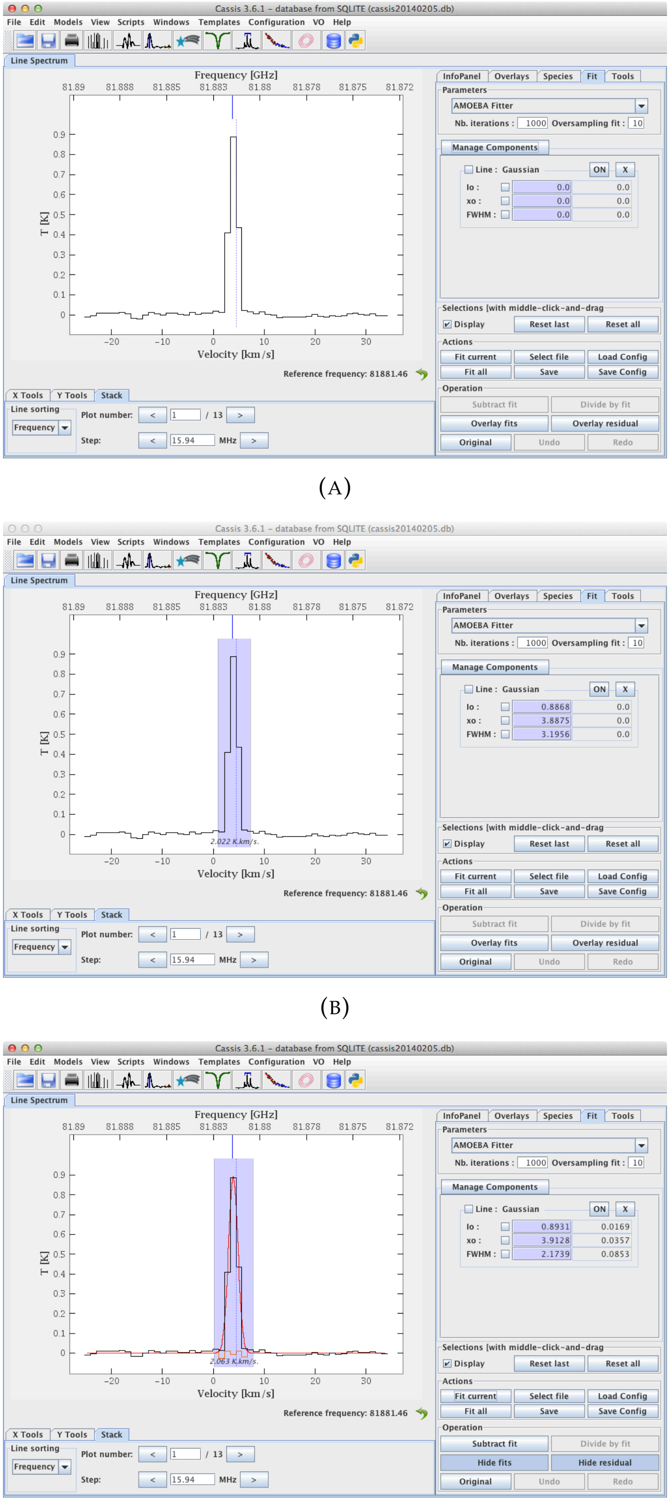

(A)

AMOEBA Fitter
Nb. iterations : 1000 Oversampling fit : 10
☐ Line : Gaussian
Io : ☐ 0.0 0.0
xo : ☐ 0.0 0.0
FWHM : ☐ 0.0 0.0
☑ Display
Reference frequency: 81881.46
Frequency
Plot number: 1 / 13
Step: 15.94 MHz

(B)

AMOEBA Fitter
Nb. iterations : 1000 Oversampling fit : 10
☐ Line : Gaussian
Io : ☐ 0.8868 0.0
xo : ☐ 3.8875 0.0
FWHM : ☐ 3.1956 0.0
☑ Display
Reference frequency: 81881.46
Frequency
Plot number: 1 / 13
Step: 15.94 MHz

(C)

AMOEBA Fitter
Nb. iterations : 1000 Oversampling fit : 10
☐ Line : Gaussian
Io : ☐ 0.8931 0.0169
xo : ☐ 3.9128 0.0357
FWHM : ☐ 2.1739 0.0853
☑ Display
Reference frequency: 81881.46
Frequency
Plot number: 1 / 13
Step: 15.94 MHz

FIGURE 3.7: Snapshot of the CASSIS panel showing the three steps of a single Gaussian fit, on a HC_3N line as example.

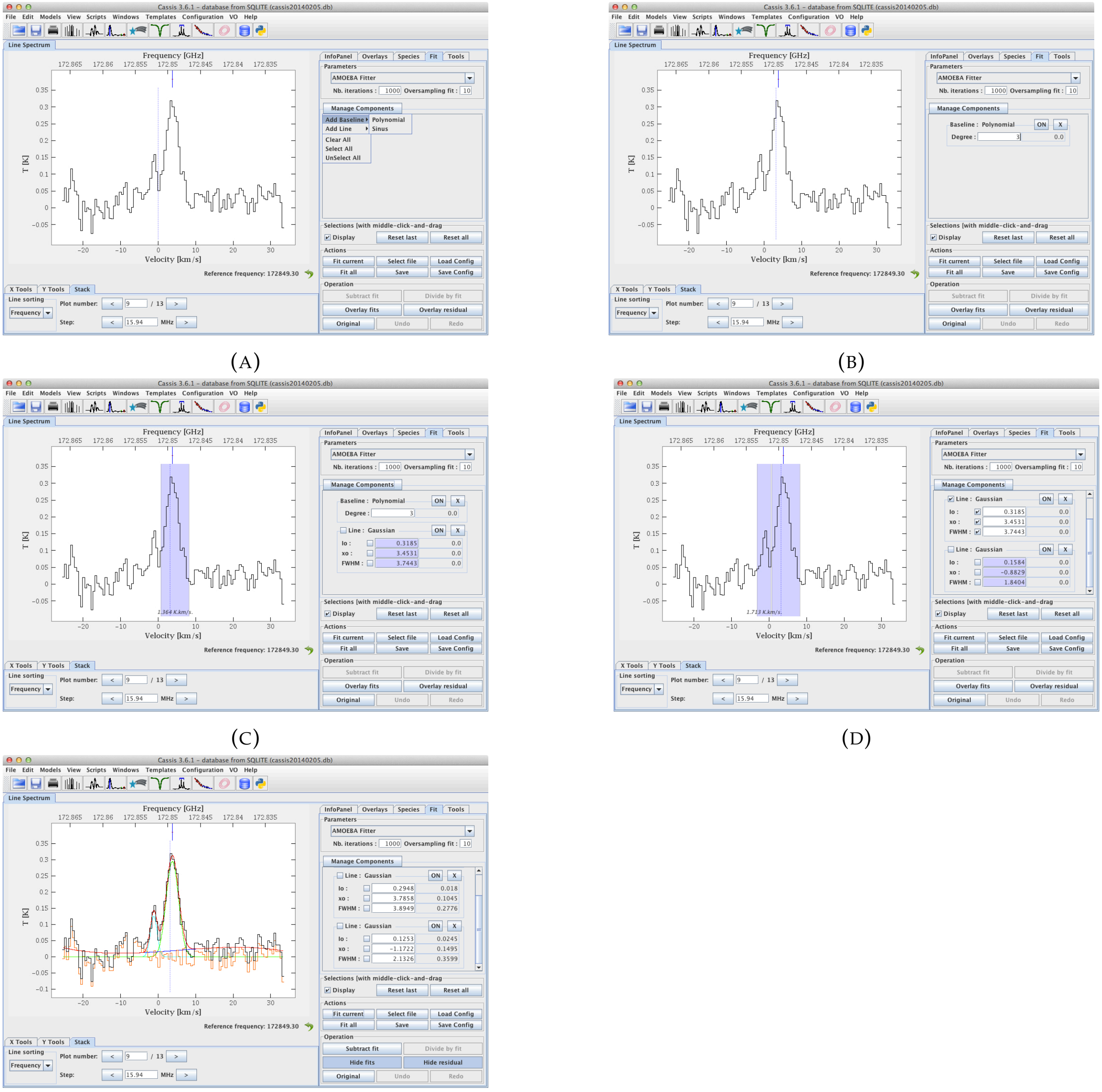

AMOEBA Fitter
Nb. iterations : 1000 Oversampling fit : 10
Reference frequency: 172849.30
Plot number: 9 / 13
Step: 15.94 MHz

(A)

Baseline : Polynomial
Degree : 3 0.0

(B)

Baseline : Polynomial
Degree : 3 0.0
Line : Gaussian
Io : 0.3185 0.0
xo : 3.4531 0.0
FWHM : 3.7443 0.0

(C)

Line : Gaussian
Io : 0.3185 0.0
xo : 3.4531 0.0
FWHM : 3.7443 0.0
Line : Gaussian
Io : 0.1584 0.0
xo : -0.8829 0.0
FWHM : 1.8404 0.0

(D)

Line : Gaussian
Io : 0.2948 0.018
xo : 3.7858 0.1045
FWHM : 3.8949 0.2776
Line : Gaussian
Io : 0.1253 0.0245
xo : -1.1722 0.1495
FWHM : 2.1326 0.3599

(E)

FIGURE 3.8: Snapshot of the CASSIS panel showing the five steps for a two Gaussian fit, with a HC_3N line as example.

- **FWHM_G(km/s):** Fitted FWHM for a Gaussian component.
- **DeltaFWHM_G :** Associated 1-sigma error.
- **FWHM_L(km/s):** Fitted FWHM for a Lorentzian component.
- **DeltaFWHM_L:** Associated 1-sigma error.
- **Int(yunit):** Fitted intensity at line center.
- **DeltaInt:** Associated 1-sigma error.
- **FitFlux(yunit.km/s):** Fitted flux in K.km/s.
- **DeltaFitFlux :** Associated 1-sigma error.
- **Freq.I_Max(xunit):** Frequency at the observed maximum intensity.
- **V.I_Max(km/s):** Velocity at the observed maximum intensity.
- **FWHM(km/s):** Parameter equal to Flux/I_Max and representing roughly the "observed" FWHM.
- **I_Max(yunit):** Observed maximum intensity.
- **Flux(yunit.km/s):** Integrated intensity (1st moment) in the region selected with the mouse.
- **RMS(unit):** Observed rms in unit=mK if spectrum is in K.
- **DeltaV(km/s):** Channel spacing in velocity scale.
- **Cal(%):** Calibration uncertainty in %.
- **Telescope:** Path to the telescope file.

3.4.2 LTE Modeling for upper limits

I obtained a full census of complex organic molecules and cyanopolyynes in IRAS16293 and calculated the upper limit of the abundance for undetected species using CASSIS LTE modeling. To model the molecular emission from undetected species in IRAS16293-2422, I considered successively that the COMs emission comes from two regions: hot corino and outer cold envelope. In each case, the LTE calculation needs the following parameters:

1. Molecular hydrogen column density
   This parameters is calculated using the physical structure from Crimier et al. (2010b). The radius where the gas temperature reaches 80K (for example, as obtained for HC_3N) corresponds to the maximum radius for the hot corino, and to the minimum value for the cold envelope.

   - **Radius$_{T=80}$:** $R_{T=80}$
   - **Density of hydrogen:** n(H)
   - **Minimum radius:** R_{min}

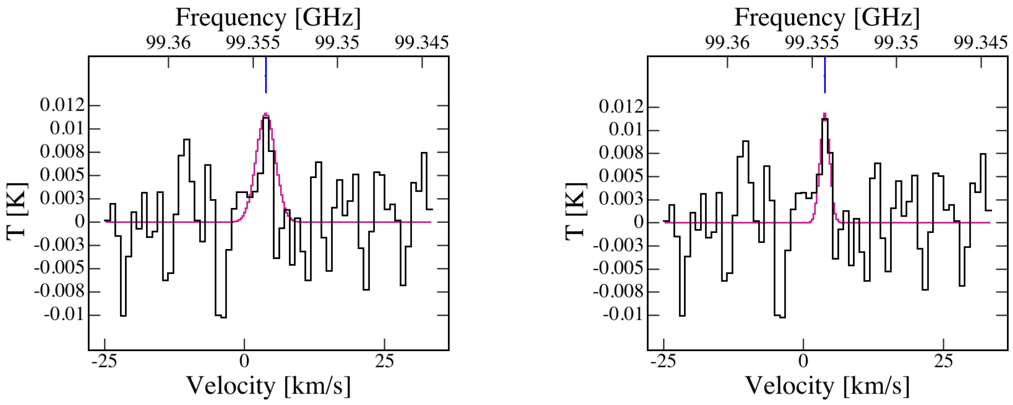

(A) Hot Corino.

(B) Outer cold envelop.

FIGURE 3.9: Upper limit abundance adjustment for an undetected molecules (here HCCNC). The red curves correspond to LTE calculations.

- **Maximum radius:** $R_{max} = R_{T=80}$
- **Distance:** d=120 pc.

Then, for the hot corino, for example, the column density of hydrogen is given by $N(H_2) = \int_{R_{min}}^{R_{T=80}} n(H_2)dR = 1.5\times10^{23} cm^{-2}$.

2. Source size in arcsecond. I calculated it for each region, hot corino and outer cold envelope. For the hot corino, for example

   $\text{Size} = \frac{2*Radius_{T=80}}{Distance} = 8.7\times10^{-6}(radian) = 2(arcsecond).$

3. Full width at half maximum (FWHM) in km/s. I assumed 6 km/s for the hot corino and 3 km/s for the outer cold envelope.

4. Excitation temperature in K. I assumed 80 K for the hot corino and 20 K for the outer cold envelope in the case of HC_3N.

After entering all these values, the molecule abundance is adjusted to give LTE-model results compatible with the observed spectra as shown in Figure 3.9a for hot corino and Figure 3.9b for outer cold envelope, for one line of HCCNC, one of the undetected COMs in IRAS16293 as example.

3.5 SLED Modeling

3.5.1 GRAPES

In order to analyse the molecular line data and derive the molecular abundances, we need a good physical model of the source. Then we need to compute the full LTE or/and non-LTE statistical equilibrium excitation of the molecule across its physical structure, to calculate the emerging radiation from the source using nonlocal radiative transfer, to convolve the predicted emission with the telescope beam, and then to compare with observations.

During my thesis, I followed this strategy to analyze the molecular lines, by using the physical models of IRAS16293 introduced by Crimier et al. (2010b) and OMC-2 FIR4 by Crimier et al. (2010a). I then used the package GRAPES (**GR**enoble **A**nalysis of **P**rotostellar **E**nvelope **S**pectra) to model the Spectral Line Energy Distribution (SLED) of the detected COMs, and to estimate the abundance of these detected molecules across the envelope and hot corino of IRAS16293 and OMC-2 FIR4 respectively. GRAPES, has been developed by Cecilia Ceccarelli from 2008, based on the code described in Ceccarelli et al. (1996, 2003a) and during my thesis, I helped developing it, particularly as I carried out an systematic debugging. General description and method of work, are presented in the next subsections.

3.5.2 General description of the package

GRAPES consists of two sub-packages: radiative-transfer fortran codes and IDL procedures to launch the codes and/or analyze the results.

1. **FORTRAN codes: Line flux calculation.** The first one is a fortran code which provides theoretical predictions of the integrated flux of the lines from a selected chemical species (notably molecules whose spectral parameters are available in the JPL database Pickett et al. (1998)). It computes the line fluxes from a gas and dust sphere for a given physical structure. Depending whether the collisional coefficients are available or not, two kinds of calculations are executed:

   - **NON-LTE computations:** If the collisional coefficients are available, the level populations are computed by solving the radiative transfer & statistical equilibrium equations simultaneously. The adopted formalism for treating the radiative transfer, following the escape probability method, is described in three articles (Ceccarelli et al. 1996, 2003a; Parise et al. 2005). Note that the level population computation take into account also the radiative pumping from the dust emission.
   - **LTE computations:** When the collisional coefficients are not available, the level population are assumed to follow the Boltzmann distribution. The opacity of the lines are, however, computed by integrating on the solid angle the optical depth, following the formalism of the above mentioned articles.

2. **IDL procedures** The second sub-package consists of several IDL procedures to run grids of models, to compare the predicted with observed line intensities and find the best fit, plus several procedures to facilitate the understanding of the model predictions.

3.5.3 Method of work

In brief, GRAPES (i) computes the species SLED from a spherical infalling envelope with a given structure; (ii) solve locally the level population statistical equilibrium equations in the beta escape formalism, consistently computing the line optical depth by integrating it over the solid angle at each point of the envelope; (iii) the predicted line flux is then integrated over the whole envelope after convolution with the telescope beam. The abundance X of the considered species is assumed to vary as a function of the radius with a power law in the cold part of the envelope and to jump to a new abundance in the warm part. The transition between the two regions is set by the dust temperature, to simulate the sublimation of the ice mantles, and occurs at T_{jump}. It holds:

$$\begin{aligned} X(r) &= X_{out}\left(\frac{r}{R_{max}}\right)^{\alpha} \qquad T_{dust} \leq T_{jump} \\ X(r) &= X_{in} \qquad\qquad\qquad T_{dust} > T_{jump} \end{aligned} \tag{3.1}$$

GRAPES allows us to run large grids of models varying the model parameters and to find the best fit to the observed fluxes, as shown in GRAPES model scheme in Figure 3.10.

GRAPES, like any others codes, has disadvantages and advantages with respect to other codes. The first and obvious disadvantage is that, the spherical assumption just holds for the large scale ($\geq$ 10": see Crimier et al. (2010b)) envelope of IRAS16293. At small scales, the presence of the binary system (as explain in Chapter 2) makes the spherical symmetry assumption wrong. Consequently, the GRAPES code is, by definition, unable to correctly estimate the emission from the two sources I16293-A and I16293-B separately. The derived inner envelope abundance, therefore, is likely a rough indication of the real abundance of the species towards I16293-A and I16293-B. The other disavantage of GRAPES is that it relies on the analysis of the SLED and not on the line profiles. Since the majority of the TIMASSS spectra have a relatively poor spectral resolution (≥ 1 km/s^{-1}), this is appropriate in this case. The great advantage of GRAPES, and the reason why we used it here, is that it is very fast, so that a large multi-parameter space can be explored. Similar arguments apply to the case of OMC-2 FIR4.

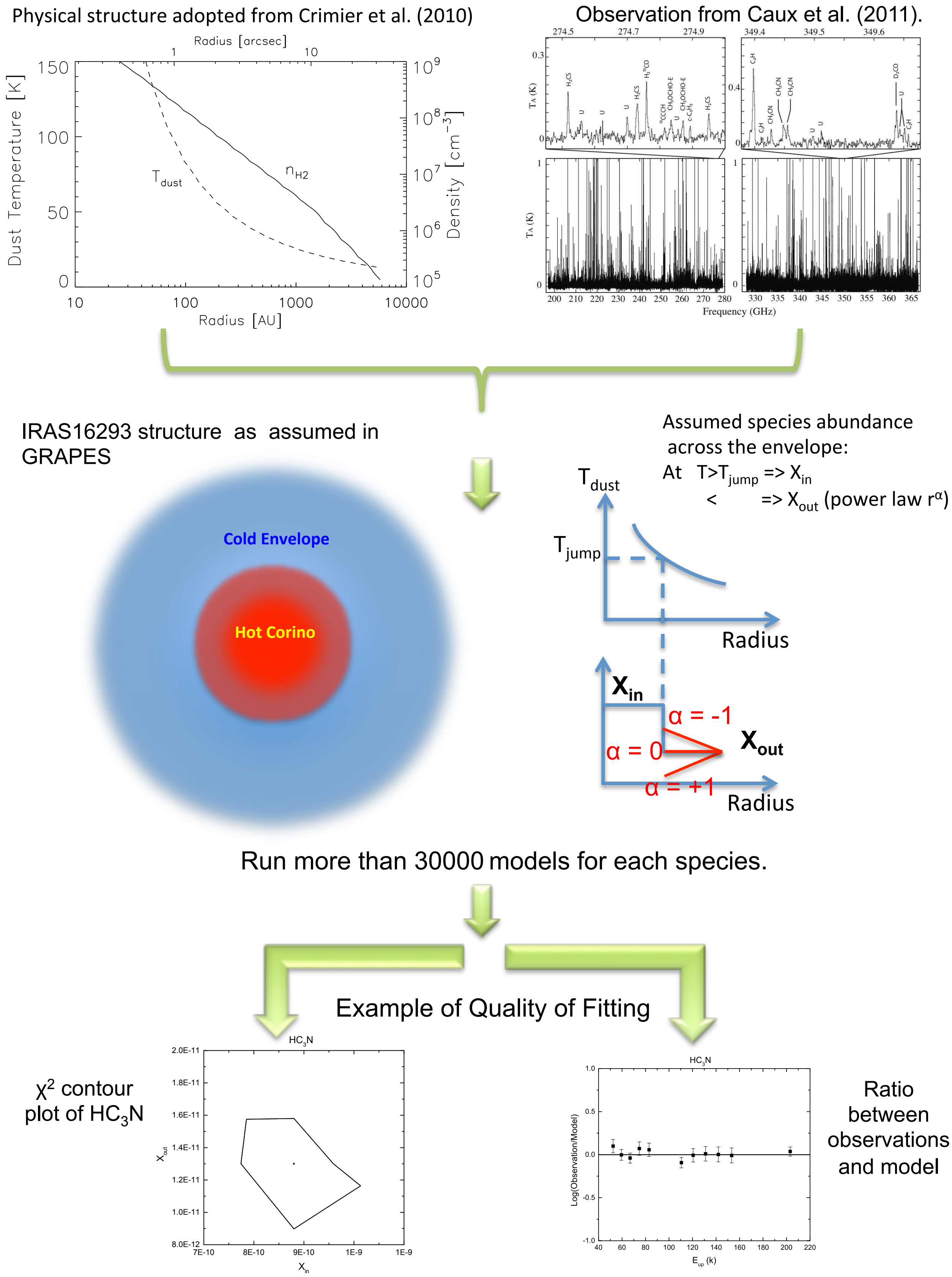

FIGURE 3.10: GRAPES model scheme of inferring abundance profiles using a full physical model of the source from Crimier et al. (2010b). The middle bottom graph indicates the typical temperature and density structure of the envelope around the IRAS16293, as function of radius R.The blue step-function indicates the likely abundance profile, with freeze-out in the cold and dense middle region of the envelope and a jump in abundance in the inner “hot corino” at the sublimation temperature.

Chapter 4

COMs in IRAS16293-2422

This chapter was published in The Astrophysical Journal with the title "The census of complex organic molecules in the solar type protostar IRAS16293-2422": Jaber, A. A., Ceccarelli, C., Kahane, C., Caux, E. 2014, ApJ, 791, 29.

4.1 Abstract

Complex Organic Molecules (COMs) are considered crucial molecules, since they are connected with organic chemistry, at the basis of the terrestrial life. More pragmatically, they are molecules in principle difficult to synthetize in the harsh interstellar environments and, therefore, a crucial test for astrochemical models. Current models assume that several COMs are synthesised on the lukewarm grain surfaces (30–40 K), and released in the gas phase at dust temperatures 100 K. However, recent detections of COMs in 20 K gas demonstrate that we still need important pieces to complete the puzzle of the COMs formation. We present here a complete census of the oxygen and nitrogen bearing COMs, previously detected in different ISM regions, towards the Solar-type protostar IRAS16293-2422. The census was obtained from the millimeter-submillimeter unbiased spectral survey TIMASSS. Six COMs, out of the 29 searched for, were detected: methyl cyanide, ketene, acetaldehyde, formamide, dimethyl ether, and methyl formate. The multifrequency analysis of the last five COMs provides clear evidence that they are present in the cold (30 K) envelope of IRAS16293-2422, with abundances 0.03–2 $\times 10^{-10}$. Our data do not allow to support the hypothesis that the COMs abundance increases with increasing dust temperature in the cold envelope, as expected if COMs were predominately formed on the lukewarm grain surfaces. Finally, when considering also other ISM sources, we find a strong correlation over five orders of magnitude, between the methyl formate and dimethyl ether and methyl formate and formamide abundances, which may point to a link between these two couples of species, in cold and warm gas.

4.2 Introduction

Complex Organic Molecules (COMs), namely organic molecules with more than six atoms (Herbst & van Dishoeck 2009), have been discovered since more than four decades (Ball et al. 1971; Rubin et al. 1971; Solomon et al. 1971; Brown et al. 1975; Blake et al. 1987). Since some COMs have a prebiotic relevance, they immediately rise a great interest and several models were developed to explain why and how these molecules are formed in space. Those models were based on this two-step process: (i) "mother" (or first generation) species were created during the cold star formation process and frozen into the grain mantles; (ii) "daughter" (or second generation) species were synthesised via gas phase reactions from mother species in the warm (200 K) regions where the grain mantles sublimate (Millar et al. 1991; Charnley et al. 1992; Caselli et al. 1993). This two-step paradigm, has enjoyed a great success for about a decade, until new observations towards low mass hot corinos (Ceccarelli et al. 2000a; Cazaux et al. 2003) and Galactic Center molecular clouds (Requena-Torres et al. 2007) challenged the assumption that COMs are formed by gas phase reactions. At the same time, new laboratory experiments and theoretical computations revisited and ruled out some gas phase reactions crucial in those models (Horn et al. 2004; Geppert et al. 2007). The attention then moved towards the possibility that grains could act as catalysers and that COMs could form on their surfaces at lukewarm (30–40 K) temperatures (Garrod et al. 2009). However, grain surface chemistry is even more difficult to understand than gas phase chemistry, both from a theoretical and experimental point of view. Let us take the example of methanol, one of the simplest COMs. It is supposed to form on the grain surface via successive hydrogenation of frozen CO (Tielens & Hagen 1982; Taquet et al. 2012). However, while laboratory experiments claim that this is the case (e.g. (Watanabe & Kouchi 2002; Pirim et al. 2010)), theoretical quantum chemistry computations show that the first and last steps towards the CH_3OH formation have large (tens of kCal) energy barriers impossible to surmount in the cold ($\sim$ 10 K) cloud conditions (Woon 2002; Marenich & Boggs 2003; Goumans et al. 2008), where the CO hydrogenation is supposed to occur. To add confusion, recent observations have revealed that some COMs (notably acetaldehyde, methyl formate and dimethyl ether) are found in definitively cold ($\leq$ 20 K) regions (Öberg et al. 2010; Bacmann et al. 2012; Cernicharo et al. 2012), challenging the theory of grain surface formation of COMs.

In this context, we examined the millimeter-submillimeter spectral survey obtained towards the solar type protostar IRAS16293-2422 (hereinafter IRAS16293; Caux et al. (2011)) with the goal to extract the line emission from all oxygen and nitrogen bearing COMs already detected in the ISM, and to estimate their abundances across its envelope. Our emphasis here is on the abundances in the cold ($\leq$ 50 K) region of the envelope, to provide astrochemical modellers with the *first systematic survey of COMs in cold gas*.

4.3 Source description

IRAS16293 is a solar type Class 0 protostar in the ρ Ophiuchus star forming region, at a distance of 120 pc (Loinard et al. 2008). It has a bolometric luminosity of 22 L (Crimier et al. 2010b). Given its proximity and brightness, it has been the target of numerous studies that have reconstructed its physical and chemical structure. Briefly, IRAS16293 has a large envelope that extends up to $\sim$6000 AU and that surrounds two sources, named I16293-A and I16293-B in the literature, separated by $\sim$ 5” ($\sim$600 AU; Wootten (1989); Mundy et al. (1992)). I16293-A sizes are $\sim$ 1”, whereas I16293-B is unresolved at a scale of $\sim$ 0.4” (Zapata et al. 2013). I16293-A itself is composed of two sources, each one emitting a molecular outflow (Mizuno et al. 1990; Loinard et al. 2013). I16293-B possesses a very compact outflow (Loinard et al. 2013) and is surrounded by infalling gas (Pineda et al. 2012; Zapata et al. 2013). From a chemical point of view, IRAS16293 can be considered as composed of an outer envelope, characterised by low molecular abundances, and a hot corino, where the abundance of many molecules increases by orders of magnitude (Ceccarelli et al. 2000a; Schöier et al. 2002; Coutens et al. 2013a). The transition between the two regions occurs at $\sim$100 K, the sublimation temperature of the icy grain mantles. In the hot corino, several abundant COMs have been detected (Cazaux et al. 2003).

4.4 The data set

4.4.1 Observations

We used the data from The IRAS16293 Millimeter And Submillimeter Spectral Survey (TIMASSS: *http://www-laog.obs.ujf-grenoble.fr/heberges/timasss/*; Caux et al. (2011)). Briefly, the survey covers the 80-280 and 328-366 GHz frequency intervals and it has been obtained at the IRAM-30m and JCMT-15m telescopes. The data are publicly available on the TIMASSS web site. Details on the data reduction and calibration can be found in Caux et al. (2011). We recall here the major features, relevant for this work. The telescope beam depends on the frequency and varies between 9" and 30". The spectral resolution varies between 0.3 and 1.25 MHz, corresponding to velocity resolutions between 0.51 and 2.25 km/s. The achieved rms is between 4 and 17 mK. Note that it is given in a 1.5 km/s bin for observations taken with a velocity resolution $\leq$1.5km/s, and in the resolution bin for larger velocity resolutions. The observations are centered on IRAS16293B at α(2000.0) = 16^h 32^m 22^s.6, δ(2000.0)= -24^o 28$'$ 33$''$. Note that the A and B components are both inside the beam of observations at all frequencies.

4.4.2 Species identification

We searched for lines of all the oxygen and nitrogen bearing COMs already detected in the ISM (as reported in the CDMS database: *http://www.astro.uni-koeln.de/cdms/molecules*), they are listed in Table 4.1. At this scope, we used the list of identified lines in Caux et al. (2011) and double-checked for possible blending and misidentifications. This was obtained via the publicly available package CASSIS (*http://cassis.irap.omp.eu*), and the CDMS (Müller et al. 2005) and JPL (Pickett et al. 1998) databases. References to the specific articles on the laboratory data of the detected species are Guarnieri & Huckauf (2003); Kleiner et al. (1996); Neustock et al. (1990); Maeda et al. (2008). In case of doubt on the line identification or in case of presence of important residual baseline effects, we did not consider the relevant line. Except for those few ($\leq$ 10%) cases, we used the line parameters (flux, linewidth, rest velocity) in Caux et al. (2011). With these tight criteria, we secured the detection of six COMs: ketene (H_2CCO: 13 lines), acetaldehyde (CH_3CHO: 130 lines), formamide (NH_2CHO: 17 lines), dimethyl ether (CH_3OCH_3: 65 lines), methyl formate ($HCOOCH_3$: 121 lines) and methyl cyanide (CH_3CN: 38 lines). For comparison, Cazaux et al. (2003) detected 5 CH_3CHO lines, 7 CH_3OCH_3 lines, and 20 CH_3CHO lines. We do not confirm the Cazaux et al. (2003) detection of acetic acid (CH_3COOH) and formic acid (HCOOH), where these authors reported the possible detection of 1 and 2 lines respectively, none of them in the TIMASSS observed frequency range.

4.5 Analysis and results

4.5.1 Model description

Our goal is to estimate the abundance of the detected COMs across the envelope of IRAS16293, with particular emphasis on the cold envelope (see Introduction). For that, we used the Spectral Line Energy Distribution (SLED) of the detected COMs, and the package GRAPES (GRenoble Analysis of Protostellar Envelope Spectra), based on the code described in Ceccarelli et al. (1996, 2003a). Briefly, GRAPES (i) computes the species SLED from a spherical infalling envelope with a given structure; (ii) it solves locally the level population statistical equilibrium equations in the beta escape formalism, consistently computing the line optical depth by integrating it over the solid angle at each point of the envelope; (iii) the predicted line flux is then integrated over the whole envelope after convolution with the telescope beam. The abundance X of the considered species is assumed to vary as a function of the radius with a power law in the cold part of the envelope and to jump to a new abundance in the warm part. The transition between the two regions is set by the dust temperature, to simulate the sublimation of the ice mantles, and occurs at T_{jump}. It holds:

$$\begin{aligned} X(r) &= X_{out}\left(\frac{r}{R_{max}}\right)^{\alpha} & T \leq T_{jump} \\ X(r) &= X_{in} & > T_{jump} \end{aligned} \tag{4.1}$$

GRAPES allows us to run large grids of models varying the four parameters, X_{in}, X_{out}, α and T_{jump}, and to find the best fit to the observed fluxes.

This code has disadvantages and advantages with respect to other codes. The first and obvious disadvantage is that the spherical assumption just holds for the large scale (10": see Crimier et al. 2010) envelope of IRAS16293. At small scales, the presence of the binary system (§5.3) makes the spherical symmetry assumption wrong. Consequently, the GRAPES code is, by definition, unable to correctly estimate the emission from the two sources I16293-A and I16293-B separately. The derived inner envelope abundance, therefore, is likely a rough indication of the real abundance of the species towards I16293-A and I16293-B. The other disavantage of GRAPES is that it relies on the analysis of the SLED and not on the line profiles. Since the majority of the TIMASSS spectra have a relatively poor spectral resolution (1 km/s), this is appropriate in this case. The great advantage of GRAPES, and the reason why we used it here, is that it is very fast, so that a large multi-parameter space can be explored.

In the specific case of this work, we used the physical structure of the envelope of IRAS16293 as derived by Crimier et al. (2010b), which is based on single dish and interferometric continuum observations. Collisional coefficients are only available for methyl cyanide, and not for the other five detected COMs. Since methyl cyanide is a top symmetric molecule, it represents a "particular case" with respect to the other detected COMs, so that, in order to have an homogeneous dataset, we decided to analyse here only the latter molecules, and assume LTE for their level populations. The analysis of the CH_3CN molecule will be the focus of a future article. Since the density of the IRAS16293 envelope is relatively high (e.g. 5×10^6 cm^{-3} at a radius of 870 AU, equivalent to 15" in diameter), we expect that the abundances derived in the LTE approximation are only moderately underestimated.

4.5.2 Results

For each of the five analysed COMs, we run a large grid of models with the following strategy. We explored the X_{in}–X_{out} parameter space (in general we obtained grids of more than 20x20) for α equal to -1, 0 and +1, and varied T_{jump} from 10 to 120 K by steps of 10 K. Note that we first started with a 3 or 4 orders of magnitude range in X_{in} and X_{out} respectively to find a first approximate solution and then we fine-tuned the grid around it. In total, therefore, we run more than 3×10^4 models for each species. The

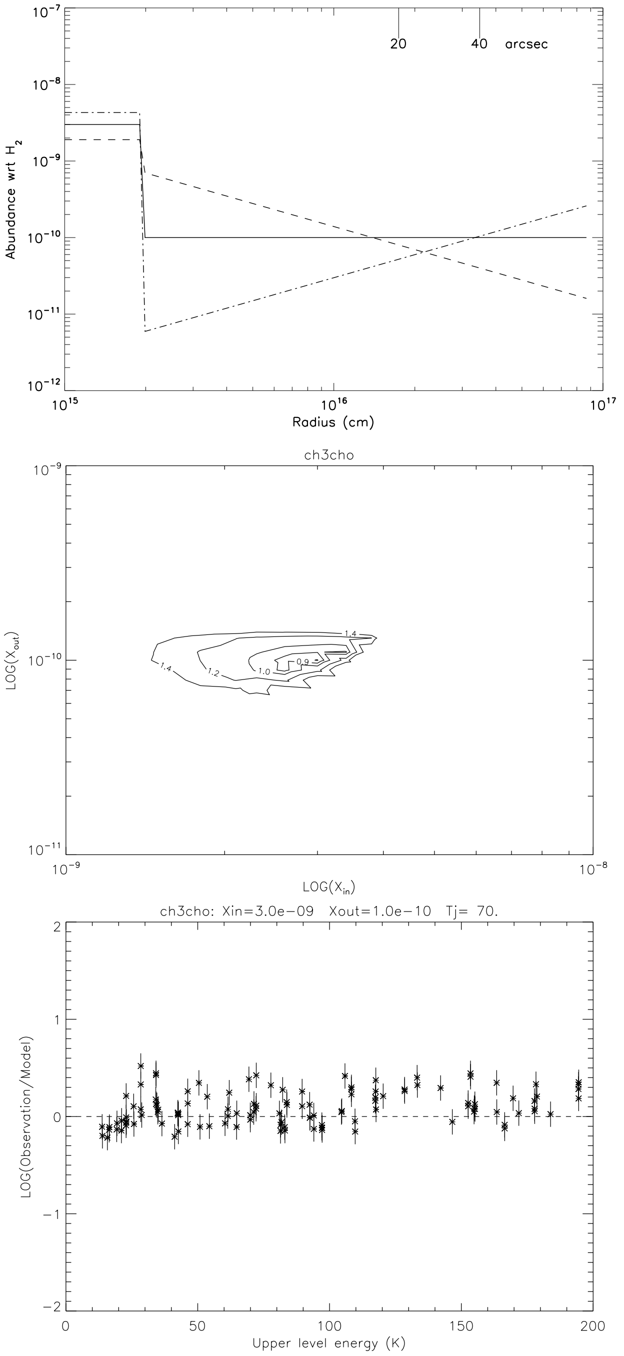

FIGURE 4.1: Example of the acetaldehyde analysis. Upper panel: Abundance profiles of the best fit obtained considering the cold envelope abundance profile following a power law dependence with radius (Eq.5.1) of α equal to -1 (dashed), 0 (solid) and 1 (dotted-dashed) respectively. Middle panel: χ^2 contour plot assuming the best fit T_{jump}=70 K and α=0. Bottom panel: Ratio of the observed over predicted line flux as a function of the upper level energy of the transition for the best fit solution (Table 4.1).

results of the best fit procedure are reported in Table 4.1. Figure 4.1 shows the example of acetaldehyde. Note that the lines are predicted to be optically thin by the best fit models of all five molecules.

TABLE 4.1: Results of the analysis.

Species	Formula	X$_{in}$ [10^{-8}]	X$_{out}$ [10^{-10}]	T_{jump} [K]	DF	χ^2	Radius [AU]	Size ["]
			Detected COMs					
Ketene	H_2CCO	0.01±0.005	0.3±0.08	20^{+20}_{-5}	10	0.63	1800	31
Acetaldehyde	CH_3CHO	0.3±0.2	1±0.2	70±5	127	0.79	127	2
Formamide	NH_2CHO	0.06±0.02	0.03±0.02	80±5	14	0.69	100	2
Dimethyl ether	CH_3OCH_3	4±1	2±1	50±10	62	0.72	240	4
Methyl formate	$HCOOCH_3$	0.9±0.2	0.3±0.1	50±5	118	0.78	240	4
			Undetected COMs					
Ethylene oxide	c-C_2H_4O	≤ 0.1	≤ 3					
Vinyl alcohol	H_2CCHOH	≤ 0.04	≤ 1					
Ethanol	C_2H_5OH	≤ 0.5	≤ 8					
Formic acid	$HCOOH$	≤ 0.03	≤ 0.8					
Propynal	HC_2CHO	≤ 0.02	≤ 0.5					
Cyclopropenone	c-H_2C_3O	≤ 0.004	≤ 0.1					
Acrolein	C_2H_3CHO	≤ 0.02	≤ 0.6					
Acetone	CH_3COCH_3	≤ 0.07	≤ 2					
Propanal	CH_3CH_2CHO	≤ 0.1	≤ 2					
Glycolaldehyde	$CH_2(OH)CHO$	≤ 0.1	≤ 3					
Ethyl methyl ether	$C_2H_5OCH_3$	≤ 0.5	≤ 9					
Ethyleneglycol	$(CH_2OH)_2$	≤ 0.2	≤ 5					
Ethyl formate	C_2H_5OCHO	≤ 0.2	≤ 5					
Methylamine	CH_3NH_2	≤ 0.1	≤ 3					
Methylisocyanide	CH_3NC	≤ 0.002	≤ 0.07					
Etheneimine	H_2CCNH	≤ 0.1	≤ 2					
Cyanoacetylene+	HC_3NH^+	≤ 0.01	≤ 0.2					
Vinyl cyanide	C_2H_3CN	≤ 0.01	≤ 0.2					
Ethyl cyanide	C_2H_5CN	≤ 0.02	≤ 0.7					
Aminoacetonitrile	H_2NCH_2CN	≤ 0.03	≤ 0.7					
Cyanopropyne	CH_3C_3N	≤ 0.002	≤ 0.07					
n-Propyl cyanide	n-C_3H_7CN	≤ 0.05	≤ 0.8					
Cyanopentadiyne	CH_3C_5N	≤ 0.01	≤ 0.3					

Note: The first two columns report the species name and formula. Third, fourth and fifth columns report the values of the inner and outer abundances X_{in} and X_{out} (with respect to H_2), and T_{jump}. Columns 6 and 7 report the degrees of freedom and the minimum reduced χ^2. The last two columns report the radius and the sizes (diameter) at which the abundance jump occurs. The error bars are at 2 σ level confidence. The top half table lists the detected species, the bottom half table the upper limit on the abundances of undetected COMs (see text).

First, we did not find a significant difference in the χ^2 best fit value if α is -1, 0 or +1, in any of the five COMs, so that Table 4.1 reports the values obtained with α=0 only. Second, the T_{jump} is different in the five COMs: it is $\sim$ 20 K for ketene, $\sim 70 - 80$ K for acetaldehyde and formamide, and ~ 50 K for dimethyl ether and methyl formate. Third, the abundance in the outer envelope ranges from $\sim 3 \times 10^{-12}$ to $\sim 2 \times 10^{-10}$: acetaldehyde and dimethyl ether have the largest values, formamide the lowest, and ketene and methyl formate intermediate values. Fourth, the abundance jumps by about a factor 100 in all COMs except ketene, which remains practically constant (when the errors are considered). Note that we find a warm envelope abundance of acetaldehyde, dimethyl ether and methyl formate about 10 times smaller than those quoted by Cazaux et al. (2003). The difference mostly derives from a combination of different T_{jump} (assumed 100 K in Cazaux et al. (2003)), which implies different emitting sizes, and a different H_2 column density. As also emphasised by Cazaux et al. (2003), their hot corino sizes and H_2 column density were best guessed and, consequently, uncertain, whereas in the present work they are self-consistently estimated from the molecular lines.

Finally, for the undetected species we derived the upper limits to the abundance in the outer (assuming N(H_2)=8×10^{22} cm^{-2}, diameter=30”, T=20 K) and inner (assuming N(H_2)=3×10^{23} cm^{-2}, diameter=3”, T=60 K) envelope listed in Table 4.1.

4.6 Discussion

The analysis of outer and inner abundances of the five detected COMs leads to three major considerations and results.

1. COMs in the cold envelope:

The first important result of this analysis is the presence of COMs in the cold part of the envelope, with an abundance approximately constant. This is the first time that we have unambiguous evidence that also the cold outer envelope of (low mass) protostars can host COMs. Bacmann et al. (2012) reported the detection of acetaldehyde, dimethyl ether and methyl formate with abundances around 10^{-11} (with an uncertainty of about one order of magnitude) towards a cold ($\leq$ 10 K) pre-stellar core. Öberg et al. (2010); Cernicharo et al. (2012) reported the detection of the same molecules in B1-b, a low mass protostar where the temperature of the emitting gas is estimated 12–15 K (but no specific analysis to separate possible emission from warm gas has been carried out in this case), with similar abundances. Finally Vastel et al. (2014) reported the detection of tricarbon monoxide, methanol, acetaldehyde, formic acid, ketene, and propyne with abundances varying from 5×10^{-11} to 6×10^{-9}, in the prestellar core L1544 at T=10 K. In the cold envelope of IRAS16293, these COMs seem to be slightly more abundant, with abundances around 10^{-10}, possibly because the gas is slightly warmer. If the dust surface chemistry dominated the formation of COMs in the outer envelope, the COM abundance would increase with increasing dust temperature, namely decreasing radius in the cold envelope. However, our analysis does not show a definitively better χ^2 for the solution corresponding to α=-1, so that it cannot support this hypothesis. These new measurements add evidence that COMs, at least the ones studied here, are possibly formed also in cold conditions in addition to the warm grain surfaces, as predicted by current models (see Introduction).

2. Comparison with other objects:

Additional information on the formation (and destruction) routes of the detected COMs can be gained by the comparison of the COM abundances in galactic objects with different conditions (temperature, density and history) and Solar System comets. We consider here the abundances normalised to that of methyl formate, a molecule which has been detected in all objects that we want to compare. Figure 4.2 graphically shows this comparison. Ketene seems to be the most sensitive species in distinguishing two groups of objects: “cold” objects, formed by the cold and Galactic Center clouds, and the outer envelope of IRAS16293, and “warm” objects, constituted by the IRAS16293 hot corino (the only hot corino where the five COMs of this study have been detected

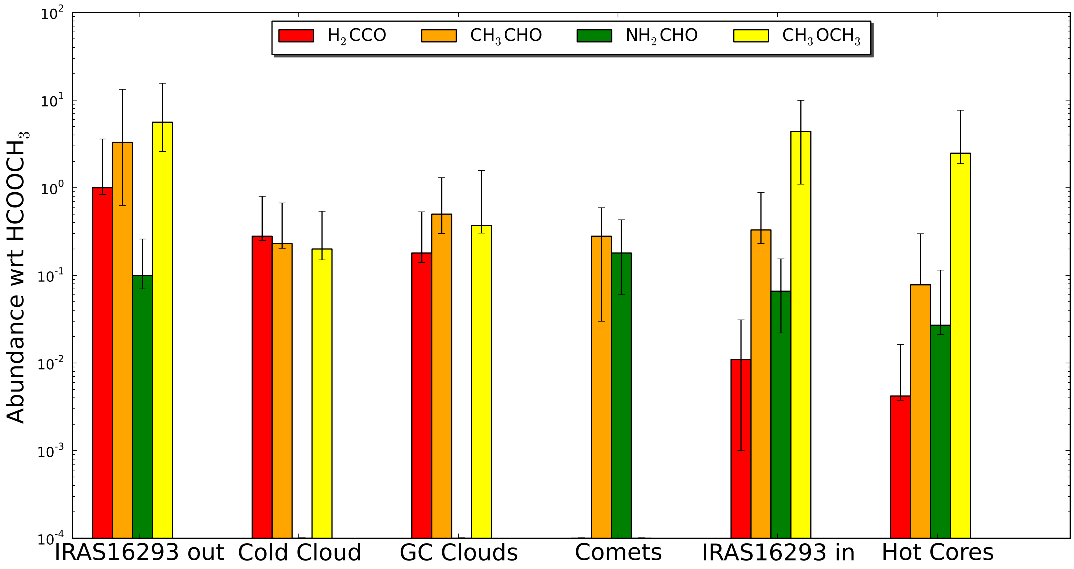

FIGURE 4.2: Abundances of the five COMs analysed in this work, normalised to the methyl formate abundance, in different objects: inner and outer envelope of IRAS16293 (this work), Cold Clouds(Bacmann et al. 2012; Cernicharo et al. 2012) , Galactic Center (GC) Clouds (Requena-Torres et al. 2006, 2008), Hot Cores (Gibb et al. 2000; Ikeda et al. 2001; Bisschop et al. 2007) note that we did not include SgrB2 in this sample), and Comets (Mumma & Charnley (2011)). Error bars represent the dispersion in each group of objects, except IRAS16293 for which error bars reflect the errors in the abundance determination (Table 4.1).

so far) and the massive hot cores. In the first group, ketene has an abundance larger than ∼0.1 with respect to methyl formate. In the second group, the relative abundance is lower than ∼0.1.

Finally, comets are definitively different from the hot cores, which are often compared with in the literature (see also the discussion in Caselli & Ceccarelli (2012)).

3. Correlations vs methyl formate.

Figure 4.3 shows the abundance of dimethyl ether, formamide, acetaldehyde and ketene as a function of the abundance of methyl formate in different ISM sources.

The linear correlation between the methyl formate and dimethyl ether is striking (Pearson correlation coefficient equal to 0.95 and power law index equal to 1.0). It covers almost five orders of magnitude, so that it persists even considering the dispersion of the measurements and the uncertainty linked to the determination of the absolute abundances mentioned above. This linear correlation, previously observed over a smaller range (e.g.Brouillet et al. (2013)), gives us an important and remarkable message: probably the precursor of methyl formate and dimethyl ether is either the same (Brouillet et al. 2013) or one of the two is the precursor of the other, an hypothesis that has not been invoked in the literature so far. We can not rule out other explanations, but they seem less likely at this stage. The bottom line is that such a link between these two species must be the same in cold and warm gas. This does not favour a formation mechanism of these two COMs on the grain surfaces for, according to the existing models, the mechanism does not work at low temperatures. Current chemical

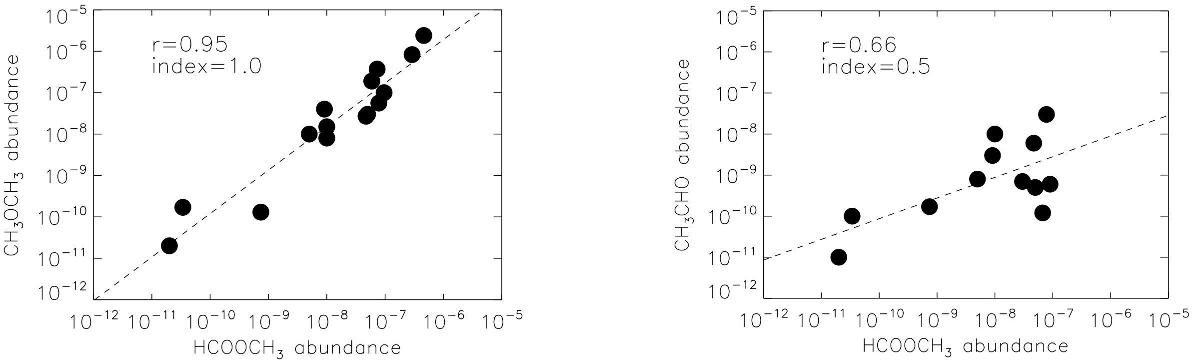

(A) Dimethyl ether

(B) Acetaldehyde

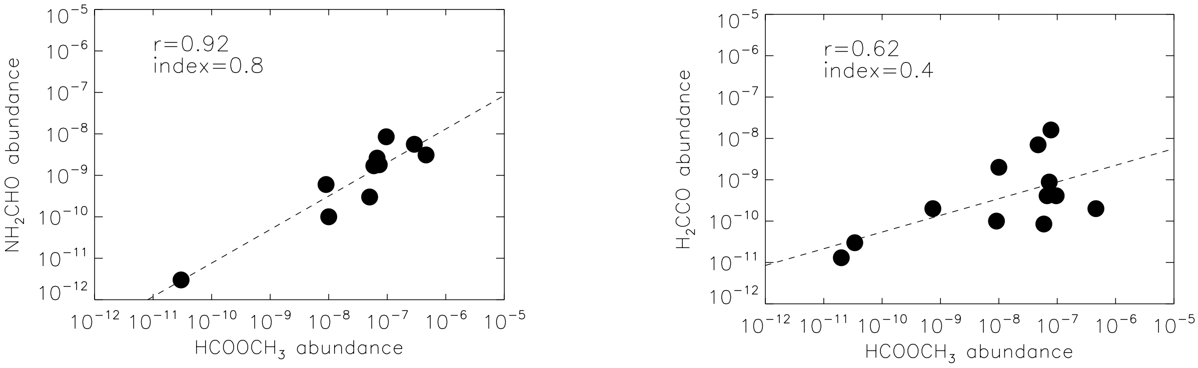

(C) Formamide

(D) Ketene

FIGURE 4.3: Abundance of dimethyl ether (top left), formamide (bottom left), acetaldehyde (top right) and ketene (bottom right) as a function of the abundance of methyl formate in different ISM sources. The correlation coefficient r and the power law index are reported for each species.

networks (e.g. KIDA at *http://kida.obs.u-bordeaux1.fr* and UMIST at *http://www.udfa.net*) do not report reactions linking the two species. Also the recent article by Vasyunin & Herbst (2013) , which proposes new reactions for explaining the Bacmann et al. (2012) and Cernicharo et al. (2012) observations, does not suggest a link between methyl formate and dimethyl ether. We suggest here that those networks are missing this important piece.

Similar analysis and conclusion (Pearson correlation coefficient equal to 0.92 and power law index equal to 0.8) apply to the methyl formate and formamide. On the contrary, the correlation between methyl formate and acetaldehyde or ketene is poorer (Pearson correlation coefficient equal to 0.66 and 0.62, power law index equal to 0.5 and 0.4, respectively).

4.7 Conclusions

We searched for all oxygen and nitrogen bearing COMs observed in the ISM, towards the envelope of IRAS16293. We detected six COMs: methyl cyanide, ketene, acetaldehyde, formamide, dimethyl ether, and methyl formate. We report the analysis of the last five species. A specific analysis of methyl cyanide emission will be presented in a subsequent paper. For each species, several lines covering a large upper level energy range (up to 150 K) are detected. This allows us to disentangle the emission originating in the cold and warm envelope, respectively, and where the transition between the two occurs. The main results of this study can be summarised in three points:
1- The five analysed COMs are all present in the cold envelope of IRAS16293. Acetaldehyde and dimethyl ether have the largest abundances, $\sim 10^{-10}$, slightly larger than the values found in other cold objects (Bacmann et al. 2012; Cernicharo et al. 2012). These new measurements add support to the idea that a relatively efficient formation mechanism for these COMs must exist in the cold gas phase.
2- When considering the abundance of the five analysed COMs, the ketene abundance relative to methyl formate is different in cold and hot objects. Besides, comets are different from the hot cores.
3- There is a remarkable correlation between the abundance of methyl formate and that of dimethyl ether and formamide. The correlation spans over five orders of magnitude. This may suggest that both dimethyl ether and formamide have a progenitor common with methyl formate, and that the mechanism of their formation is gas phase reactions. We suggest that the current chemical networks still miss important pieces.

Chapter 5

Cyanopolyynes in IRAS16293-2422

This chapter was accepted to publish in Astronomy & Astrophysics Journal with the title " The history of the solar type protostar IRAS16293–2422 as told by the cyanopolyynes" : A. Jaber Al-Edhari, C. Ceccarelli, C. Kahane, S. Viti, N. Balucani, E. Caux, B. Lefloch, F. Lique, E. Mendoza, D. Quenard, and L. Wiesenfeld.

5.1 Abstract

Cyanopolyynes are chains of carbon atoms with an atom of hydrogen and a CN group on either side. They are detected almost everywhere in the ISM, as well as in comets. In the past, they have been used to constrain the age of some molecular clouds, since their abundance is predicted to be a strong function of time. Finally, cyanopolyynes can potentially contain a large fraction of molecular carbon. We present an extensive study of the cyanopolyynes distribution in the Solar-type protostar IRAS16293-2422. The goals are: (i) to obtain a census of the cyanopolyynes present in this source, as well as of their isotopologues; (ii) to derive how their abundance varies across the protostar envelope; (iii) to obtain constraints on the history of IRAS16293-2422 by comparing the observations with the predictions of a chemical model. We analyse the data from the IRAM-30m unbiased millimeter and submillimeter spectral survey towards IRAS16293-2422 named TIMASSS. The derived Spectral Line Energy Distribution (SLED) of each detected cyanopolyyne is compared with the predictions from the radiative transfer code GRAPES (GRenoble Analysis of Protostellar Envelope Spectra) to derive the cyanopolyynes abundance across the envelope of IRAS16293-2422. Finally, the derived abundances are compared with the predictions of the chemical model UCL_CHEM. We detect several lines from cyanoacetylene (HC_3N) and cyanodiacetylene (HC_5N), and report the first detection of deuterated cyanoacetylene, DC_3N, in a Solar-type protostar. We found that the HC_3N abundance is roughly constant ($\sim 1.3 \times 10^{-11}$) in the outer cold envelope of IRAS16293-2422 and it increases by about a factor 100 in the inner region where the dust temperature exceeds 80 K, namely when the "volcano" ice desorption is predicted to occur. The HC_5N has an abundance similar to HC_3N in the outer envelope and about a factor of ten lower in the inner region. The comparison with the chemical model predictions provides constraints on the oxygen and carbon gaseous abundance in the outer envelope and, most importantly, on the age of the source. The HC_3N abundance derived in the inner region, and where the increase occurs, also provide strong constraints on the time taken for the dust to warm up to 80 K, which has to be less than $\sim 10^3 - 10^4$ yr. Finally, the cyanoacetylene deuteration is about 50% in the outer envelope and $\sim$ 5% in the warm inner region. The relatively low deuteration in the warm region suggests that we are witnessing a fossil of the HC_3N abundantly formed in the tenuous phase of the pre-collapse and then frozen into the grain mantles at a later phase. The accurate analysis of the cyanopolyynes in

IRAS16293-2422 unveils an important part of its past story. It tells us that IRAS16293-2422 underwent a relatively fast ($\leq 10^5$ yr) collapse and a very fast ($\leq 10^3 - 10^4$ yr) warming up of the cold material to 80 K.

5.2 Introduction

Cyanopolyynes, H-C_{2n}-CN, are linear chains of $2n+1$ carbon bonded at the two extremities with a hydrogen atom and a CN group, respectively. They seem to be ubiquitous in the ISM, as they have been detected in various environments, from molecular clouds to late type carbon rich AGB stars. The detection of the largest cyanopolyyne, $HC_{11}N$, has been reported and then dismissed in the molecular cloud TMC-1 (Bell et al. 1997; Loomis et al. 2016), which shows an anomalously large abundance of cyanopolyynes with respect to other molecular clouds. Curiously enough, in star forming regions, only relatively short chains have been reported in the literature so far, up to HC_7N, in dense cold cores and WCCC (Warm Carbon Chain Chemistry) sources (e.g. Sakai et al. 2008; Cordiner et al. 2012; Friesen et al. 2013). For many years, cyanopolyynes have been suspected to be possible steps towards the formation of simple amino acids (e.g. Brack 1998). More recently, the rich N-chemistry leading to large cyanopolyynes chains observed in Titan has renewed the interest towards this family of molecules, as Titan is claimed to be a possible analogue of the early Earth (Lunine 2009). An important property of cyanopolyynes, and particularly relevant for astrobiological purposes, is that they are more stable and robust against the harsh interstellar environment compared to their monomer, and hence they may better resist the exposure to UV and cosmic rays (Clarke & Ferris 1995). Very recent observations towards the comet 67P/Churyumov-Gerasimenko by Rosetta seem to support the idea that cyanide polymers, and, by analogy, cyanopolyynes, are abundant on the comet's surface (Goesmann et al. 2015).

Whatever the role of cyanopolyynes in prebiotic chemistry, when trapped in interstellar ices, they for sure can carry large quantities of carbon atoms. It is, therefore, of interest to understand in detail their formation, carbon chain accretion and evolution in Solar-like star forming regions. The goal of this article is to provide the first census of cyanopolyynes in a Solar-like protostar. To this end, we used the 3-1mm unbiased spectral survey TIMASSS (§5.4) towards the well studied protostar IRAS16293-2422 (§5.3), to derive the abundance across the envelope and hot corino for HC_3N, HC_5N and their respective isotopologues (§5.5). The measured abundance profiles provide us with constraints on the formation routes of these species (§5.6). Section (§5.7) discusses the implications of the analysis and Section (§5.8) summarizes our conclusions.

5.3 Source description

IRAS16293-2422 (hereinafter IRAS16293) is a Solar-type Class 0 protostar in the ρ Ophiuchus star forming region, at a distance of 120 pc (Loinard et al. 2008). It has a bolometric luminosity of 22 L (Crimier et al. 2010b). Given its proximity and brightness, it has been the target of numerous studies that have reconstructed its physical and chemical structure. Briefly, IRAS16293 has a large envelope that extends up to ∼6000 AU and that surrounds two sources, named I16293-A and I16293-B in the literature, separated by ~ 5 (∼600 AU; Wootten (1989); Mundy et al. (1992)). I16293-A sizes are ~ 1, whereas I16293-B is unresolved at a scale of ~ 0.4 (Zapata et al. 2013). I16293-A itself is composed of at least two sources, each one emitting a molecular outflow (Mizuno

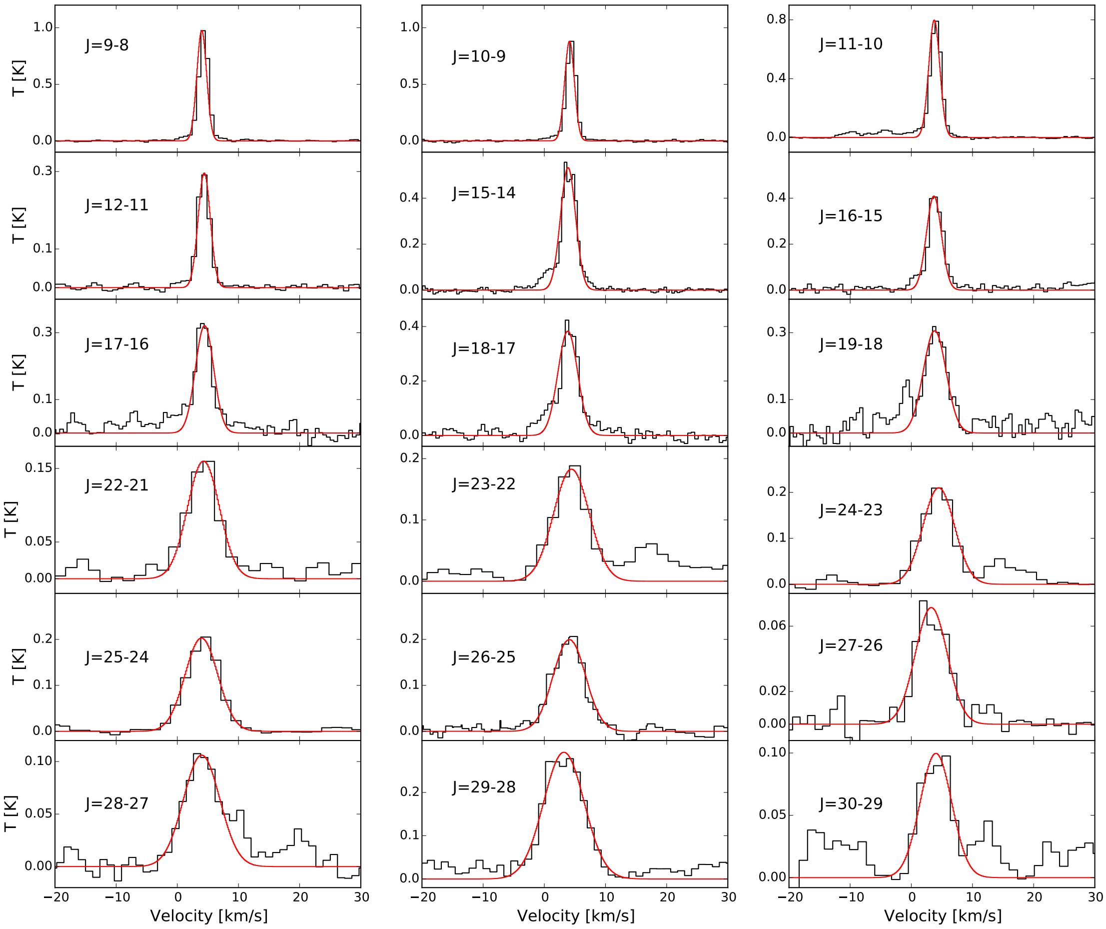

FIGURE 5.1: Observed spectra of the detected lines of HC_3N. The red curves show the Gaussian fits. The temperature is a main beam antenna temperature.

et al. 1990; Loinard et al. 2013). I16293-B possesses a very compact outflow (Loinard et al. 2013) and is surrounded by infalling gas (Pineda et al. 2012; Zapata et al. 2013). From a chemical point of view, IRAS16293 can be considered as composed of an outer envelope, characterised by low molecular abundances, and a hot corino, where the abundance of many molecules increases by orders of magnitude (e.g. Ceccarelli et al. 2000a; Schöier et al. 2002; Coutens et al. 2013a; Jaber et al. 2014). The transition between the two regions occurs at ∼100 K, the sublimation temperature of the icy grain mantles.

5.4 The data set

5.4.1 Observations

We used data from The IRAS16293 Millimeter And Submillimeter Spectral Survey (TIMASSS; Caux et al. (2011)). Briefly, the survey covers the 80-280 GHz frequency interval and it has been obtained at the IRAM-30m, during the period January 2004 to August 2006 (∼ 200 hr). Details on the data reduction and calibration can be found in Caux et al. (2011). We recall here the major features, relevant for this work. The

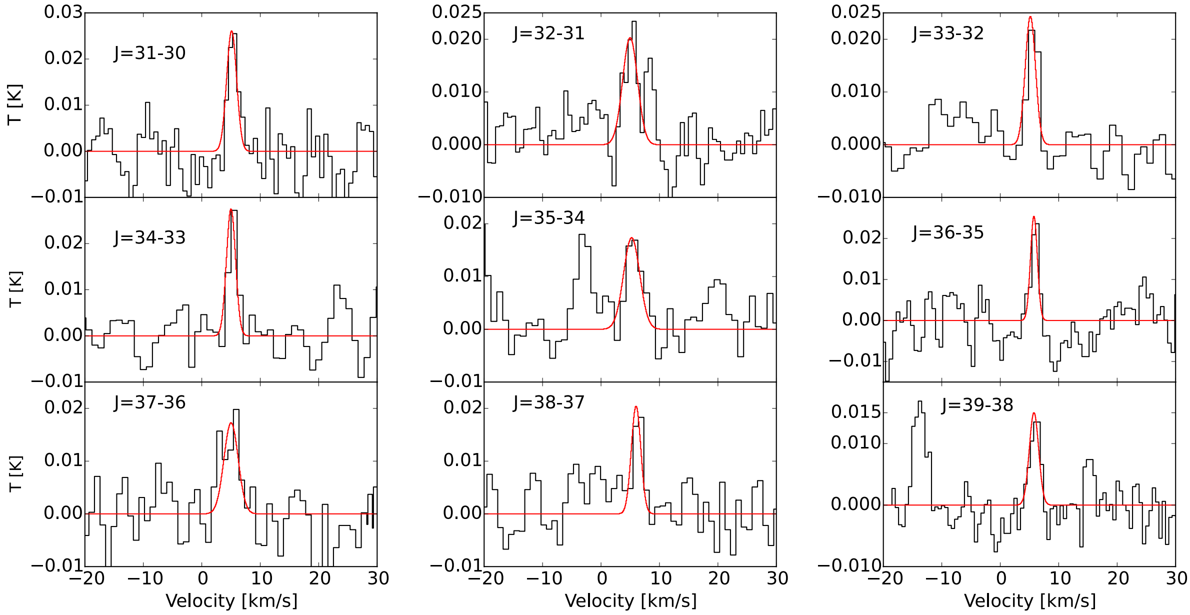

FIGURE 5.2: Observed spectra of the detected lines of HC_5N. The red curves show the Gaussian fits. The temperature is a main beam antenna temperature.

telescope beam depends on the frequency and varies between 9" and 30". The spectral resolution varies between 0.3 and 1.25 MHz, corresponding to velocity resolutions between 0.51 and 2.25 km/s. The achieved rms ranges from 4 to 17 mK. Note that it is given in a 1.5 km/s bin for observations taken with a velocity resolution $\leq$1.5km/s, and in the resolution bin for larger velocity resolutions. The observations are centered on I16293-B at α(2000.0) = 16^h 32^m 22^s.6 and δ(2000.0)= -24^o 28$'$ 33$''$. Note that the I16293-A and I16293-B components are both inside the beam of the observations at all frequencies.

5.4.2 Species identification

We searched for the lines of the cyanopolyynes and their isotopologues using the spectroscopic databases JPL(Jet Propulsion Laboratory) (Pickett et al. 1998) and CDMS (Cologne Database for Molecular Spectroscopy) (Müller et al. 2005), and the package CASSIS (Centre d'Analyse Scientifique de Spectres Instrumentaux et Synthétiques) (*http://cassis.irap.omp.eu*) for gaussian fitting to the lines. For the line identification we adopted the following criteria:

1. The line is detected with more than 3σ in the integrated line intensity.
2. The line is not blended with other molecular lines.
3. The line intensity is "compatible" with the Spectral Line Energy Distribution (SLED): since cyanopolyyynes are linear molecules, their SLED is a smooth curve, so that lines having intensities that are out of the SLED defined by the majority of the lines are discarded, as shown in Figure A.1.
4. The line FWHM is similar to that of the other cyanopolyynes lines with a similar upper level energy. In practice, *a posteriori* the FWHM is about 2 km/s for lines with J$\leq$12, and increases to 6–7 for J=22–30 lines.

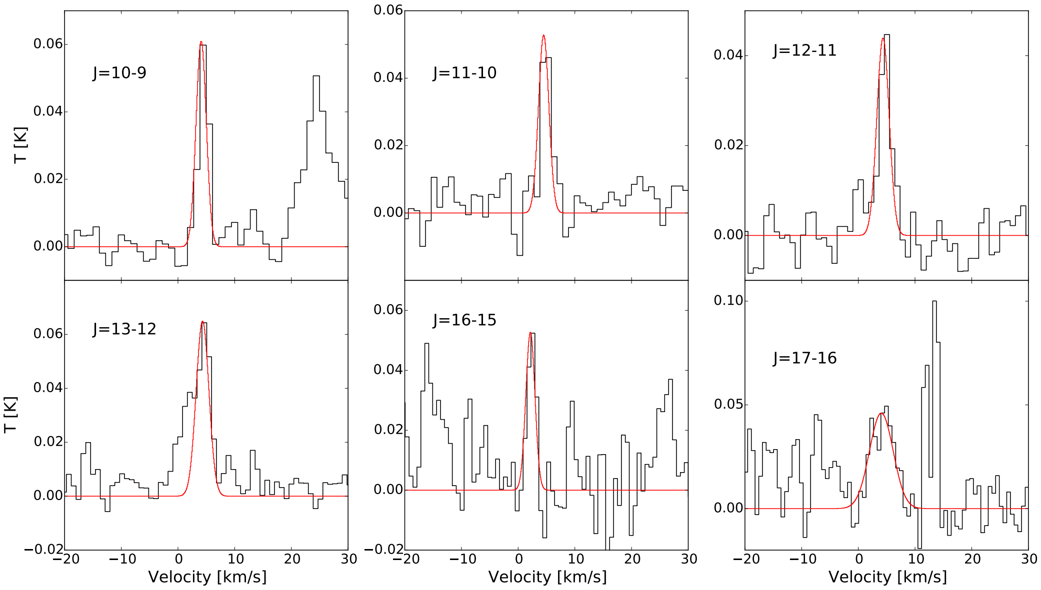

FIGURE 5.3: Observed spectra of the detected lines of DC_3N. The red curves show the Gaussian fits. The temperature is a main beam antenna temperature.

5. The line rest velocity V_{LRS} does not differ by more than 0.5 km/s from the V_{LRS} of the other cyanopolyynes lines.

Following the first two criteria leads to the detection of 18 lines of HC_3N (from J=9-8 to J=30-29), 9 lines of HC_5N (from J=31-30 to J=39-38) and the detection of 6 lines of DC_3N (from J=10-9 to J=17-16). The full list of detected lines with their spectroscopic parameters is reported in Table 5.1. All the spectra are shown in Figures 5.1, 5.2 and 5.3 for HC_3N, HC_5N and DC_3N, respectively. We did not detect any line from the ^{13}C isotopologues of HC_3N.

The application of the remaining three criteria leads us to discard four HC_3N lines (at 109.173, 245.606, 254.699 and 263.792 GHz), which suffer of calibration problems Caux et al. (2011) and/or blending with unidentified species (see Figure A.1). Similarly, one HC_5N line (at 95.850 GHz) was discarded, because of its abnormal value for the intensity, FWHM and velocity compared to the rest of the lines (see Tab. 5.1). Finally, one DC_3N (at 135.083 GHz) is considered as tentatively detected.

In summary, we clearly detected HC_3N, HC_5N and DC_3N, for which 14, 8 and 6 lines have been identified following the five criteria above. We did not detect any ^{13}C isotopologue of HC_3N, nor cyanopolyynes larger than HC_5N.

5.5 Line modeling

5.5.1 Model description

As in our previous work (Jaber et al. 2014, hereinafter Paper I), we used the package GRAPES (GRenoble Analysis of Protostellar Envelope Spectra), based on the code described in Ceccarelli et al. (1996, 2003a), to interpret the Spectral Line Energy Distribution (SLED) of the detected cyanopolyynes. Briefly, GRAPES computes the SLED from a spherical infalling envelope for a given density and temperature structure. The code uses the beta escape formalism to locally solve the level population statistical equilibrium equations and consistently computes each line optical depth by integrating it over the solid angle at each point of the envelope. The predicted line flux is then integrated over the whole envelope after convolution with the telescope beam. The abundance X (with respect to H_2) of the considered species is assumed to vary as a function of the radius with a power law α in the cold part of the envelope, and as a "jump" to a new abundance in the warm part, corresponding to the sublimation of ices (see, e.g. Caselli & Ceccarelli (2012)). The transition between the two regions is set by the dust temperature, to simulate the sublimation of the ice mantles, and occurs at T_{jump}.

The abundance is, therefore, given by:

$$\begin{aligned} X(r) &= X_{out} \left(\frac{r}{R_{max}} \right)^{\alpha} & T_{dust} \leq T_{jump} \\ X(r) &= X_{in} & T_{dust} > T_{jump} \end{aligned} \tag{5.1}$$

where R_{max} represents the largest radius of the envelope. In the present study, we use the physical structure of the IRAS16293 envelope derived by Crimier et al. (2010b), where the maximum radius is 1×10^{17} cm.

We carried out non-LTE calculations for all species. We have used the collisional coefficients for HC_3N computed by Faure et al. (2016). For DC_3N collisional coefficients, we have assumed the same as those of HC_3N. Finally, the collisional coefficients for HC_5N have been computed by Lique et. al. (in preparation). Briefly, HC_5N rate coefficients were extrapolated from HCN (Ben Abdallah et al. 2012) and HC_3N (Wernli et al. 2007) considering that the cyanopolyynes rate coefficients are proportional to the size of the molecules as first suggested by Snell et al. (1981). However, in order to improve the accuracy of the estimation, we consider scaling factors depending also on the transition and the temperature. Hence, the ratio of HC_3N over HCN rate coefficients was also used to evaluate the HC_5N ones as follow :

$$k_{HC_5N}(T) = k_{HC_3N}(T) * [\frac{1}{2} + \frac{1}{2}\frac{k_{HC_3N}(T)}{k_{HCN}(T)}] \tag{5.2}$$

Finally, note that the disadvantage of GRAPES, namely its incapacity to compute the emission separately for the two sources I16293-A and I16293-B (Jaber et al. 2014), can be neglected here because previous interferometric observations by Chandler et al. (2005) and Jørgensen et al. (2011) have demonstrated that the cyanopolyynes line emission arises from source I16293-A, as also found by the analysis by Caux et al. (2011).

We ran large grids of models varying the four parameters, X_{in}, X_{out}, α and T_{jump}, and found the best fit to the observed fluxes. In general, we explored the X_{in}–X_{out} parameter space by running 10x10 and 20x20 grids for α equal to -1, 0, +1 and +2, and T_{jump} from 10 to 200 K by steps of 10 K. Note that we first started with a 3 or 4 orders of magnitude range in X_{in} and X_{out} to find a first approximate solution and then we fine-tuned the grid around it

5.5.2 Results

HC_3N

The HC_3N SLED has been analysed in two steps, as follows.

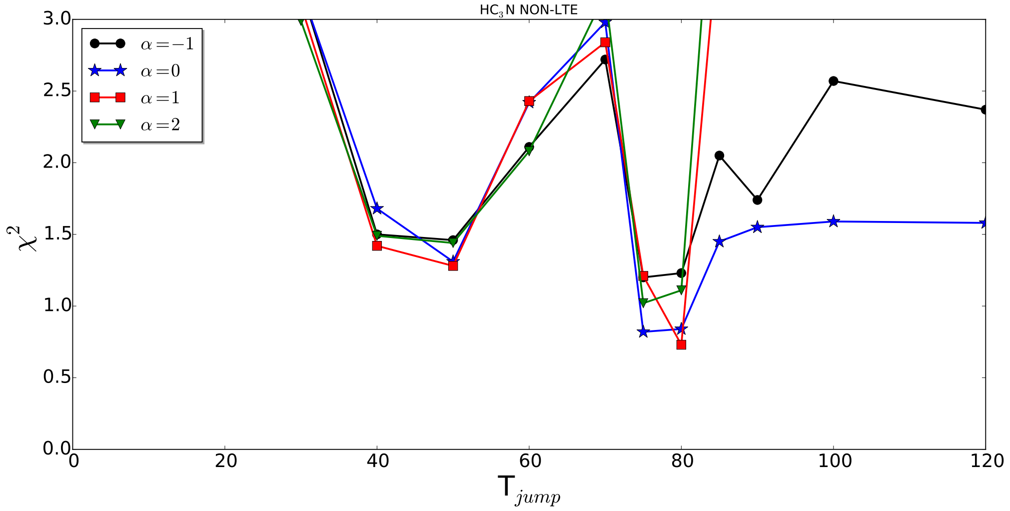

FIGURE 5.4: Results of the HC3N modeling. The best reduced χ^2 optimised with respect to X_{in} and X_{out} as a function of T_{jump}.

Step 1: We first ran a grid of models varying T$_{jump}$, X_{in} and X_{out} with α=0. The best fit for this first step is obtained with T$_{jump}$=80 K, $X_{in} = 3.6 \times 10^{-10}$, and $X_{out} = 6.0 \times 10^{-11}$. However, the fit is not very good (reduced χ^2=1.7). We plotted for each line the predicted velocity-integrated flux emitted from a shell at a radius r (namely $dF/dr * r$) as a function of the radius, as shown in Figure A.2. For the three lines with the lowest J (from J=9 to 11) the predicted shell-flux increases with the radius and abruptly stops at the maximum radius of the envelope. Therefore, these three lines are very likely contaminated by the molecular cloud, which could explain the bad χ^2. In the second modeling step, thus, we excluded these lines and repeated the modeling, as described below.

Step 2: We ran a grid of models as in step 1 and, indeed, found a better χ^2 (0.8). We, therefore, extended the analysis varying the α parameter between -1 and +2, together with the other three parameters T$_{jump}$, X_{in} and X_{out}. The results are reported in Figure 5.4 and Table 5.2. Note that, in Table 5.2, we also report the values of the abundance of the envelope, X_{T20}, at a radius equal to the angular size of the beam with the lowest frequencies, namely 29".5 in diameter. At that radius, which is 2.75×10^{16} cm (around 1800 AU), the envelope dust temperature is 20 K.

Figure 5.4 shows the χ^2 obtained for each value of α, minimised with respect to X_{in} and X$_{out}$, as a function of T$_{jump}$. A χ^2 less than unity is obtained with T$_{jump}$ equal to 80 K and α equal to 0 and 1 (Table 5.2). Figure 5.5 shows the abundance profiles of HC$_3$N as predicted by the best fit models. Note that the four models have the same T$_{jump}$ (80 K), and the same X_{in} (9×10^{-10}) and X_{T20} at 20 K ($\sim 1 \times 10^{-11}$), within a factor 2. Therefore, the determination of T$_{jump}$, X_{in} and X_{out} at 20 K is very robust and depends very little on the assumption of the HC$_3$N abundance distribution.

Given the similarity of our results regardless of α, in the following, we will only consider the case of α=0. Figure A.3 shows the χ^2 contour plots as a function of the inner X_{in} and outer X_{out} with T_{jump}=80 K. Figure A.4 reports the ratio of the observed over predicted line fluxes as a function of the upper level energy of the transition, to show the goodness of the best fit model. Finally, Figure A.5 shows the predicted shell-flux as a function of the radius for a sample of lines. As a final remark, we note that we

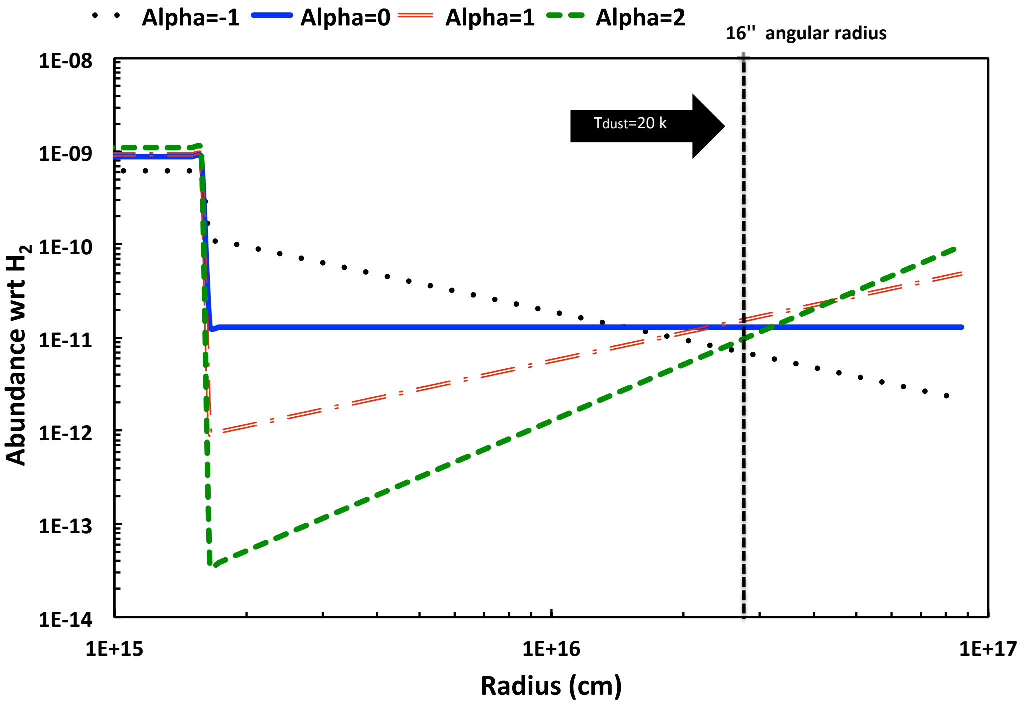

FIGURE 5.5: Abundance profiles of the four HC_3N best fit models of Tab. 5.2.

also ran LTE models and obtained approximately the same results.

HC_5N

Having fewer lines, we decided to assume that HC_5N follows the spatial distribution of HC_3N and ran a grid of models with α=0, and T=80 K and X_{in} and X_{out} as free parameters. The X_{in}–X_{out} χ^2 surface is shown in Figure A.3 and the ratio between the observed and best fit predicted intensities is shown in Figure A.4. Table 5.3 summarises the best fit values. We only obtained an upper limit to the X_{in} abundance, $\leq 8 \times 10^{-11}$, while the X_{out} abundance is $\sim 1 \times 10^{-11}$. When compared to HC_3N, the HC_5N abundance is, therefore, more than ten times lower in the hot corino region, while it is the same in the outer cold envelope.

DC_3N

Following the discussion on the HC_3N line analysis, we did not consider the three DC_3N lines with the lowest upper level energy, as they are likely contaminated by the molecular cloud.

For the remaining three lines, we adopted the same strategy as for HC_5N for the SLED analysis, namely we adopted α=0, and T=80 K and varied X_{in} and X_{out}. The results are shown in Figs. A.3 and A.4, and summarised in Table 5.3. We obtained an upper limit of X_{in}, $\leq 4 \times 10^{-11}$, while X_{out} is $\sim 5 \times 10^{-12}$. This implies a deuteration ratio of $\sim$ 5% and 50% in the hot corino and cold envelope, respectively.

Undetected species and conclusive remarks

As mentioned earlier, we do not detect larger cyanopolyynes nor ^{13}C isotopologues. For the undetected species we derived the upper limits to the abundance by assuming that the non-detected emission arises in the hot corino (with a temperature of 80 K, diameter = 2, N(H_2) = 1.5×10^{23} cm^{-2}, line FWHM = 6 km/s), and cold envelope (with a temperature of 20 K, diameter = 30", N(H_2) = 3.5×10^{22} cm^{-2}, line FWHM = 3 km/s), respectively. The results are listed in Table 5.3.

From the HC_5N and DC_3N modeling, we conclude that the detected lines of both species are dominated by the emission from the cold outer envelope, as we only obtain upper limits to their abundance in the warm inner region. This conclusion is coherent with the line widths reported in Table 5.1. Indeed, the HC_3N lines (see also Figure A.1) show a clear separation between the low energy transitions, for which the FWHM is around 3 km/s, and the high energy ones, for which the FWHM is around 6 km/s or higher. This difference strongly suggests that the two sets of lines probe different regions. As the low energy lines correspond to E_{up} values lower than 80 K, a very natural explanation is that they are dominated by emission from the cold envelope, whereas the high energy lines ($E_{up} \geq 110$ K) are dominated by emission from the inner warm region. As the HC_5N and DC_3N lines have FWHM around 3 km/s, it is not surprising that our modeling concludes that they are dominated by emission from the cold envelope.

5.6 The chemical origin of HC_3N

As discussed in the Introduction, HC_3N is an ubiquitous molecule in the ISM. There are several routes by which a high HC_3N abundance may arise. Briefly, HC_3N can form via the following neutral-neutral reactions (e.g. Wakelam et al. 2015):

$C_2H_2 + CN \longrightarrow HC_3N + H$

$C_4H + N \longrightarrow HC_3N + C$

$C_3H_2 + N \longrightarrow HC_3N + H$

$C_2H + HNC \longrightarrow HC_3N + H$

in order of importance under the typical dense cloud conditions. Roughly, the first reaction contributes to about 80–90% of the formation of HC_3N, with the other three 'swaping' in importance depending on the initial conditions but together contributing the remaining 20%. Its main destruction channels are either via reactions with He^+ or reactions with atomic carbon, both contributing 30-40% to the destruction, depending on the initial conditions assumed. In dark clouds ($n_H \sim 10^4$–10^5 cm^{-3}), it is well known that HC_3N, together with other carbon chain molecules, is abundant (e.g. Suzuki et al. (1992); Caselli et al. (1998)). Thus, based on its routes of formation and destruction, one would expect the HC_3N abundance to increase as a function of gas density, at least before freeze-out onto the dust grains takes over. Interestingly, however, the HC_3N abundance with respect to H_2 estimated in both the envelope and the hot corino of IRAS16293 is rather low ($\sim 10^{-11}$ and $\sim 10^{-9}$ respectively). In this section we, therefore, discuss the possible physical conditions that may lead to such low abundances of HC_3N.

5.6.1 Cold envelope

First of all, we investigate, qualitatively, what conditions in the cold envelope may lead to a fractional abundance of HC_3N as low as 10^{-11}. We would like to emphasise that this is not an easy task as very small changes in the main atomic elements (O, C, N) or molecular species (CO) can lead to very large changes in the abundances of tracers species. Hence, it is likely that small uncertainties in the initial elemental abundances of the cloud as well as its depletion history (which is dependent on the time the gas 'sits' at a particular gas density) can easily lead to differences in the abundances of species such as HC_3N of orders of magnitude.

For our analysis, we make use of the time dependent chemical model UCL_CHEM (Viti et al. 2004). The code is used in its simplest form, namely we only included gas phase chemistry with no dynamics (the gas is always kept at a constant density and temperature). The gas phase chemical network is based on the UMIST database (McElroy et al. 2013) augmented with updates from the KIDA database as well as new rate coefficients for the HC_3N and HC_5N network as estimated by Loison et al. (2014). The chemical evolution is followed until chemical equilibrium is reached. In order to understand the chemical origin of the HC_3N abundance that we measured in the cold envelope of IRAS16293 ($\sim 10^{-11}$), we modeled a gas density of 2×10^6 cm^{-3} and a gas temperature of 20 K, which are the values inferred by Crimier et al. (2010b) at a radius equivalent to the observations telescope beam (see §5.5.2).

We ran a small grid of models where we varied:

- the carbon and oxygen elemental abundances in the range of 0.3–1 and 1–3 $\times 10^{-4}$, respectively;
- the nitrogen elemental abundance: 6 (solar) and 2 $\times 10^{-5}$;
- the cosmic ray ionisation rate: 5×10^{-17} s^{-1} (assumed as our standard value) and 10 times higher.

Note that varying the C, O and N elemental abundances can be considered, coarsely, as mimicking, qualitatively, the degree of depletion of these elements onto the grain mantles. Furthermore, we varied the cosmic ray ionisation rate as it is a rather uncertain parameter that could be enhanced with respect to the "standard" value because of the presence of X-rays or an energetic $\geq$MeV particles source embedded inside the envelope (e.g. Doty et al. (2004); Ceccarelli et al. (2014b)).

The results of the modelling are plotted in Figure 5.6. The top left panel is our reference model, with standard cosmic ray ionization rate (5×10^{-17} s^{-1}), at chemical equilibrium ($\geq 10^6$ yr), and with a solar abundance of nitrogen (6.2×10^{-5}). Note that the values of the HC_3N abundances are log of the fractional abundance with respect to the total number of hydrogen nuclei, hence the best match with the observations is for a value of -11.3. We find that this value is reached within our reference model for low values of O/H ($\leq 1.5 \times 10^{-4}$) and for a O/C ratio between 1.5 and 2, with the lowest O/C ratio needed with the highest O/H abundance. This implies that both oxygen and carbon are mostly frozen onto the grain icy mantles by about the same factor, as the O/C ratio is similar to the one in the Sun (1.8; see e.g. Asplund et al. (2009)) and in the HII regions (1.4; see e.g. García-Rojas & Esteban (2007)). Increasing the cosmic rays ionisation rate by a factor of ten changes little the above conclusions, having as an effect a slightly larger parameter space in O/H and O/C to reproduce the observed HC_3N abundance. On the contrary, decreasing N/H by a factor of three slightly diminishes the O/H and O/C parameter space. Finally, the largest O/H and O/C parameter space that reproduces the observed HC_3N abundance in the cold envelope of IRAS16293 is obtained by considering earlier times, 10^5 years (bottom right of Figure 5.6). This possibly implies that the gas in the envelope is at a similar age to that of the protostar.

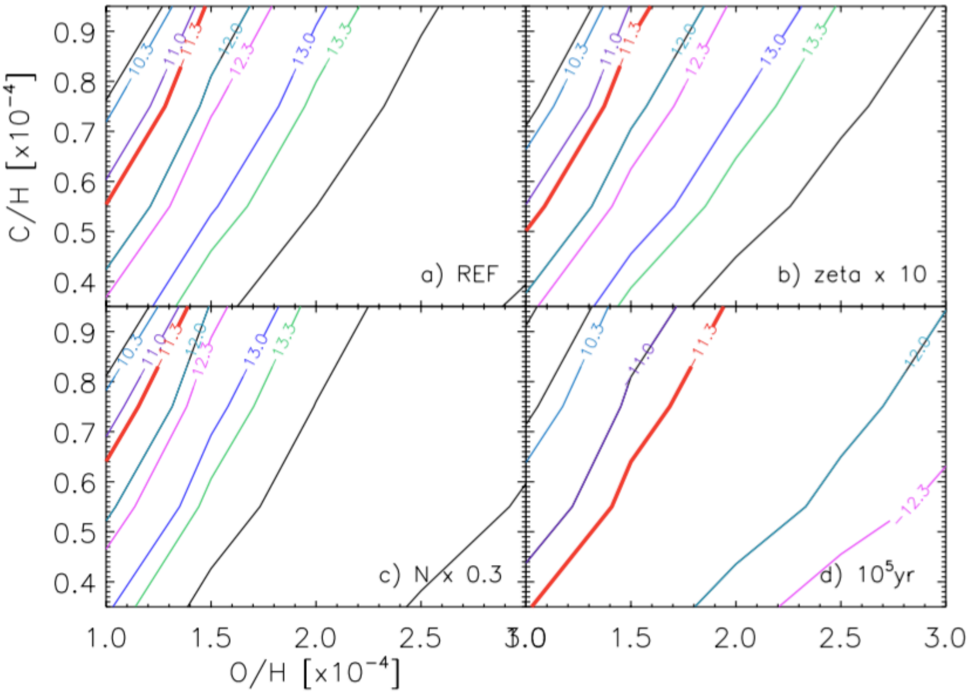

FIGURE 5.6: Predicted HC_3N abundance (in log) as a function of the O/H (x-axis) and C/H (y-axis) for four cases: the reference model, described in the text (upper left panel), and then the same but with a cosmic ray ionisation rate increased by a factor ten (upper right panel), a nitrogen elemental abundance decreased by a factor three (lower left panel) and at a time of 10^5yr (lower right panel). The thick red lines mark the HC_3N abundance measured in the cold envelope of IRAS16293.

5.6.2 Hot corino

As we move towards the centre of the protostar(s) a jump in the HC_3N abundance by roughly two orders of magnitude is observed at around 80 K. So the first question to answer is what this 80 K represents. According to the TPD (Temperature Programmed Desorption) experiments by Collings et al. (2004), and successive similar works, in general, the ice sublimation is a complex process and it does not occur at one single temperature but occurs in several steps. In the particular case of iced HC_3N, it is expected to have two sublimation peaks, at a dust temperature of about 80 and 100 K, respectively (see Viti et al. (2004) for details). The first one corresponds to the so-called *volcano* ice desorption, whereas the second one corresponds to the ice co-desorption, namely the whole ice sublimation. Therefore, our *measured* jump temperature of 80 K indicates that the most important sublimation is due to the volcano desorption, while the co-desorption injects back only a fraction of the frozen HC_3N. In addition, the 80 K jump also tells us that, whatever other process contributing to the formation of HC_3N at lower ($\leq$ 80 K) temperatures, has to be negligible. In other words, considering the reactions in the synthesis of HC_3N reported at the beginning of §5.6, the desorption of C-bearing iced species, like for example CH_4, has to provide a negligible contribution to the HC_3N abundance.

In order to understand what all this implies, we ran UCL_CHEM again, but this time we included freeze-out of the gas species in the cold phase, to simulate the cold and dense prestellar phase. We then allowed thermal evaporation of the icy mantles as

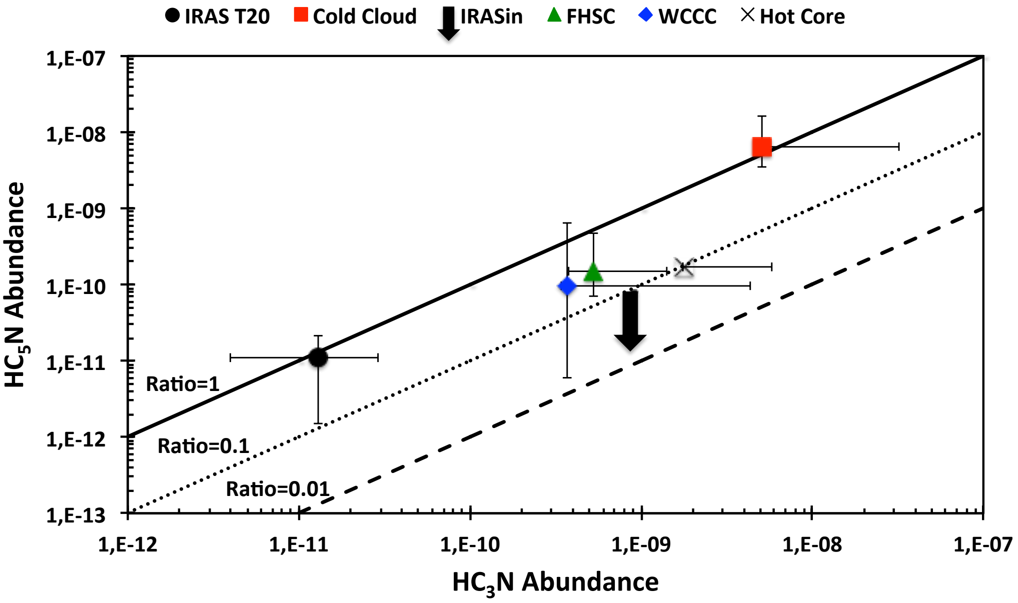

FIGURE 5.7: Abundance of HC_5N as a function of the abundance of HC_3N in different protostellar and cold sources: inner (black arrow) and outer envelope (T_{20}) of IRAS16293 (black filled circle) presented in this work, Warm Carbon-Chain Chemistry (WCCC) sources (blue diamond) (Sakai et al. 2008; Jørgensen et al. 2004), First Hydrostatic Core (FHSC) source (green triangle) (Cordiner et al. 2012), Hot Cores sources (cross) (Schöier et al. 2002; Esplugues et al. 2013), and Galactic Center Clouds (red square) (Marr et al. 1993; Aladro et al. 2011).

a function of the species and temperature of the dust following the 'recipe' of Collings et al. (2004), in which the ice sublimation occurs in several steps (see (Viti et al. 2004) for the details). We find that the jump in the HC_3N abundance from 10^{-11} to 10^{-9} occurs only if thermal evaporation due to the volcano peak occurs quickly, on a timescale of $\leq 10^{3-4}$yr, implying that the increase of the dust temperature to ~ 80 K must indeed also occur quickly, on a similar timescale. In addition, if frozen species containing C, like CO and CH_4, sublimate at earlier times, namely at colder temperatures, and remain in the gas for too long prior to the volcano explosion, then the HC_3N abundance reaches much too high abundances too quickly. In other words, the sublimation of those species must have occurred not much before the volcano sublimation, again on timescales of $\leq 10^3$ yr.

5.6.3 HC_5N

We finally note that none of our models can reproduce an HC_5N abundance comparable to the one of HC_3N, as observed in the cold envelope of IRAS16293. All models predict indeed a much lower HC_5N abundance, by more than a factor ten, than the HC_3N abundance. Since in the warm ($T \geq 80$ K) region we only derive an upper limit for the HC_5N abundance (which is at least ten times lower than the HC_3N one), the models can not be constrained. The failure of our models to reproduce HC_5N in the cold envelope is likely due to a lack of a comprehensive network for the formation and destruction of the species HC_5N and, therefore, calls for a revision of its gaseous chemistry. Here we briefly summarize the main routes of formation and destruction for this

species in our models:
$C_2H_2 + C_3N \longrightarrow HC_5N + H$
$C_4H + HNC \longrightarrow HC_5N + H$
contributing to its formation $\sim$ 70% and 30% respectively, and
$H_3^+ + HC_5N \longrightarrow HC_5NH^+ + H_2$
$HCO^+ + HC_5N \longrightarrow HC_5NH^+ + CO$
contributing to its destruction $\sim$ 50% and 40% respectively.

It is clear that since both HC_3N and HC_5N are, at least in this particular source, tracer species (with abundances $\leq 10^{-9}$), a more complete network, possibly including cyanopolynes with a higher number of carbon than included here, is required, together with a proper treatment of the gas-grain chemistry which is needed to properly model the cold envelope. This shall be the scope of future work.

5.7 Discussion

5.7.1 General remarks on cyanopolyynes in different environments

In the Introduction, we mentioned that cyanopolyynes are almost ubiquitous in the ISM. Here we compare the cyanopolyynes abundance derived in this work with that found in various galactic and extragalactic environments, which possess different conditions (temperature, density, and history). Figure 5.8 graphically shows this comparison. From this figure, we note the following: (i) HC_3N is present everywhere in the ISM with relatively high abundances; (ii) the abundance in the cold envelope of IRAS16293 is the lowest in the plot, implying a high degree of freezing of oxygen and carbon, as indeed suggested by the chemical model analysis; (iii) HC_3N and HC_5N have relatively similar abundances in the IRAS16293 outer envelope, Cold Cloud, First Hydrostatic Core (FHSC) and Warm Carbon-Chain Chemistry (WCCC) sources, namely in the cold objects of the figure, implying that the derived ratio $HC_5N/HC_3N \sim 1$ in IRAS16293 cold envelope is not, after all, a peculiarity, but likely due to the cold temperature; (iv) DC_3N is only detected in cold objects except in the warm envelope of IRAS16293 and the Hot Cores, suggesting that, in those sources, it is linked to the mantle sublimation, in a way or another, as, again, found by our chemical modelling.

5.7.2 The present and past history of IRAS16293

Our analysis of the TIMASSS spectral survey reveals the presence of HC_3N, HC_5N and DC_3N in IRAS16293. HC_3N was previously detected by van Dishoeck et al. (1993) and its abundance has been analysed by Schöier et al. (2002) with a two step abundance model, where the jump was assumed to occur at 90 K. Schöier et al. (2002) found $HC_3N/H_2 \sim 10^{-9}$ in the inner warm part and $\leq\sim 10^{-10}$ in the outer envelope. Note that they could not derive a value for the outer envelope, nor estimate where the jump occurs, because they only detected 3 lines. Nonetheless, their estimates are in excellent agreement with our new estimates (Table 5.3).

A very important point is that we not only could estimate the cold envelope abundance, but we were also able to determine where the jump occurs, an essential information for the determination of the origin of HC_3N in IRAS16293. Our chemical modeling (§ 5.6) shows that, in the cold envelope, the HC_3N abundance is reproduced for low values of oxygen and carbon in the gas phase, implying that these species are heavily frozen onto the grain mantles. The O/C ratio is between 1.5 and 2, similar to the solar one, if the chemistry of the envelope is a fossil, namely built up during the

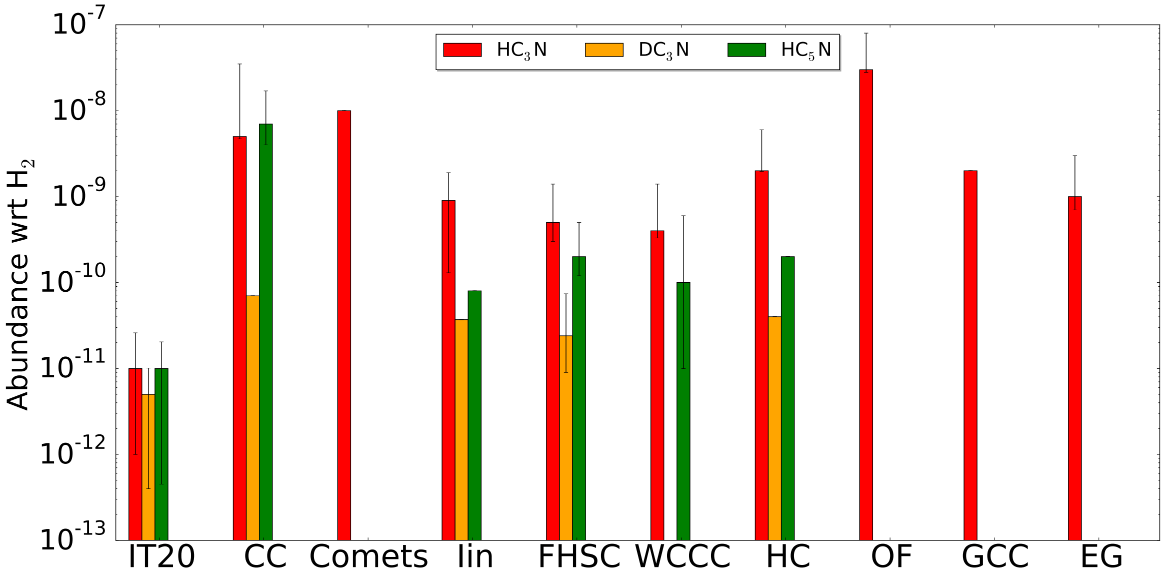

FIGURE 5.8: Abundances of cyanopolynes in different sources: IRAS16293 outer envelope (IT20) and inner region (Iin) (this work), cold clouds (CC) (Winstanley & Nejad 1996; Miettinen 2014), comet Hale-Bopp at 1 AU assuming $H_2O/H_2=5\times10^{-5}$ (Comets) (Bockelée-Morvan et al. 2000), first hydrostatic core sources (FHSC) (Cordiner et al. 2012), Warm Carbon-Chain Chemistry sources (WCCC) (Sakai et al. 2008; Jørgensen et al. 2004), massive hot cores (HC) (Schöier et al. 2002; Esplugues et al. 2013), outflow sources (OF) (Bachiller & Pérez Gutiérrez 1997; Schöier et al. 2002), Galactic Center clouds (GCC) (Marr et al. 1993; Aladro et al. 2011), and external galaxies (EG) (Aladro et al. 2011).

$\sim 10^7$ yr life of the parental molecular cloud. If, on the contrary, the chemistry was reset (for whatever reason) and evolved in a shorter time, e.g. in 10^5 yr, the O/C ratio that reproduces the observations could be as high as 3, but the oxygen and carbon have, anyway, remained mostly frozen onto the grain mantles. Probably the most important point to remark is that the HC_3N abundance is very low, a very tiny fraction of the CO abundance, the major reservoir of the carbon, so that little variations in the CO abundance result in large ones in the HC_3N abundance.

A second extremely interesting point is that the HC_3N abundance undergoes a jump of about one hundred when the dust temperature reaches 80 K. These two values provide us with very strong constraints on how the collapse of IRAS16293 occurred: it must have occurred so fast that the sublimation of C-bearing ices, such as CO and methane, has not yet produced HC_3N in enough large abundances to 'mask' the jump due to the volcano sublimation of the ices at 80 K Collings et al. (2004); Viti et al. (2004). An approximate value of this time is $\sim 10^3$ yr, based on our modeling. In other words, the HC_3N measured abundance jump temperature and abundance in the warm envelope both suggest that IRAS16293 is a very young object, not surprisingly, and that the envelope dust heating took no more than $\sim 10^3$ yr to occur.

A third result from the present study is the large measured abundance of HC_5N, for the first time detected in a Solar-type protostar. It is indeed only ten times lower than HC_3N in the inner warm region and similar to the HC_3N abundance in the outer cold envelope. When compared to other protostellar sources where HC_5N has been

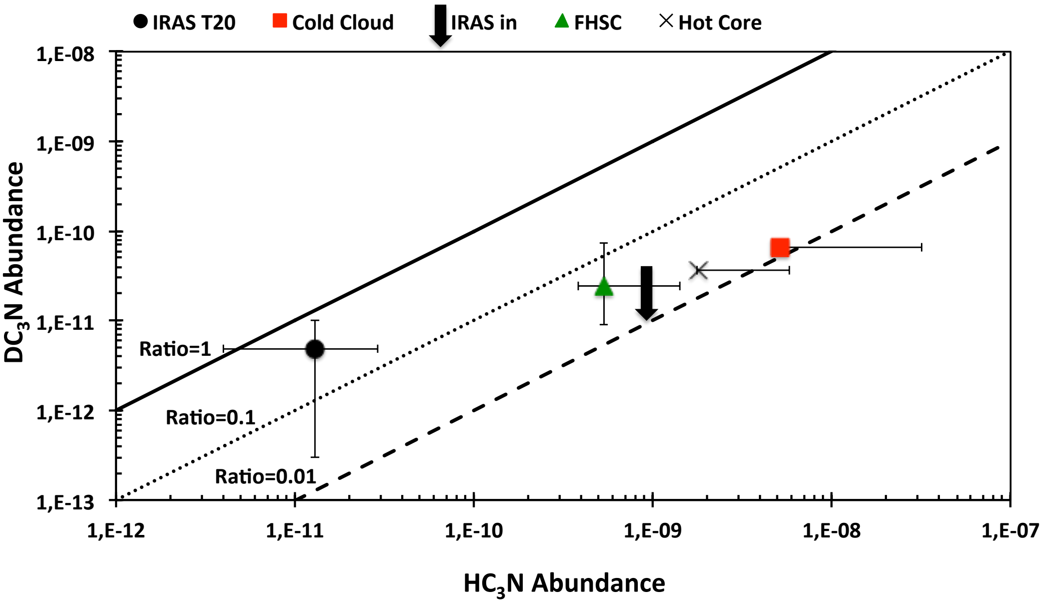

FIGURE 5.9: Abundance of DC_3N as a function of the abundance of HC_3N in different protostellar and cold sources. The symbols are the same that those in Figure 5.7.

detected, indeed, this ratio is not so anomalous. Figure 5.7 shows the two abundances in several protostellar sources and cold clouds. The two coldest sources have both an $HC_5N/HC_3N \sim 1$, while in the other sources this ratio is ~ 0.1. However, our chemical model fails to reproduce such a high abundance of HC_5N, despite including part of the most updated chemical network, recently revised by Loison et al. (2014). Evidently, we are missing key reactions that form this species.

5.7.3 The HC_3N deuteration

Finally, we detected, for the first time, the DC_3N in a Solar-type protostar. The deuteration of HC_3N is about 50% in the outer cold envelope and less than 5% in the warm part. This also provides us with important clues on the present and past history of IRAS16293. First, the high deuteration in the cold envelope tells us that this is, indeed, a present day product, namely it is caused by a cold and CO depleted gas, in agreement with previous observations and theoretical predictions (e.g. Ceccarelli et al. (2014a)).

The very low deuteration in the warm part is, on the contrary, more intriguing. Indeed, it cannot be the result of an initial high deuteration which has been diminished by gas phase reactions, because, as we have argued above, HC_3N is the result of the volcano sublimation which occurred because of a quick, $\leq 10^3$yr, heating of the dust. So it must be a fossil from the dust before the warming phase. Probably, this is one of the few very clear cases of fossil deuteration where there are no doubts that it is pristine (another one, to our knowledge, is the one of HDCO in the protostellar molecular shock L1157-B1; Fontani et al. (2014)). The deuteration in IRAS16293 is, in general, very high, with, for example, a doubly deuterated ratio of formaldehyde of $\sim 30\%$ (Ceccarelli et al. 1998a) and a triply deuterated ratio of methanol of a few percent (Parise et al. 2004). While at present we still do not have a clear measure of the formaldehyde deuteration in the warmer and colder envelope separately (e.g. Ceccarelli et al. (2001)), methanol should be entirely concentrated in the warm region. However, recently, deuterated formamide (NH_2CDO and NHDCHO) has been reported in IRAS16293, measured from ALMA observations, which clearly show that formamide line emission is associated with the warm hot corino (Coutens et al. 2016). They measured a deuteration ratio of a few percent, actually similar to that found in HC_3N in the present work. So clearly the molecular deuteration is a complex phenomenon even within the same source.

If our reasoning above is correct, namely the present day gaseous HC_3N is the sublimation product of previously frozen HC_3N, then its relatively small deuteration tells us that this species is an "early" chemical product, namely it was formed in a time when the gas temperature was not too low and, mostly importantly, the CO was not depleted yet (see e.g. Ceccarelli et al. (2014a)). This is in perfect agreement, indeed, with the models of HC_3N formation, which show that HC_3N is *abundantly* formed *before* the full trapping of carbon into CO (e.g. Loison et al. (2014)). Therefore, the low DC_3N/HC_3N in the warm part is well explained by the picture that abundant HC_3N has been formed during the tenuous molecular cloud phase and then frozen onto the ice mantles when the condensation that gave birth to IRAS16293 increased in density while decreased in temperature. Then, we predict that the deuteration of HC_3N in the hot corino regions could be a good probe of the timescale of the collapse too. Of course, detailed modeling will be necessary to quantify this prediction.

Meanwhile, the collection of previous measures of DC_3N/HC_3N, shown in Figure 5.9, provides support to our thesis. With the exception of the cold envelope of IRAS16293, all other sources where DC_3N has been observed, possess a HC_3N deuteration of a few percent, in agreement with the hypothesis that HC_3N is an early chemical product.

5.8 Conclusions

We detect several lines from cyanoacetylene (HC_3N) and cyanodiacetylene (HC_5N), and provide an upper limit to the abundance of cyanotriacetylene (HC_7N) and other undetected cyanopolyynes. Also, we report the first detection of deuterated cyanoacetylene, DC_3N, in a Solar-type protostar. On the contrary, we did not detect any ^{13}C cyanopolyyne isotopologue. We found that the HC_3N abundance is roughly constant($\sim 1.3 \times 10^{-11}$) in the outer cold envelope of IRAS16293-2422 and it increases, as a step-function, by about a factor 100 in the inner region where the dust temperature exceeds 80 K. The HC_5N has an abundance similar to HC_3N in the outer envelope and about a factor of ten lower in the inner region.

A comparison with a chemical model provides constraints on the oxygen and carbon gaseous abundance in the outer envelope and, most importantly, on the age of the source. The HC_3N abundance derived in the inner region and where the jump occurs also provide strong constraints on the time taken for the dust to warm up to 80 K, which has to be less than $\sim 10^3 - 10^4$ yr.

Finally, the cyanoacetylene deuteration is about 50% in the outer envelope and $\sim$ 5% in the warm inner region. The relatively low deuteration in the warm region suggests that we are seeing an almost 'untouched' fossil of the HC_3N, abundantly formed in the tenuous phase of the pre-collapse and then frozen into the grain mantles at a later phase.

TABLE 5.1: Parameters of the detected cyanopolyynes lines.

Transition	Frequency[c] [MHz]	E_{up} [K]	V_{LSR} [km/s]	FWHM [km/s]	Int. [K.km/s]	beam ['']
HC_3N						
9-8[a]	81881.4	19.6	3.9(0.6)	2.2(0.6)	2.5(0.4)	29.5
10-9[a]	90979.0	24.0	3.9(0.5)	2.1(0.5)	2.3(0.4)	26.5
11-10[a]	100076.3	28.8	3.9(0.4)	2.2(0.4)	2.2(0.3)	24.1
12-11[b]	109173.6	34.1	3.9(0.4)	2.3(0.4)	0.9(0.1)	22.1
15-14	136464.4	52.4	3.9(0.3)	2.9(0.3)	2.1(0.3)	17.7
16-15	145560.9	59.4	3.6(0.2)	2.8(0.3)	1.7(0.3)	16.6
17-16	154657.2	66.8	3.9(0.2)	3.1(0.3)	1.6(0.2)	15.6
18-17	163753.3	74.7	3.9(0.2)	3.5(0.3)	2.1(0.3)	14.7
19-18	172849.3	82.9	3.8(0.2)	4.4(0.2)	2.1(0.3)	14.0
22-21	200135.3	110.5	3.2(0.5)	6.1(0.7)	1.6(0.2)	12.1
23-22	209230.2	120.5	3.4(0.5)	6.5(0.6)	2.1(0.3)	11.5
24-23	218324.7	131.0	3.4(0.5)	6.1(0.5)	2.2(0.3)	11.1
25-24	227418.9	141.9	3.4(0.4)	6.3(0.5)	2.3(0.3)	10.6
26-25	236512.7	153.2	3.4(0.4)	6.2(0.5)	2.3(0.3)	10.2
27-26[b]	245606.3	165.0	2.7(0.5)	6.1(0.7)	0.8(0.1)	9.8
28-27[b]	254699.5	177.2	3.4(0.4)	7.0(0.4)	1.5(0.2)	9.5
29-28[b]	263792.3	189.9	2.5(0.3)	7.8(0.5)	4.7(0.7)	9.1
30-29	272884.7	203.0	3.4(0.6)	6.6(1.0)	1.4(0.2)	8.8
HC_5N[c]						
31-30	82539.0	63.4	3.7(0.7)	1.7(0.7)	0.08(0.01)	29.2
32-31	85201.3	67.5	3.9(0.6)	2.6(0.7)	0.07(0.01)	28.3
33-32	87863.6	71.7	4.0(0.6)	2.0(0.6)	0.06(0.01)	27.5
34-33	90525.9	76.0	3.9(0.6)	1.8(0.6)	0.06(0.01)	26.7
35-34	93188.1	80.5	3.9(0.5)	2.7(0.5)	0.06(0.01)	25.9
36-35[b]	95850.3	85.1	4.5(0.6)	1.4(0.7)	0.04(0.01)	25.2
37-36	98512.5	89.8	3.8(0.6)	2.7(1.2)	0.06(0.01)	24.5
38-37	101174.7	94.7	4.6(0.5)	1.8(0.6)	0.05(0.01)	23.9
39-38	103836.8	99.6	4.3(0.5)	1.9(0.5)	0.03(0.01)	23.2
DC_3N						
10-9	84429.8	22.3	3.9(0.6)	2.1(0.6)	0.17(0.06)	28.6
11-10	92872.4	26.7	4.4(0.5)	2.1(0.7)	0.14(0.05)	26.0
12-11	101314.8	31.6	4.3(0.4)	2.6(0.5)	0.15(0.05)	23.8
13-12	109757.1	36.9	4.1(0.4)	2.7(0.5)	0.26(0.10)	22.1
16-15[d]	135083.1	55.1	2.1(0.3)	1.7(0.4)	0.13(0.05)	17.7
17-16	143524.8	62.0	4.3(0.2)	3.8(0.4)	0.27(0.10)	16.6

The first three columns report the transition, frequency and upper energy level (E_{up}). The next three columns report the result of the gaussian fitting: V_{LSR} velocity, full width at half maximum (FWHM) and velocity-integrated line intensity (Int.). The last column reports the telescope beam at the frequency of the line.

[a]: Discarded line because likely contaminated by the molecular cloud (see text, §5.5.2).

[b]: Discarded line because it does not satisfy criteria 3 to 5 of §5.4.2.

[c] The HC_3N and DC_3N line frequencies are the same in the CDMS and JPL database. On the contrary, the JPL HC_5N line frequencies are systematically overestimated with respect to those of CDMS, giving V_{LSR} shifted by $\sim$ 1 km/s with respect to the V_{LSR} derived for the HC_3N and DC_3N lines. Thus, we used the HC_5N line frequencies from the CDMS database.

[d] We consider the detection of this line to be tentative.

TABLE 5.2: Results of the HC_3N modeling. Values of the best fit using four different values of α.

Model No.	α	T_{jump} [K]	X_{in} [10^{-10}]	X_{out} [10^{-10}]	X_{T20} [10^{-10}]	X_{in}/X_{out}	X_{in}/X_{T20}	χ^2
Model 1	-1	80±5	6±1	$0.020^{+0.009}_{-0.001}$	$0.07^{+0.03}_{-0.01}$	300^{+70}_{-130}	90^{+30}_{-40}	1.2
Model 2	0	80±5	9±1	$0.13^{+0.03}_{-0.04}$	$0.13^{+0.03}_{-0.04}$	90^{+20}_{-40}	90^{+20}_{-40}	0.8
Model 3	1	80±5	9±1	$0.5^{+0.1}_{-0.2}$	0.2±0.1	18^{+15}_{-5}	45^{+55}_{-20}	0.7
Model 4	2	80±5	11±1	$1.0^{+0.1}_{-0.4}$	$0.10^{+0.01}_{-0.04}$	11^{+9}_{-2}	110^{+90}_{-20}	1.1

TABLE 5.3: Results of the analysis.

Species	Formula	X_{in} [10^{-10}]	X_{T20} [10^{-10}]	X/HC_3N [In]	[T20]	χ^2
Detected cyanopolyynes						
Cyanoacetylene	HC_3N	9±1	$0.13^{+0.03}_{-0.04}$	1	1	0.8
Cyanodiacetylene	HC_5N	≤0.8	0.110±0.005	≤0.1	$0.8^{+0.2}_{-0.4}$	1.1
Deuterated Cyanoacetylene	DC_3N	≤0.4	$0.049^{+0.002}_{-0.003}$	≤0.04	$0.4^{+0.1}_{-0.2}$	1.9
Undetected cyanopolyynes						
Ethynylisocyanide	HCCNC	≤ 7.5	≤ 0.10			
3-Imino-1,2-propa-dienylidene	HNCCC	≤ 1.2	≤ 0.01			
Cyanoacetylene, ^{13}C	HCCC-13-N	≤ 4.5	≤ 0.10			
Cyanoacetylene, ^{13}C	HCC-13-CN	≤ 4.5	≤ 0.09			
Cyanoacetylene, ^{13}C	HC-13-CCN	≤ 7.5	≤ 0.15			
Cyanoacetylene, ^{15}N	HCCCN-15	≤ 1.5	≤ 0.15			
	DNCCC	≤ 1.5	≤ 0.04			
Cyanodiacetylene, ^{13}C	HCCCCC-13-N	≤ 6.0	≤ 0.60			
Cyanodiacetylene, ^{13}C	HCCCC-13-CN	≤ 7.5	≤ 0.60			
Cyanodiacetylene, ^{13}C	HCCC-13-CCN	≤ 4.5	≤ 0.45			
Cyanodiacetylene, ^{13}C	HCC-13-CCCN	≤ 7.5	≤ 0.75			
Cyanodiacetylene, ^{13}C	HC-13-CCCCN	≤ 6.0	≤ 0.60			
Cyanodiacetylene, ^{15}N	HCCCCCN-15	≤ 7.5	≤ 0.75			
Cyanodiacetylene, D	DCCCCCN	≤ 7.5	≤ 0.75			
Cyanohexatriyne	HC_7N	≤ 15	≤ 15			

Note: The first two columns report the species name and formula. Third and fourth columns report the values of the inner abundance X_{in} and the abundances at T_{dust}=20 K X_{T20}. Columns 5 and 6 report the values of the abundance ratios DC_3N/HC_3N and HC_5N/HC_3N, in the inner region and where T_{dust}=20 K respectively. Last column reports the χ^2 for the best fit of HC_5N and DC_3N (note that in this last case the χ^2 is not reduced). The top half table lists the detected species, the bottom half table the upper limits to the abundance of undetected cyanopolyynes (see text, §5.5).

Chapter 6

Formamide in Low- and Intermediate-Mass Objects

This chapter was published in Monthly Notices of the Royal Astronomical Society journal with the title "Shedding light on the formation of the pre-biotic molecule formamide with ASAI": A. Lopez-Sepulcre, Ali A. Jaber, E. Mendoza, B. Lefloch, C. Ceccarelli, C. Vastel, R. Bachiller, J. Cernicharo, C. Codella, C. Kahane, M. Kama and M. Tafalla. 2015, MNRAS, 499, 2438.

6.1 Abstract

Formamide (NH_2CHO) has been proposed as a pre-biotic precursor with a key role in the emergence of life on Earth. While this molecule has been observed in space, most of its detections correspond to high-mass star-forming regions. Motivated by this lack of investigation in the low-mass regime, we searched for formamide, as well as isocyanic acid (HNCO), in 10 low- and intermediate-mass pre-stellar and protostellar objects. The present work is part of the IRAM Large Programme ASAI (Astrochemical Surveys At IRAM), which makes use of unbiased broadband spectral surveys at millimetre wavelengths. We detected HNCO in all the sources and NH_2CHO in five of them. We derived their abundances and analysed them together with those reported in the literature for high-mass sources. For those sources with formamide detection, we found a tight and almost linear correlation between HNCO and NH_2CHO abundances, with their ratio being roughly constant –between 3 and 10– across 6 orders of magnitude in luminosity. This suggests the two species are chemically related. The sources without formamide detection, which are also the coldest and devoid of hot corinos, fall well off the correlation, displaying a much larger amount of HNCO relative to NH_2CHO. Our results suggest that, while HNCO can be formed in the gas phase during the cold stages of star formation, NH_2CHO forms most efficiently on the mantles of dust grains at these temperatures, where it remains frozen until the temperature rises enough to sublimate the icy grain mantles. We propose hydrogenation of HNCO as a likely formation route leading to NH_2CHO.

6.2 Introduction

One of the major questions regarding the origin of life on Earth is whether the original chemical mechanism that led from simple molecules to life was connected to metabolism or to genetics, both intimately linked in living beings. Formamide (NH_2CHO) contains the four most important elements for biological systems: C, H, O, and N, and it has recently been proposed as a pre-biotic precursor of both metabolic and genetic material, suggesting a common chemical origin for the two mechanisms (Saladino et al. 2012).

Formamide was detected for the first time in space by Rubin et al. (1971) towards Sgr B2 and later in Orion KL. However, dedicated studies of NH_2CHO in molecular clouds have started only very recently, as its potential as a key prebiotic molecule has become more evident. These studies present observations of formamide in a number of massive hot molecular cores (Bisschop et al. 2007, Adande et al. 2011), the low-mass protostellar object IRAS 16293–2422 (Kahane et al. 2013), and the outflow shock regions L1157-B1 and B2 (Yamaguchi et al. 2012; Mendoza et al. 2014). Its detection in comet Hale-Bopp has also been reported (Bockelée-Morvan et al. 2000). Formamide is therefore present in a variety of star-forming environments, as well as on a comet of the Solar System. Whether this implies an exogenous delivery onto a young Earth in the past is a suggestive possibility that needs more evidence to be claimed.

Establishing the formation route(s) of formamide in space remains a challenge. Different chemical pathways have been proposed, both in the gas-phase (e.g. Redondo et al. 2014) and on grain surfaces (e.g. Raunier et al. 2004, Jones et al. 2011). The present work represents an effort to try to understand the dominant mechanisms that lead to the formation of formamide in the interstellar medium. In particular, it seeks to investigate the possible chemical connection between NH_2CHO and HNCO, which was proposed by Mendoza et al. (2014). To this aim, we have performed a homogeneous search of NH_2CHO and HNCO in a representative sample of 10 star-forming regions (SFRs) of low- to intermediate-mass type, since most of the formamide detections so far reported concentrate on high-mass SFRs. This is the first systematic study conducted within the context of the IRAM Large Program ASAI (Astrochemical Surveys At IRAM; P.I.s: B. Lefloch, R. Bachiller), which is dedicated to millimetre astrochemical surveys of low-mass SFRs with the IRAM 30-m telescope.

The source sample and the observations are described in Sects. 6.3 and 6.4, respectively. Section 6.5 presents the spectra and describes the analysis carried out to obtain the abundances of NH_2CHO and HNCO. Sect. 6.6 compares the derived abundances with those found in the literature for other SFRs, and discusses the formation mechanisms that are favoured by our results. Our conclusions are summarised in Sect. 6.7.

TABLE 6.1: Source sample and their properties.

Source	R.A.(J2000)	Dec.(J2000)	$V_{\rm lsr}$ (km s^{-1})	d (pc)	M (M$_\odot$)	$L_{\rm bol}$ (L$_\odot$)	Type*	References
ASAI								
L1544	05:04:17.21	+25:10:42.8	+7.3	140	2.7	1.0	PSC	1,2,3
TMC1	04:41:41.90	+25:41:27.1	+6.0	140	21	—	PSC	1,4
B1	03:33:20.80	+31:07:34.0	+6.5	200	1.9	1.9	Class 0	5,6
L1527	04:39:53.89	+26:03:11.0	+5.9	140	0.9	1.9	Class 0, WCCC	1,7,8
L1157-mm	20:39:06.30	+68:02:15.8	+2.6	325	1.5	4.7	Class 0	7,8
IRAS 4A	03:29:10.42	+31:13:32.2	+7.2	235	5.6	9.1	Class 0, HC	7,8
SVS13A	03:29:03.73	+31:16:03.8	+6.0	235	0.34	21	Class 0/1	9,10
OMC-2 FIR 4	05:35:26.97	–05:09:54.5	+11.4	420	30	100	IM proto-cluster	11,12
Cep E	23:03:12.80	+61:42:26.0	–10.9	730	35	100	IM protostar	13
TIMASSS								
I16293	16:32:22.6	–24:28:33	+4.0	120	3	22	Class 0, HC	14,15

*PSC: pre-stellar core; HC: hot corino; WCCC: warm carbon-chain chemistry; IM: intermediate-mass.

References: [1]Elias (1978), [2]Evans et al. (2001), [3]Shirley et al. (2000), [4]Tóth et al. (2004), [5]Hirano et al. (1999), [6]Marcelino et al. (2005), [7]Kristensen et al. (2012), [8]Karska et al. (2013), [9]Hirota et al. (2008), [10]Chen et al. (2009), [11]Crimier et al. (2009), [12]Furlan et al. (2014), [13]Crimier et al. (2010a), [14]Loinard et al. (2008), [15]Correia et al. (2004).

6.3 Source sample

Our source sample consists of 10 well-known pre-stellar and protostellar objects representing different masses and evolutionary states, thus providing a complete view of the various types of objects encountered along the first phases of star formation. Their basic properties are listed in Table 6.1. All of them belong to the ASAI source sample except one: the Class 0 protobinary IRAS 16293–2422 (hereafter I16293), whose millimetre spectral survey, TIMASSS (The IRAS16293-2422 Millimeter And Submillimeter Spectral Survey), was published by Caux et al. (2011). A dedicated study of Complex Organic Molecules (COMs) in this source, including NH_2CHO, was recently carried out by Jaber et al. (2014).

6.4 Observations and data reduction

The data presented in this work were acquired with the IRAM 30-m telescope near Pico Veleta (Spain) and consist of unbiased spectral surveys at millimetre wavelengths. These are part of the Large Programme ASAI, whose observations and data reduction procedures will be presented in detail in an article by Lefloch & Bachiller (2015). Briefly, we gathered the spectral data in several observing runs between 2011 and 2014 using the EMIR receivers at 3 mm (80–116 GHz), 2 mm (129–173 GHz), and 1.3 mm (200–276 GHz). The main beam sizes for each molecular line analysed are listed in Tables C.1 and C.2. The three bands were covered for most of the sources. For Cep E, additional observations were carried out at 0.9-mm (E330 receiver), while just a few frequencies were covered at 2 mm. The Fourier Transform Spectrometer (FTS) units were connected to the receivers, providing a spectral resolution of 195 kHz, except in the case of L1544, for which we used the FTS50 spectrometer, with a resolution of 50 kHz, to resolve the narrow lines ($\Delta V \sim 0.5$ km s^{-1}) that characterise this region. The observations were performed in wobbler switching mode with a throw of 180″.

The data were reduced with the package CLASS90 of the GILDAS software collection.[1] Through comparison of line intensities among different scans and between horizontal and vertical polarisations, the calibration uncertainties are estimated to be lower than 10 % at 3 mm and 20% in the higher frequency bands. After subtraction of the continuum emission via first-order polynomial fitting, a final spectrum was obtained for each source and frequency band after stitching the spectra from each scan and frequency setting. The intensity was converted from antenna temperature ($T^*_{\rm ant}$) to main beam temperature ($T_{\rm mb}$) using the beam efficiencies provided at the IRAM web site[2]. In order to improve the signal-to-noise (S/N) ratio, the 2- and 1-mm ASAI data were smoothed to 0.5 km s^{-1}, except in the case of L1544, for which we kept the original spectral resolution.

For I16293, we used the TIMASSS spectral data obtained with the IRAM 30-m telescope at 1, 2, and 3 mm. A detailed description of the observations and an overview of the dataset are reported in Caux et al. (2011).

---

[1] http://www.iram.fr/IRAMFR/GILDAS/

[2] http://www.iram.es/IRAMES/mainWiki/Iram30mEfficiencies

TABLE 6.2: Number of NH_2CHO and HNCO detected lines

	NH_2CHO		HNCO	
Source	#	E_u (K)	#	E_u (K)
L1544[a]	0	—	2	10–16
TMC1	0	—	3	10–16
B1	0	—	4	10–30
L1527	0	—	4	10–30
L1157-mm	0	—	4	10–30
IRAS 4A	7	15–70	10	10–130
SVS13A	13	15–130	19	10–130
OMC-2 FIR 4	21	10–130	9	10–100
Cep E	5	10–22	5	10–85
I16293	12	10–160	16	10–95

[a] Only 3-mm data available.

6.5 Results

6.5.1 Line spectra

We searched for formamide (NH_2CHO) and isocyanic acid (HNCO) in our dataset using the CASSIS software[3] and the Cologne Database for Molecular Spectroscopy (CDMS[4]; Müller et al. 2005) to identify the lines. For NH_2CHO, we detected transitions with upper level energies, $E_{\rm up}$, below 150 K, and spontaneous emission coefficients, A_{ij}, above 10^{-5} s^{-1} and 5×10^{-5} s^{-1}, respectively for the 2/3-mm and the 1-mm data. For HNCO, we detected transitions with $E_{\rm u} < 150$ K and $A_{ij} > 10^{-5}$ s^{-1}. Tables C.1 and C.2 list all the NH_2CHO and HNCO transitions fulfilling these criteria in the observed millimetre bands, as well as the 3σ detections for each source. The sources where no NH_2CHO lines were detected (see below) are not included in Table C.1. For some sources with not many clear formamide detections (e.g. IRAS4A, Cep E), we included a few additional lines with peak intensities between 2σ to 3σ, as indicated in the tables. We then fitted the lines with a Gaussian function, and excluded from further analysis those falling well below or above the systemic velocity, and/or displaying too narrow or too broad line widths with respect to the typical values encountered for each source.

Table 6.2 lists, for each source, the number of NH_2CHO and HNCO lines detected and used in our analysis (Sect 6.5.2). While HNCO is easily detected in all the sources, NH_2CHO remains undetected in five objects: L1544, TMC-1, B1, L1527, and L1157mm. Moreover, in those sources where it is detected, the lines are typically weak (S/N$\sim 3-5$). OMC-2 FIR 4 has the highest number of detected formamide lines, which are also the most intense. The results from the Gaussian fitting to the detected lines are presented in Tables C.3 – C.12. A sample of lines for all the ASAI sources are shown in Figures D.1 – D.3.

---

[3] CASSIS has been developed by IRAP-UPS/CNRS (http://cassis.irap.omp.eu)

[4] http://www.astro.uni-koeln.de/cdms/

6.5.2 Derivation of physical properties

Rotational diagram analysis

In order to determine the excitation conditions –i.e. excitation temperature, column density and, eventually, abundance with respect to H_2– of NH_2CHO and HNCO for each source in a uniform way, we employed the CASSIS software to build rotational diagrams. This approach assumes (i) that the lines are optically thin, and (ii) Local Thermodynamic Equilibrium (LTE), meaning that a single Boltzmann temperature, known as *rotational temperature*, describes the relative distribution of the population of all the energy levels for a given molecule. Under these assumptions, the upper-level column density

$$N_u = \frac{8\pi k\nu^2}{hc^3 A_{ul}} \frac{1}{\eta_{\rm bf}} \int T_{\rm mb} dV \tag{6.1}$$

and the rotational temperature, $T_{\rm rot}$, are related as follows:

$$\ln \frac{N_u}{g_u} = lnN_{\rm tot} - lnQ(T_{\rm rot}) - \frac{E_u}{kT_{\rm rot}} \tag{6.2}$$

where k, ν, h, and c are, respectively, Boltzmann's constant, the frequency of the transition, Planck's constant, and the speed of light; $g_{\rm u}$ is the degeneracy of the upper level, and $N_{\rm tot}$ is the total column density of the molecule. The second fraction in Eq. 6.1 is the inverse of the beam-filling factor. We estimated it assuming sources with a gaussian intensity distribution:

$$\eta_{\rm bf} = \frac{\theta_{\rm s}^2}{\theta_{\rm s}^2 + \theta_{\rm b}^2} \tag{6.3}$$

with $\theta_{\rm s}$ and $\theta_{\rm b}$ being, respectively, the source and telescope beam sizes. We adopted the source sizes indicated in Table 6.3. In those sources where a hot ($T > 100$ K) inner region is believed to exist, we considered two possible solutions: (i) the emission originates from a compact size representing this inner region or *hot corino*, which typically shows enhanced abundances of Complex Organic Molecules (COMs); and (ii) the emission homogeneously arises from the entire extended molecular envelope of the protostar. We determined the sizes of the compact hot corino regions either from published interferometric maps (SVS13A) or from the gas density structure, $n(r)$, reported in the literature (I16293, IRAS 4A, OMC-2, Cep E), as indicated in Table 6.3. In the latter case, we assumed a size equal to the diameter within which the dust temperature is above 100 K.

Some sources, such as IRAS 4A, OMC-2, and Cep E, show extended velocity wings in a few of their lines. In order to separate their contribution to the line emission, we determined their line flux, $\int T_{\rm mb} dV$, by fitting a Gaussian function to the affected lines after masking their high-velocity wings. In sources with two to four well-aligned data points in the rotational diagrams, we took into account the relatively large error bars by fitting two additional "extreme" lines passing through the tips of the error bars of the lowest and largest energy points. An example is shown for B1 in Figure 6.1, where the two extreme solutions are depicted in blue, while the best solution is marked in red. The remaining rotational diagrams and the best fit to their data points using Eq. 6.2 are shown in Figures D.4 and D.5, where the error bars take into account calibration errors as well as the rms value around each line.

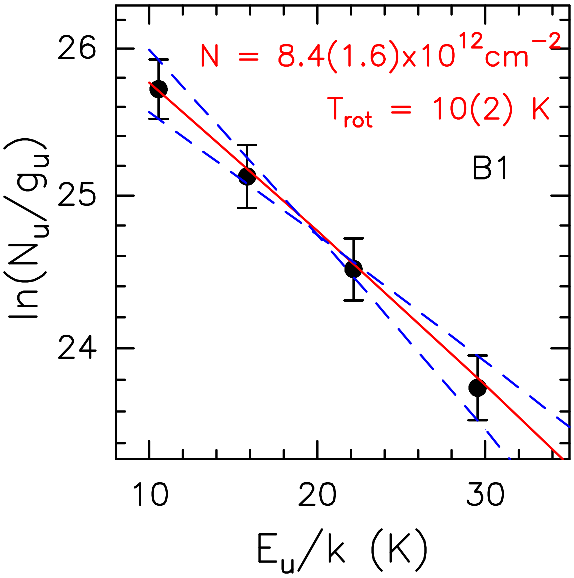

FIGURE 6.1: HNCO rotational diagram of B1. Data points are depicted in black. The red lines correspond to the best fit to the data points. The extreme solutions taking into account the error bars are displayed in dashed blue.

We compared our rotational diagram results with those reported in Marcelino et al. (2009) for the four sources common to both studies: L1544, TMC-1, B1, and L1527. The column densities of HNCO are in perfect agreement within the uncertainties, while the rotational temperatures agree within 1 K.

For homogeneity with the methodology used for NH_2CHO, we estimated the properties of HNCO in the LTE approximation. In addition, by adopting the same source sizes for HNCO and NH_2CHO, we assumed that the emission from both molecules originates in the same region(s). The similar average line widths between the two species suggest this is a reasonable assumption. Table 6.3 and Figures D.4 and D.5 present the results of the rotational diagram analysis. For most of the sources, a single component fits well both the NH_2CHO and HNCO points and therefore LTE seems to reproduce well the observations. This can also be seen in Figures D.1 to D.3, where the observed spectra (in black) and the best fit models (in red) match fairly well. However, for SVS13A, Cep E, and OMC-2, the compact solutions correspond to HNCO lines that are moderately optically thick ($\tau \sim 1 - 10$). The most extreme case is Cep E, for which also the NH_2CHO lines are optically thick. This is in contradiction with the underlying assumption of optically thin lines in the rotational diagram method. We find, however, that this caveat can be easily overcome by adopting a slightly larger source size, of 3″, 2″, and 2″, respectively for SVS13A, Cep E, and OMC-2. Doing this, the resulting column densities are reduced by a factor 2 (OMC-2) to 15 (Cep E), τ becomes much smaller than 1, and the lines can be well fitted by the solutions. Consequently, the uncertainties in the compact-solution column densities in these three sources are larger than reported in Table 6.3, but they are taken into account in the discussion (Sect. 6.6: see Figures 6.2 and 6.3).

There are two objects where a single component does not appear to explain the emission of all the lines: IRAS 4A and I16293, two well-known hot corino sources. Indeed, their rotational diagrams suggest either the contribution of two components, or non-LTE effects, coming into play. Considering the former, Table 6.3 presents the results of a two-component solution to the rotational diagrams of these two objects, where C1 is assumed to represent the cold extended envelope of the protostar, and C2 the small inner hot corino. While this 2-component solution reproduces well the observations, non-LTE effects cannot be ruled out.

TABLE 6.3: Results from the rotational diagram analysis of NH_2CHO and HNCO: Adopted size and H_2 column densities ($N_{\rm H2}$), derived rotational temperatures, $T_{\rm rot}$, derived HNCO and HN_2CHO column densities ($N_{\rm HNCO}$, $N_{\rm NH2CHO}$), resulting abundances with respect to H_2 ($X_{\rm HNCO}$, $X_{\rm NH2CHO}$), and ratio of HNCO to NH_2CHO column densities (R).

Source	Size[a] ($''$)	$N^{\rm b}_{\rm H2}$ (10^{22}cm^{-2})	$T_{\rm rot(HNCO)}$ (K)	$N_{\rm HNCO}$ (10^{12}cm^{-2})	$X_{\rm HNCO}$ (10^{-11})	$T^{\rm c}_{\rm rot(NH2CHO)}$ (K)	$N^{\rm c}_{\rm NH2CHO}$ (10^{12}cm^{-2})	$X_{\rm NH2CHO}$ (10^{-11})	R
				1-component fit					
L1544	BF	9.4 ± 1.6[1]	7 ± 3	5 ± 3	5 ± 3	7	< 0.036	< 0.046	> 130
TMC1[d]	BF	1.0 ± 0.1[2]	4 ± 1	8 ± 5	80 ± 50	4	< 0.47	< 5.2	> 17
B1	BF	7.9 ± 0.3[3]	10 ± 2	8.4 ± 1.6	11 ± 2	10	< 0.087	< 0.11	> 97
L1527	BF	4.1[4]	7.5 ± 1.4	2.5 ± 1.5	6 ± 4	7.5	< 0.062	< 0.15	> 40
L1157-mm	30	120[5]	8 ± 1	4 ± 1	0.35 ± 0.03	8	< 1	< 0.008	> 40
SVS13A (ext)[e]	20	10[6]	58 ± 6	11 ± 2	11 ± 2	64 ± 6	3.0 ± 0.4	3.0 ± 0.4	4 ± 1
(com)[e]	1	1000[7]	36 ± 3	1500 ± 300	15 ± 3	40 ± 4	320 ± 60	3.2 ± 0.6	5 ± 1
OMC-2 (ext)	25	19[8]	25 ± 3	16 ± 3	1.9 ± 0.4	58 ± 4	3.1 ± 0.2	0.36 ± 0.02	5 ± 1
(com)	2	4.6[8]	19 ± 1	900 ± 100	910 ± 80	32 ± 2	110 ± 10	110 ± 10	8 ± 1
Cep E (ext)	40	4.8[9]	30 ± 5	6.2 ± 0.3	13 ± 1	9 ± 2	0.2 ± 0.1	0.4 ± 0.2	30 ± 13
(com)	0.5	230[9]	17 ± 1	6000 ± 1000	130 ± 15	6 ± 1	500 ± 300	11 ± 5	12 ± 6
				2-component fit					
IRAS 4A (C1)	30	2.9[10]	11 ± 3	10 ± 1	34 ± 2	19 ± 15	0.6 ± 0.5	1.9 ± 0.2	18 ± 2
IRAS 4A (C2)	0.5	250[10]	43 ± 8	2000 ± 1000	80 ± 40	30 ± 5	500 ± 100	20 ± 5	4 ± 2
I16293 (C1)	30	2.9[11]	14 ± 5	20 ± 2	69 ± 7	5 ± 1	1.7 ± 0.6	6 ± 2	12 ± 4
I16293 (C2)	1.2	53[11]	47 ± 4	4400 ± 700	830 ± 130	83 ± 33	590 ± 190	110 ± 40	8 ± 3

[a] BF: beam-filling assumed. For the other sources, the size has been adopted as follows: L1157mm and IRAS 4A (extended) from Jørgensen et al. (2002); SVS13A (extended) from Lefloch et al. (1998); SVS13A (compact) from Looney et al. (2000); OMC-2 FIR 4 (extended) from Furlan et al. (2014); OMC-2 FIR 4 (compact) from Crimier et al. (2009); Cep E from Chini et al. (2001); IRAS 4A (compact) from Maret et al. (2002); IRAS 16293 from Jaber et al. (2014).

[b] References: [1]Crapsi et al. (2005), [2]Maezawa et al. (1999), [3]Daniel et al. (2013), [4]Parise et al. (2014), [5]Jørgensen et al. (2002) [6]Lefloch et al. (1998), [7]Looney et al. (2000), [8]Crimier et al. (2009), [9]Crimier et al. (2010a), [10]Maret et al. (2002), [11]Crimier et al. (2010b).

[c] For the non-detections of NH_2CHO, we have computed a 3σ upper limit to its column density adopting the same $T_{\rm rot}$ derived for HNCO (see text).

[d] Data for NH_2CHO upper limit derived from 3-mm data by N. Marcelino.

[e] N(HNCO) is probably a lower limit due to contamination from the OFF position.

As for the five objects where formamide was not detected, we determined a 3σ upper limit to its column density under the assumption of LTE and adopting the corresponding value of $T_{\rm rot}$ derived for HNCO. To this end, we used the spectral data around the NH_2CHO $4_{0,4} - 3_{0,3}$ transition at 84.542 GHz, expected to be the most intense at the cold temperatures implied by the HNCO results. The upper limits thus derived are shown in Table 6.3.

Once the column densities of HNCO and NH_2CHO were obtained, we derived their respective abundances with respect to molecular hydrogen (H_2) using the H_2 column densities, $N_{\rm H2}$, listed in Table 6.3, which correspond to the indicated source sizes. The uncertainty on $N_{\rm H2}$ is included for those sources where this was provided in the corresponding bibliographic reference. The resulting abundances span more than two orders of magnitude and are shown in Table 6.3, together with their ratio, $R = X({\rm HNCO})/X({\rm NH_2CHO})$.

Radiative transfer analysis taking into account the source structure

The source structures of I16293, IRAS 4A, and OMC-2, are reported in the literature (Maret et al. 2002, Crimier et al. 2010b). Therefore, for these objects, a more sophisticated radiative transfer analysis is possible that takes into account the temperature and gas density as a function of distance to the central protostar. Cep E also has a known structure (Crimier et al. 2010a), but having only 5 line detections, both in HNCO and NH_2CHO, we do not consider it here. We have analysed the I16293, IRAS 4A, and OMC-2 lines by means of the code GRAPES (GRenoble Analysis of Protostellar Envelope Spectra), whose details are described in Ceccarelli et al. (2003b) and Jaber et al. (2014).

Briefly, GRAPES computes the Spectral Line Energy Distribution (SLED) of a free-infalling spherical envelope with given gas and dust density and temperature profiles, and for a given mass of the central object. The dust to gas ratio is assumed to be the standard one, 0.01 in mass, and the grains have an average diameter of 0.1 μm. The species abundance is assumed to follow a step-function, with a jump at the dust temperature $T_{\rm jump}$, which simulates the thermal desorption of species from icy mantles (e.g. Ceccarelli et al. 2000a). The abundance $X_{\rm i}$ in the warm ($T \geq T_{\rm jump}$) envelope is constant. In the outer envelope, we assumed that the abundance follows a power law as a function of the radius, $X_{\rm o} r^a$, with an index equal to 0, –1 and –2, as in Jaber et al. (2014). $X_{\rm i}$ and $X_{\rm o}$ are considered parameters of the model. Since, to our knowledge, the binding energy of NH_2CHO is not available in the literature, we treat $T_{\rm jump}$ as a parameter too. However, if the molecules are trapped in water ice, the binding energy of H_2O will largely determine the dust temperature at which NH_2CHO is injected into the gas phase.

The radiative transfer is solved with the escape probability formalism and the escape probability is computed integrating each line opacity over the 4π solid angle. We ran models assuming LTE populations for formamide and, for comparison with Sect. 6.5.2, HNCO, and models taking into account non-LTE effects for HNCO. In the latter case, we used the collisional coefficients by Green (1986), retrieved from the LAMDA database (Schöier et al. 2005).

For each molecule and source, we ran a large grid of models varying the four parameters above: $X_{\rm i}$, $X_{\rm o}$, $T_{\rm jump}$, and a. In total, we ran about 20,000 models per source. The computed SLED of each model was then compared with the observed SLED to find the solution with the best fit. The results of this analysis are reported in Table 6.4, where we give the best fit values and the range of $X_{\rm i}$, $X_{\rm o}$, $T_{\rm jump}$ with $\chi^2 \leq 1$. We note

TABLE 6.4: Results of grapes analysis for NH_2CHO and HNCO considering the source structure of IRAS 4A, I16293 and OMC2*

	IRAS 4A	I16293	OMC-2
	HNCO LTE		
X_o (10^{-11})	3 ± 1	0.1 ± 0.1	5.5 ± 1.5
X_i (10^{-11})	20 ± 10	90 ± 10	< 170
T_{jump} (K)	100	40	80
T_{jump} range (K)	60 – 120	30 – 50	≥ 30
χ^2	1.2	2.0	1.0
	HNCO non-LTE		
X_o (10^{-11})	3 ± 1	0.5 ± 0.4	4 ± 1
X_i (10^{-11})	30 ± 20	600 ± 300	< 20
T_{jump} (K)	100	90	80
T_{jump} range (K)	≥ 50	≥ 60	≥ 30
χ^2	1.0	1.5	0.7
	NH_2CHO		
X_o (10^{-11})	2 ± 1	0.3 ± 0.2	0.3 ± 0.3
X_i (10^{-11})	50 ± 10	60 ± 20	200 ± 50
T_{jump} (K)	100	90	80
T_{jump} range (K)	≥ 100	≥ 50	60 – 100
χ^2	2.0	0.7	1.3
	$R = X(\mathrm{HNCO})/X(\mathrm{NH_2CHO})$		
R_o (LTE)	1.5 ± 0.9	< 1.7	18 ± 18
R_i (LTE)	0.4 ± 0.2	1.5 ± 0.5	< 0.85
R_o (non-LTE)	1.5 ± 0.9	1.7 ± 1.7	13 ± 13
R_i (non-LTE)	0.6 ± 0.4	10 ± 6	< 0.1

*Abundances with respect to H_2 are times 10^{-11}. X_o and X_i are the outer and inner abundances, respectively.

that the there is no appreciable difference in the best χ^2 when using a different value of a, so we took the simplest solution: $a = 0$. In this respect, the situation is similar to what Jaber et al. (2014) found in their study of IRAS16293.

A comparison between the results obtained for HNCO with the LTE and non-LTE level populations shows that the LTE approximation is quite good in the case of IRAS 4A and OMC-2, but not for I16293. The reason for that is probably a lower density envelope of I16293 compared to the other two sources. Therefore, the LTE results are likely reliable also for the formamide in IRAS 4A and OMC-2, while in I16293 these have to be taken with some more caution.

A second result of the GRAPES analysis is that both HNCO and formamide have a jump in their abundances at roughly the same dust temperature, 80–100 K. This is an important result reflecting the two molecules have similar behaviours with changes in temperature. It suggests they trace the same regions within the analysed protostars.

In order to evaluate whether the rotational diagram (hereafter RD) and GRAPES analyses are in agreement, we compare their respective abundance values, which roughly agree within an order of magnitude, in the Appendix A. We note here that, while the GRAPES analysis is likely more accurate, we are not able to apply it to the other sources of this study due to the lack of known source structure and/or lack of a sufficient amount of molecular lines. The absence of interferometric imaging of the HNCO and NH_2CHO emission also hinders the study of the inner structure of the protostellar emission. Therefore, we base the discussion below largely on the RD results, with a note of caution that those values may not strictly represent the physical properties of the sources.

6.6 Discussion

6.6.1 Formation routes of NH_2CHO

The formation mechanism(s) of interstellar formamide, as that of other COMs, is still far from being established. Several routes have been proposed so far which include both gas-phase and grain-surface processes. Concerning the former, Quan & Herbst (2007) suggested NH_2CHO forms via the radiative association reaction

$$\mathrm{NH_4^+ + H_2CO \rightarrow NH_4CH_2O^+ + h\nu} \tag{6.4}$$

followed by dissociative recombination. Halfen et al. (2011) proposed the following ion-molecule reaction and subsequent electron recombination:

$$\mathrm{NH_4^+ + H_2CO \rightarrow NH_3CHO^+ + H_2} \tag{6.5}$$

$$\mathrm{NH_3CHO^+ + e^- \rightarrow NH_2CHO + H} \tag{6.6}$$

These reactions all have unknown rates. Thus, further experimental work will be needed in order to evaluate their effectiveness in producing formamide.

Neutral neutral reactions have also been discussed as possible gas-phase routes leading to NH_2CHO. In particular, Garrod et al. (2008) proposed the radical-neutral reaction

$$\mathrm{H_2CO + NH_2 \rightarrow NH_2CHO + H} \tag{6.7}$$

However, as recently mentioned by Redondo et al. (2014), it presents a net activation barrier of > 1000 K that makes it inviable in interstellar conditions. Other neutral-neutral reactions evaluated by these authors also revealed to have large activation barriers, thus ruling them out as dominant or efficient mechanisms to produce NH_2CHO.

Formamide may also be formed on the icy mantles of dust grains. Jones et al. (2011) conducted some experimental work in which they irradiate a mixture of ammonia (NH_3) and carbon monoxide (CO) ices with high-energy (keV) electrons, resulting in NH_2CHO as one of the final products. The authors discuss several possible reactions and conclude that the most plausible route towards formamide begins with the cleavage of the nitrogen-hydrogen bond of ammonia, forming the NH_2 radical and atomic H. The latter, containing excess kinetic energy, can then add to CO, overcoming the entrance barrier, to produce the formyl radical (HCO). Finally, HCO can combine with NH_2 to yield NH_2CHO.

A different grain-mantle mechanism was proposed by Garrod et al. (2008), who considered hydrogenation (i.e. addition of H atoms) of OCN in their chemical models. However, this route resulted in an overabundance of NH_2CHO and an underabundance HNCO, since the latter was efficiently hydrogenated to yield formamide, the final product. Raunier et al. (2004) performed experimental Vacuum Ultra Violet (VUV) irradiation of solid HNCO at 10 K, which led to NH_2CHO among the final products.

They proposed that photodissociation of HNCO yields free H atoms that subsequently hydrogenate other HNCO molecules in the solid to finally give NH_2CHO. The limitation of this experiment is that it was carried out with pure solid HNCO. Jones et al. (2011) mentioned that, in the presence of NH_3, quite abundant in grain mantles, HNCO will preferentially react with it, resulting in $NH_4^+ + OCN^-$. Despite these caveats, hydrogenation of HNCO on grain mantles was recently found to be a most likely solution in the case of the outflow shock regions L1157-B1 and B2 (Mendoza et al. 2014). More experiments and calculations are needed in order to assess the efficiency of this formation route.

6.6.2 Correlation between HNCO and NH_2CHO

From the previous section, it is clear that, until more gas-phase and surface reaction rates involving the mentioned species are measured, it will be difficult to establish the exact synthesis mechanisms of formamide in space.

In this section, we assess, from an observational point of view, whether hydrogenation of HNCO leading to NH_2CHO on the icy mantles of dust grains could be a dominant formation route. To this aim, we plot in Figure 6.2, the NH_2CHO versus HNCO abundances of all our sources (Table 6.3), as well as the shock regions analysed by Mendoza et al. (2014), and the high-mass SFRs reported in Bisschop et al. (2007) and Nummelin et al. (2000), for comparison. The latter were obtained by the cited authors via the RD method assuming the emission comes from the inner hot core regions. Thus, for homogeneity, we split the plot into two panels, the upper one showing only the compact/inner solutions of the RD analysis, classified by masses. The best power law fit to these points is marked with a dashed line, and is given by the equation $X(\mathrm{NH_2CHO}) = 0.04X(\mathrm{HNCO})^{0.93}$, with a Pearson coefficient of 0.96, indicating a tight correlation. The fact that this correlation is almost linear and holds for more than three orders of magnitude in abundance suggests that HNCO and NH_2CHO are chemically related. This result confirms, on a more statistical basis, what was recently found by Mendoza et al. (2014).

However, this correlation does not hold for the objects without formamide detections, which are plotted in the lower panel of Figure 6.2 together with the extended envelope solutions of the RD analysis. Here, it is clearly seen that all the upper limits lie well below the best fit line, indicating a significantly larger amount of gas-phase HNCO relative to NH_2CHO in comparison to the other sources. These objects are the coldest in our sample, representing either pre-stellar cores or protostars with no detectable hot corino within them. The rotational temperatures inferred from the HNCO RD analysis are also among the lowest in our sample. In this same plot, the points representing formamide detections (extended envelope component) also show a tendency towards lower relative values of $X(\mathrm{NH_2CHO})$, although not as pronounced.

Thus, it appears that regions with colder temperatures are more deficient in NH_2CHO than protostars with hot inner regions, indicating that higher temperatures are needed for NH_2CHO to become relatively abundant in the gas phase. This might be explained by (i) NH_2CHO forming in the gas phase at temperatures above ~ 100 K, and/or (ii) NH_2CHO forming predominantly on the icy mantles of dust grains at low temperatures, and subsequently sublimating into the gas-phase when the temperature in the inner regions rises sufficiently. As for the former possibility, Mendoza et al. (2014) quantitatively argued that reaction 6.7 does not suffice to explain the amount of gas-phase formamide in the shock regions of L1157 protostellar outflow. In addition, the high activation barrier the reaction needs to overcome makes this an unviable route. Other

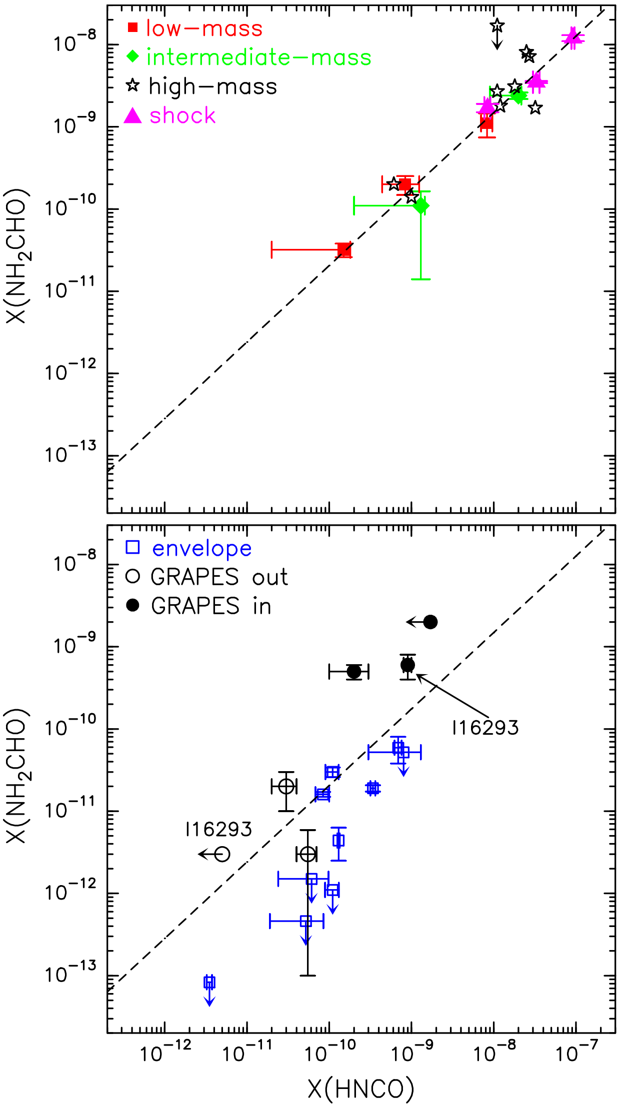

FIGURE 6.2: Plot of NH_2CHO versus HNCO abundances with respect to H_2. *Top*: Data points included in the power-law fit (dashed line; see text). Red squares and green diamonds denote the compact or inner RD solutions of low- and intermediate-mass sources in this study, respectively. Magenta triangles and black stars correspond, respectively, to outflow shock regions (from Mendoza et al. 2014) and high-mass sources (from Bisschop et al. 2007 and Nummelin et al. 2000). *Bottom*: Data points not included in the power-law fit (see text). Blue open squares represent the extended or outer RD solutions, while black open and filled circles denote the GRAPES LTE values for the outer and inner components, respectively.

purely gas-phase formation routes still need more investigation in terms of reaction rates and activation barriers, as discussed in Sect. 6.6.1. Mendoza et al. (2014) favoured a grain formation mechanism followed by mantle-grain evaporation/sputtering on the basis of the comparable abundance enhancements of HNCO, NH_2CHO, and CH_3OH in the gas-phase between the two protostellar shocks studied by the authors. Therefore, grain formation of NH_2CHO appears to be the most likely possibility.

On the other hand, while grain formation of HNCO is likely to occur in the cold phases of star formation (Hasegawa & Herbst 1993), gas-phase reactions leading to HNCO at such cold temperatures can also take place efficiently (see e.g. Marcelino et al. 2009 and references therein), overcoming strong depletion. This would explain its relatively high gas-phase abundance already in the very early –and cold– phases of star formation, and also the high values of HNCO to NH_2CHO abundance ratios we find in the coldest sources of our sample.

In Figure 6.3, we plot the HNCO abundance, the NH_2CHO abundance, and their ratio, R, as a function of bolometric luminosity for those sources with a reported luminosity estimate (see Table 6.1). For the objects in our study with formamide detection, we only plot the points corresponding to the inner or compact component (red circles), since these regions are expected to be the dominant contributors to the overall luminosity. The HNCO and NH_2CHO abundance panels both show the high-mass sources lying on top of the plot, while the points representing our sample sources are more scattered, with the coldest objects (in blue) showing the lowest abundances. This trend is much more pronounced in the case of NH_2CHO, for which hot corino regions (red points) display higher NH_2CHO abundances than the colder objects by more than an order of magnitude. More interesting is the plot of R, which illustrates how this quantity remains roughly constant along 6 orders of magnitude in luminosity for the NH_2CHO-emitting sources, with values ranging from 3 to 10 approximately. This reflects the almost-linearity of the correlation between the abundance of the two species. On the other hand, this value rises considerably for the lower luminosity sources, reenforcing our interpretation that formamide mostly forms on grains at cold temperatures, while HNCO may form both on grains and in the gas.

The strikingly tight and almost linear correlation between the abundance of the two molecules once NH_2CHO becomes detectable suggests one of the two following possibilities: (i) HNCO and NH_2CHO are both formed from the same parent species on dust grain mantles, or (ii) one forms from the other. Among the grain formation routes that have been proposed so far, hydrogenation of HNCO leading to NH_2CHO is the only mechanism that would explain our observational results. While this route is found to have some caveats (see Sect. 6.6.1), it is also true that more experimental work is needed to better assess its efficiency.

If the abundance of gaseous NH_2CHO truly depends on temperature, we should find a difference in R between the hot corino and the cold envelope regions of IRAS 4A and I16293. Looking at Table 6.3, this is indeed the case. As for OMC-2, Cep E, and SVS13A, only one component was necessary to describe their rotational temperatures and column densities. Therefore, we cannot compare the extended and compact values as in the case of a 2-component solution. We can nevertheless guess that, excluding the case of Cep E, for which only low-energy formamide lines were detected, the compact solution is likely the best, given the low values of R and the relatively high rotational temperatures derived. This would imply most of the emission arises in the inner hot corino regions. For Cep E, more molecular observations at higher frequencies are needed to confirm this.

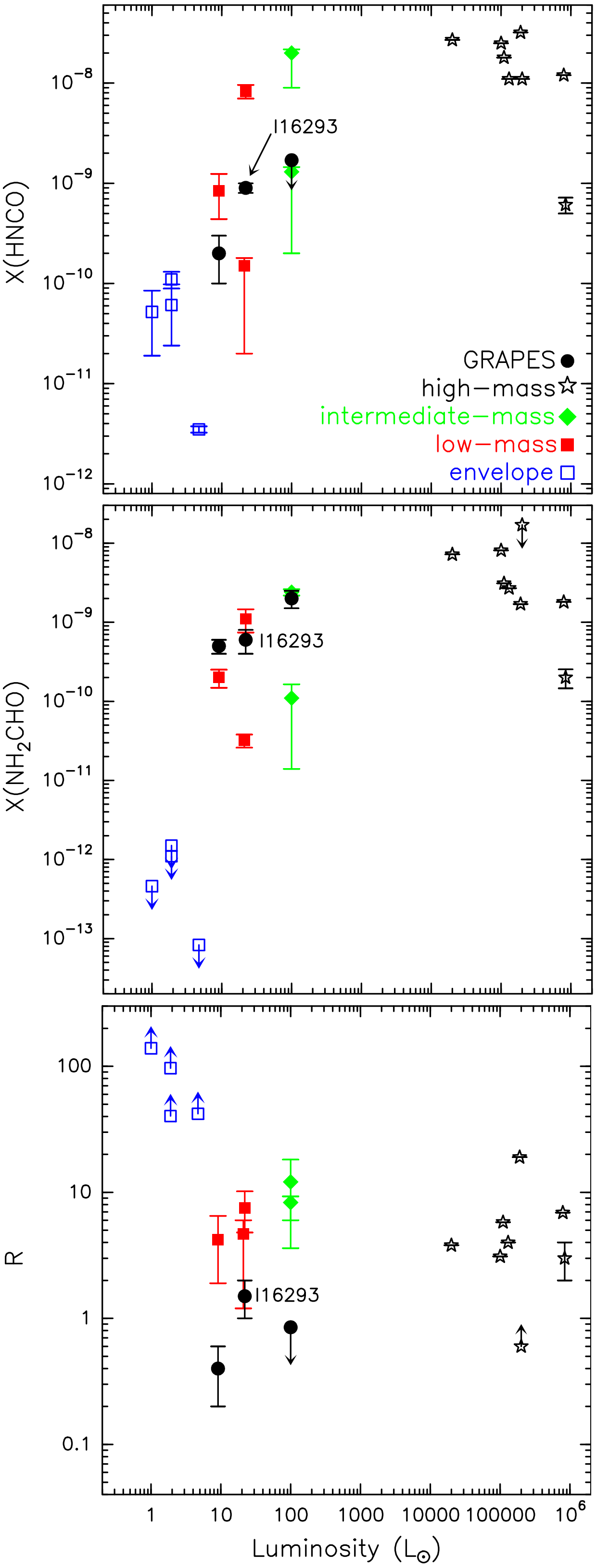

FIGURE 6.3: Abundance of HNCO (*top*), NH_2CHO (*middle*) and their ratio (*bottom*) against bolometric luminosity. Symbols are as in Figure 6.2.

Figures 6.2 and 6.3 also include the results from the LTE GRAPES analysis. I16293 (labelled in the plots) is included for completeness despite the fact that the GRAPES analysis suggests non-LTE effects should be taken into account for this object. While these points introduce more scatter in the plots, it can be clearly seen that the inner components of the sources analysed with GRAPES have a lower HNCO abundance relative to NH_2CHO, compared to what is found via the RD analysis. This yields lower R values, indicating a considerable amount of formamide with respect to HNCO in these regions and suggesting, as mentioned in Sect. B.1, that the 2-component approximation in the RD analysis is over simplistic: while we assumed that only the higher-energy formamide lines arose from the compact inner region, it is likely that a significant amount of emission from the low-energy lines also originates here and not exclusively in the outer envelope.

The trend showing higher R in the outer envelope than in the inner regions holds for both IRAS 4A and OMC-2, which further supports the fact that NH_2CHO requires higher temperatures than HNCO to be detectable in the gas phase. This kind of analysis, taking into account the source structure, is needed in a larger sample of objects in order to draw conclusions about both the chemistry and the validity of our RD analysis on a more statistical basis. Interferometric mapping would also greatly help disentangling source multiplicity and verifying whether the emission of HNCO and NH_2CHO trace the same regions, as has been assumed in this work.

6.7 Conclusions

As part of the IRAM Large programme ASAI, we searched for millimetre spectral lines from formamide (NH_2CHO), a presumably crucial precursor of pre-biotic material, and isocyanic acid (HNCO), in ten low- and intermediate-mass star forming regions with different properties. The dataset, obtained with the IRAM 30-m telescope, consists mainly of unbiased broadband spectral surveys at 1, 2, and 3-mm. Our aim was to investigate the chemical connection between these two molecular species and gain some observational insights into the formation mechanisms of formamide in interstellar conditions. The present work represents the first systematic study within ASAI and statistically completes the low-mass end of similar studies performed towards high-mass star-forming regions. Our main findings are summarised as follows.

1. The high sensitivity and large frequency range of the spectral surveys allowed us to evaluate the detectability of numerous NH_2CHO and HNCO transitions. We detect formamide in five out of the ten objects under study (IRAS 4A, IRAS 16293, SVS13A, Cep E, and OMC-2), and HNCO in all of them. Since formamide had already been detected in IRAS 16293 –also investigated here for completeness– this study raises the number of known low- and intermediate-mass formamide-emitting protostars to five, thus significantly improving the statistics.

2. We derived HNCO and NH_2CHO column densities via the rotational diagram method for all the sources. As a result, we found NH_2CHO abundances with respect to H_2 in the range 10^{-11} – 10^{-9}, and HNCO abundances between 10^{-12} and 10^{-8}. For those objects without formamide detection, we provided an upper limit to its column density and abundance.

3. For three targets (IRAS 4A, IRAS 16293, and OMC-2), the source density and temperature structures are known and published, and we were thus able to take them

into account through a more sophisticated analysis using the code GRAPES. This method fits an abundance profile that consists of a step function, with the separation between the two values roughly corresponding to the hot corino size. A comparison between the two radiative transfer analyses employed reveals overall agreement within an order of magnitude. The GRAPES analysis also indicates that one of the studied objects, IRAS 16293, requires a non-LTE radiative transfer analysis, which at the moment is not possible due to the lack of collisional coefficients for NH_2CHO. LTE appears to describe correctly the other two sources analysed with GRAPES, and is assumed to be a good approximation for all the other sources in our sample.

4. For the sources where formamide was detected, i.e. hot corino sources, we found an almost linear correlation between HNCO and NH_2CHO abundances that holds for several orders of magnitude. This suggests that the two molecules may be chemically associated. On the other hand, those sources with no formamide detection do not follow this correlation, but instead show much larger amounts of HNCO relative to NH_2CHO. These objects are the coldest in this study, and unlike the rest of our sample, they contain no known hot corinos.

5. Our findings and the NH_2CHO formation routes proposed so far in the literature suggest that, unlike HNCO, NH_2CHO does not form efficiently in the gas phase at cold temperatures and may be formed on the mantles of dust grains, where it remains frozen at cold temperatures. As soon as the temperature rises sufficiently to sublimate the icy grain mantles, formamide is incorporated into the gas and becomes detectable. The tight and almost linear correlation with HNCO suggests a possible formation route of NH_2CHO via hydrogenation of HNCO, although other possibilities should not be ruled out. In particular, two potentially viable gas-phase pathways leading to formamide involve formaldehyde (H_2CO). It is therefore worth exploring the connection between H_2CO and NH_2CHO, which will be the subject of a forthcoming paper.

6. In order to evaluate the validity of our conclusions, several aspects need to be explored more thoroughly. From an observational point of view, interferometric imaging is necessary to assess the relative spatial distribution of HNCO and NH_2CHO, and retrieve more accurate abundance ratios, in particular in the hot corino sources. In addition, more detailed and sophisticated radiative transfer analysis requires, on the one hand, knowledge of the source density and temperature profiles, and on the other hand, collisional coefficient calculations for NH_2CHO, currently unavailable. Finally, more chemical experiments are needed to estimate the efficiency of the hydrogenation processes leading from isocyanic acid to formamide on interstellar dust grains, as well as the viability of purely gas-phase reactions.

Chapter 7

Conclusions and Future Work

7.1 Conclusions

The work presented in this thesis mainly deals with a theoretical study of the chemical structure, specifically the corino and cold envelope around the low-mass protostar IRAS16293-2422, and of proto-cluster OMC-2 FIR 4.

Understanding the chemistry of these regions is essential in order to understand also their physical conditions. For this reason in **Chapter 1**, I explained briefly the story of low mass star formation and how the chemistry progresses through this evolution process. Then I summarized the census of detected molecules in several galactic objects, in addition to extragalactic sources to give a general idea about the chemistry in the interstellar medium. From this census I noted an interesting relation between these very different objects, which is the presence of a similar peak at molecular weight around 40 to 49 as shown in these graphs.

The thesis focuses on modelling a particular source and gives a general insight on the chemistry of such source. It has been shown that very likely all low-mass protostars have inner regions warm enough that the grain mantles evaporate. The regions enriched in complex organic molecules are known as "hot corinos" because their chemistry is as rich as that in "hot cores", around massive stars. Hot corinos are warm (100 K) and dense (10^8 cm^{-3}) cores surrounding low-mass star forming regions. The first hot corino was discovered towards IRAS 16293-2422, which has been the target source of my thesis. In **Chapter 2**, I described in some details the IRAS16293-2422 physical structure, outflow system and the chemical & deuteration structure. In addition, I carried out a study toward the proto-cluster OMC-2 FIR 4, and I reported a brief description of this source in the same Chapter. The summary of the COMs and deuterated species detected so far in IRAS16293-2422 shows that it is a very chemically rich source. OMC-2 FIR 4 is kinematically and chemically complex. It is indeed a protocluster where the near-infrared, mid-infrared and millimetre-wavelength emission peaks are all offset from one-another by $\sim 5''$. Interferometric continuum observations at 2 and 3.3 mm showed a clumpy substructure at the $5''$ scale, with the presence of at least three cores. I updated the list for all the detected molecules in this source so far. The origin of the chemical enrichment in this source is still under discussions.

In order to study the structure and the chemistry of these sources, several tools were used through out this thesis. In **Chapter 3**, I described in details these tools, starting from the observations: the IRAS16293 Millimeter And Submillimeter Spectral Survey (**TIMASSS**) and the large program (**ASAI**:**A**strochemical **S**urveys at **I**RAM). For line identification I used the CASSIS (**C**entre d'**A**nalyse **S**cientifique de **S**pectres **I**nstrumentaux et **S**ynthétiques) package. This software has also been used to do the Gaussian fits and to calculate the upper limits to the abundance of undetected molecules. In order to analyse molecular line data and derive the molecular abundances, we need a good physical model of the source, then compute the full LTE or/and non-LTE statistical equilibrium excitation of the molecule through this physical structure, calculate the emerging radiation from the source using nonlocal radiative transfer, convolve the simulated emission with the telescope beam, and then compare with observations. By following this strategy to analyze molecular lines, I used the radiative transfer modeling package GRAPES (**G**Renoble **A**nalysis of **P**rotostellar **E**nvelope **S**pectra), to model the Spectral Line Energy Distribution (SLED) of the detected COMs and to estimate the abundance of these detected molecules.

In **Chapter 4**, I made the first full census of detected COMs in IRAS16293-2422. COMs are considered crucial molecules, since they are connected with organic chemistry, at the basis of the terrestrial life. More pragmatically, they are molecules in principle difficult to synthetize in the harsh interstellar environment and, therefore, a crucial test for astrochemical models. The census of the oxygen and nitrogen bearing COMs was obtained from the millimeter-submillimeter unbiased spectral survey TIMASSS. Six COMs, out of the 29 searched for, were detected: methyl cyanide, ketene, acetaldehyde, formamide, dimethyl ether, and methyl formate. The multifrequency analysis of the last five COMs provides clear evidence that they are present in the cold (30 K) envelope of IRAS16293-2422, with abundances 0.03–2 $\times10^{-10}$. The data do not allow to support the hypothesis that the COMs abundance increases with increasing dust temperature in the cold envelope, as expected if COMs were predominately formed on the lukewarm grain surfaces as predicted by the present models. Finally, when considering also other ISM sources, we find a strong correlation, over five orders of magnitude, between the methyl formate and dimethyl ether, and between methyl formate and formamide abundances, which may point to a link between these two couples of species, in cold and warm gas.

In **Chapter 5**, we turned our attention to the cyanopolyynes in IRAS16293-2422. We presented an extensive study of the cyanopolyynes distribution in this source. The goals was: (i) to obtain the census of the cyanopolyynes present in this source, as well as of their isotopologues; (ii) to derive how their abundance varies across the protostar envelope; (iii) to obtain constraints on the history of IRAS16293-2422 by comparing the observations with the predictions of a chemical model. We did this by analysis the data from TIMASSS again. The derived SLED of each detected cyanopolyyne was compared with the predictions from the radiative transfer code GRAPES, to derive the cyanopolyynes abundances across the IRAS16293-2422 envelope. Finally, the derived abundances were compared with the predictions from the chemical model UCL_CHEM. We detected several lines from cyanoacetylene (HC_3N) and cyanodiacetylene (HC_5N), and report the first detection of deuterated cyanoacetylene, DC_3N, in a solar type protostar. We found that the HC_3N abundance is roughly constant ($\sim 1.3 \times 10^{-11}$) in the outer cold envelope of IRAS16293-2422 and it jumps by about a factor 100 in the inner region where the dust temperature exceeds 80K, namely when the "volcano" ice desorption is predicted to occur. The HC_5N has an abundance similar to HC_3N in the outer envelope and about a factor ten lower in the inner region. The comparison with the chemical model predictions provides constraints on the oxygen and carbon gaseous abundance in the outer envelope and, most important, on the age of the source. The HC_3N abundance derived in the inner region and where the jump occurs also provide strong constraints on the time taken for the dust to warm up to 80 K, which has to be less than $\sim 10^3 - 10^4$ yr. Finally, the cyanoacetylene deuteration is about 50% in the outer envelope and $\sim$ 5% in the warm inner region. The relatively high deuteration in the warm region suggests that there is an almost untouched fossile of the HC_3N abundantly formed in the tenuous phase of the pre-collapse and then frozen into the grain mantles at a later phase.

Formamide (NH_2CHO) has been proposed as a pre-biotic precursor with a key role in the emergence of life on Earth. While this molecule has been observed in space, most of its detections correspond to high-mass star-forming regions. The lack of investigation in the low-mass regime, however motivated me to participate in the work presented in **Chapter 6**. In this study we searched for formamide, as well as isocyanic acid (HNCO), in 10 low- and intermediate-mass pre-stellar and protostellar objects. For this, we used the IRAM Large Programme ASAI, which makes use of unbiased broadband spectral surveys at millimetre wavelengths. We detected HNCO in all the sources and NH_2CHO in five of them. We derived their abundances and analysed them together with those reported in the literature for high-mass sources. For those sources with formamide detection, we found a tight and almost linear correlation between HNCO and NH_2CHO abundances, with their ratio being roughly constant –between 3 and 10– across 6 orders of magnitude in luminosity. This suggests that the two species are chemically related. The sources without formamide detection, which are also the coldest and devoid of hot corinos, fall well off the correlation, displaying a much larger amount of HNCO relative to NH_2CHO.

In summary, from the census and abundances of COMs in IRAS16293-2422, I study the formation mechanism of some detected COMs in the cold envelope. I found a mother daughter relationship between some molecular species like DME and MF, and between HNCO and NH_2CHO. This latter molecular couple it is interesting because formamide is thought to be important for biomolecules formation. Furthermore, by studying cyanopolyynes abundances I could derive a better understanding of the formation history of IRAS16293-2422.

7.2 Future Work

1. In my thesis, I discovered and studied six COMs, out of the 29 searched for, in IRAS16293-2422. I would like to complete the analysis of the data from the TIMASSS survey in order to identify the nature and abundance of other complex molecules and obtain the chemical structure of this source. In additional to analysis data from other ASAI (Astrochemical Surveys At IRAM) sources.

2. More powerful telescopes are now becoming available (for example: NOEMA and ALMA) and the tools that I used and helped to develop during my thesis could allow to search for even more complex molecules of obvious biological interest such as glycine, the simplest amino acid. One can ask which region would be best suited for this search? From this thesis the first choice would be to start with the same object IRAS16293-2422, because it has been studied for several years, is known to posses a very rich chemistry and numerous data remain to be mined. Indeed a first small unbiased spectral survey towards IRAS16293-2422 has been just obtained with ALMA by Jørgensen et al. (2016).

3. So far COMs have been found in a limited number of environments. It will be important to study other sources for their presence, such as protoplanetary disks, because the inventory and spatial heterogeneity of complex molecules will help us to constrain the molecules that might be present as planets form.

To finish on a personal note, the primary objective of coming to France and pursue my studies is to bring what I have learned during my PhD years back to my country

Iraq and to continue participating with other colleagues in developing astronomy. At first glance this goal might seem absurd, given the current circumstances in Iraq, but we have an old saying: Life is narrower without the expanse of hope.

Appendix A

Figures on the HC_3N modeling for the Chapter 5

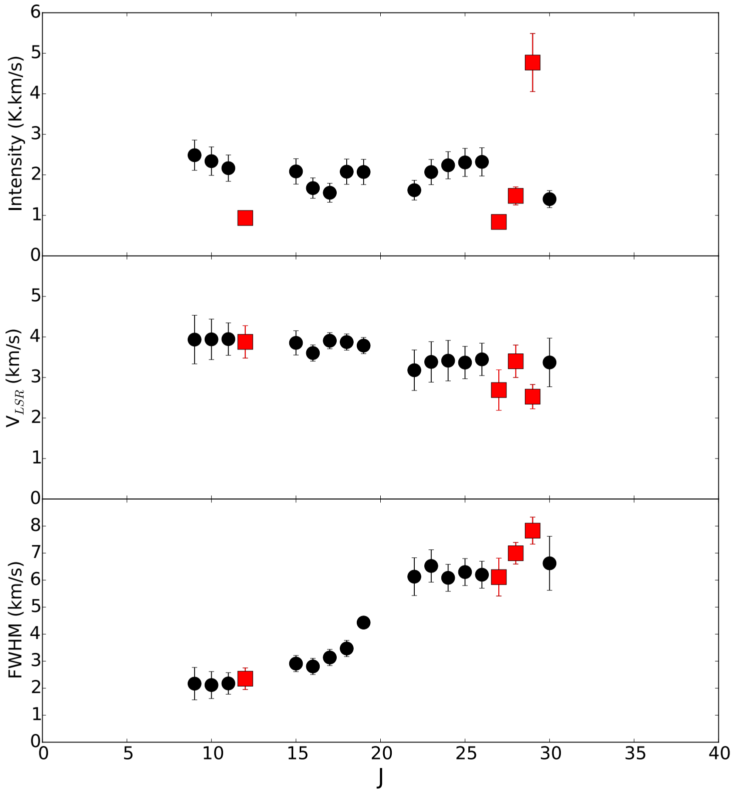

FIGURE A.1: HC$_3$N line intensity (upper panel), rest velocity V$_{LSR}$ (middle panel) and FWHM (bottom panel) as a function of the upper J of the transition. The red squares show the lines that have been discarded because they do not satisfy all criteria 3 to 5 of §5.4.2 (see text).

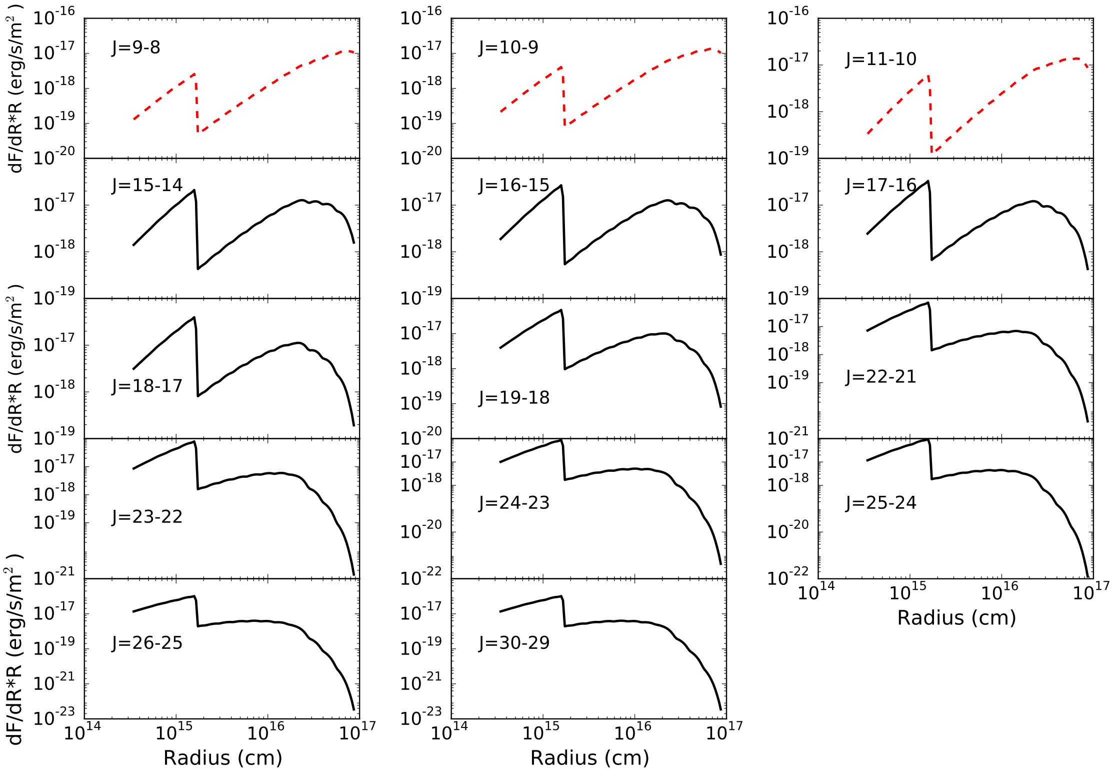

FIGURE A.2: Predicted contribution to the integrated line intensity ($dF/dr * r$) of a shell at a radius r for the HC$_3$N lines. This model corresponds to α=0, T$_{jump}$=80 K, $X_{in} = 3.6 \times 10^{-10}$, and $X_{out} = 6.0 \times 10^{-11}$. The 3 upper red dashed curves show an increasing emission towards the maximum radius and very likely contaminated by the molecular cloud (see 5.5.2).

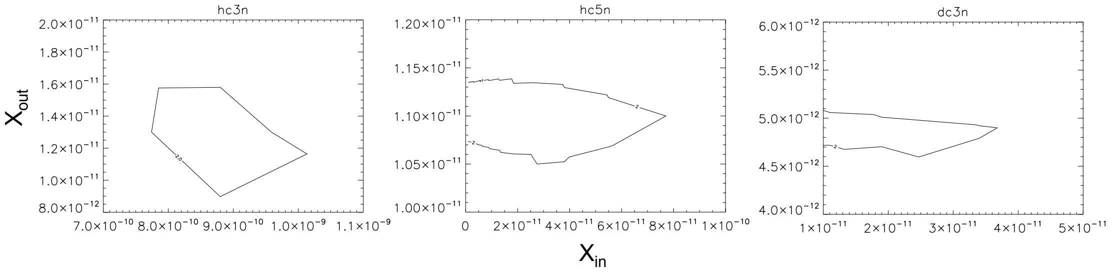

FIGURE A.3: χ^2 contour plots for HC$_3$N (left), HC$_5$N (middle) and DC$_3$N (right) as a function of X_{in} and X_{out}. The predictions refer to a model with T_{jump}=80 K and α=0.

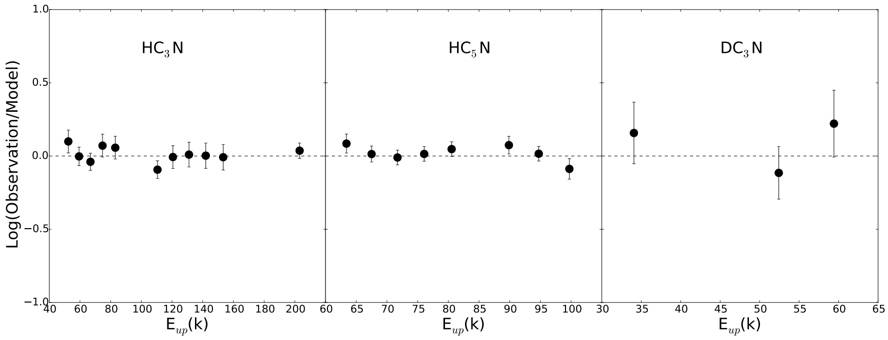

FIGURE A.4: Ratio of the observed over predicted line flux as a function of the upper level energy of the transition for the model 2 (T_{jump}=80 K and α=0), for HC$_3$N (left), HC$_5$N (middle) and DC$_3$N (right), respectively.

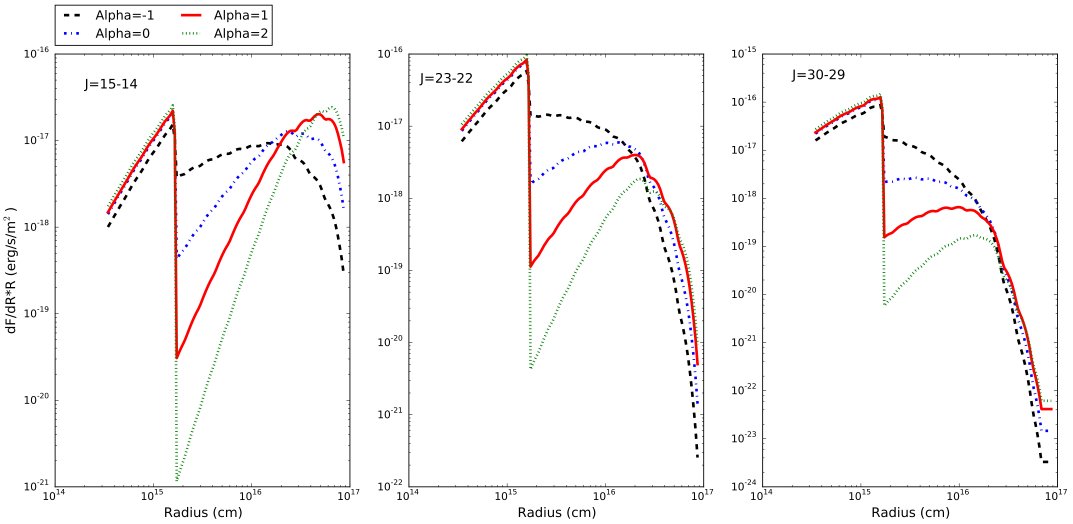

FIGURE A.5: The velocity-integrated flux emitted from each shell at a radius r ($dF/dr * r$) as a function of the radius for the HC$_3$N four best NON-LTE model, for three low, middle and high value of J.

Appendix B

Analyses comparison in Chapter 6

B.1 Comparison between GRAPES and rotational diagram analyses

This section aims to compare the agreement between the rotational diagram and GRAPES methods. As described in Sect 6.5.2, the line emission in I16293 does not appear to be well described by LTE, and a more realistic radiative transfer treatment will need to wait until collisional coefficients are available for NH_2CHO. Therefore, we do not consider it here, while it is worth noticing that a rotational diagram analysis is likely too simplistic to analyse the HNCO and NH_2CHO lines in this source.

In OMC-2, the GRAPES analysis tells us that the temperature that separates the inner and outer components is 80 K, both in the LTE and non-LTE approximations. Thus, for consistency in the comparison, we re-computed the inner and outer abundances resulting from the RD analysis using the same inner sizes as in GRAPES, instead of those corresponding to a temperature of the 100 K (see Sect. 6.5.2). We note that, while the RD analysis allowed for a separation of two components (inner and outer) for IRAS 4A, a single component was sufficient for OMC-2. It should be kept in mind, therefore, that for the latter the comparison is not equivalent, since we are not comparing a two-component solution with another two-component solution as in the case of the other two protostars.

The results of the comparison are listed in Table B.1 and illustrated in Fig. B.1, where we present the comparison using both the LTE and non-LTE results from GRAPES. It is evident that LTE and non-LTE yield practically the same results for these two sources. It can also be seen that the errors are quite high in some cases, up to 100%, which are caused by the large uncertainties resulting from the GRAPES analysis. Taking these into account, we find the following behaviours:

- HNCO abundance: Generally, both methods agree within an order of magnitude, but there is a tendency towards higher values in the RD analysis, by a factor of a few.
- NH_2CHO abundance: Again, we find agreement within a factor of a few. The compact solution is systematically lower in the RD treatment. This suggests that a non-negligible amount of emission from low-energy molecular lines actually comes from the inner region, and not exclusively from the extended envelope, as assumed in the linear fitting of the RD. Such a finding reflects the necessity of analysis like that performed with GRAPES if we want to properly disentangle the inner and outer components in hot corino or hot core sources.
- HNCO to NH_2CHO abundance ratio, R: In this case, the two analysis methods agree within a factor of a few.

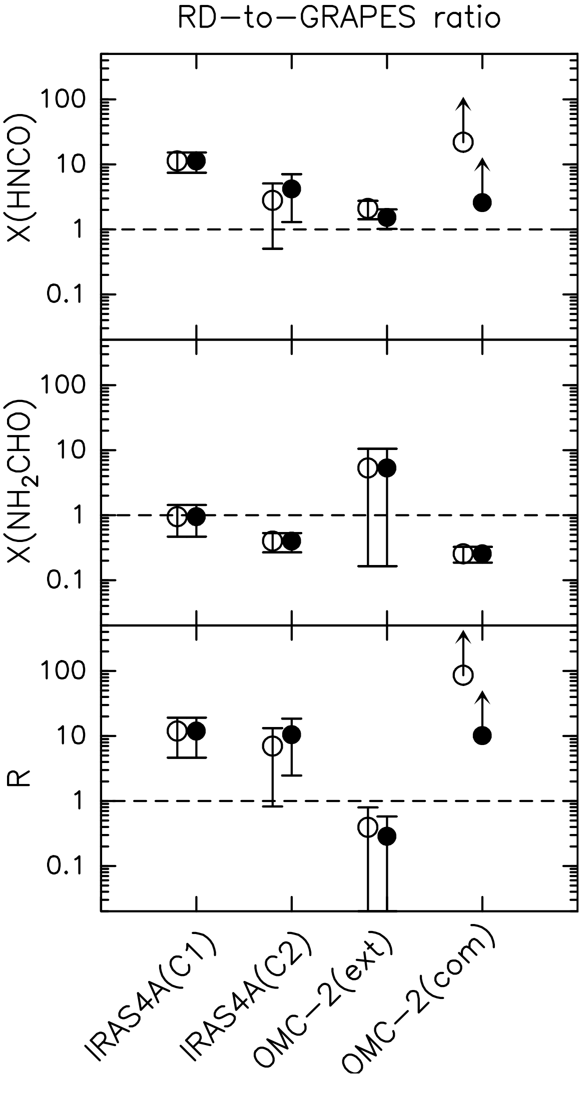

FIGURE B.1: Ratio of RD-to-GRAPES abundances. *Top*: HNCO abundance. *Middle*: NH_2CHO abundance. *Bottom*: HNCO to NH_2CHO abundance ratio. Filled and open circles represent, respectively, the LTE and non-LTE HNCO solution in the GRAPES analysis. The horizontal dashed lines mark equality between RD and GRAPES values.

TABLE B.1: Comparison between GRAPES and RD analyses*

	IRAS 4A	OMC-2
Inner size ($''$)	1.5	3.1
RD-to-GRAPES ratio (LTE)		
X_o(HNCO)	11 ± 4	1.5 ± 0.5
X_i(HNCO)	4 ± 3	> 2.5
X_o(NH_2CHO)	1 ± 1	5 ± 5
X_i(NH_2CHO)	0.4 ± 0.4	0.3 ± 0.3
R_o	12 ± 7	0.3 ± 0.3
R_i	11 ± 8	> 10
RD-to-GRAPES ratio (non-LTE)		
X_o(HNCO)	11 ± 4	2.1 ± 0.7
X_i(HNCO)	3 ± 2	> 22
X_o(NH_2CHO)	1 ± 1	5 ± 5
X_i(NH_2CHO)	0.4 ± 0.4	0.3 ± 0.3
R_o	12 ± 7	0.4 ± 0.4
R_i	7 ± 6	> 85

*Abundances with respect to H_2 are times 10^{-11}.

Appendix C

Chapter 6 Tables

TABLE C.1: NH_2CHO transitions searched for in this study and 3σ detections[a]

Transition	ν (MHz)	E_u (K)	A_{ul} (10^{-5} s^{-1})	θ_b ($''$)	OMC-2	CepE	SVS13A	IRAS4A	I16293	Blends
$4_{1,4}-3_{1,3}$	81693.446	12.8	3.46	30	N	Y*	N	N	N	
$4_{0,4}-3_{0,3}$	84542.330	10.2	4.09	29	Y	Y	N	N	Y	
$4_{2,3}-3_{2,2}$	84807.795	22.1	3.09	29	N	N	N	N	N	
$4_{3,2}-3_{3,1}$	84888.994	37.0	1.81	29	N	N	N	N	N	
$4_{3,1}-3_{3,0}$	84890.987	37.0	1.81	29	N	N	N	N	N	
$4_{2,2}-3_{2,1}$	85093.272	22.1	3.13	29	N	Y	N	N	N	
$4_{1,3}-3_{1,2}$	87848.873	13.5	4.30	28	Y	Y*	N	N	Y	
$5_{1,5}-4_{1,4}$	102064.267	17.7	7.06	24	Y	Y	N	B	Y	H_2COH^+?
$5_{0,5}-4_{0,4}$	105464.219	15.2	8.11	23	Y	Y	Y	Y	Y	
$5_{2,4}-4_{2,3}$	105972.599	27.2	6.92	23	Y	N	N	N	N	
$5_{4,2}-4_{4,1}$	106107.870	63.0	2.98	23	N	N	B	B	N	NH_2CHO
$5_{4,1}-4_{4,0}$	106107.895	63.0	2.98	23	N	N	B	B	N	NH_2CHO
$5_{3,3}-4_{3,2}$	106134.427	42.1	5.29	23	N	N	N	N	N	
$5_{3,2}-4_{3,1}$	106141.400	42.1	5.29	23	N	N	N	N	N	
$5_{2,3}-4_{2,2}$	106541.680	27.2	7.03	23	N	N	N	Y	N	
$5_{1,4}-4_{1,3}$	109753.503	18.8	8.78	22	N	N	N	N	N	
$6_{1,5}-5_{1,4}$	131617.902	25.1	15.6	19	Y	—	N	N	N	
$7_{1,7}-6_{1,6}$	142701.325	30.4	20.2	17	Y	—	Y	Y	N	
$7_{0,7}-6_{0,6}$	146871.475	28.3	22.5	17	B	—	B	B	B	CH_3OCH_3
$7_{2,6}-6_{2,5}$	148223.143	40.4	21.2	17	B	—	N	N	B	$HCNH^+$
$7_{6,1}-6_{6,0}$	148555.852	135.7	6.18	17	N	—	N	N	N	
$7_{6,2}-6_{6,1}$	148555.852	135.7	6.18	17	N	—	N	N	N	
$7_{5,3}-6_{5,2}$	148566.822	103.0	11.4	17	N	—	N	N	N	
$7_{5,2}-6_{5,1}$	148566.823	103.0	11.4	17	N	—	N	N	N	
$7_{4,4}-6_{4,3}$	148598.970	76.2	15.7	17	N	—	N	N	N	
$7_{4,3}-6_{4,2}$	148599.354	76.2	15.7	17	N	—	N	N	N	
$7_{3,5}-6_{3,4}$	148667.301	55.3	19.1	17	Y	—	N	N	N	
$7_{3,4}-6_{3,3}$	148709.018	55.4	19.1	17	Y	—	Y	N	N	
$7_{6,2}-6_{6,1}$	149792.574	40.6	21.9	16	N	—	N	N	Y*	
$7_{1,6}-6_{1,5}$	153432.176	32.5	25.1	16	Y	—	N	N	N	
$13_{2,11}-13_{1,12}$	155894.300	105.9	1.26	16	N	—	N	N	N	
$12_{2,10}-12_{1,11}$	155934.098	92.4	1.23	16	N	—	N	N	N	
$11_{2,9}-11_{1,10}$	157072.457	79.9	1.22	16	N	—	N	N	N	

Transition	ν (MHz)	E_u (K)	A_{ul} (10^{-5} s^{-1})	θ_b ($''$)	OMC-2	CepE	SVS13A	IRAS4A	I16293	Blends
$14_{2,12}-14_{1,13}$	157115.035	120.5	1.32	16	N	—	N	N	N	
$10_{2,8}-10_{1,9}$	159127.569	68.4	1.21	15	—	—	N	N	N	
$15_{2,13}-15_{1,14}$	159739.080	136.2	1.39	15	—	—	N	N	N	
$9_{2,7}-9_{1,8}$	161899.774	58.1	1.22	15	—	—	N	N	N	
$8_{1,8}-7_{1,7}$	162958.657	38.2	30.5	15	—	—	N	Y*	Y	
$8_{2,6}-8_{1,7}$	165176.756	48.8	1.22	15	—	—	N	N	N	
$8_{0,8}-7_{0,7}$	167320.697	36.4	33.5	15	—	—	N	Y*	Y	
$7_{2,5}-7_{1,6}$	168741.408	40.6	1.23	15	—	—	N	N	N	
$8_{2,7}-7_{2,6}$	169299.154	48.5	32.6	15	—	—	N	N	N	
$8_{6,2}-7_{6,1}$	169790.683	143.9	15.3	14	—	—	N	N	N	
$8_{6,3}-7_{6,2}$	169790.683	143.9	15.3	14	—	—	N	N	N	
$8_{5,4}-7_{5,3}$	169810.709	111.1	21.4	14	—	—	N	N	N	
$8_{5,3}-7_{5,2}$	169810.715	111.1	21.4	14	—	—	N	N	N	
$8_{4,5}-7_{4,4}$	169861.469	84.3	26.3	14	—	—	N	N	N	
$8_{4,4}-7_{4,3}$	169862.523	84.3	26.3	14	—	—	N	N	N	
$8_{3,6}-7_{3,5}$	169955.835	63.5	30.2	14	—	—	N	N	N	
$8_{3,5}-7_{3,4}$	170039.076	63.5	30.3	14	—	—	N	N	Y	
$8_{2,6}-7_{2,5}$	171620.760	48.8	33.9	14	—	—	N	N	N	
$6_{2,4}-6_{1,5}$	172381.012	33.4	1.24	14	—	—	N	N	N	
$10_{1,10}-9_{1,9}$	203335.761	56.8	60.3	12	Y	—	N	N	Y*	
$10_{0,10}-9_{0,9}$	207679.189	55.3	64.7	12	Y	—	N	Y*	N	
$10_{2,9}-9_{2,8}$	211328.960	67.8	65.6	12	Y	—	Y	Y	Y^{b}	
$10_{5,6}-9_{5,5}$	212323.555	130.5	52.0	12	N	—	N	N	N	
$10_{5,5}-9_{5,4}$	212323.555	130.5	52.0	12	N	—	N	N	N	
$10_{4,7}-9_{4,6}$	212428.020	103.7	58.4	12	N	—	N	N	B	NH_2CHO
$10_{4,6}-9_{4,5}$	212433.449	103.7	58.4	12	N	—	N	N	B	NH_2CHO
$10_{3,8}-9_{3,7}$	212572.837	82.9	63.3	12	Y	—	Y	N	N	

Transition	ν (MHz)	E_u (K)	A_{ul} (10^{-5} s^{-1})	θ_b ($''$)	OMC-2	CepE	SVS13A	IRAS4A	**I16293**	Blends
$10_{3,7}-9_{3,6}$	212832.307	82.9	63.6	12	N	—	N	N	N	
$10_{2,8}-9_{2,7}$	215687.009	68.4	69.8	11	Y	—	N	N	Y	
$10_{1,9}-9_{1,8}$	218459.213	60.8	74.7	11	B	—	N	N	N	CH_3OH
$11_{1,11}-10_{1,10}$	223452.512	67.5	80.5	11	Y	—	N	N	N	
$11_{0,11}-10_{0,10}$	227605.658	66.2	85.5	11	Y	—	N	N	N	
$11_{2,10}-10_{2,9}$	232273.646	78.9	88.2	11	N	—	N	N	Y	
$11_{5,7}-10_{5,6}$	233594.501	141.7	73.6	11	N	—	B	N	N	
$11_{5,6}-10_{5,5}$	233594.501	141.7	73.6	11	N	—	B	N	N	
$11_{4,8}-10_{4,7}$	233734.724	114.9	80.7	11	N	—	Y	N	N	
$11_{4,7}-10_{4,6}$	233745.613	114.9	80.7	11	N	—	Y	N	N	
$11_{3,9}-10_{3,8}$	233896.577	94.1	86.2	11	Y	—	Y	N	Y	
$11_{3,8}-10_{3,7}$	234315.498	94.2	86.7	10	—	—	N	N	N	
$11_{2,9}-10_{2,8}$	237896.684	79.9	94.8	10	Y	—	Y	N	B	?
$11_{1,10}-10_{1,9}$	239951.800	72.3	99.6	10	Y	—	Y	N	N	
$12_{1,12}-11_{1,11}$	243521.044	79.2	105	10	N	—	B	N	B	CH_2DOH
$12_{0,12}-11_{0,11}$	247390.719	78.1	110	10	N	—	N	N	N	
$12_{2,11}-11_{2,10}$	253165.793	91.1	115	10	Y	—	N	N	N	
$12_{4,9}-11_{4,8}$	255058.533	127.2	108	10	Y*	—	Y*	N	N	
$12_{4,8}-11_{4,7}$	255078.912	127.2	108	10	N	—	N	N	N	
$12_{3,10}-11_{3,9}$	255225.651	106.4	114	10	Y	—	Y	N	N	
$12_{3,9}-11_{3,8}$	255871.830	106.4	115	10	Y	—	N	N	N	
$12_{2,10}-11_{2,9}$	260189.090	92.4	125	9	B	—	B	N	B	H_2C_2O
$12_{1,11}-11_{1,10}$	261327.450	84.9	129	9	N	—	Y	N	N	
$13_{1,13}-12_{1,12}$	263542.236	91.8	133	9	Y	—	Y	N	N	

[a] Y: Detected above $T_{\rm mb} = 3\sigma$. Y*: Weakly detected (S/N $\sim 2-3$; see Sect. 6.5.1). N: undetected. B: possibly detected but blended. —: not observed.

[b] Detected but with an anomalously high flux (maybe blended): removed from analysis.

TABLE C.2: HNCO transitions searched for in this study and 3σ detections[a]

Transition	ν (MHz)	E_u (K)	A_{ul} (10^{-5} s^{-1})	θ_b ($''$)	OMC-2	CepE	SVS13A	IRAS4A	I16293	L1157	L1527	B1	L1544	**TMC-1**
$4_{1,4}-3_{1,3}$	87597.330	53.8	0.80	**28**	N	N	Y	Y[b]	N	N	N	N	N	—
$4_{0,4}-3_{0,3}$	87925.237	10.5	0.88	**28**	Y	Y	Y	Y	Y	Y	Y	Y	Y	—
$4_{1,3}-3_{1,2}$	88239.020	53.9	0.82	**28**	Y*	N	Y*	Y[b]	N	N	N	N	N	—
$5_{1,5}-4_{1,4}$	109495.996	59.0	1.7	**22**	N	N	Y	N	Y	W	N	N	N	**N**
$5_{0,5}-4_{0,4}$	109905.749	15.8	1.8	**22**	Y	Y	Y	Y	Y	Y	Y	Y	Y	**Y**
$5_{1,4}-4_{1,3}$	110298.089	59.2	1.7	**22**	Y*	N	Y	N	Y	N	N	N	N	**N**
$6_{1,6}-5_{1,5}$	131394.230	65.3	2.9	**19**	N	N	Y	N	Y	N	N	N	—	**N**
$6_{0,6}-5_{0,5}$	131885.734	22.2	3.1	**19**	Y	Y	Y	Y	Y	Y	Y	Y	—	**Y**
$6_{1,5}-5_{1,4}$	132356.701	65.5	3.0	**19**	N	N	N	N	Y	Y	N	N	—	**N**
$7_{1,7}-6_{1,6}$	153291.935	72.7	4.7	**16**	N	—	Y	N	Y	N	N	N	—	**N**
$7_{0,7}-6_{0,6}$	153865.086	29.5	4.9	**16**	Y	—	Y	Y	Y	Y	Y	Y	—	**Y**
$7_{1,6}-6_{1,5}$	154414.765	72.9	4.8	**16**	N	—	Y	N	Y	N	N	N	—	**N**
$10_{1,10}-9_{1,9}$	218981.009	101.1	14.2	**11**	N	N	Y	N	Y	N	N	N	—	—
$10_{0,10}-9_{0,9}$	219798.274	58.0	14.7	**11**	Y	Y	Y	Y	Y	N	N	Y	—	—
$10_{1,9}-9_{1,8}$	220584.751	101.5	14.5	**11**	Y	N	Y	Y	Y	N	N	N	—	—
$11_{1,11}-10_{1,10}$	240875.727	112.6	19.0	**10**	N	—	Y	Y	Y	N	N	N	—	—
$11_{0,11}-10_{0,10}$	241774.032	69.6	19.6	**10**	B	—	B	B	B	N	N	N	—	—
$11_{1,10}-10_{1,9}$	242639.704	113.1	19.5	**10**	N	—	Y	N	N	N	N	—	—	
$12_{1,12}-11_{1,11}$	262769.477	125.3	24.8	**9**	N	N	Y	Y	Y[c]	N	N	N	—	—
$12_{0,12}-11_{0,11}$	263748.625	82.3	25.6	**9**	Y	Y	Y	Y	Y	N	N	N	—	—
$12_{1,11}-11_{1,10}$	264693.655	125.9	25.4	**9**	N	N	Y	Y	Y	N	N	N	—	—

[a] Y: Detected above $T_{\rm mb} = 3\sigma$. Y*: Weakly detected (S/N $\sim 2-3$; see Sect. 6.5.1). N: undetected. B: detected but blended. —: not observed.

[b] Detected but with an anomalously high flux (maybe blended): removed from analysis.

[c] Blended with an unidentified feature: removed from analysis.

Blends: CH_3OH at 241.774 GHz

TABLE C.3: L1544: Gaussian fits to the detected HNCO lines

Transition	ν (MHz)	RMS (mK)	$T_{\rm peak}$ (mK)	$V_{\rm lsr}$ (km s^{-1})	ΔV (km s^{-1})	$\int T_{\rm mb} dV$ (mK km s^{-1})
$4_{0,4}-3_{0,3}$	87925.237	11.9	459 (2)	7.2 (1)	0.7 (2)	342 (9)
$5_{0,5}-4_{0,4}$	109905.996	4.8	601 (2)	7.6 (1)	0.7 (1)	448 (5)

TABLE C.4: TMC-1: Gaussian fits to the detected HNCO lines

Transition	ν (MHz)	RMS (mK)	$T_{\rm peak}$ (mK)	$V_{\rm lsr}$ (km s^{-1})	ΔV (km s^{-1})	$\int T_{\rm mb} dV$ (mK km s^{-1})
$5_{0,5}-4_{0,4}$	109905.996	6.8	157 (8)	5.8 (1)	1.2 (1)	203 (11)
$6_{0,6}-5_{0,5}$	131885.734	6.7	94 (7)	5.8 (1)	0.5 (3)	50 (5)
$7_{0,7}-6_{0,6}$	153865.086	3.2	28 (3)	5.9 (1)	0.5 (4)	15 (2)

TABLE C.5: B1: Gaussian fits to the detected HNCO lines

Transition	ν (MHz)	RMS (mK)	$T_{\rm peak}$ (mK)	$V_{\rm lsr}$ (km s^{-1})	ΔV (km s^{-1})	$\int T_{\rm mb} dV$ (mK km s^{-1})
$4_{0,4}-3_{0,3}$	87925.237	3.0	530 (12)	6.7 (1)	1.4 (1)	765 (5)
$5_{0,5}-4_{0,4}$	109905.996	22.2	480 (6)	6.6 (1)	1.3 (1)	662 (32)
$6_{0,6}-5_{0,5}$	131885.734	6.3	345 (7)	6.7 (1)	1.4 (1)	521 (8)
$7_{0,7}-6_{0,6}$	153865.086	7.4	224 (6)	6.6 (1)	1.4 (1)	326 (10)

TABLE C.6: L1527: Gaussian fits to the detected HNCO lines

Transition	ν (MHz)	RMS (mK)	$T_{\rm peak}$ (mK)	$V_{\rm lsr}$ (km s^{-1})	ΔV (km s^{-1})	$\int T_{\rm mb} dV$ (mK km s^{-1})
$4_{0,4}-3_{0,3}$	87925.237	2.3	145 (2)	5.9 (1)	1.3 (1)	198 (3)
$5_{0,5}-4_{0,4}$	109905.996	7.9	135 (7)	5.9 (1)	1.2 (1)	175 (11)
$6_{0,6}-5_{0,5}$	131885.734	6.7	138 (1)	5.9 (1)	0.8 (1)	115 (8)
$7_{0,7}-6_{0,6}$	153865.086	8.0	63 (1)	5.8 (1)	0.7 (1)	47 (6)

TABLE C.7: L1157mm: Gaussian fits to the detected HNCO lines

Transition	ν (MHz)	RMS (mK)	$T_{\rm peak}$ (mK)	$V_{\rm lsr}$ (km s^{-1})	ΔV (km s^{-1})	$\int T_{\rm mb} dV$ (mK km s^{-1})
$4_{0,4}-3_{0,3}$	87925.237	3.3	113 (7)	2.6 (1)	1.6 (1)	198 (7)
$5_{0,5}-4_{0,4}$	109905.996	7.8	142 (5)	2.5 (1)	1.2 (1)	177 (13)
$6_{0,6}-5_{0,5}$	131885.734	5.5	81 (3)	2.6 (1)	1.5 (1)	126 (11)
$7_{0,7}-6_{0,6}$	153865.086	5.3	71 (1)	2.6 (1)	1.1 (1)	81 (8)

TABLE C.8: IRAS 4A: Gaussian fits to the detected NH_2CHO and HNCO lines

Transition	ν (MHz)	RMS (mK)	$T_{\rm peak}$ (mK)	$V_{\rm lsr}$ (km s^{-1})	ΔV (km s^{-1})	$\int T_{\rm mb} dV$ (mK km s^{-1})
			NH_2CHO			
$5_{0,5} - 4_{0,4}$	105464.219	3.3	9.8 (1)	6.7 (4)	4.0 (13)	41 (11)
$5_{2,3} - 4_{2,2}$	106541.680	2.2	7.7 (17)	7.6 (3)	2.8 (9)	23 (5)
$7_{1,7} - 6_{1,6}$	142701.325	5.0	15 (4)	8.1 (3)	2.6 (5)	40 (8)
$8_{1,8} - 7_{1,7}$ $^{\rm w}$	162958.657	38.2	14 (6)	8.5 (4)	2.9 (7)	44 (9)
$8_{0,8} - 7_{0,7}$ $^{\rm w}$	167320.697	36.4	13 (4)	7.2 (4)	3.2 (7)	43 (10)
$10_{0,10} - 9_{0,9}$ $^{\rm w}$	207679.189	55.3	19 (10)	6.6 (5)	3.3 (10)	66 (19)
$10_{2,9} - 9_{2,8}$	211328.960	7.1	31 (3)	6.7 (2)	2.4 (5)	82 (15)
			HNCO			
$4_{0,4} - 3_{0,3}$	87925.237	3.1	195 (16)	7.2 (1)	2.2 (1)	458 (6)
$5_{0,5} - 4_{0,4}$	109905.749	8.0	198 (15)	7.1 (1)	2.3 (1)	495 (16)
$6_{0,6} - 5_{0,5}$	131885.734	5.9	203 (12)	7.0 (1)	2.5 (1)	545 (11)
$7_{0,7} - 6_{0,6}$	153865.086	6.8	168 (11)	7.1 (1)	2.2 (1)	395 (12)
$10_{0,10} - 9_{0,9}$	219798.274	9.0	88 (8)	6.8 (1)	3.3 (3)	307 (19)
$10_{1,9} - 9_{1,8}$	220584.751	6.8	37 (6)	6.5 (3)	2.8 (7)	111 (22)
$11_{1,11} - 10_{1,10}$	240875.727	7.2	23 (2)	6.6 (2)	1.7 (6)	42 (13)
$12_{1,12} - 11_{1,11}$	262769.477	8.9	44 (4)	6.6 (2)	3.8 (6)	177 (21)
$12_{0,12} - 11_{0,11}$	263748.625	12.9	54 (4)	6.5 (8)	3.9 (29)	230 (130)
$12_{1,11} - 11_{1,10}$	264693.655	9.1	26 (5)	6.3 (4)	3.7 (9)	103 (21)

$^{\rm w}$ Transition weakly detected (see Chapter 6) but included in the analysis for completeness.

TABLE C.9: I16293: Gaussian fits to the detected NH_2CHO and HNCO lines (intensity in $T^*_{\rm ant}$ units)

Transition	ν (MHz)	RMS (mK)	$T_{\rm peak}$ (mK)	$V_{\rm lsr}$ (km s^{-1})	ΔV (km s^{-1})	$\int T_{\rm a} dV$ (mK km s^{-1})
			NH_2CHO			
$4_{0,4} - 3_{0,3}$	84542.330	5.3	17 (6)	3.2 (12)	6.7 (20)	120 (40)
$4_{1,3} - 3_{1,2}$	87848.873	2.6	12 (4)	2.6 (5)	3.8 (11)	50 (13)
$5_{1,5} - 4_{1,4}$	102064.267	3.3	16 (5)	2.0 (3)	2.4 (9)	42 (12)
$5_{0,5} - 4_{0,4}$	105464.219	5.3	20 (7)	5.1 (4)	3.0 (10)	64 (19)
$7_{6,2} - 6_{6,1}$ $^{\rm w}$	149792.574	10.0	29 (10)	2.6 (4)	3.0 (7)	93 (22)
$8_{1,8} - 7_{1,7}$	162958.657	10.1	26 (10)	2.8 (4)	2.5 (13)	69 (27)
$8_{0,8} - 7_{0,7}$	167320.697	10.6	55 (11)	2.0 (2)	2.3 (5)	136 (24)
$8_{3,5} - 7_{3,4}$	170039.076	15.3	50 (80)	2.7 (17)	2.4 (46)	120 (170)
$10_{1,10} - 9_{1,9}$ $^{\rm w}$	203335.761	6.8	19 (7)	0.5 (10)	6.7 (27)	135 (43)
$10_{2,8} - 9_{2,7}$	215687.009	5.5	30 (10)	1.0 (13)	5.5 (34)	175 (90)
$11_{2,10} - 10_{2,9}$	232273.646	4.6	23 (18)	1.5 (19)	5.0 (39)	120 (90)
$11_{2,9} - 10_{2,8}$	237896.684	8.2	45 (9)	2.8 (3)	3.1 (15)	148 (42)
			HNCO			
$4_{0,4} - 3_{0,3}$	87925.237	3.2	162 (3)	4.0 (1)	3.9 (1)	671 (11)
$5_{1,5} - 4_{1,4}$	109495.996	5.4	38 (6)	2.0 (3)	4.5 (11)	182 (35)
$5_{0,5} - 4_{0,4}$	109905.749	5.9	254 (6)	3.9 (1)	3.2 (1)	853 (18)
$5_{1,4} - 4_{1,3}$	110298.089	5.4	16 (5)	5.4 (6)	5.4 (18)	90 (23)
$6_{1,6} - 5_{1,5}$	131394.230	5.4	39 (17)	2.5 (8)	5.2 (27)	217 (88)
$6_{0,6} - 5_{0,5}$	131885.734	7.3	263 (8)	3.9 (1)	3.0 (1)	825 (18)
$6_{1,5} - 5_{1,4}$	132356.701	6.9	39 (8)	3.6 (5)	5.3 (13)	218 (48)
$7_{1,7} - 6_{1,6}$	153291.935	9.5	73 (27)	5.1 (5)	3.0 (16)	230 (90)
$7_{0,7} - 6_{0,6}$	153865.086	12.3	224 (18)	3.9 (1)	4.0 (3)	950 (50)
$7_{1,6} - 6_{1,5}$	154414.765	11.1	57 (28)	2.7 (7)	3.4 (21)	200 (90)
$10_{1,10} - 9_{1,9}$	218981.009	6.2	103 (8)	2.8 (2)	6.0 (5)	664 (47)
$10_{0,10} - 9_{0,9}$	219798.274	4.4	260 (12)	3.3 (1)	5.7 (3)	1580 (60)
$10_{1,9} - 9_{1,8}$	220584.751	6.4	85 (10)	2.9 (3)	6.2 (7)	560 (50)
$11_{1,11} - 10_{1,10}$	240875.727	14.5	132 (16)	2.8 (3)	6.6 (9)	930 (100)
$12_{0,12} - 11_{0,11}$	263748.625	7.9	270 (70)	3.7 (6)	5.6 (15)	1640 (360)
$12_{1,11} - 11_{1,10}$	264693.655	6.9	119 (11)	3.4 (2)	6.6 (6)	840 (60)

[w] Transition weakly detected (see Chapter 6) but included in the analysis for completeness.

TABLE C.10: SVS13A: Gaussian fits to the detected NH_2CHO and HNCO lines

Transition	ν (MHz)	RMS (mK)	$T_{\rm peak}$ (mK)	$V_{\rm lsr}$ (km s^{-1})	ΔV (km s^{-1})	$\int T_{\rm mb} dV$ (mK km s^{-1})
			NH_2CHO			
$5_{0,5}-4_{0,4}$	105464.219	3.9	16 (1)	8.1 (2)	1.8 (5)	14 (1)
$7_{1,7}-6_{1,6}$	142701.325	6.4	28 (3)	8.6 (2)	2.2 (5)	22 (5)
$7_{3,4}-6_{3,3}$	148709.018	7.1	26 (2)	7.1 (3)	2.2 (7)	22 (3)
$10_{2,9}-9_{2,8}$	211328.960	7.3	62 (5)	7.5 (5)	4.4 (14)	31 (2)
$10_{3,8}-9_{3,7}$	212572.837	7.2	43 (7)	8.4 (2)	2.7 (6)	29 (2)
$11_{4,8}-10_{4,7}$	233734.724	6.6	26 (2)	6.9 (4)	3.0 (9)	23 (5)
$11_{4,7}-10_{4,6}$	233745.613	7.5	26 (2)	8.2 (3)	1.5 (7)	26 (1)
$11_{3,9}-10_{3,8}$	233896.577	6.6	49 (14)	8.2 (4)	2.9 (9)	20 (3)
$11_{2,9}-10_{2,8}$	237896.684	6.9	48 (6)	8.1 (3)	4.3 (8)	28 (4)
$11_{1,10}-10_{1,9}$	239951.800	8.1	66 (7)	7.6 (4)	3.4 (9)	23 (2)
$12_{3,10}-11_{3,9}$	255225.651	5.6	45 (2)	8.8 (12)	3.3 (36)	24 (4)
$12_{1,11}-11_{1,10}$	261327.450	8.7	26 (2)	8.4 (2)	4.6 (6)	38 (5)
$13_{1,13}-12_{1,12}$	263542.236	7.6	54 (5)	7.7 (6)	4.4 (15)	32 (5)
			HNCO			
$4_{1,4}-3_{1,3}$	87597.330	3.5	11 (3)	6.4 (4)	3.3 (8)	40 (9)
$4_{0,4}-3_{0,3}$	87925.237	9.1	46 (4)	8.6 (2)	3.1 (6)	155 (23)
$4_{1,3}-3_{1,2}{}^{\rm w}$	88239.020	3.0	13 (3)	7.3 (4)	3.3 (20)	45 (17)
$5_{1,5}-4_{1,4}$	109495.996	3.9	16 (1)	7.1 (2)	2.0 (5)	35 (8)
$5_{0,5}-4_{0,4}{}^{*}$	109905.749	5.4	76 (5)	8.5 (1)	1.2 (1)	100 (8)
$5_{1,4}-4_{1,3}$	110298.089	6.2	28 (4)	8.2 (3)	4.7 (8)	139 (19)
$6_{1,6}-5_{1,5}$	131394.230	6.6	19 (3)	8.2 (4)	3.6 (8)	72 (15)
$6_{0,6}-5_{0,5}{}^{*}$	131885.734	6.0	77 (10)	8.5 (1)	1.6 (3)	129 (15)
$7_{1,7}-6_{1,6}$	153291.935	5.7	25 (2)	8.5 (5)	5.1 (13)	140 (30)
$7_{0,7}-6_{0,6}{}^{*}$	153865.086	6.1	70 (6)	7.5 (1)	3.4 (5)	258 (19)
$7_{1,6}-6_{1,5}$	154414.765	6.0	32 (3)	8.3 (6)	4.4 (15)	149 (40)
$10_{1,10}-9_{1,9}$	218981.009	6.8	46 (3)	8.2 (2)	4.3 (4)	212 (15)
$10_{0,10}-9_{0,9}$	219798.274	7.1	89 (4)	8.4 (1)	3.2 (2)	309 (16)
$10_{1,9}-9_{1,8}$	220584.751	6.0	35 (3)	8.5 (4)	3.7 (9)	136 (27)
$11_{1,11}-10_{1,10}$	240875.727	6.7	46 (4)	8.2 (5)	4.9 (17)	236 (66)
$11_{1,10}-10_{1,9}$	242639.704	8.7	42 (5)	8.1 (3)	4.6 (6)	206 (24)
$12_{1,12}-11_{1,11}$	262769.477	9.9	68 (4)	8.5 (2)	5.3 (5)	380 (32)
$12_{0,12}-11_{0,11}$	263748.625	9.3	60 (5)	8.2 (4)	3.4 (9)	213 (48)
$12_{1,11}-11_{1,10}$	264693.655	8.9	39 (4)	8.5 (3)	4.4 (6)	183 (23)

* Transition affected by emission at OFF position: lower limit point in the rotational diagram.

w Transition weakly detected (see Chapter 6) but included in the analysis for completeness.

TABLE C.11: Cep E: Gaussian fits to the detected NH_2CHO and HNCO lines

Transition	ν (MHz)	RMS (mK)	$T_{\rm peak}$ (mK)	$V_{\rm lsr}$ (km s^{-1})	ΔV (km s^{-1})	$\int T_{\rm mb} dV$ (mK km s^{-1})
			NH_2CHO			
$4_{0,4}-3_{0,3}$	84542.330	1.9	7.7 (1)	–11.5 (4)	2.8 (10)	23 (7)
$4_{2,2}-3_{2,1}$	85093.272	1.3	4.3 (1)	–11.8 (3)	3.5 (7)	16 (3)
$4_{1,3}-3_{1,2}$ [w]	87848.873	1.2	6.3 (1)	–10.5 (2)	2.6 (5)	17 (3)
$5_{1,5}-4_{1,4}$	102064.267	1.6	7.6 (1)	–10.6 (2)	1.7 (5)	13 (3)
$5_{0,5}-4_{0,4}$	105464.219	2.1	4.1 (1)	–10.6 (6)	2.9 (11)	13 (4)
			HNCO			
$4_{0,4}-3_{0,3}$	87925.237	1.4	90 (4)	–11.1 (1)	1.9 (1)	179 (3)
$5_{0,5}-4_{0,4}$	109905.749	2.8	104 (12)	–11.1 (1)	2.4 (1)	262 (6)
$6_{0,6}-5_{0,5}$	131885.734	7.8	128 (9)	–11.1 (1)	2.2 (3)	299 (23)
$10_{0,10}-9_{0,9}$	219798.274	7.5	45 (10)	–10.1 (73)	8.0 (80)	380 (65)
$12_{0,12}-11_{0,11}$	263748.625	6.0	38 (8)	–10.2 (5)	5.6 (14)	226 (45)

[w] Transition weakly detected (see Chapter 6) but included in the analysis for completeness.

TABLE C.12: OMC-2 FIR 4: Gaussian fits to the detected NH_2CHO and HNCO lines

Transition	ν (MHz)	RMS (mK)	$T_{\rm peak}$ (mK)	$V_{\rm lsr}$ (km s^{-1})	ΔV (km s^{-1})	$\int T_{\rm mb} dV$ (mK km s^{-1})
NH_2CHO						
$4_{0,4} - 3_{0,3}$	84542.330	2.8	15 (2)	10.8 (2)	2.2 (4)	35 (5)
$4_{1,3} - 3_{1,2}$	87848.873	2.8	9 (2)	11.0 (4)	3.6 (6)	37 (7)
$5_{1,5} - 4_{1,4}$	102064.267	3.5	15 (1)	11.0 (2)	2.9 (5)	46 (6)
$5_{0,5} - 4_{0,4}$	105464.219	4.7	16 (1)	11.5 (4)	3.7 (10)	64 (15)
$5_{2,4} - 4_{2,3}$	105972.599	4.6	15 (5)	11.3 (2)	1.7 (5)	28 (8)
$6_{1,5} - 5_{1,4}$	131617.902	5.6	29 (3)	11.2 (2)	3.8 (6)	115 (13)
$7_{1,7} - 6_{1,6}$	142701.325	6.4	28 (3)	11.5 (2)	3.1 (7)	91 (14)
$7_{3,4} - 6_{3,3}$	148709.018	5.6	26 (2)	11.5 (2)	1.8 (5)	51 (10)
$7_{1,6} - 6_{1,5}$	153432.176	8.2	40 (3)	11.8 (3)	2.7 (10)	114 (31)
$10_{1,10} - 9_{1,9}$	203335.761	10.8	52 (4)	11.3 (2)	2.8 (5)	156 (20)
$10_{0,10} - 9_{0,9}$	207679.189	8.8	49 (3)	11.6 (1)	1.8 (4)	97 (14)
$10_{3,8} - 9_{3,7}$	212572.837	12.7	43 (7)	11.7 (3)	2.9 (6)	131 (23)
$11_{1,11} - 10_{1,10}$	223452.512	12.6	44 (6)	11.7 (5)	3.0 (12)	142 (48)
$11_{0,11} - 10_{0,10}$	227605.658	14.5	61 (10)	11.9 (3)	3.7 (7)	237 (33)
$11_{3,9} - 10_{3,8}$	233896.577	16.9	49 (14)	11.6 (3)	2.9 (10)	151 (36)
$11_{2,9} - 10_{2,8}$	237896.684	10.1	48 (6)	11.4 (2)	3.7 (6)	186 (23)
$11_{1,10} - 10_{1,9}$	239951.800	10.5	66 (7)	11.5 (1)	2.5 (4)	175 (21)
$12_{2,11} - 11_{2,10}$	253165.793	12.4	44 (9)	11.2 (3)	3.2 (7)	152 (27)
$12_{4,9} - 11_{4,8}$ $^{\rm w}$	255058.533	12.5	39 (12)	11.6 (2)	1.9 (4)	80 (17)
$12_{3,10} - 11_{3,9}$	255225.651	11.4	45 (2)	11.5 (4)	1.6 (9)	74 (4)
$12_{3,9} - 11_{3,8}$	255871.830	11.8	41 (7)	11.8 (2)	2.7 (5)	119 (19)
HNCO						
$4_{0,4} - 3_{0,3}$	87925.237	2.8	128 (13)	11.2 (1)	2.5 (1)	344 (6)
$4_{1,3} - 3_{1,2}$ $^{\rm w}$	88239.020	2.3	9 (2)	12.7 (3)	3.1 (6)	31 (5)
$5_{0,5} - 4_{0,4}$	109905.749	6.9	224 (22)	11.4 (1)	2.1 (1)	512 (14)
$5_{1,4} - 4_{1,3}$ $^{\rm w}$	110298.089	6.2	18 (5)	12.8 (2)	1.4 (5)	26 (7)
$6_{0,6} - 5_{0,5}$	131885.734	4.7	267 (27)	11.2 (1)	2.7 (1)	775 (11)
$7_{0,7} - 6_{0,6}$	153865.086	8.8	304 (38)	11.2 (1)	3.0 (4)	962 (89)
$10_{0,10} - 9_{0,9}$	219798.274	9.2	343 (28)	11.4 (1)	2.5 (1)	918 (17)
$10_{1,9} - 9_{1,8}$	220584.751	11.0	36 (1)	11.7 (4)	2.1 (13)	79 (35)
$12_{0,12} - 11_{0,11}$	263748.625	5.1	202 (9)	11.9 (3)	3.0 (5)	648 (24)

$^{\rm w}$ Transition weakly detected (see Chapter 6) but included in the analysis for completeness.

Appendix D

Chapter 6 Figures

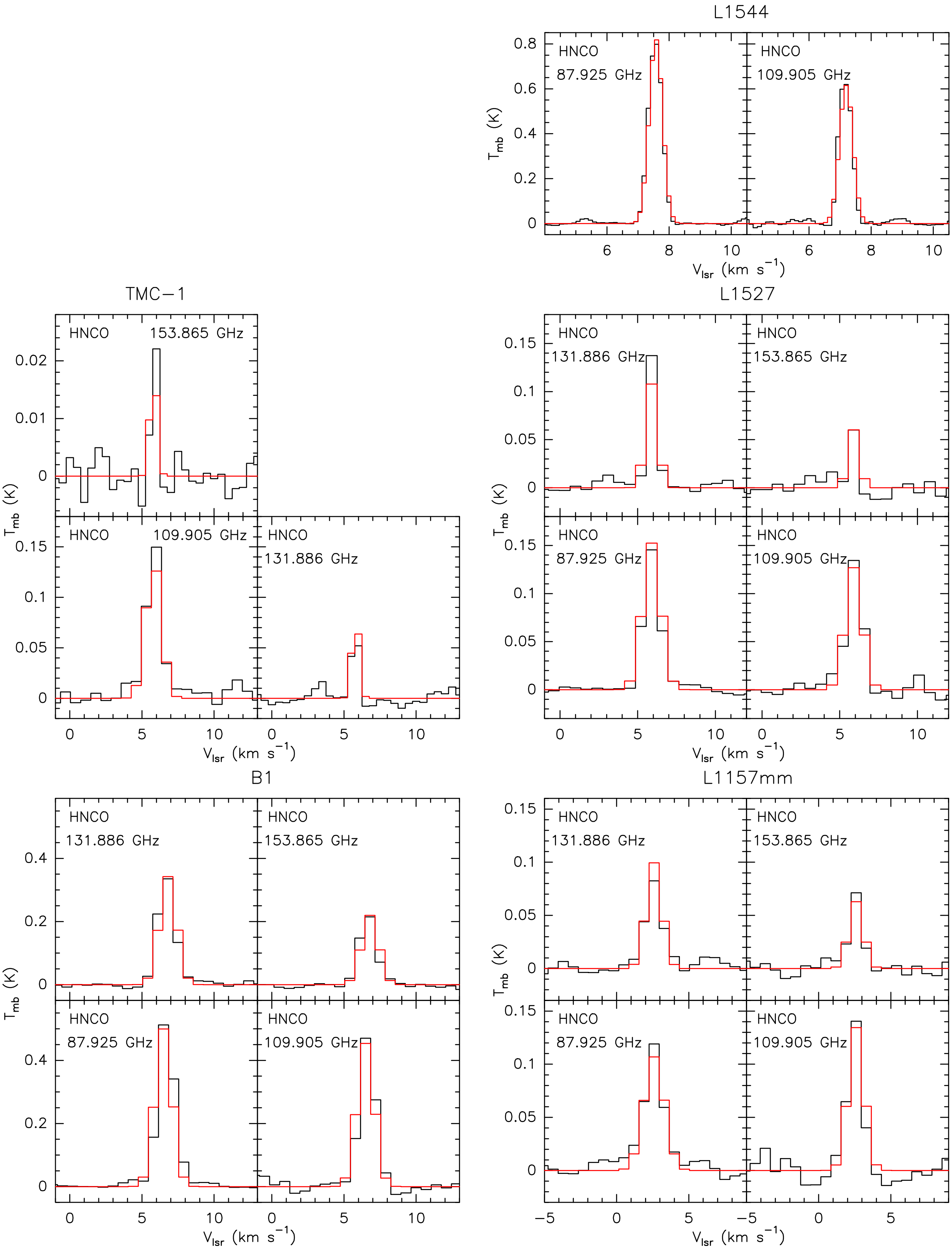

FIGURE D.1: HNCO observed spectral lines (black) in L1544, TMC-1, B1, L1527, and L1157mm, and the spectra predicted by best fit LTE model (red).

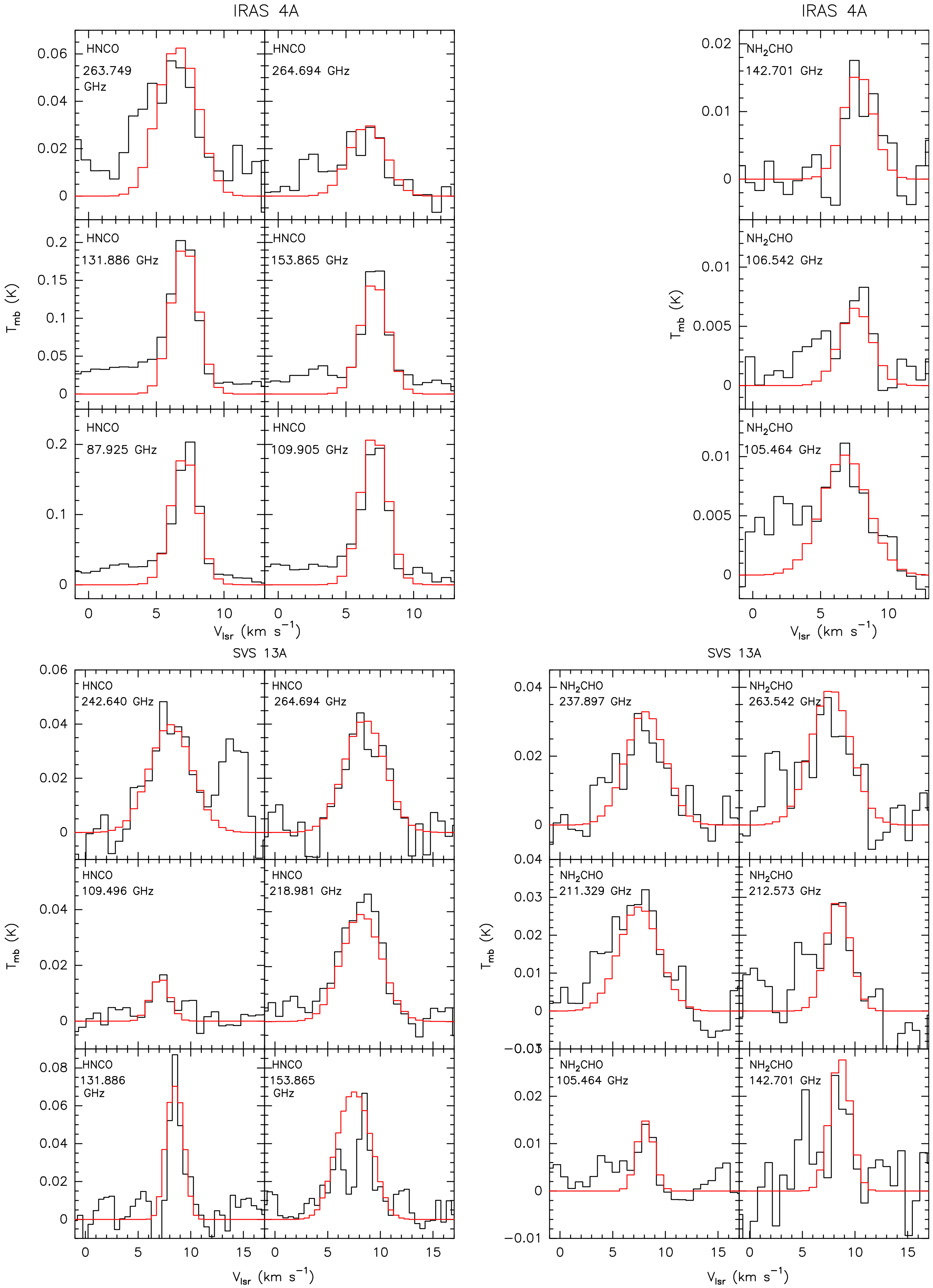

FIGURE D.2: Sample of HNCO (*left*) and NH_2CHO (*right*) observed spectral lines (black) in IRAS 4A and SVS13A (compact solution), and the spectra predicted by best fit LTE model (red).

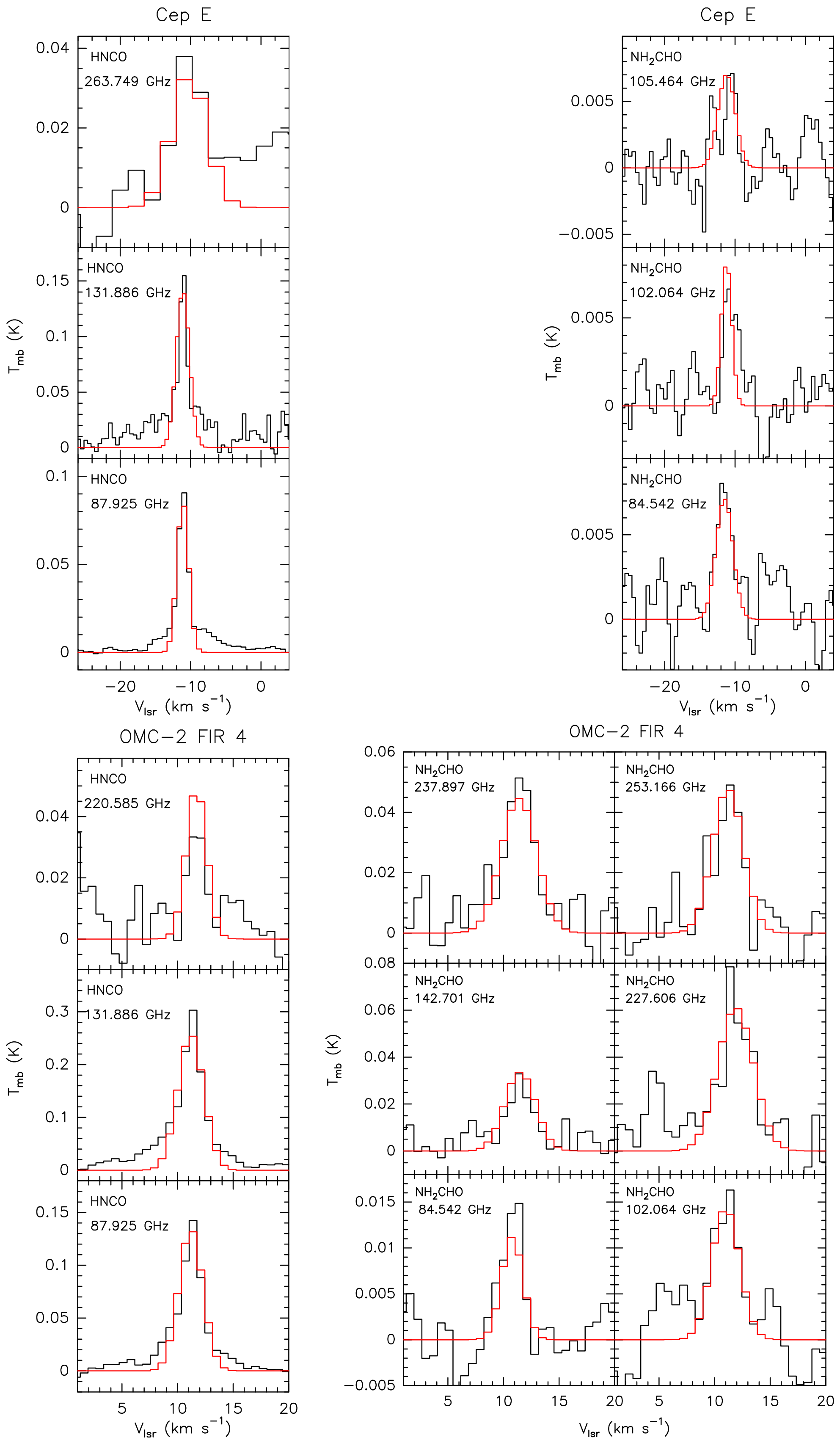

FIGURE D.3: Sample of HNCO (*left*) and NH_2CHO (*right*) observed spectral lines (black) in Cep E and OMC-2 FIR 4 (extended solutions), and the spectra predicted by best fit LTE model (red).

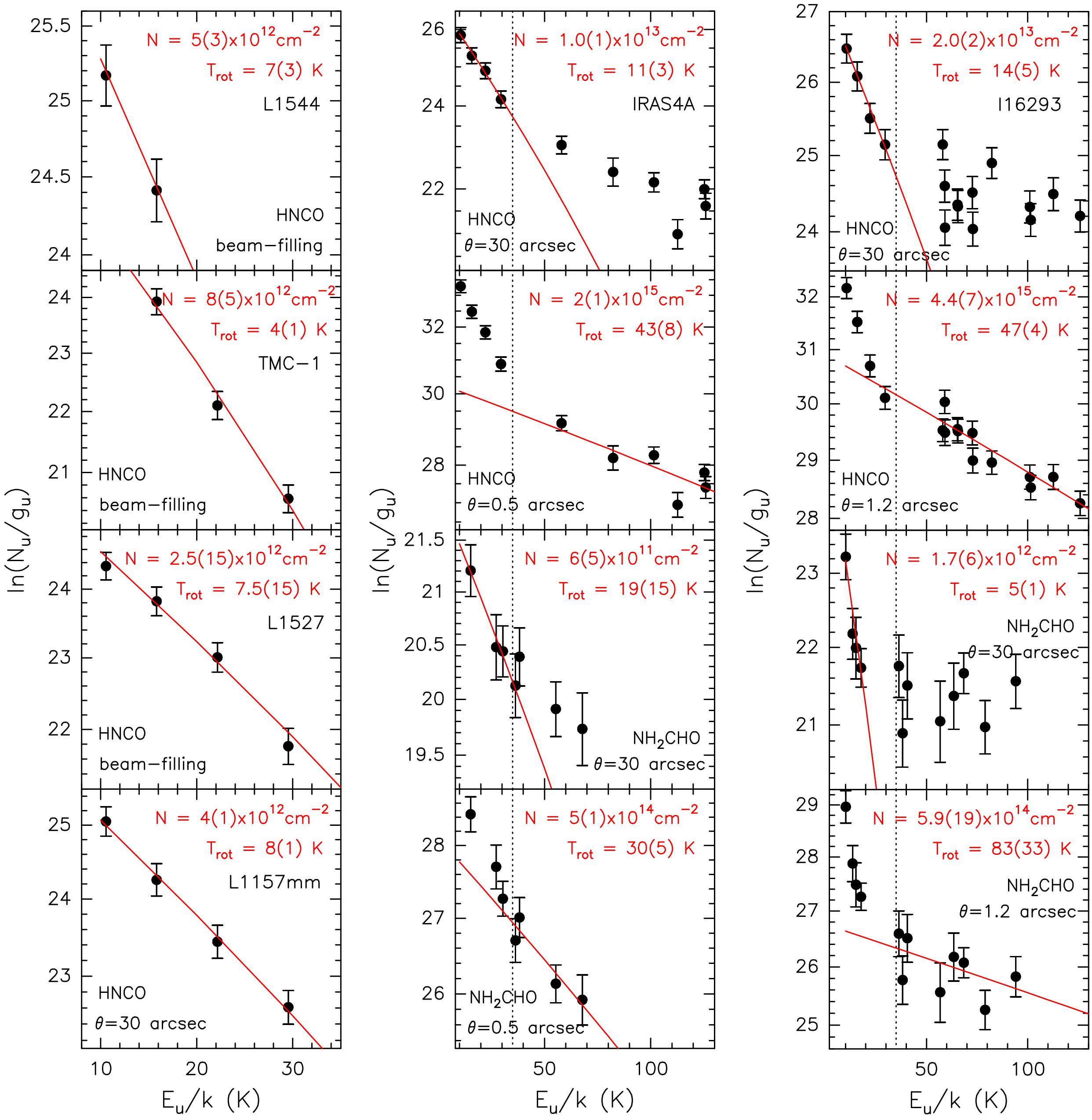

FIGURE D.4: Rotational diagrams for L1544, TMC-1, L1527, and L1157mm (*left*), IRAS 4A (*middle*), and I16293 (*right*). Data points are depicted in black. The red lines correspond to the best fit to the data points. The dashed vertical lines in the middle and right panels indicate the upper-level energy (35 K) at which the division of the 2-component fitting was made.

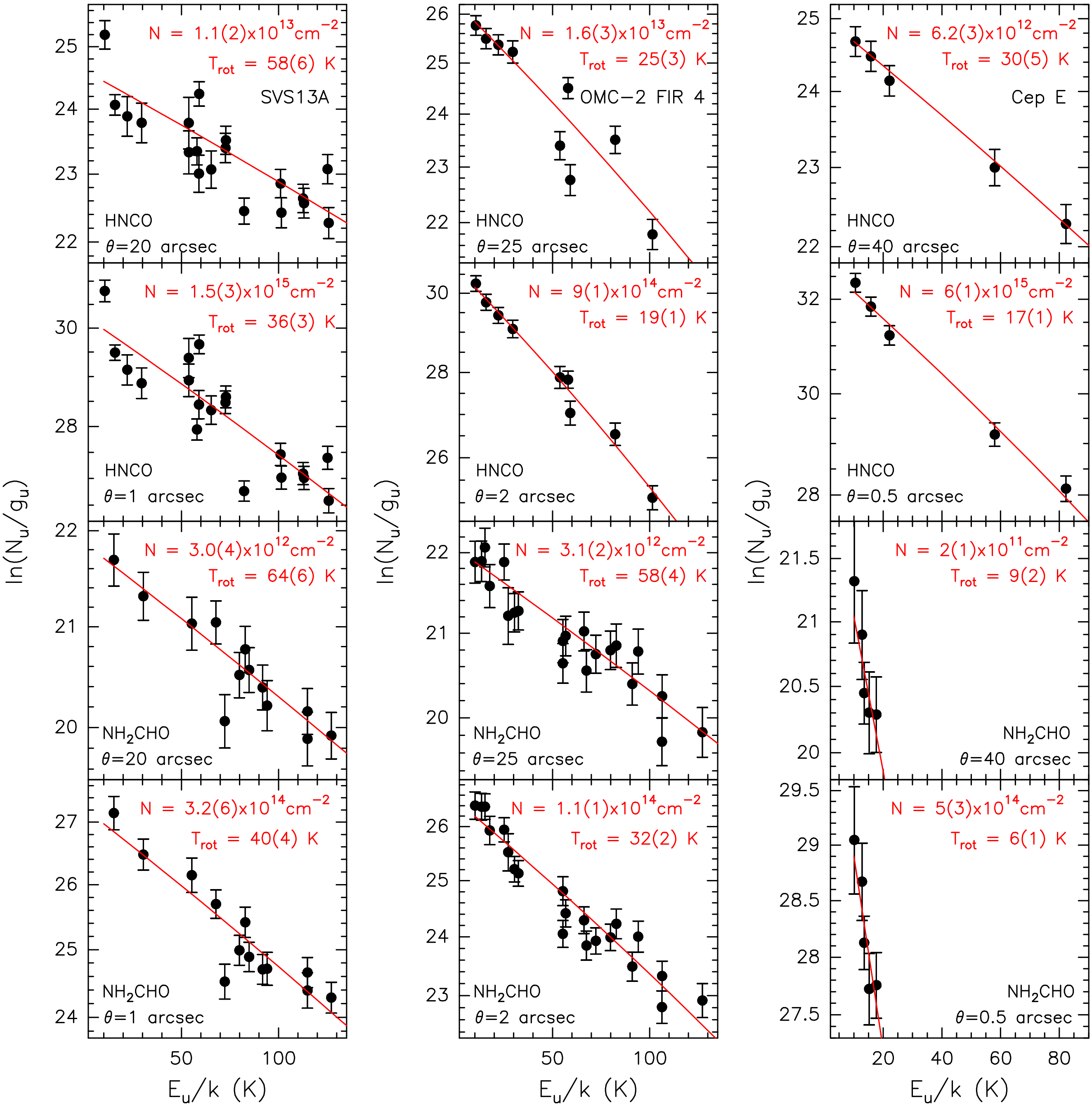

FIGURE D.5: Rotational diagrams for SVS13A (*left*), OMC-2 FIR 4 (*middle*), and Cep E (*right*). Data points are depicted in black. The red lines correspond to the best fit to the data points. .

Appendix E

Publications

The Astrophysical Journal, 791:29 (6pp), 2014 August 10 doi:10.1088/0004-637X/791/1/29

THE CENSUS OF COMPLEX ORGANIC MOLECULES IN THE SOLAR-TYPE PROTOSTAR IRAS16293-2422

Ali A. Jaber[1,2,3], C. Ceccarelli[1,2], C. Kahane[1,2], and E. Caux[4,5]
[1] Université Grenoble Alpes, IPAG, F-38000 Grenoble, France
[2] CNRS, IPAG, F-38000 Grenoble, France
[3] University of AL-Muthana, AL-Muthana, Iraq
[4] Université de Toulouse, UPS-OMP, IRAP, F-31400 Toulouse, France
[5] CNRS, IRAP, 9 Av. Colonel Roche, BP 44346, F-31028 Toulouse Cedex 4, France
Received 2014 January 14; accepted 2014 June 23; published 2014 July 23

ABSTRACT

Complex organic molecules (COMs) are considered to be crucial molecules, since they are connected with organic chemistry, at the basis of terrestrial life. More pragmatically, they are molecules which in principle are difficult to synthesize in harsh interstellar environments and, therefore, are a crucial test for astrochemical models. Current models assume that several COMs are synthesized on lukewarm grain surfaces ($\gtrsim$30–40 K) and released in the gas phase at dust temperatures of $\gtrsim$100 K. However, recent detections of COMs in $\lesssim$20 K gas demonstrate that we still need important pieces to complete the puzzle of COMs formation. Here, we present a complete census of the oxygen- and nitrogen-bearing COMs, previously detected in different Interstellar Medium (ISM) regions, toward the solar-type protostar IRAS16293-2422. The census was obtained from the millimeter–submillimeter unbiased spectral survey TIMASSS. Of the 29 COMs searched for, 6 were detected: methyl cyanide, ketene, acetaldehyde, formamide, dimethyl ether, and methyl formate. Multifrequency analysis of the last five COMs provides clear evidence that they are present in the cold ($\lesssim$30 K) envelope of IRAS16293-2422, with abundances of 0.03–2 × 10^{-10}. Our data do not allow us to support the hypothesis that the COMs abundance increases with increasing dust temperature in the cold envelope, as expected if COMs were predominately formed on lukewarm grain surfaces. Finally, when also considering other ISM sources, we find a strong correlation over five orders of magnitude between methyl formate and dimethyl ether, and methyl formate and formamide abundances, which may point to a link between these two couples of species in cold and warm gas.

Key words: ISM: abundances – ISM: molecules – stars: formation

Online-only material: color figure

1. INTRODUCTION

Complex organic molecules (COMs), namely, organic molecules with more than six atoms (Herbst & van Dishoeck 2009), have been known for more than four decades (Ball et al. 1971; Rubin et al. 1971; Solomon et al. 1971; Brown et al. 1975; Blake et al. 1987). Since some COMs have a prebiotic relevance, they immediately evoke great interest and several models were developed to explain why and how these molecules are formed in space. Those models were based on a two-step process: (1) "mother" (or first generation) species were created during the cold star formation process and frozen into the grain mantles; (2) "daughter" (or second generation) species were synthesized via gas phase reactions from mother species in the warm ($\gtrsim$200 K) regions where the grain mantles sublimate (Millar et al. 1991; Charnley et al. 1992; Caselli et al. 1993). This two-step paradigm enjoyed great success for about a decade, until new observations toward low mass hot corinos (Ceccarelli et al. 2000; Cazaux et al. 2003) and Galactic center molecular clouds (Requena-Torres et al. 2006) challenged the assumption that COMs are formed by gas phase reactions. At the same time, new laboratory experiments and theoretical computations revisited and ruled out some gas phase reactions which are crucial to those models (Horn et al. 2004; Geppert et al. 2007). Attention then moved toward the possibility that grains could act as catalyzers and that COMs could form on their surfaces at lukewarm ($\gtrsim$30–40 K) temperatures (Garrod et al. 2009). However, grain surface chemistry is even more difficult to understand than gas phase chemistry, both from theoretically and experimentally. Let us take the example of methanol, one of the simplest COMs. It is supposed to form on grain surfaces via successive hydrogenation of frozen CO (Tielens & Hagen 1982; Taquet et al. 2012). However, while laboratory experiments claim that this is the case (e.g., Watanabe & Kouchi 2002; Pirim et al. 2010), theoretical quantum chemistry computations show that the first and last steps toward CH_3OH formation have large (tens of kCal) energy barriers that are impossible to surmount in the cold ($\sim$10 K) cloud conditions (Woon 2002; Marenich & Boggs 2003; Goumans et al. 2008) where CO hydrogenation is supposed to occur. To add to the confusion, recent observations have revealed that some COMs (notably acetaldehyde, methyl formate, and dimethyl ether) are found in definitively cold ($\lesssim$20 K) regions (Öberg et al. 2010; Bacmann et al. 2012; Cernicharo et al. 2012), challenging the theory of the grain surface formation of COMs.

In this context, we examined the millimeter–submillimeter spectral survey performed toward the solar-type protostar IRAS16293-2422 (hereinafter IRAS16293; Caux et al. 2011) with the goal of extracting line emission from all oxygen- and nitrogen-bearing COMs already detected in the ISM, and to estimate their abundances across its envelope. Our emphasis here is on the abundances in the cold ($\lesssim$50 K) region of the envelope in order to provide astrochemical modellers with the first systematic survey of COMs in cold gas.

2. SOURCE DESCRIPTION

IRAS16293 is a solar-type Class 0 protostar in the ρ Ophiuchus star forming region, at a distance of 120 pc (Loinard et al. 2008). It has a bolometric luminosity of 22 $L_\odot$ (Crimier et al. 2010). Given its proximity and brightness, it has been the target of numerous studies that have reconstructed its physical and chemical structure. Briefly, IRAS16293 has a large envelope that extends up to ∼6000 AU and that surrounds two sources, named I16293-A and I16293-B in the literature, separated by $\sim5''$ (∼600 AU; Wootten 1989; Mundy et al. 1992). I16293-A sizes are $\sim1''$, whereas I16293-B is unresolved at a scale of $\sim0''.4$ (Zapata et al. 2013). I16293-A itself is composed of two sources, each one emitting a molecular outflow (Mizuno et al. 1990; Loinard et al. 2013). I16293-B possesses a very compact outflow (Loinard et al. 2013) and is surrounded by infalling gas (Pineda et al. 2012; Zapata et al. 2013). From a chemical point of view, IRAS16293 can be considered to be composed of an outer envelope, characterized by low molecular abundances, and a hot corino, where the abundance of many molecules increases by orders of magnitude (Ceccarelli et al. 2000; Schöier et al. 2002; Coutens et al. 2013). The transition between the two regions occurs at ∼100 K, the sublimation temperature of the icy grain mantles. In the hot corino, several abundant COMs have been detected (Cazaux et al. 2003).

3. THE DATA SET

3.1. Observations

We used the data from The IRAS16293 Millimeter And Submillimeter Spectral Survey (TIMASSS[6]; Caux et al. 2011). Briefly, the survey covers the 80–280 and 328–366 GHz frequency intervals and was conducted with the IRAM 30 m and James Clerk Maxwell telescope 15 m telescopes. The data are publicly available on the TIMASSS Web site. Details on the data reduction and calibration can be found in Caux et al. (2011). Here, we review the major features which are relevant for this work. The telescope beam depends on the frequency and varies between $9''$ and $30''$. The spectral resolution varies between 0.3 and 1.25 MHz, corresponding to velocity resolutions between 0.51 and 2.25 km s^{-1}. The achieved rms is between 4 and 17 mK. Note that it is given in a 1.5 km s^{-1} bin for observations taken with a velocity resolution of $\leqslant 1.5$ km s^{-1}, and in the resolution bin for larger velocity resolutions. The observations are centered on IRAS16293B at $\alpha(2000.0) = 16^h32^m22^s.6$, $\delta(2000.0) = -24^\circ28'33''$. Note that the A and B components are both inside the beam of observations at all frequencies.

3.2. Species Identification

We searched for the lines of all the oxygen- and nitrogen-bearing COMs already detected in the ISM (as reported in the CDMS database[7]); they are listed in Table 1. From this perspective, we used the list of identified lines in Caux et al. (2011) and double-checked for possible blending and misidentifications. This was obtained via the publicly available package CASSIS[8], and the CDMS (Müller et al. 2005) and JPL (Pickett et al. 1998) databases. References to the specific articles on the laboratory data of the detected species are Guarnieri & Huckauf (2003), Kleiner et al. (1996), Neustock et al. (1990), and Maeda et al. (2008). If the line identification is in doubt or if we detect the presence of important residual baseline effects, we do not consider the relevant line. Except for those few ($\leqslant$10%) cases, we used the line parameters (flux, linewidth, and rest velocity) from Caux et al. (2011). Using these tight criteria, we secured the detection of six COMs: ketene (H_2CCO: 13 lines), acetaldehyde (CH_3CHO: 130 lines), formamide (NH_2CHO: 17 lines), dimethyl ether (CH_3OCH_3: 65 lines), methyl formate ($HCOOCH_3$: 121 lines), and methyl cyanide (CH_3CN: 38 lines). For comparison, Cazaux et al. (2003) detected 5 CH_3CHO lines, 7 CH_3OCH_3 lines, and 20 CH_3CHO lines. We do not confirm the Cazaux et al. (2003) detection of acetic acid (CH_3COOH) and formic acid (HCOOH), where these authors reported the possible detection of 1 and 2 lines, respectively, none of which are in the TIMASSS observed frequency range.

4. ANALYSIS AND RESULTS

4.1. Model Description

Our goal is to estimate the abundance of the detected COMs across the envelope of IRAS16293, with particular emphasis on the cold envelope (see the Introduction). For this purpose, we used the spectral line energy distribution (SLED) of the detected COMs, and the GRenoble Analysis of Protostellar Envelope Spectra (GRAPES) package, based on the code described in Ceccarelli et al. (1996, 2003). Briefly, (1) GRAPES computes the species SLED from a spherical infalling envelope with a given structure; (2) it solves locally the level population statistical equilibrium equations in the beta escape formalism, consistently computing the line optical depth by integrating it over the solid angle at each point of the envelope; and (3) the predicted line flux is then integrated over the whole envelope after convolution with the telescope beam. The abundance X of the considered species is assumed to vary as a function of the radius with power law in the cold part of the envelope and to jump to a new abundance in the warm part. The transition between the two regions is set by the dust temperature, to simulate the sublimation of the ice mantles, and occurs at T_{jump}. It holds:

$$\begin{aligned} X(r) &= X_{\mathrm{out}}\left(\frac{r}{R_{\mathrm{max}}}\right)^{\alpha} T \leqslant T_{\mathrm{jump}} \\ X(r) &= X_{\mathrm{in}} > T_{\mathrm{jump}}. \end{aligned} \qquad (1)$$

GRAPES allows us to run large grids of models varying the four parameters (X_{in}, X_{out}, α, and T_{jump}) and to find the best fit to the observed fluxes.

This code has disadvantages and advantages compared with other codes. The first, obvious disadvantage is that the spherical assumption only holds for the large-scale ($\gtrsim 10''$: see Crimier et al. 2010) envelope of IRAS16293. At small scales, the presence of the binary system (Section 2) causes the spherical symmetry assumption to be wrong. Consequently, the GRAPES code is, by definition, unable to correctly estimate the emission from the two sources I16293-A and I16293-B separately. The derived inner envelope abundance is therefore likely a rough indication of the real abundance of the species toward I16293-A and I16293-B. The other disadvantage of GRAPES is that it relies on the analysis of the SLED and not on the line profiles. Since the majority of the TIMASSS spectra have a relatively poor spectral resolution ($\gtrsim$1 km s^{-1}), this is appropriate in this case. The great advantage of GRAPES, and the reason why we used it here, is that it is very fast, and so a large multi-parameter space can be explored.

In this work, we used the physical structure of the envelope of IRAS16293 as derived by Crimier et al. (2010), which is based on single-dish and interferometric continuum observations. Collisional coefficients are only available for methyl cyanide,

---

[6] http://www-laog.obs.ujf-grenoble.fr/heberges/timasss/

[7] http://www.astro.uni-koeln.de/cdms/molecules

[8] http://cassis.irap.omp.eu

Table 1
Results of the Analysis

Species	Formula	$X_{\rm in}$ (10^{-8})	$X_{\rm out}$ (10^{-10})	$T_{\rm jump}$ (K)	DF	χ^2	Radius (AU)	Size ($''$)
				Detected COMs				
Ketene	H_2CCO	0.01 ± 0.005	0.3 ± 0.08	20^{+20}_{-5}	10	0.63	1800	31
Acetaldehyde	CH_3CHO	0.3 ± 0.2	1 ± 0.2	70 ± 5	127	0.79	127	2
Formamide	NH_2CHO	0.06 ± 0.02	0.03 ± 0.02	80 ± 5	14	0.69	100	2
Dimethyl ether	CH_3OCH_3	4 ± 1	2 ± 1	50 ± 10	62	0.72	240	4
Methyl formate	$HCOOCH_3$	0.9 ± 0.2	0.3 ± 0.1	50 ± 5	118	0.78	240	4
				Undetected COMs				
Ethylene oxide	c-C_2H_4O	$\lesssim 0.1$	$\lesssim 3$					
Vinyl alcohol	H_2CCHOH	$\lesssim 0.04$	$\lesssim 1$					
Ethanol	C_2H_5OH	$\lesssim 0.5$	$\lesssim 8$					
Formic acid	$HCOOH$	$\lesssim 0.03$	$\lesssim 0.8$					
Propynal	HC_2CHO	$\lesssim 0.02$	$\lesssim 0.5$					
Cyclopropenone	c-H_2C_3O	$\lesssim 0.004$	$\lesssim 0.1$					
Acrolein	C_2H_3CHO	$\lesssim 0.02$	$\lesssim 0.6$					
Acetone	CH_3COCH_3	$\lesssim 0.07$	$\lesssim 2$					
Propanal	CH_3CH_2CHO	$\lesssim 0.1$	$\lesssim 2$					
Glycolaldehyde	$CH_2(OH)CHO$	$\lesssim 0.1$	$\lesssim 3$					
Ethyl methyl ether	$C_2H_5OCH_3$	$\lesssim 0.5$	$\lesssim 9$					
Ethyleneglycol	$(CH_2OH)_2$	$\lesssim 0.2$	$\lesssim 5$					
Ethyl formate	C_2H_5OCHO	$\lesssim 0.2$	$\lesssim 5$					
Methylamine	CH_3NH_2	$\lesssim 0.1$	$\lesssim 3$					
Methylisocyanide	CH_3NC	$\lesssim 0.002$	$\lesssim 0.07$					
Etheneimine	H_2CCNH	$\lesssim 0.1$	$\lesssim 2$					
Cyanoacetylene+	HC_3NH^+	$\lesssim 0.01$	$\lesssim 0.2$					
Vinyl cyanide	C_2H_3CN	$\lesssim 0.01$	$\lesssim 0.2$					
Ethyl cyanide	C_2H_5CN	$\lesssim 0.02$	$\lesssim 0.7$					
Aminoacetonitrile	H_2NCH_2CN	$\lesssim 0.03$	$\lesssim 0.7$					
Cyanopropyne	CH_3C_3N	$\lesssim 0.002$	$\lesssim 0.07$					
n-Propyl cyanide	n-C_3H_7CN	$\lesssim 0.05$	$\lesssim 0.8$					
Cyanopentadiyne	CH_3C_5N	$\lesssim 0.01$	$\lesssim 0.3$					

Notes. Note that the first two columns report the species name and formula. The third, fourth, and fifth columns report the values of the inner and outer abundances $X_{\rm in}$ and $X_{\rm out}$ (with respect to H_2), and $T_{\rm jump}$. The sixth and seventh columns report the degrees of freedom and the minimum reduced χ^2. The last two columns report the radius and the sizes (diameter) at which the abundance jump occurs. The error bars are at a 2σ confidence level. The top half of the table lists the detected species, while the bottom half of the table lists the upper limit on the abundances of undetected COMs (see the text).

and not for the other five detected COMs. Since methyl cyanide is a top symmetric molecule, it represents a "particular case" with respect to the other detected COMs, so that in order to have a homogeneous data set, we decided here to analyze only the latter molecules and assume LTE for their level populations. The analysis of the CH_3CN molecule will be the focus of a future article. Since the density of the IRAS16293 envelope is relatively high (e.g., 5×10^6 cm^{-3} at a radius of 870 AU, equivalent to 15$''$ in diameter), we expect that the abundances derived in the LTE approximation are only moderately underestimated.

4.2. Results

For each of the five analyzed COMs, we run a large grid of models using the following strategy. We explored the $X_{\rm in}$–$X_{\rm out}$ parameter space (in general, we obtained grids of more than 20×20) for α equal to -1, 0, and +1, and varied $T_{\rm jump}$ from 10 to 120 K by steps of 10 K. Note that we first started with a 3 or 4 orders-of-magnitude range in $X_{\rm in}$ and $X_{\rm out}$, respectively, to find a first approximate solution and then we fine-tuned the grid around that solution. In total, therefore, we run more than 3×10^4 models for each species. The results of the best-fit procedure are reported in Table 1. Figure 1 shows the example of acetaldehyde. Note that the lines are predicted to be optically thin by the best-fit models of all five molecules.

First, we did not find a significant difference in the χ^2 best-fit value if α is -1, 0, or +1 in any of the five COMs, so that Table 1 reports the values obtained with $\alpha = 0$ only. Second, the $T_{\rm jump}$ is different in the five COMs: it is ~20 K for ketene, ~70–80 K for acetaldehyde and formamide, and ~50 K for dimethyl ether and methyl formate. Third, the abundance in the outer envelope ranges from $\sim 3 \times 10^{-12}$ to $\sim 2 \times 10^{-10}$: acetaldehyde and dimethyl ether have the largest values, formamide the lowest, and ketene and methyl formate intermediate values. Fourth, the abundance jumps by about a factor 100 in all COMs except for ketene, which remains practically constant (when the errors are considered). Note that we find warm envelope abundances of acetaldehyde, dimethyl ether, and methyl formate about 10 times smaller than those quoted by Cazaux et al. (2003). The difference mostly derives from a combination of different $T_{\rm jump}$ (assumed to be 100 K in Cazaux et al. 2003), which implies different emitting sizes and a different H_2 column density. As was also emphasized by Cazaux et al. (2003), their hot corino sizes and H_2 column density were best guesses and, consequently, uncertain, whereas in the present work these values are self-consistently estimated from the molecular lines.

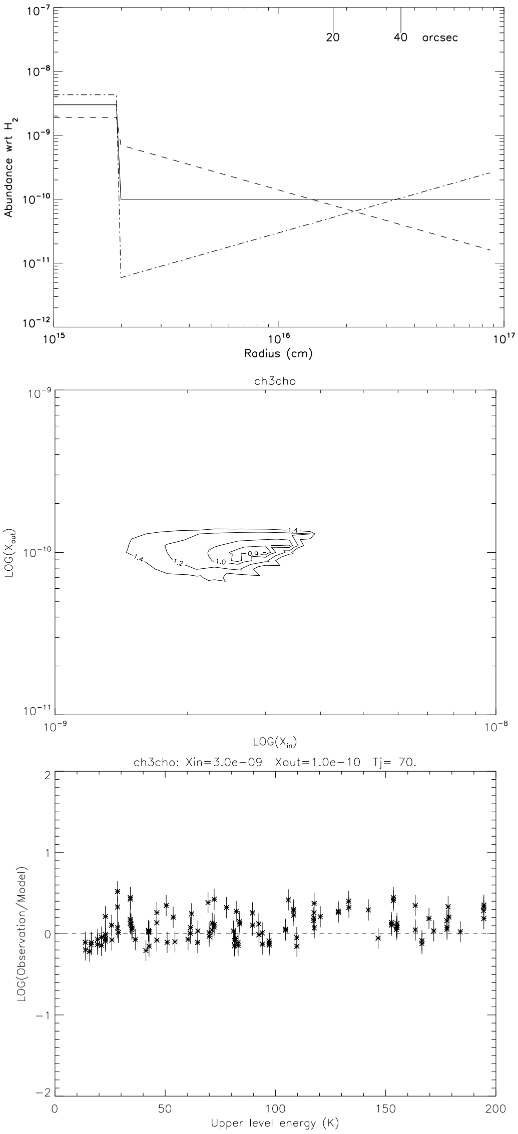

Figure 1. Example of the acetaldehyde analysis. Upper panel: abundance profiles of the best fit obtained considering the cold envelope abundance profile following a power-law dependence with a radius (Equation (1)) of α equal to -1 (dashed), 0 (solid), and 1 (dotted-dashed), respectively. Middle panel: χ^2 contour plot assuming the best-fit $T_{\rm jump} = 70$ K and $\alpha = 0$. Bottom panel: ratio of the observed over-predicted line flux as a function of the upper level energy of the transition for the best-fit solution (Table 1).

Finally, for the undetected species, we derived upper limits to the abundance in the outer (assuming N(H$_2$) $= 8 \times 10^{22}$ cm^{-2}, diameter $= 30''$, $T = 20$ K) and inner (assuming N(H$_2$) $= 3 \times 10^{23}$ cm^{-2}, diameter $= 3''$, $T = 60$ K) envelope listed in Table 1.

5. DISCUSSION

The analysis of outer and inner abundances of the five detected COMs leads to three major considerations and results.

1. *COMs in the Cold Envelope.* The first important result of this analysis is the presence of COMs in the cold part of the envelope, with an approximately constant abundance. This is the first time that we have unambiguous evidence that the cold outer envelope of (low mass) protostars can also host COMs. Bacmann et al. (2012) reported the detection of acetaldehyde, dimethyl ether, and methyl formate with abundances around 10^{-11} (with an uncertainty of about one order of magnitude) toward a cold ($\lesssim$10 K) pre-stellar core. Öberg et al. (2010) and Cernicharo et al. (2012) reported the detection of the same molecules in B1-b, a low mass protostar where the temperature of the emitting gas is estimated to be 12–15 K (but no specific analysis to separate possible emission from warm gas has been carried out in this case) with similar abundances. In the cold envelope of IRAS16293, these COMs seem to be slightly more abundant, with abundances around 10^{-10}, possibly because the gas is slightly warmer. If the dust surface chemistry dominated the formation of COMs in the outer envelope, then the COM abundance would increase with increasing dust temperature, namely, with decreasing radius in the cold envelope. However, our analysis does not show a definitively better χ^2 for the solution corresponding to $\alpha = -1$, so that it cannot support this hypothesis. These new measurements add evidence that COMs, at least the ones studied here, may also be formed in cold conditions in addition to warm grain surfaces as predicted by current models (see the Introduction).
2. *Comparison with Other Objects.* Additional information on the formation (and destruction) routes of the detected COMs can be gained by comparing the COM abundances in galactic objects with different conditions (temperature, density, and history) and solar system comets. Here, we consider the abundances normalized to that of methyl formate, a molecule which has been detected in all of the objects that we want to compare. Figure 2 graphically shows this comparison. Ketene seems to be the most sensitive species for distinguishing two groups of objects: “cold” objects, formed by the cold and Galactic center clouds and the outer envelope of IRAS16293; and “warm” objects, constituted by the IRAS16293 hot corino (the only hot corino where the five COMs of this study have been detected so far) and the massive hot cores. In the first group, ketene has an abundance larger than ~0.1 with respect to methyl formate. In the second group, the relative abundance is lower than ~0.1. Finally, comets are definitively different from hot cores, with which they are often compared in the literature (see also the discussion in Caselli & Ceccarelli 2012).
3. *Correlations versus Methyl Formate.* Figure 3 shows the abundance of dimethyl ether, formamide, acetaldehyde, and ketene as a function of the abundance of methyl formate in different ISM sources. The linear correlation between the methyl formate and dimethyl ether is striking (with a Pearson correlation coefficient equal to 0.95 and power-law index equal to 1.0). It covers almost five orders of magnitude, so that it persists even when considering the dispersion of the measurements and the uncertainty linked to the determination of the absolute abundances mentioned

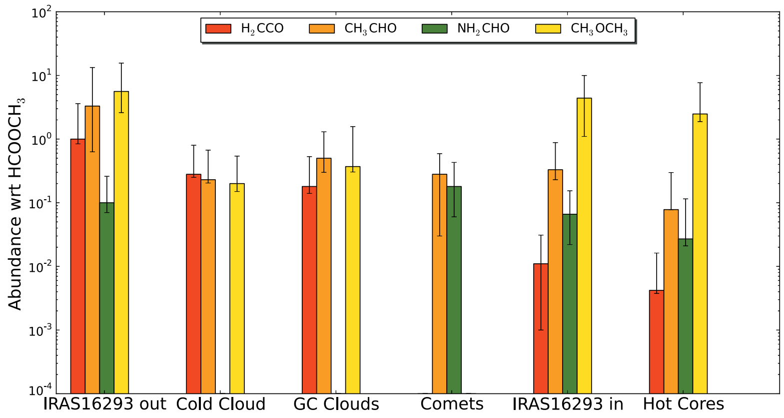

Figure 2. Abundances of the five COMs analyzed in this work, normalized to the methyl formate abundance, in different objects: inner and outer envelope of IRAS16293 (this work), cold clouds (Bacmann et al. 2012; Cernicharo et al. 2012), Galactic center (GC) clouds (Requena-Torres et al. 2006, 2008), hot cores (Gibb et al. 2000; Ikeda et al. 2001; Bisschop et al. 2007: note that we did not include SgrB2 in this sample), and comets (Mumma & Charnley 2011). Error bars represent the dispersion in each group of objects, except IRAS16293, for which error bars reflect the errors in the abundance determination (Table 1).

(A color version of this figure is available in the online journal.)

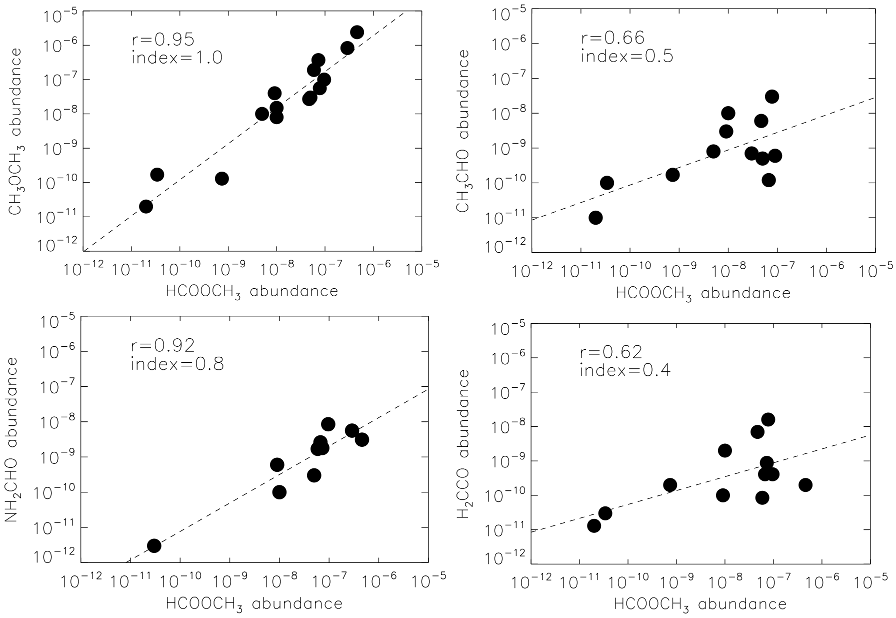

Figure 3. Abundance of dimethyl ether (top left), formamide (bottom left), acetaldehyde (top right), and ketene (bottom right) as a function of the abundance of methyl formate in different ISM sources. The correlation coefficient *r* and the power-law index are reported for each species.

above. This linear correlation, previously observed over a smaller range (e.g., Brouillet et al. 2013), gives us an important and remarkable message: the precursor of methyl formate and dimethyl ether is probably either the same (Brouillet et al. 2013) or one of the two is the precursor of the other, a hypothesis that has not been invoked previously in the literature. We cannot rule out other explanations, but they seem less likely at this stage. The bottom line is that such a link between these two species must be the same in both cold and warm gas. This does not favor a formation mechanism of these two COMs on the grain surfaces since, according to the existing models, the mechanism does not work at low temperatures. Current chemical networks[9] do not report reactions linking the two species. Also, the recent article by Vasyunin & Herbst (2013), which proposes new reactions to explain the Bacmann et al. (2012) and Cernicharo et al. (2012) observations, does not suggest

---

[9] For example, KIDA at http://kida.obs.u-bordeaux1.fr and UMIST at http://www.udfa.net.

a link between methyl formate and dimethyl ether. We suggest here that those networks are missing this important piece.

Similar analyses and conclusions (a Pearson correlation coefficient equal to 0.92 and a power-law index equal to 0.8) apply to the methyl formate and formamide. On the contrary, the correlation between methyl formate and acetaldehyde or ketene is poorer (a Pearson correlation coefficient equal to 0.66 and 0.62, and a power-law index equal to 0.5 and 0.4, respectively).

6. CONCLUSIONS

We searched for all oxygen- and nitrogen-bearing COMs observed in the ISM toward the envelope of IRAS16293. We detected six COMs: methyl cyanide, ketene, acetaldehyde, formamide, dimethyl ether, and methyl formate. We report the analysis of the last five species. A specific analysis of methyl cyanide emission will be presented in a subsequent paper. For each species, several lines covering a large upper-level energy range (up to 150 K) are detected. This allows us to disentangle the emission originating in the cold and warm envelope, respectively, and where the transition between the two occurs. The main results of this study can be summarized in three points.

1. The five analyzed COMs are all present in the cold envelope of IRAS16293. Acetaldehyde and dimethyl ether have the largest abundances, $\sim 10^{-10}$, slightly larger than the values found in other cold objects (Bacmann et al. 2012; Cernicharo et al. 2012). These new measurements add support to the idea that a relatively efficient formation mechanism for these COMs must exist in the cold gas phase.
2. When considering the abundance of the five analyzed COMs, the ketene abundance relative to methyl formate is different in cold and hot objects. Besides, comets are different from hot cores.
3. There is a remarkable correlation between the abundance of methyl formate and those of dimethyl ether and formamide. The correlation spans over five orders of magnitude. This may suggest that both dimethyl ether and formamide have a progenitor in common with methyl formate, and that the mechanism of their formation is gas-phase reactions. We suggest that the current chemical networks still miss important pieces.

We thank the anonymous referee for useful comments that helped to improve the article. This work has been supported by l' Agence Nationale pour la Recherche (ANR), France (project FORCOMS, contracts ANR-08-BLAN-0225). We acknowledge the financial support from the university of Al-Muthana and ministry of higher education and scientific research in Iraq.

REFERENCES

Bacmann, A., Taquet, V., Faure, A., Kahane, C., & Ceccarelli, C. 2012, A&A, 541, L12
Ball, J. A., Gottlieb, C. A., Lilley, A. E., & Radford, H. E. 1971, IAUC, 2350, 1
Bisschop, S. E., Jorgensen, J. K., van Dishoeck, E. F., & de Wachter, E. B. M. 2007, A&A, 465, 913
Blake, G. A., Sutton, E. C., Masson, C. R., & Phillips, T. G. 1987, ApJ, 315, 621
Brouillet, N., Despois, D., Baudry, A., et al. 2013, A&A, 550, A46
Brown, R. D., Crofts, J. G., Godfrey, P. D., et al. 1975, ApJL, 197, L29
Caselli, P., & Ceccarelli, C. 2012, A&ARv, 20, 56
Caselli, P., Hasegawa, T. I., & Herbst, E. 1993, ApJ, 408, 548
Caux, E., Kahane, C., Castets, A., et al. 2011, A&A, 532, A23
Cazaux, S., Tielens, A. G. G. M., Ceccarelli, C., et al. 2003, ApJL, 593, L51
Ceccarelli, C., Castets, A., Caux, E., et al. 2000, A&A, 355, 1129
Ceccarelli, C., Hollenbach, D. J., & Tielens, A. G. G. M. 1996, ApJ, 471, 400
Ceccarelli, C., Maret, S., Tielens, A. G. G. M., Castets, A., & Caux, E. 2003, A&A, 410, 587
Cernicharo, J., Marcelino, N., Roueff, E., et al. 2012, ApJL, 759, L43
Charnley, S. B., Tielens, A. G. G. M., & Millar, T. J. 1992, ApJL, 399, L71
Coutens, A., Vastel, C., Cabrit, S., et al. 2013, A&A, 560, A39
Crimier, N., Ceccarelli, C., Maret, S., et al. 2010, A&A, 519, A65
Garrod, R. T., Vasyunin, A. I., Semenov, D. A., Wiebe, D. S., & Henning, T. 2009, ApJL, 700, L43
Geppert, W. D., Vigren, E., Hamberg, M., et al. 2007, in European Planetary Science Congress 2007, Dissociative Recombination—A Key Process in Ionospheres of Giant Planets and Their Satellites, 613
Gibb, E., Nummelin, A., Irvine, W. M., Whittet, D. C. B., & Bergman, P. 2000, ApJ, 545, 309
Goumans, T. P. M., Catlow, C. R. A., & Brown, W. A. 2008, JChPh, 128, 13
Guarnieri, A., & Huckauf, A. 2003, Naturforsch, 58, 275
Herbst, E., & van Dishoeck, E. F. 2009, ARA&A, 47, 427
Horn, A., Møllendal, H., Sekiguchi, O., et al. 2004, ApJ, 611, 605
Ikeda, M., Ohishi, M., Nummelin, A., et al. 2001, ApJ, 560, 792
Kleiner, I., Lovas, F. J., & Godefroid, M. 1996, JPCRD, 25, 1113
Loinard, L., Torres, R. M., Mioduszewski, A. J., & Rodríguez, L. F. 2008, ApJL, 675, L29
Loinard, L., Zapata, L. A., Rodríguez, L. F., et al. 2013, MNRAS, 430, L10
Maeda, A., De Lucia, F. C., & Herbst, E. 2008, JMoSp, 251, 293
Marenich, A., & Boggs, J. 2003, JChPh, 107, 2343
Millar, T. J., Herbst, E., & Charnley, S. B. 1991, ApJ, 369, 147
Mizuno, A., Fukui, Y., Iwata, T., Nozawa, S., & Takano, T. 1990, ApJ, 356, 184
Müller, H. S. P., Schlöder, F., Stutzki, J., & Winnewisser, G. 2005, JMoSt, 742, 215
Mumma, M. J., & Charnley, S. B. 2011, ARA&A, 49, 471
Mundy, L. G., Wootten, A., Wilking, B. A., Blake, G. A., & Sargent, A. I. 1992, ApJ, 385, 306
Neustock, W., Guarnieri, A., & G, D. 1990, Naturforsch, 45, 702
Öberg, K. I., Bottinelli, S., Jørgensen, J. K., & van Dishoeck, E. F. 2010, ApJ, 716, 825
Pickett, H. M., Poynter, R. L., Cohen, E. A., et al. 1998, JQSRT, 60, 883
Pineda, J. E., Maury, A. J., Fuller, G. A., et al. 2012, A&A, 544, L7
Pirim, C., Krim, L., & Laffon, C. 2010, JChPh, 114, 3320
Requena-Torres, M. A., Martin-Pintado, J., Martin, S., & Morris, M. R. 2008, ApJ, 672, 352
Requena-Torres, M. A., Martin-Pintado, J., Rodriguez-Franco, A., et al. 2006, A&A, 455, 971
Rubin, R. H., Swenson, G. W., Jr., Benson, R. C., Tigelaar, H. L., & Flygare, W. H. 1971, ApJL, 169, L39
Schöier, F. L., Jørgensen, J. K., van Dishoeck, E. F., & Blake, G. A. 2002, A&A, 390, 1001
Solomon, P. M., Jefferts, K. B., Penzias, A. A., & Wilson, R. W. 1971, ApJL, 168, L107
Taquet, V., Ceccarelli, C., & Kahane, C. 2012, A&A, 538, A42
Tielens, A. G. G. M., & Hagen, W. 1982, A&A, 114, 245
Vasyunin, A. I., & Herbst, E. 2013, ApJ, 769, 34
Watanabe, N., & Kouchi, A. 2002, ApJL, 571, L173
Woon, D. E. 2002, ApJL, 571, L177
Wootten, A. 1989, ApJ, 337, 858
Zapata, L. A., Loinard, L., Rodríguez, L. F., et al. 2013, ApJL, 764, L14

Monthly Notices
of the
ROYAL ASTRONOMICAL SOCIETY
MNRAS **449,** 2438–2458 (2015) doi:10.1093/mnras/stv377

Shedding light on the formation of the pre-biotic molecule formamide with ASAI

A. López-Sepulcre,[1,2,3★] Ali A. Jaber,[1,2,4] E. Mendoza,[5] B. Lefloch,[1,2]
C. Ceccarelli,[1,2] C. Vastel,[6,7] R. Bachiller,[8] J. Cernicharo,[9] C. Codella,[10]
C. Kahane,[1,2] M. Kama[11] and M. Tafalla[8]

[1] *Univ. Grenoble Alpes, IPAG, F-38000 Grenoble, France*
[2] *CNRS, IPAG, F-38000 Grenoble, France*
[3] *Department of Physics, The University of Tokyo, Bunkyo-ku, Tokyo 113-0033, Japan*
[4] *University of AL-Muthana, AL-Muthana, Iraq*
[5] *Observatório do Valongo, Universidade Federal do Rio de Janeiro - UFRJ, Rio de Janeiro, Brazil*
[6] *Université de Toulouse, UPS-OMP, IRAP, Toulouse, France*
[7] *CNRS, IRAP, 9 Av. colonel Roche, BP 44346, F-31028 Toulouse Cedex 4, France*
[8] *IGN Observatorio Astronómico Nacional (IGN), Calle Alfonso XII 3, E-28014 Madrid, Spain*
[9] *LAM, CAB-CSIC/INTA, Ctra de Torrejón a Ajalvir km 4, E-28850 Torrejón de Ardoz, Madrid, Spain*
[10] *INAF, Osservatorio Astrofisico di Arcetri, Largo E. Fermi 5, I-50125, Firenze, Italy*
[11] *Leiden Observatory, PO Box 9513, NL-2300 RA, Leiden, the Netherlands*

Accepted 2015 February 19. Received 2015 February 6; in original form 2014 December 12

ABSTRACT

Formamide (NH_2CHO) has been proposed as a pre-biotic precursor with a key role in the emergence of life on Earth. While this molecule has been observed in space, most of its detections correspond to high-mass star-forming regions. Motivated by this lack of investigation in the low-mass regime, we searched for formamide, as well as isocyanic acid (HNCO), in 10 low- and intermediate-mass pre-stellar and protostellar objects. The present work is part of the IRAM Large Programme ASAI (Astrochemical Surveys At IRAM), which makes use of unbiased broad-band spectral surveys at millimetre wavelengths. We detected HNCO in all the sources and NH_2CHO in five of them. We derived their abundances and analysed them together with those reported in the literature for high-mass sources. For those sources with formamide detection, we found a tight and almost linear correlation between HNCO and NH_2CHO abundances, with their ratio being roughly constant – between 3 and 10 – across 6 orders of magnitude in luminosity. This suggests the two species are chemically related. The sources without formamide detection, which are also the coldest and devoid of hot corinos, fall well off the correlation, displaying a much larger amount of HNCO relative to NH_2CHO. Our results suggest that, while HNCO can be formed in the gas-phase during the cold stages of star formation, NH_2CHO forms most efficiently on the mantles of dust grains at these temperatures, where it remains frozen until the temperature rises enough to sublimate the icy grain mantles. We propose hydrogenation of HNCO as a likely formation route leading to NH_2CHO.

Key words: astrochemistry – methods: observational – stars: formation – ISM: abundances – ISM: molecules.

1 INTRODUCTION

One of the major questions regarding the origin of life on Earth is whether the original chemical mechanism that led from simple molecules to life was connected to metabolism or to genetics, both intimately linked in living beings. Formamide (NH_2CHO) contains the four most important elements for biological systems: C, H, O, and N, and it has recently been proposed as a pre-biotic precursor of both metabolic and genetic material, suggesting a common chemical origin for the two mechanisms (Saladino et al. 2012).

★ E-mail: ana@taurus.phys.s.u-tokyo.ac.jp

Published by Oxford University Press on behalf of the Royal Astronomical Society

Table 1. Source sample and their properties.

Source	R.A.(J2000)	Dec.(J2000)	$V_{\rm lsr}$ (km s^{-1})	d (pc)	M (M$_\odot$)	$L_{\rm bol}$ (L$_\odot$)	Type*	References
ASAI								
L1544	05:04:17.21	+25:10:42.8	+7.3	140	2.7	1.0	PSC	1,2,3
TMC1	04:41:41.90	+25:41:27.1	+6.0	140	21	–	PSC	1,4
B1	03:33:20.80	+31:07:34.0	+6.5	200	1.9	1.9	Class 0	5,6
L1527	04:39:53.89	+26:03:11.0	+5.9	140	0.9	1.9	Class 0, WCCC	1,7,8
L1157-mm	20:39:06.30	+68:02:15.8	+2.6	325	1.5	4.7	Class 0	7,8
IRAS 4A	03:29:10.42	+31:13:32.2	+7.2	235	5.6	9.1	Class 0, HC	7,8
SVS13A	03:29:03.73	+31:16:03.8	+6.0	235	0.34	21	Class 0/1	9,10
OMC-2 FIR 4	05:35:26.97	−05:09:54.5	+11.4	420	30	100	IM proto-cluster	11,12
Cep E	23:03:12.80	+61:42:26.0	− 10.9	730	35	100	IM protostar	13
TIMASSS								
I16293	16:32:22.6	−24:28:33	+4.0	120	3	22	Class 0, HC	14,15

Notes. *PSC: pre-stellar core; HC: hot corino; WCCC: warm carbon-chain chemistry; IM: intermediate-mass.
References: [1]Elias (1978), [2]Evans et al. (2001), [3]Shirley et al. (2000), [4]Tóth et al. (2004), [5]Hirano et al. (1999), [6]Marcelino et al. (2005), [7]Kristensen et al. (2012), [8]Karska et al. (2013), [9]Hirota et al. (2008), [10]Chen, Launhardt & Henning (2009), [11]Crimier et al. (2009), [12]Furlan et al. (2014), [13]Crimier et al. (2010a), [14]Loinard et al. (2008), [15]Correia, Griffin & Saraceno (2004).

Formamide was detected for the first time in space by Rubin et al. (1971) towards Sgr B2 and later in Orion KL. However, dedicated studies of NH_2CHO in molecular clouds have started only very recently, as its potential as a key prebiotic molecule has become more evident. These studies present observations of formamide in a number of massive hot molecular cores (Bisschop et al. 2007; Adande, Woolf & Ziurys 2011), the low-mass protostellar object IRAS 16293−2422 (Kahane et al. 2013), and the outflow shock regions L1157-B1 and B2 (Yamaguchi et al. 2012; Mendoza et al. 2014). Its detection in comet Hale-Bopp has also been reported (Bockelée-Morvan et al. 2000). Formamide is therefore present in a variety of star-forming environments, as well as on a comet of the Solar system. Whether this implies an exogenous delivery on to a young Earth in the past is a suggestive possibility that needs more evidence to be claimed.

Establishing the formation route(s) of formamide in space remains a challenge. Different chemical pathways have been proposed, both in the gas-phase (e.g. Redondo, Barrientos & Largo 2014) and on grain surfaces (e.g. Raunier et al. 2004; Jones et al. 2011). The present work represents an effort to try to understand the dominant mechanisms that lead to the formation of formamide in the interstellar medium. In particular, it seeks to investigate the possible chemical connection between NH_2CHO and HNCO, which was proposed by Mendoza et al. (2014). To this aim, we have performed a homogeneous search of NH_2CHO and HNCO in a representative sample of 10 star-forming regions (SFRs) of low- to intermediate-mass type, since most of the formamide detections so far reported concentrate on high-mass SFRs. This is the first systematic study conducted within the context of the IRAM Large Program ASAI (Astrochemical Surveys At IRAM; P.I.s: B. Lefloch, R. Bachiller), which is dedicated to millimetre astrochemical surveys of low-mass SFRs with the IRAM 30-m telescope.

The source sample and the observations are described in Sections 2 and 3, respectively. Section 4 presents the spectra and describes the analysis carried out to obtain the abundances of NH_2CHO and HNCO. Section 5 compares the derived abundances with those found in the literature for other SFRs, and discusses the formation mechanisms that are favoured by our results. Our conclusions are summarized in Section 6.

2 SOURCE SAMPLE

Our source sample consists of 10 well-known pre-stellar and protostellar objects representing different masses and evolutionary states, thus providing a complete view of the various types of objects encountered along the first phases of star formation. Their basic properties are listed in Table 1. All of them belong to the ASAI source sample except one: the Class 0 protobinary IRAS 16293−2422 (hereafter I16293), whose millimetre spectral survey, TIMASSS (The IRAS16293−2422 Millimeter And Submillimeter Spectral Survey), was published by Caux et al. (2011a). A dedicated study of Complex Organic Molecules (COMs) in this source, including NH_2CHO, was recently carried out by Jaber et al. (2014).

3 OBSERVATIONS AND DATA REDUCTION

The data presented in this work were acquired with the IRAM 30-m telescope near Pico Veleta (Spain) and consist of unbiased spectral surveys at millimetre wavelengths. These are part of the Large Programme ASAI, whose observations and data reduction procedures will be presented in detail in an article by Lefloch & Bachiller (in preparation). Briefly, we gathered the spectral data in several observing runs between 2011 and 2014 using the EMIR receivers at 3 mm (80–116 GHz), 2 mm (129–173 GHz), and 1.3 mm (200–276 GHz). The main beam sizes for each molecular line analysed are listed in Tables B1 and B2. The three bands were covered for most of the sources. For Cep E, additional observations were carried out at 0.9-mm (E330 receiver), while just a few frequencies were covered at 2 mm. The Fourier Transform Spectrometer (FTS) units were connected to the receivers, providing a spectral resolution of 195 kHz, except in the case of L1544, for which we used the FTS50 spectrometer, with a resolution of 50 kHz, to resolve the narrow lines ($\Delta V \sim 0.5$ km s^{-1}) that characterize this region. The observations were performed in wobbler switching mode with a throw of 180 arcsec.

The data were reduced with the package CLASS90 of the GILDAS software collection.[1] Through comparison of line intensities among

---

[1] http://www.iram.fr/IRAMFR/GILDAS/

different scans and between horizontal and vertical polarizations, the calibration uncertainties are estimated to be lower than 10 per cent at 3 mm and 20 per cent in the higher frequency bands. After subtraction of the continuum emission via first-order polynomial fitting, a final spectrum was obtained for each source and frequency band after stitching the spectra from each scan and frequency setting. The intensity was converted from antenna temperature ($T^{*}_{\rm ant}$) to main beam temperature ($T_{\rm mb}$) using the beam efficiencies provided at the IRAM web site.[2] In order to improve the signal-to-noise ratio (S/N), the 2- and 1-mm ASAI data were smoothed to 0.5 km s^{-1}, except in the case of L1544, for which we kept the original spectral resolution.

For I16293, we used the TIMASSS spectral data obtained with the IRAM 30-m telescope at 1, 2, and 3 mm. A detailed description of the observations and an overview of the data set are reported in Caux et al. (2011b).

Table 2. Number of NH_2CHO and HNCO detected lines.

Source	NH_2CHO No.	NH_2CHO $E_{\rm u}$ (K)	HNCO No.	HNCO $E_{\rm u}$ (K)
L1544[a]	0	–	2	10–16
TMC1	0	–	3	10–16
B1	0	–	4	10–30
L1527	0	–	4	10–30
L1157-mm	0	–	4	10–30
IRAS 4A	7	15–70	10	10–130
SVS13A	13	15–130	19	10–130
OMC-2 FIR 4	21	10–130	9	10–100
Cep E	5	10–22	5	10–85
I16293	12	10–160	16	10–95

Note. [a]Only 3-mm data available.

4 RESULTS

4.1 Line spectra

We searched for formamide (NH_2CHO) and isocyanic acid (HNCO) in our data set using the CASSIS software[3] (Caux et al. 2011a) and the Cologne Database for Molecular Spectroscopy (CDMS;[4] Müller et al. 2001, 2005) to identify the lines. For NH_2CHO, we detected transitions with upper level energies, $E_{\rm up}$, below 150 K, and spontaneous emission coefficients, A_{ij}, above 10^{-5} s^{-1} and 5×10^{-5} s^{-1}, respectively, for the 2/3-mm and the 1-mm data. For HNCO, we detected transitions with $E_{\rm u} < 150$ K and $A_{ij} > 10^{-5}$ s^{-1}. Tables B1 and B2 list all the NH_2CHO and HNCO transitions fulfilling these criteria in the observed millimetre bands, as well as the 3σ detections for each source. The sources where no NH_2CHO lines were detected (see below) are not included in Table B1. For some sources with not many clear formamide detections (e.g. IRAS4A, Cep E), we included a few additional lines with peak intensities between 2σ and 3σ, as indicated in the tables. We then fitted the lines with a Gaussian function, and excluded from further analysis those falling well below or above the systemic velocity, and/or displaying too narrow or too broad linewidths with respect to the typical values encountered for each source.

Table 2 lists, for each source, the number of NH_2CHO and HNCO lines detected and used in our analysis (Section 4.2). While HNCO is easily detected in all the sources, NH_2CHO remains undetected in five objects: L1544, TMC-1, B1, L1527, and L1157mm. Moreover, in those sources where it is detected, the lines are typically weak (S/N$\sim$ 3–5). OMC-2 FIR 4 has the highest number of detected formamide lines, which are also the most intense. The results from the Gaussian fitting to the detected lines are presented in Tables B3–B12. A sample of lines for all the ASAI sources are shown in Figs C1–C3.

4.2 Derivation of physical properties

4.2.1 *Rotational diagram analysis*

In order to determine the excitation conditions – i.e. excitation temperature, column density and, eventually, abundance with respect to H_2– of NH_2CHO and HNCO for each source in a uniform way, we employed the CASSIS software to build rotational diagrams. This approach assumes (i) that the lines are optically thin, and (ii) Local Thermodynamic Equilibrium (LTE), meaning that a single Boltzmann temperature, known as *rotational temperature*, describes the relative distribution of the population of all the energy levels for a given molecule. Under these assumptions, the upper-level column density

$$N_{\rm u} = \frac{8\pi k \nu^2}{hc^3 A_{\rm ul}} \frac{1}{\eta_{\rm bf}} \int T_{\rm mb} {\rm d}V \quad (1)$$

and the rotational temperature, $T_{\rm rot}$, are related as follows:

$$\ln \frac{N_{\rm u}}{g_{\rm u}} = \ln N_{\rm tot} - \ln Q(T_{\rm rot}) - \frac{E_{\rm u}}{kT_{\rm rot}} \quad (2)$$

where k, ν, h, and c are, respectively, Boltzmann's constant, the frequency of the transition, Planck's constant, and the speed of light; $g_{\rm u}$ is the degeneracy of the upper level, and $N_{\rm tot}$ is the total column density of the molecule. The second fraction in equation (1) is the inverse of the beam-filling factor. We estimated it assuming sources with a Gaussian intensity distribution:

$$\eta_{\rm bf} = \frac{\theta_{\rm s}^2}{\theta_{\rm s}^2 + \theta_{\rm b}^2} \quad (3)$$

with $\theta_{\rm s}$ and $\theta_{\rm b}$ being, respectively, the source and telescope beam sizes. We adopted the source sizes indicated in Table 3. In those sources where a hot ($T > 100$ K) inner region is believed to exist, we considered two possible solutions: (i) the emission originates from a compact size representing this inner region or *hot corino*, which typically shows enhanced abundances of COMs; and (ii) the emission homogeneously arises from the entire extended molecular envelope of the protostar. We determined the sizes of the compact hot corino regions either from published interferometric maps (SVS13A) or from the gas density structure, $n(r)$, reported in the literature (I16293, IRAS 4A, OMC-2, Cep E), as indicated in Table 3. In the latter case, we assumed a size equal to the diameter within which the dust temperature is above 100 K.

Some sources, such as IRAS 4A, OMC-2, and Cep E, show extended velocity wings in a few of their lines. In order to separate their contribution to the line emission, we determined their line flux, $\int T_{\rm mb}{\rm d}V$, by fitting a Gaussian function to the affected lines after masking their high-velocity wings. In sources with two to four well-aligned data points in the rotational diagrams, we took into account the relatively large error bars by fitting two additional 'extreme' lines passing through the tips of the error bars of the lowest and largest energy points. An example is shown for B1 in Fig. 1, where the two extreme solutions are depicted in blue, while

---

[2] http://www.iram.es/IRAMES/mainWiki/Iram30mEfficiencies

[3] CASSIS has been developed by IRAP-UPS/CNRS (http://cassis.irap.omp.eu)

[4] http://www.astro.uni-koeln.de/cdms/

Table 3. Results from the rotational diagram analysis of NH_2CHO and HNCO: Adopted size and H_2 column densities (N_{H2}), derived rotational temperatures, T_{rot}, derived HNCO and HN_2CHO column densities (N_{HNCO}, N_{NH_2CHO}), resulting abundances with respect to H_2(X_{HNCO}, X_{NH_2CHO}), and ratio of HNCO to NH_2CHO column densities (R).

Source	Size^{a} (arcsec)	N^{b}_{H2} (10^{22}cm^{-2})	$T_{rot(HNCO)}$ (K)	N_{HNCO} (10^{12}cm^{-2})	X_{HNCO} (10^{-11})	$T^{c}_{rot(NH_2CHO)}$ (K)	$N^{c}_{NH_2CHO}$ (10^{12}cm^{-2})	X_{NH_2CHO} (10^{-11})	R
One-component fit									
L1544	BF	9.4 ± 1.6^{1}	7 ± 3	5 ± 3	5 ± 3	7	<0.036	<0.046	>130
TMC1^{d}	BF	1.0 ± 0.1^{2}	4 ± 1	8 ± 5	80 ± 50	4	<0.47	<5.2	>17
B1	BF	7.9 ± 0.3^{3}	10 ± 2	8.4 ± 1.6	11 ± 2	10	<0.087	<0.11	>97
L1527	BF	4.1^{4}	7.5 ± 1.4	2.5 ± 1.5	6 ± 4	7.5	<0.062	<0.15	>40
L1157-mm	30	120^{5}	8 ± 1	4 ± 1	0.35 ± 0.03	8	<1	<0.008	>40
SVS13A (ext)^{e}	20	10^{6}	58 ± 6	11 ± 2	11 ± 2	64 ± 6	3.0 ± 0.4	3.0 ± 0.4	4 ± 1
(com)^{e}	1	1000^{7}	36 ± 3	1500 ± 300	15 ± 3	40 ± 4	320 ± 60	3.2 ± 0.6	5 ± 1
OMC-2 (ext)	25	19^{8}	25 ± 3	16 ± 3	1.9 ± 0.4	58 ± 4	3.1 ± 0.2	0.36 ± 0.02	5 ± 1
(com)	2	4.6^{8}	19 ± 1	900 ± 100	910 ± 80	32 ± 2	110 ± 10	110 ± 10	8 ± 1
Cep E (ext)	40	4.8^{9}	30 ± 5	6.2 ± 0.3	13 ± 1	9 ± 2	0.2 ± 0.1	0.4 ± 0.2	30 ± 13
(com)	0.5	230^{9}	17 ± 1	6000 ± 1000	130 ± 15	6 ± 1	500 ± 300	11 ± 5	12 ± 6
Two-component fit									
IRAS 4A (C1)	30	2.9^{10}	11 ± 3	10 ± 1	34 ± 2	19 ± 15	0.6 ± 0.5	1.9 ± 0.2	18 ± 2
IRAS 4A (C2)	0.5	250^{10}	43 ± 8	2000 ± 1000	80 ± 40	30 ± 5	500 ± 100	20 ± 5	4 ± 2
I16293 (C1)	30	2.9^{11}	14 ± 5	20 ± 2	69 ± 7	5 ± 1	1.7 ± 0.6	6 ± 2	12 ± 4
I16293 (C2)	1.2	53^{11}	47 ± 4	4400 ± 700	830 ± 130	83 ± 33	590 ± 190	110 ± 40	8 ± 3

Notes. [a]BF: beam-filling assumed. For the other sources, the size has been adopted as follows: L1157mm and IRAS 4A (extended) from Jørgensen, Schöier & van Dishoeck (2002); SVS13A (extended) from Lefloch et al. (1998); SVS13A (compact) from Looney, Mundy & Welch (2000); OMC-2 FIR 4 (extended) from Furlan et al. (2014); OMC-2 FIR 4 (compact) from Crimier et al. (2009); Cep E from Chini et al. (2001); IRAS 4A (compact) from Maret et al. (2002); IRAS 16293 from Jaber et al. (2014).

[b]References: [1]Crapsi et al. (2005), [2]Maezawa et al. (1999), [3]Daniel et al. (2013), [4]Parise, Bergman & Menten (2014), [5]Jørgensen et al. (2002) [6]Lefloch et al. (1998), [7]Looney et al. (2000), [8]Crimier et al. (2009), [9]Crimier et al. (2010a), [10]Maret et al. (2002), [11]Crimier et al. (2010b).

[c]For the non-detections of NH_2CHO, we have computed a 3σ upper limit to its column density adopting the same T_{rot} derived for HNCO (see text).

[d]Data for NH_2CHO upper limit derived from 3-mm data by N. Marcelino.

[e]N(HNCO) is probably a lower limit due to contamination from the OFF position.

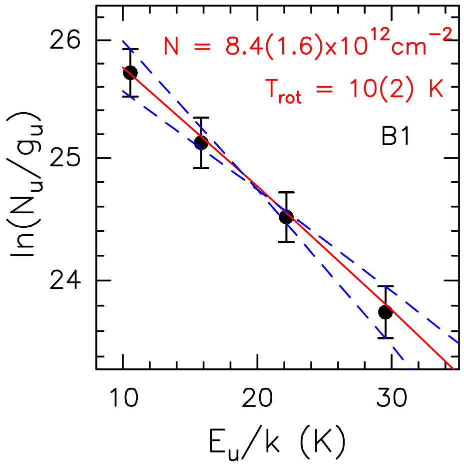

Figure 1. HNCO rotational diagram of B1. Data points are depicted in black. The red lines correspond to the best fit to the data points. The extreme solutions taking into account the error bars are displayed in dashed blue.

the best solution is marked in red. The remaining rotational diagrams and the best fit to their data points using equation (2) are shown in Figs C4 and C5, where the error bars take into account calibration errors as well as the rms value around each line.

We compared our rotational diagram results with those reported in Marcelino et al. (2009) for the four sources common to both studies: L1544, TMC-1, B1, and L1527. The column densities of HNCO are in perfect agreement within the uncertainties, while the rotational temperatures agree within 1 K.

For homogeneity with the methodology used for NH_2CHO, we estimated the properties of HNCO in the LTE approximation. In addition, by adopting the same source sizes for HNCO and NH_2CHO, we assumed that the emission from both molecules originates in the same region(s). The similar average linewidths between the two species suggest this is a reasonable assumption. Table 3 and Figs C4 and C5 present the results of the rotational diagram analysis. For most of the sources, a single component fits well both the NH_2CHO and HNCO points and therefore LTE seems to reproduce well the observations. This can also be seen in Figs C1 to C3, where the observed spectra (in black) and the best-fitting models (in red) match fairly well. However, for SVS13A, Cep E, and OMC-2, the compact solutions correspond to HNCO lines that are moderately optically thick ($\tau \sim$ 1–10). The most extreme case is Cep E, for which also the NH_2CHO lines are optically thick. This is in contradiction with the underlying assumption of optically thin lines in the rotational diagram method. We find, however, that this caveat can be easily overcome by adopting a slightly larger source size, of 3, 2, and 2 arcsec, respectively, for SVS13A, Cep E, and OMC-2. Doing this, the resulting column densities are reduced by a factor of 2 (OMC-2) to 15 (Cep E), τ becomes much smaller than 1, and the lines can be well fitted by the solutions. Consequently, the uncertainties in the compact-solution column densities in these three sources are larger than reported in Table 3, but they are taken into account in the discussion (Section 5: see Figs 2 and 3).

There are two objects where a single component does not appear to explain the emission of all the lines: IRAS 4A and I16293, two

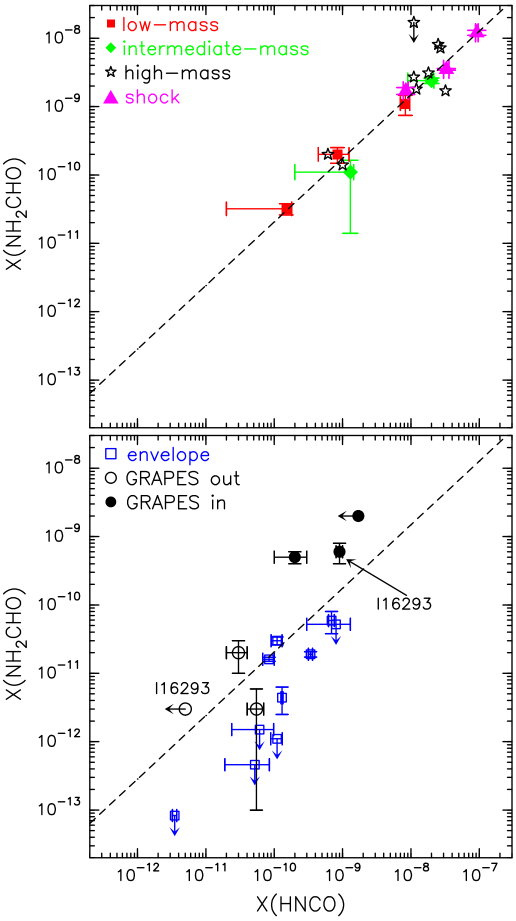

Figure 2. Plot of NH_2CHO versus HNCO abundances with respect to H_2. Top: data points included in the power-law fit (dashed line; see text). Red squares and green diamonds denote the compact or inner RD solutions of low- and intermediate-mass sources in this study, respectively. Magenta triangles and black stars correspond, respectively, to outflow shock regions (from Mendoza et al. 2014) and high-mass sources (from Bisschop et al. 2007 and Nummelin et al. 2000). Bottom: data points not included in the power-law fit (see text). Blue open squares represent the extended or outer RD solutions, while black open and filled circles denote the GRAPES LTE values for the outer and inner components, respectively.

well-known hot corino sources. Indeed, their rotational diagrams suggest either the contribution of two components, or non-LTE effects, coming into play. Considering the former, Table 3 presents the results of a two-component solution to the rotational diagrams of these two objects, where C1 is assumed to represent the cold extended envelope of the protostar, and C2 the small inner hot corino. While this two-component solution reproduces well the observations, non-LTE effects cannot be ruled out.

As for the five objects where formamide was not detected, we determined a 3σ upper limit to its column density under the assumption of LTE and adopting the corresponding value of $T_{\rm rot}$ derived for HNCO. To this end, we used the spectral data around the NH_2CHO

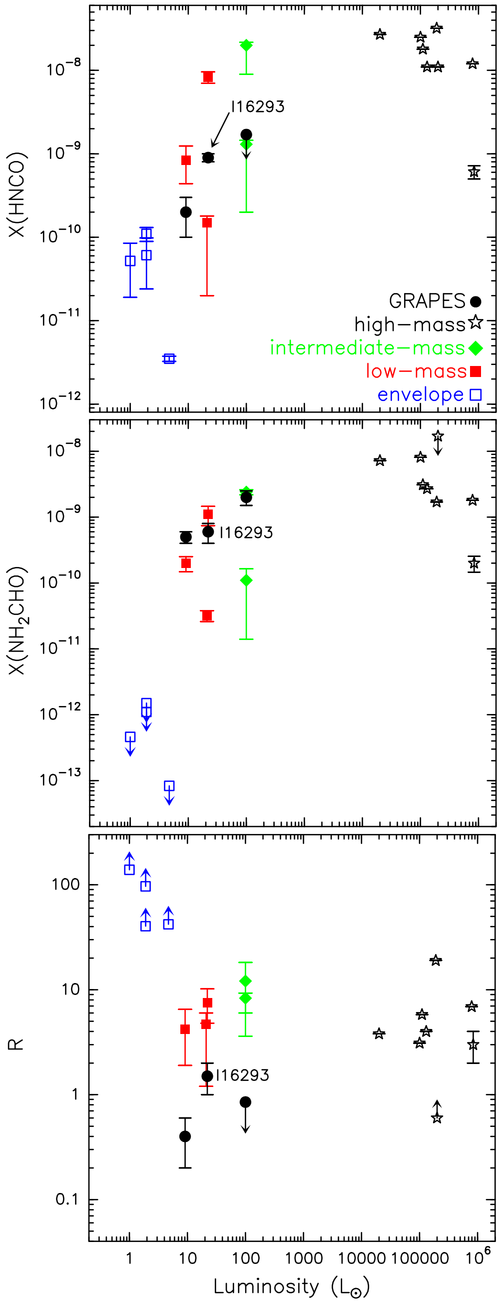

Figure 3. Abundance of HNCO (top), NH_2CHO (middle) and their ratio (bottom) against bolometric luminosity. Symbols are as in Fig. 2.

$4_{0,4}$–$3_{0,3}$ transition at 84.542 GHz, expected to be the most intense at the cold temperatures implied by the HNCO results. The upper limits thus derived are shown in Table 3.

Once the column densities of HNCO and NH_2CHO were obtained, we derived their respective abundances with respect to molecular hydrogen (H_2) using the H_2 column densities, N_{H2}, listed in Table 3, which correspond to the indicated source sizes. The uncertainty on N_{H2} is included for those sources where this was provided in the corresponding bibliographic reference. The resulting abundances span more than two orders of magnitude and are shown in Table 3, together with their ratio, $R = X(\mathrm{HNCO})/X(\mathrm{NH_2CHO})$.

4.2.2 Radiative transfer analysis taking into account the source structure

The source structures of I16293, IRAS 4A, and OMC-2 are reported in the literature (Maret et al. 2002; Crimier et al. 2010b). Therefore, for these objects, a more sophisticated radiative transfer analysis is possible that takes into account the temperature and gas density as a function of distance to the central protostar. Cep E also has a known structure (Crimier et al. 2010a), but having only five line detections, both in HNCO and in NH_2CHO, we do not consider it here. We have analysed the I16293, IRAS 4A, and OMC-2 lines by means of the code GRAPES (GRenoble Analysis of Protostellar Envelope Spectra), whose details are described in Ceccarelli et al. (2003) and Jaber et al. (2014).

Briefly, GRAPES computes the Spectral Line Energy Distribution (SLED) of a free-infalling spherical envelope with given gas and dust density and temperature profiles, and for a given mass of the central object. The dust-to-gas ratio is assumed to be the standard one, 0.01 in mass, and the grains have an average diameter of 0.1 µm. The species abundance is assumed to follow a step-function, with a jump at the dust temperature T_{jump}, which simulates the thermal desorption of species from icy mantles (e.g. Ceccarelli et al. 2000). The abundance X_{i} in the warm ($T \geq T_{\mathrm{jump}}$) envelope is constant. In the outer envelope, we assumed that the abundance follows a power law as a function of the radius, $X_{\mathrm{o}}r^{a}$, with an index equal to 0, −1 and −2, as in Jaber et al. (2014). X_{i} and X_{o} are considered parameters of the model. Since, to our knowledge, the binding energy of NH_2CHO is not available in the literature, we treat T_{jump} as a parameter too. However, if the molecules are trapped in water ice, the binding energy of H_2O will largely determine the dust temperature at which NH_2CHO is injected into the gas-phase.

The radiative transfer is solved with the escape probability formalism and the escape probability is computed integrating each line opacity over the 4π solid angle. We ran models assuming LTE populations for formamide and, for comparison with Section 4.2.1, HNCO, and models taking into account non-LTE effects for HNCO. In the latter case, we used the collisional coefficients by Green (1986), retrieved from the LAMDA data base (Schöier et al. 2005).

For each molecule and source, we ran a large grid of models varying the four parameters mentioned above: X_{i}, X_{o}, T_{jump}, and a. In total, we ran about 20 000 models per source. The computed SLED of each model was then compared with the observed SLED to find the solution with the best fit. The results of this analysis are reported in Table 4, where we give the best-fitting values and the range of X_{i}, X_{o}, T_{jump} with $\chi^2 \leq 1$. We note that there is no appreciable difference in the best χ^2 when using a different value of a, so we took the simplest solution: $a = 0$. In this respect, the situation is similar to what Jaber et al. (2014) found in their study of IRAS16293.

Table 4. Results of GRAPES analysis for NH_2CHO and HNCO considering the source structure of IRAS 4A, I16293 and OMC-2.*

	IRAS 4A	I16293	OMC-2
HNCO LTE			
X_{o} (10^{-11})	3 ± 1	0.1 ± 0.1	5.5 ± 1.5
X_{i} (10^{-11})	20 ± 10	90 ± 10	<170
T_{jump} (K)	100	40	80
T_{jump} range (K)	60–120	30–50	≥30
χ^2	1.2	2.0	1.0
HNCO non-LTE			
X_{o} (10^{-11})	3 ± 1	0.5 ± 0.4	4 ± 1
X_{i} (10^{-11})	30 ± 20	600 ± 300	<20
T_{jump} (K)	100	90	80
T_{jump} range (K)	≥50	≥60	≥30
χ^2	1.0	1.5	0.7
NH_2CHO			
X_{o} (10^{-11})	2 ± 1	0.3 ± 0.2	0.3 ± 0.3
X_{i} (10^{-11})	50 ± 10	60 ± 20	200 ± 50
T_{jump} (K)	100	90	80
T_{jump} range (K)	≥100	≥50	60–100
χ^2	2.0	0.7	1.3
$R = X(\mathrm{HNCO})/X(\mathrm{NH_2CHO})$			
R_{o} (LTE)	1.5 ± 0.9	<1.7	18 ± 18
R_{i} (LTE)	0.4 ± 0.2	1.5 ± 0.5	<0.85
R_{o} (non-LTE)	1.5 ± 0.9	1.7 ± 1.7	13 ± 13
R_{i} (non-LTE)	0.6 ± 0.4	10 ± 6	<0.1

Note. *Abundances with respect to H_2 are times 10^{-11}. X_{o} and X_{i} are the outer and inner abundances, respectively.

A comparison between the results obtained for HNCO with the LTE and non-LTE level populations shows that the LTE approximation is quite good in the case of IRAS 4A and OMC-2, but not for I16293. The reason for that is probably a lower density envelope of I16293 compared to the other two sources. Therefore, the LTE results are likely reliable also for the formamide in IRAS 4A and OMC-2, while in I16293 these have to be taken with some more caution.

A second result of the GRAPES analysis is that both HNCO and formamide have a jump in their abundances at roughly the same dust temperature, 80–100 K. This is an important result reflecting the two molecules have similar behaviours with changes in temperature. It suggests they trace the same regions within the analysed protostars.

In order to evaluate whether the rotational diagram (hereafter RD) and GRAPES analyses are in agreement, we compare their respective abundance values, which roughly agree within an order of magnitude, in the Appendix A. We note here that, while the GRAPES analysis is likely more accurate, we are not able to apply it to the other sources of this study due to the lack of known source structure and/or lack of a sufficient amount of molecular lines. The absence of interferometric imaging of the HNCO and NH_2CHO emission also hinders the study of the inner structure of the protostellar emission. Therefore, we base the discussion below largely on the RD results, with a note of caution that those values may not strictly represent the physical properties of the sources.

5 DISCUSSION

5.1 Formation routes of NH_2CHO

The formation mechanism(s) of interstellar formamide, as that of other COMs, is still far from being established. Several routes have been proposed so far which include both gas-phase and grain-surface processes. Concerning the former, Quan & Herbst (2007) suggested NH_2CHO forms via the radiative association reaction

$$NH_4^+ + H_2CO \rightarrow NH_4CH_2O^+ + h\nu \quad (4)$$

followed by dissociative recombination. Halfen, Ilyushin & Ziurys (2011) proposed the following ion–molecule reaction and subsequent electron recombination:

$$NH_4^+ + H_2CO \rightarrow NH_3CHO^+ + H_2 \quad (5)$$

$$NH_3CHO^+ + e^- \rightarrow NH_2CHO + H. \quad (6)$$

These reactions all have unknown rates. Thus, further experimental work will be needed in order to evaluate their effectiveness in producing formamide.

Neutral–neutral reactions have also been discussed as possible gas-phase routes leading to NH_2CHO. In particular, Garrod, Weaver & Herbst (2008) proposed the radical-neutral reaction

$$H_2CO + NH_2 \rightarrow NH_2CHO + H. \quad (7)$$

However, as recently mentioned by Redondo et al. (2014), it presents a net activation barrier of >1000 K that makes it inviable in interstellar conditions. Other neutral–neutral reactions evaluated by these authors also revealed to have large activation barriers, thus ruling them out as dominant or efficient mechanisms to produce NH_2CHO.

Formamide may also be formed on the icy mantles of dust grains. Jones et al. (2011) conducted some experimental work in which they irradiate a mixture of ammonia (NH_3) and carbon monoxide (CO) ices with high-energy (keV) electrons, resulting in NH_2CHO as one of the final products. The authors discuss several possible reactions and conclude that the most plausible route towards formamide begins with the cleavage of the nitrogen–hydrogen bond of ammonia, forming the NH_2 radical and atomic H. The latter, containing excess kinetic energy, can then add to CO, overcoming the entrance barrier, to produce the formyl radical (HCO). Finally, HCO can combine with NH_2 to yield NH_2CHO.

A different grain-mantle mechanism was proposed by Garrod et al. (2008), who considered hydrogenation (i.e. addition of H atoms) of OCN in their chemical models. However, this route resulted in an overabundance of NH_2CHO and an underabundance of HNCO, since the latter was efficiently hydrogenated to yield formamide, the final product. Raunier et al. (2004) performed experimental Vacuum Ultra Violet (VUV) irradiation of solid HNCO at 10 K, which led to NH_2CHO among the final products. They proposed that photodissociation of HNCO yields free H atoms that subsequently hydrogenate other HNCO molecules in the solid to finally give NH_2CHO. The limitation of this experiment is that it was carried out with pure solid HNCO. Jones et al. (2011) mentioned that, in the presence of NH_3, quite abundant in grain mantles, HNCO will preferentially react with it, resulting in $NH_4^+ + OCN^-$. Despite these caveats, hydrogenation of HNCO on grain mantles was recently found to be a most likely solution in the case of the outflow shock regions L1157-B1 and B2 (Mendoza et al. 2014). More experiments and calculations are needed in order to assess the efficiency of this formation route.

5.2 Correlation between HNCO and NH_2CHO

From the previous section, it is clear that, until more gas-phase and surface reaction rates involving the mentioned species are measured, it will be difficult to establish the exact synthesis mechanisms of formamide in space.

In this section, we assess, from an observational point of view, whether hydrogenation of HNCO leading to NH_2CHO on the icy mantles of dust grains could be a dominant formation route. To this aim, we plot in Fig. 2 the NH_2CHO versus HNCO abundances of all our sources (Table 3), as well as the shock regions analysed by Mendoza et al. (2014), and the high-mass SFRs reported in Bisschop et al. (2007) and Nummelin et al. (2000), for comparison. The latter were obtained by the cited authors via the RD method assuming the emission comes from the inner hot core regions. Thus, for homogeneity, we split the plot into two panels, the upper one showing only the compact/inner solutions of the RD analysis, classified by masses. The best power-law fit to these points is marked with a dashed line, and is given by the equation $X(NH_2CHO) = 0.04X(HNCO)^{0.93}$, with a Pearson coefficient of 0.96, indicating a tight correlation. The fact that this correlation is almost linear and holds for more than three orders of magnitude in abundance suggests that HNCO and NH_2CHO are chemically related. This result confirms, on a more statistical basis, what was recently found by Mendoza et al. (2014).

However, this correlation does not hold for the objects without formamide detections, which are plotted in the lower panel of Fig. 2 together with the extended envelope solutions of the RD analysis. Here, it is clearly seen that all the upper limits lie well below the best-fitting line, indicating a significantly larger amount of gas-phase HNCO relative to NH_2CHO in comparison to the other sources. These objects are the coldest in our sample, representing either prestellar cores or protostars with no detectable hot corino within them. The rotational temperatures inferred from the HNCO RD analysis are also among the lowest in our sample. In this same plot, the points representing formamide detections (extended envelope component) also show a tendency towards lower relative values of $X(NH_2CHO)$, although not as pronounced.

Thus, it appears that regions with colder temperatures are more deficient in NH_2CHO than protostars with hot inner regions, indicating that higher temperatures are needed for NH_2CHO to become relatively abundant in the gas-phase. This might be explained by (i) NH_2CHO forming in the gas-phase at temperatures above ~100 K, and/or (ii) it forming predominantly on the icy mantles of dust grains at low temperatures, and subsequently sublimating into the gas-phase when the temperature in the inner regions rises sufficiently. As for the former possibility, Mendoza et al. (2014) quantitatively argued that reaction 7 does not suffice to explain the amount of gas-phase formamide in the shock regions of L1157 protostellar outflow. In addition, the high activation barrier the reaction needs to overcome makes this an unviable route. Other purely gas-phase formation routes still need more investigation in terms of reaction rates and activation barriers, as discussed in Section 5.1. Mendoza et al. (2014) favoured a grain formation mechanism followed by mantle-grain evaporation/sputtering on the basis of the comparable abundance enhancements of HNCO, NH_2CHO, and CH_3OH in the gas-phase between the two protostellar shocks studied by the authors. Therefore, grain formation of NH_2CHO appears to be the most likely possibility.

On the other hand, while grain formation of HNCO is likely to occur in the cold phases of star formation (Hasegawa & Herbst 1993), gas-phase reactions leading to HNCO at such cold temperatures can also take place efficiently (see e.g. Marcelino et al. 2009 and references therein), overcoming strong depletion. This would explain its relatively high gas-phase abundance already in the very early – and cold – phases of star formation, and also the high values of HNCO to NH_2CHO abundance ratios we find in the coldest sources of our sample.

In Fig. 3, we plot the HNCO abundance, the NH_2CHO abundance, and their ratio, *R*, as a function of bolometric luminosity for those sources with a reported luminosity estimate (see Table 1). For the objects in our study with formamide detection, we only plot the points corresponding to the inner or compact component (red circles), since these regions are expected to be the dominant contributors to the overall luminosity. The HNCO and NH_2CHO abundance panels both show the high-mass sources lying on top of the plot, while the points representing our sample sources are more scattered, with the coldest objects (in blue) showing the lowest abundances. This trend is much more pronounced in the case of NH_2CHO, for which hot corino regions (red points) display higher NH_2CHO abundances than the colder objects by more than an order of magnitude. More interesting is the plot of *R*, which illustrates how this quantity remains roughly constant along 6 orders of magnitude in luminosity for the NH_2CHO-emitting sources, with values ranging from 3 to 10 approximately. This reflects the almost-linearity of the correlation between the abundance of the two species. On the other hand, this value rises considerably for the lower luminosity sources, re-enforcing our interpretation that formamide mostly forms on grains at cold temperatures, while HNCO may form both on grains and in the gas.

The strikingly tight and almost linear correlation between the abundance of the two molecules once NH_2CHO becomes detectable suggests one of the two following possibilities: (i) HNCO and NH_2CHO are both formed from the same parent species on dust grain mantles, or (ii) one forms from the other. Among the grain formation routes that have been proposed so far, hydrogenation of HNCO leading to NH_2CHO is the only mechanism that would explain our observational results. While this route is found to have some caveats (see Section 5.1), it is also true that more experimental work is needed to better assess its efficiency.

If the abundance of gaseous NH_2CHO truly depends on temperature, we should find a difference in *R* between the hot corino and the cold envelope regions of IRAS 4A and I16293. Looking at Table 3, this is indeed the case. As for OMC-2, Cep E, and SVS13A, only one component was necessary to describe their rotational temperatures and column densities. Therefore, we cannot compare the extended and compact values as in the case of a two-component solution. We can nevertheless guess that, excluding the case of Cep E, for which only low-energy formamide lines were detected, the compact solution is likely the best, given the low values of *R* and the relatively high rotational temperatures derived. This would imply most of the emission arises in the inner hot corino regions. For Cep E, more molecular observations at higher frequencies are needed to confirm this.

Figs 2 and 3 also include the results from the LTE GRAPES analysis. I16293 (labelled in the plots) is included for completeness despite the fact that the GRAPES analysis suggests non-LTE effects should be taken into account for this object. While these points introduce more scatter in the plots, it can be clearly seen that the inner components of the sources analysed with GRAPES have a lower HNCO abundance relative to NH_2CHO, compared to what is found via the RD analysis. This yields lower *R* values, indicating a considerable amount of formamide with respect to HNCO in these regions and suggesting, as mentioned in Section A, that the two-component approximation in the RD analysis is oversimplistic: while we assumed that only the higher-energy formamide lines arose from the compact inner region, it is likely that a significant amount of emission from the low-energy lines also originates here and not exclusively in the outer envelope.

The trend showing higher *R* in the outer envelope than in the inner regions holds for both IRAS 4A and OMC-2, which further supports the fact that NH_2CHO requires higher temperatures than HNCO to be detectable in the gas-phase. This kind of analysis, taking into account the source structure, is needed in a larger sample of objects in order to draw conclusions about both the chemistry and the validity of our RD analysis on a more statistical basis. Interferometric mapping would also greatly help disentangling source multiplicity and verifying whether the emission of HNCO and NH_2CHO trace the same regions, as has been assumed in this work.

6 CONCLUSIONS

As part of the IRAM Large programme ASAI, we searched for millimetre spectral lines from formamide (NH_2CHO), a presumably crucial precursor of pre-biotic material, and isocyanic acid (HNCO), in 10 low- and intermediate-mass SFRs with different properties. The data set, obtained with the IRAM 30-m telescope, consists mainly of unbiased broad-band spectral surveys at 1, 2, and 3 mm. Our aim was to investigate the chemical connection between these two molecular species and gain some observational insights into the formation mechanisms of formamide in interstellar conditions. The present work represents the first systematic study within ASAI and statistically completes the low-mass end of similar studies performed towards high-mass SFRs. Our main findings are summarized as follows.

(1) The high sensitivity and large frequency range of the spectral surveys allowed us to evaluate the detectability of numerous NH_2CHO and HNCO transitions. We detect formamide in five out of the 10 objects under study (IRAS 4A, IRAS 16293, SVS13A, Cep E, and OMC-2), and HNCO in all of them. Since formamide had already been detected in IRAS 16293 – also investigated here for completeness – this study raises the number of known low- and intermediate-mass formamide-emitting protostars to five, thus significantly improving the statistics.

(2) We derived HNCO and NH_2CHO column densities via the rotational diagram method for all the sources. As a result, we found NH_2CHO abundances with respect to H_2 in the range 10^{-11}–10^{-9}, and HNCO abundances between 10^{-12} and 10^{-8}. For those objects without formamide detection, we provided an upper limit to its column density and abundance.

(3) For three targets (IRAS 4A, IRAS 16293, and OMC-2), the source density and temperature structures are known and published, and we were thus able to take them into account through a more sophisticated analysis using the code GRAPES. This method fits an abundance profile that consists of a step function, with the separation between the two values roughly corresponding to the hot corino size. A comparison between the two radiative transfer analyses employed reveals overall agreement within an order of magnitude. The GRAPES analysis also indicates that one of the studied objects, IRAS 16293, requires a non-LTE radiative transfer analysis, which at the moment is not possible due to the lack of collisional coefficients for NH_2CHO. LTE appears to describe correctly the other two sources analysed with GRAPES, and is assumed to be a good approximation for all the other sources in our sample.

(4) For the sources where formamide was detected, i.e. hot corino sources, we found an almost linear correlation between HNCO and NH_2CHO abundances that holds for several orders of magnitude. This suggests that the two molecules may be chemically associated.

On the other hand, those sources with no formamide detection do not follow this correlation, but instead show much larger amounts of HNCO relative to NH_2CHO. These objects are the coldest in this study, and unlike the rest of our sample, they contain no known hot corinos.

(5) Our findings and the NH_2CHO formation routes proposed so far in the literature suggest that, unlike HNCO, NH_2CHO does not form efficiently in the gas-phase at cold temperatures and may be formed on the mantles of dust grains, where it remains frozen at cold temperatures. As soon as the temperature rises sufficiently to sublimate the icy grain mantles, formamide is incorporated into the gas and becomes detectable. The tight and almost linear correlation with HNCO suggests a possible formation route of NH_2CHO via hydrogenation of HNCO, although other possibilities should not be ruled out. In particular, two potentially viable gas-phase pathways leading to formamide involve formaldehyde (H_2CO). It is therefore worth exploring the connection between H_2CO and NH_2CHO, which will be the subject of a forthcoming paper.

(6) In order to evaluate the validity of our conclusions, several aspects need to be explored more thoroughly. From an observational point of view, interferometric imaging is necessary to assess the relative spatial distribution of HNCO and NH_2CHO, and retrieve more accurate abundance ratios, in particular in the hot corino sources. In addition, more detailed and sophisticated radiative transfer analysis requires, on the one hand, knowledge of the source density and temperature profiles and, on the other hand, collisional coefficient calculations for NH_2CHO, currently unavailable. Finally, more chemical experiments are needed to estimate the efficiency of the hydrogenation processes leading from isocyanic acid to formamide on interstellar dust grains, as well as the viability of purely gas-phase reactions.

ACKNOWLEDGEMENTS

We would like to thank the staff members at IRAM, who greatly helped before, during, and after the ASAI observations. We are also grateful to our anonymous referee, whose comments helped us to improve the manuscript, and to Y. Watanabe, N. Sakai, and S. Yamamoto for very useful discussions. ALS acknowledges financial support from Grant-in-Aids from the Ministry of Education, Culture, Sports, Science, and Technologies of Japan (25108005). This work is partly supported by the French Space Agency CNES (Centre National d'Études Spatiales) and the PRIN INAF 2012 – JEDI and by the Italian Ministero dell'Istruzione, Università e Ricerca through the grant Progetti Premiali 2012 – iALMA. MK acknowledges support from a Royal Netherlands Academy of Arts and Sciences (KNAW) professor prize. MT and RB gratefully acknowledge partial support from MINECO Grant FIS2012-32096. This article is based on observations carried out with the IRAM 30-m Telescope. IRAM is supported by INSU/CNRS (France), MPG (Germany) and IGN (Spain). It is also based on analysis carried out with the CASSIS software.

REFERENCES

Adande G. R., Woolf N. J. G., Ziurys L. M., 2011, Astrobiology, 13, 439
Bisschop S. E., Jørgensen J. K., van Dishoeck E. F., de Wachter E. B. M., 2007, A&A, 465, 913
Bockelée-Morvan D. et al., 2000, A&A, 53, 1101
Caux E., Bottinelli S., Vastel C., Glorian J. M., 2011a, IAUS, 280, 120
Caux E. et al., 2011b, A&A, 532, A23
Ceccarelli C., Castets A., Caux E., Hollenbach D., Loinard L., Molinari S., Tielens A. G. G. M., 2000, A&A, 355, 1129
Ceccarelli C., Maret S., Tielens A. G. G. M., Castets A., Caux E., 2003, A&A, 410, 587
Chen X., Launhardt R., Henning Th ., 2009, ApJ, 691, 729
Chini R., Ward-Thompson D., Kirk J. M., Nielbock M., Reipurth B., Sievers A., 2001, A&A, 369, 155
Correia J. C., Griffin N., Saraceno P., 2004, A&A, 418, 607
Crapsi A., Caselli P., Walmsley C. M., Myers P. C., Tafalla M., Lee C. W., Bourke T. L., 2005, ApJ, 619, 379
Crimier. N., Ceccarelli C., Lefloch B., Faure A., 2009, A&A, 506, 1229
Crimier N. et al., 2010a, A&A, 516, A102
Crimier N., Ceccarelli C., Maret S., Bottinelli S., Caux E., Kahane C., Lis D. C., Olofsson J., 2010b, A&A, 519, A65
Daniel F. et al., 2013, A&A, 560, A3
Elias J., 1978, ApJ, 224, 857
Evans N. J., II, Rawlings J. M. C., Shirley Y. L., Mundy L. G., 2001, ApJ, 557, 193
Furlan E. et al., 2014, ApJ, 786, 6
Garrod R. T., Weaver S. L. W., Herbst E., 2008, ApJ, 682, 283
Green S., 1986, ApJ, 309, 331
Halfen D. T., Ilyushin V., Ziurys L. M., 2011, ApJ, 743, 60
Hasegawa T. I., Herbst E., 1993, MNRAS, 263, 589
Hirano N., Kamazaki T., Mikami H., Ohashi N., Umemoto T., 1999, in Nakamoto T., ed., Proc. Star Formation, Nobeyama Radio Observatory, p. 181
Hirota T. et al., 2008, PASJ, 60, 37
Jaber A. A., Ceccarelli C., Kahane C., Caux E., 2014, ApJ, 791, 29
Jones B. M., Bennett C. J. Kaiser, Ralf I., 2011, ApJ, 734, 78
Jørgensen K., Schöier F. L., van Dishoeck E. F., 2002, A&A, 389, 908
Kahane C., Ceccarelli C., Faure A., Caux E., 2013, ApJ, 763, L38
Karska A. et al., 2013, A&A, 552, A141
Kristensen L. E. et al., 2012, A&A, 542, A8
Lefloch B., Castets A., Cernicharo J., Langer W. D., Zylka R., 1998, A&A, 334, 269
Loinard L., Torres R. M., Mioduszewski A. J., Rodríguez L. F., 2008, ApJ, 675, L29
Looney L. W., Mundy L. G., Welch W. J., 2000, ApJ, 529, 477
Maezawa H. et al., 1999, ApJ, 524, L129
Marcelino N., Cernicharo J., Roueff E., Gerin M., Mauersberger R., 2005, ApJ, 620, 308
Marcelino N., Cernicharo J., Tercero B., Roueff E., 2009, ApJ, 690, 27
Maret S., Ceccarelli C., Caux E., Tielens A. G. G. M., Castets A., 2002, A&A, 395, 573
Mendoza E., Lefloch B., López-Sepulcre A., Ceccarelli C., Codella C., Boechat-Roberty H. M., Bachiller R., 2014, MNRAS, 445, 151
Müller H. S. P., Thorwirth S., Roth D. A., Winnewisser G., 2001, A&A, 370, L49
Müller H. S. P., Schlöder F., Stutzki J., Winnewisser G., 2005, J. Mol. Struct., 742, 215
Nummelin A., Bergman P., Hjalmarson Å., Friberg P., Irvine W. M., Millar T. J., Ohishi M., Saito S., 2000, ApJS, 128, 213
Parise B., Bergman P., Menten K., 2014, Faraday Discussion, p. 168
Quan D., Herbst E., 2007, A&A, 474, 521
Raunier S., Chiavassa T., Duvernay F., Borget F., Aycard J. P., Dartois E., d'Hendecourt L., 2004, A&A, 416, 65
Redondo P., Barrientos C., Largo A., 2014, ApJ, 780, 181
Rubin R. H., Swenson G. W., Jr, Benson R. C., Tigelaar H. L., Flygare W. H., 1971, ApJ, 169, L39
Saladino R., Botta G., Pino S., Costanzo G., Di Mauro E., 2012, Chem Soc Rev, 41, 5526
Schöier F. L., van der Tak F. F. S., van Dishoeck E. F., Black J. H., 2005, A&A, 432, 369
Shirley Y. L., Evans N. J., II, Rawlings J. M. C., Gregersen E. M., 2000, ApJS, 131, 249
Tóth L. V., Haas M., Lemke D., Mattila K., Onishi T., 2004, A&A, 420, 533
Yamaguchi T. et al., 2012, PASJ, 64, 105

APPENDIX A: COMPARISON BETWEEN GRAPES AND ROTATIONAL DIAGRAM ANALYSES

This section aims to compare the agreement between the rotational diagram and GRAPES methods. As described in Section 4.2.2, the line emission in I16293 does not appear to be well described by LTE, and a more realistic radiative transfer treatment will need to wait until collisional coefficients are available for NH_2CHO. Therefore, we do not consider it here, while it is worth noticing that a rotational diagram analysis is likely too simplistic to analyse the HNCO and NH_2CHO lines in this source.

In OMC-2, the GRAPES analysis tells us that the temperature that separates the inner and outer components is 80 K, in both the LTE and non-LTE approximations. Thus, for consistency in the comparison, we re-computed the inner and outer abundances resulting from the RD analysis using the same inner sizes as in GRAPES, instead of those corresponding to a temperature of the 100 K (see Section 4.2.1). We note that, while the RD analysis allowed for a separation of two components (inner and outer) for IRAS 4A, a single component was sufficient for OMC-2. It should be kept in mind, therefore, that for the latter the comparison is not equivalent, since we are not comparing a two-component solution with another two-component solution as in the case of the other two protostars.

The results of the comparison are listed in Table A1 and illustrated in Fig. A1 , where we present the comparison using both the LTE and non-LTE results from GRAPES. It is evident that LTE and non-LTE yield practically the same results for these two sources. It can also be seen that the errors are quite high in some cases, up to 100 per cent, which are caused by the large uncertainties resulting from the GRAPES analysis. Taking these into account, we find the following behaviours:

(i) HNCO abundance: generally, both methods agree within an order of magnitude, but there is a tendency towards higher values in the RD analysis, by a factor of a few.

Table A1. Comparison between GRAPES and RD analyses.*

	IRAS 4A	OMC-2
Inner size (arcsec)	1.5	3.1
RD-to-GRAPES ratio (LTE)		
X_o(HNCO)	11 ± 4	1.5 ± 0.5
X_i(HNCO)	4 ± 3	>2.5
X_o(NH_2CHO)	1 ± 1	5 ± 5
X_i(NH_2CHO)	0.4 ± 0.4	0.3 ± 0.3
R_o	12 ± 7	0.3 ± 0.3
R_i	11 ± 8	>10
RD-to-GRAPES ratio (non-LTE)		
X_o(HNCO)	11 ± 4	2.1 ± 0.7
X_i(HNCO)	3 ± 2	>22
X_o(NH_2CHO)	1 ± 1	5 ± 5
X_i(NH_2CHO)	0.4 ± 0.4	0.3 ± 0.3
R_o	12 ± 7	0.4 ± 0.4
R_i	7 ± 6	>85

Note. *Abundances with respect to H_2 are times 10^{-11}.

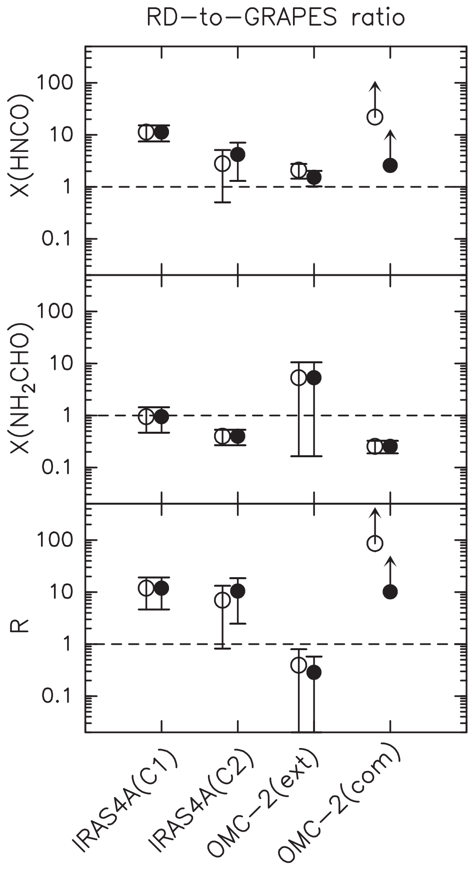

Figure A1. Ratio of RD-to-GRAPES abundances. Top: HNCO abundance. Middle: NH_2CHO abundance. Bottom: HNCO to NH_2CHO abundance ratio. Filled and open circles represent, respectively, the LTE and non-LTE HNCO solution in the GRAPES analysis. The horizontal dashed lines mark equality between RD and GRAPES values.

(ii) NH_2CHO abundance: again, we find agreement within a factor of a few. The compact solution is systematically lower in the RD treatment. This suggests that a non-negligible amount of emission from low-energy molecular lines actually comes from the inner region, and not exclusively from the extended envelope, as assumed in the linear fitting of the RD. Such a finding reflects the necessity of analysis like that performed with GRAPES if we want to properly disentangle the inner and outer components in hot corino or hot core sources.

(iii) HNCO to NH_2CHO abundance ratio, R: in this case, the two analysis methods agree within a factor of a few.

APPENDIX B: TABLES

Table B1. NH_2CHO transitions searched for in this study and 3σ detections.[a]

Transition	ν (MHz)	E_u (K)	A_{ul} (10^{-5} s^{-1})	θ_b (arcsec)	OMC-2	CepE	SVS13A	IRAS4A	I16293	Blends
$4_{1,4}-3_{1,3}$	81 693.446	12.8	3.46	30	N	Y*	N	N	N	
$4_{0,4}-3_{0,3}$	84 542.330	10.2	4.09	29	Y	Y	N	N	Y	
$4_{2,3}-3_{2,2}$	84 807.795	22.1	3.09	29	N	N	N	N	N	
$4_{3,2}-3_{3,1}$	84 888.994	37.0	1.81	29	N	N	N	N	N	
$4_{3,1}-3_{3,0}$	84 890.987	37.0	1.81	29	N	N	N	N	N	
$4_{2,2}-3_{2,1}$	85 093.272	22.1	3.13	29	N	Y	N	N	N	
$4_{1,3}-3_{1,2}$	87 848.873	13.5	4.30	28	Y	Y*	N	N	Y	
$5_{1,5}-4_{1,4}$	102 064.267	17.7	7.06	24	Y	Y	N	B	Y	H_2COH^+?
$5_{0,5}-4_{0,4}$	105 464.219	15.2	8.11	23	Y	Y	Y	Y	Y	
$5_{2,4}-4_{2,3}$	105 972.599	27.2	6.92	23	Y	N	N	N	N	
$5_{4,2}-4_{4,1}$	106 107.870	63.0	2.98	23	N	N	B	B	N	NH_2CHO
$5_{4,1}-4_{4,0}$	106 107.895	63.0	2.98	23	N	N	B	B	N	NH_2CHO
$5_{3,3}-4_{3,2}$	106 134.427	42.1	5.29	23	N	N	N	N	N	
$5_{3,2}-4_{3,1}$	106 141.400	42.1	5.29	23	N	N	N	N	N	
$5_{2,3}-4_{2,2}$	106 541.680	27.2	7.03	23	N	N	N	Y	N	
$5_{1,4}-4_{1,3}$	109 753.503	18.8	8.78	22	N	N	N	N	N	
$6_{1,5}-5_{1,4}$	131 617.902	25.1	15.6	19	Y	–	N	N	N	
$7_{1,7}-6_{1,6}$	142 701.325	30.4	20.2	17	Y	–	Y	Y	N	
$7_{0,7}-6_{0,6}$	146 871.475	28.3	22.5	17	B	–	B	B	B	CH_3OCH_3
$7_{2,6}-6_{2,5}$	148 223.143	40.4	21.2	17	B	–	N	N	B	$HCNH^+$
$7_{6,1}-6_{6,0}$	148 555.852	135.7	6.18	17	N	–	N	N	N	
$7_{6,2}-6_{6,1}$	148 555.852	135.7	6.18	17	N	–	N	N	N	
$7_{5,3}-6_{5,2}$	148 566.822	103.0	11.4	17	N	–	N	N	N	
$7_{5,2}-6_{5,1}$	148 566.823	103.0	11.4	17	N	–	N	N	N	
$7_{4,4}-6_{4,3}$	148 598.970	76.2	15.7	17	N	–	N	N	N	
$7_{4,3}-6_{4,2}$	148 599.354	76.2	15.7	17	N	–	N	N	N	
$7_{3,5}-6_{3,4}$	148 667.301	55.3	19.1	17	Y	–	N	N	N	
$7_{3,4}-6_{3,3}$	148 709.018	55.4	19.1	17	Y	–	Y	N	N	
$7_{6,2}-6_{6,1}$	149 792.574	40.6	21.9	16	N	–	N	N	Y*	
$7_{1,6}-6_{1,5}$	153 432.176	32.5	25.1	16	Y	–	N	N	N	
$13_{2,11}-13_{1,12}$	155 894.300	105.9	1.26	16	N	–	N	N	N	
$12_{2,10}-12_{1,11}$	155 934.098	92.4	1.23	16	N	–	N	N	N	
$11_{2,9}-11_{1,10}$	157 072.457	79.9	1.22	16	N	–	N	N	N	
$14_{2,12}-14_{1,13}$	157 115.035	120.5	1.32	16	N	–	N	N	N	
$10_{2,8}-10_{1,9}$	159 127.569	68.4	1.21	15	–	–	N	N	N	
$15_{2,13}-15_{1,14}$	159 739.080	136.2	1.39	15	–	–	N	N	N	
$9_{2,7}-9_{1,8}$	161 899.774	58.1	1.22	15	–	–	N	N	N	
$8_{1,8}-7_{1,7}$	162 958.657	38.2	30.5	15	–	–	N	Y*	Y	
$8_{2,6}-8_{1,7}$	165 176.756	48.8	1.22	15	–	–	N	N	N	
$8_{0,8}-7_{0,7}$	167 320.697	36.4	33.5	15	–	–	N	Y*	Y	
$7_{2,5}-7_{1,6}$	168 741.408	40.6	1.23	15	–	–	N	N	N	
$8_{2,7}-7_{2,6}$	169 299.154	48.5	32.6	15	–	–	N	N	N	
$8_{6,2}-7_{6,1}$	169 790.683	143.9	15.3	14	–	–	N	N	N	
$8_{6,3}-7_{6,2}$	169 790.683	143.9	15.3	14	–	–	N	N	N	
$8_{5,4}-7_{5,3}$	169 810.709	111.1	21.4	14	–	–	N	N	N	
$8_{5,3}-7_{5,2}$	169 810.715	111.1	21.4	14	–	–	N	N	N	
$8_{4,5}-7_{4,4}$	169 861.469	84.3	26.3	14	–	–	N	N	N	
$8_{4,4}-7_{4,3}$	169 862.523	84.3	26.3	14	–	–	N	N	N	
$8_{3,6}-7_{3,5}$	169955.835	63.5	30.2	14	–	–	N	N	N	
$8_{3,5}-7_{3,4}$	170039.076	63.5	30.3	14	–	–	N	N	Y	
$8_{2,6}-7_{2,5}$	171620.760	48.8	33.9	14	–	–	N	N	N	
$6_{2,4}-6_{1,5}$	172381.012	33.4	1.24	14	–	–	N	N	N	
$10_{1,10}-9_{1,9}$	203335.761	56.8	60.3	12	Y	–	N	N	Y*	
$10_{0,10}-9_{0,9}$	207679.189	55.3	64.7	12	Y	–	N	Y*	N	
$10_{2,9}-9_{2,8}$	211328.960	67.8	65.6	12	Y	–	Y	Y	Y[b]	
$10_{5,6}-9_{5,5}$	212323.555	130.5	52.0	12	N	–	N	N	N	
$10_{5,5}-9_{5,4}$	212323.555	130.5	52.0	12	N	–	N	N	N	

Table B1. – *continued*

Transition	ν (MHz)	E_u (K)	A_{ul} (10^{-5} s^{-1})	θ_b (arcsec)	OMC-2	CepE	SVS13A	IRAS4A	I16293	Blends
$10_{4,7}$–$9_{4,6}$	212428.020	103.7	58.4	12	N	–	N	N	B	NH_2CHO
$10_{4,6}$–$9_{4,5}$	212433.449	103.7	58.4	12	N	–	N	N	B	NH_2CHO
$10_{3,8}$–$9_{3,7}$	212572.837	82.9	63.3	12	Y	–	Y	N	N	
$10_{3,7}$–$9_{3,6}$	212 832.307	82.9	63.6	12	N	–	N	N	N	
$10_{2,8}$–$9_{2,7}$	215 687.009	68.4	69.8	11	Y	–	N	N	Y	
$10_{1,9}$–$9_{1,8}$	218 459.213	60.8	74.7	11	B	–	N	N	N	CH_3OH
$11_{1,11}$–$10_{1,10}$	223 452.512	67.5	80.5	11	Y	–	N	N	N	
$11_{0,11}$–$10_{0,10}$	227 605.658	66.2	85.5	11	Y	–	N	N	N	
$11_{2,10}$–$10_{2,9}$	232 273.646	78.9	88.2	11	N	–	N	N	Y	
$11_{5,7}$–$10_{5,6}$	233 594.501	141.7	73.6	11	N	–	B	N	N	
$11_{5,6}$–$10_{5,5}$	233 594.501	141.7	73.6	11	N	–	B	N	N	
$11_{4,8}$–$10_{4,7}$	233 734.724	114.9	80.7	11	N	–	Y	N	N	
$11_{4,7}$–$10_{4,6}$	233 745.613	114.9	80.7	11	N	–	Y	N	N	
$11_{3,9}$–$10_{3,8}$	233 896.577	94.1	86.2	11	Y	–	Y	N	Y	
$11_{3,8}$–$10_{3,7}$	234 315.498	94.2	86.7	10	–	–	N	N	N	
$11_{2,9}$–$10_{2,8}$	237 896.684	79.9	94.8	10	Y	–	Y	N	B	?
$11_{1,10}$–$10_{1,9}$	239 951.800	72.3	99.6	10	Y	–	Y	N	N	
$12_{1,12}$–$11_{1,11}$	243 521.044	79.2	105	10	N	–	B	N	B	CH_2DOH
$12_{0,12}$–$11_{0,11}$	247 390.719	78.1	110	10	N	–	N	N	N	
$12_{2,11}$–$11_{2,10}$	253 165.793	91.1	115	10	Y	–	N	N	N	
$12_{4,9}$–$11_{4,8}$	255 058.533	127.2	108	10	Y*	–	Y*	N	N	
$12_{4,8}$–$11_{4,7}$	255 078.912	127.2	108	10	N	–	N	N	N	
$12_{3,10}$–$11_{3,9}$	255 225.651	106.4	114	10	Y	–	Y	N	N	
$12_{3,9}$–$11_{3,8}$	255 871.830	106.4	115	10	Y	–	N	N	N	
$12_{2,10}$–$11_{2,9}$	260 189.090	92.4	125	9	B	–	B	N	B	H_2C_2O
$12_{1,11}$–$11_{1,10}$	261 327.450	84.9	129	9	N	–	Y	N	N	
$13_{1,13}$–$12_{1,12}$	263 542.236	91.8	133	9	Y	–	Y	N	N	

Notes. [a]Y: Detected above $T_{mb} = 3\sigma$. Y*: Weakly detected (S/N ~ 2–3; see Section 4.1). N: undetected. B: possibly detected but blended. —: not observed.

[b]Detected but with an anomalously high flux (maybe blended): removed from analysis.

Table B2. HNCO transitions searched for in this study and 3σ detections.[a]

Transition	ν (MHz)	E_u (K)	A_{ul} (10^{-5} s^{-1})	θ_b (arcsec)	OMC-2	CepE	SVS13A	IRAS4A	I16293	L1157	L1527	B1	L1544	TMC-1
$4_{1,4}$–$3_{1,3}$	87 597.330	53.8	0.80	28	N	N	Y	Y[b]	N	N	N	N	N	–
$4_{0,4}$–$3_{0,3}$	87 925.237	10.5	0.88	28	Y	Y	Y	Y	Y	Y	Y	Y	Y	–
$4_{1,3}$–$3_{1,2}$	88 239.020	53.9	0.82	28	Y*	N	Y*	Y[b]	N	N	N	N	N	–
$5_{1,5}$–$4_{1,4}$	109 495.996	59.0	1.7	22	N	N	Y	N	Y	W	N	N	N	**N**
$5_{0,5}$–$4_{0,4}$	109 905.749	15.8	1.8	22	Y	Y	Y	Y	Y	Y	Y	Y	Y	**Y**
$5_{1,4}$–$4_{1,3}$	110 298.089	59.2	1.7	22	Y*	N	Y	N	Y	N	N	N	N	**N**
$6_{1,6}$–$5_{1,5}$	131 394.230	65.3	2.9	19	N	N	Y	N	Y	N	N	N	–	**N**
$6_{0,6}$–$5_{0,5}$	131 885.734	22.2	3.1	19	Y	Y	Y	Y	Y	Y	Y	Y	–	**Y**
$6_{1,5}$–$5_{1,4}$	132 356.701	65.5	3.0	19	N	N	N	N	Y	Y	N	N	–	**N**
$7_{1,7}$–$6_{1,6}$	153 291.935	72.7	4.7	16	N	–	Y	N	Y	N	N	N	–	**N**
$7_{0,7}$–$6_{0,6}$	153 865.086	29.5	4.9	16	Y	–	Y	Y	Y	Y	Y	Y	–	**Y**
$7_{1,6}$–$6_{1,5}$	154 414.765	72.9	4.8	16	N	–	Y	N	Y	N	N	N	–	**N**
$10_{1,10}$–$9_{1,9}$	218 981.009	101.1	14.2	11	N	N	Y	N	Y	N	N	N	–	–
$10_{0,10}$–$9_{0,9}$	219 798.274	58.0	14.7	11	Y	Y	Y	Y	Y	N	N	Y	–	–
$10_{1,9}$–$9_{1,8}$	220 584.751	101.5	14.5	11	Y	N	Y	Y	Y	N	N	N	–	–
$11_{1,11}$–$10_{1,10}$	240 875.727	112.6	19.0	10	N	–	Y	Y	Y	N	N	N	–	–
$11_{0,11}$–$10_{0,10}$	241 774.032	69.6	19.6	10	B	–	B	B	B	N	N	N	–	–
$11_{1,10}$–$10_{1,9}$	242 639.704	113.1	19.5	10	N	–	Y	N	N	N	N	–	–	
$12_{1,12}$–$11_{1,11}$	262 769.477	125.3	24.8	9	N	N	Y	Y	Y[c]	N	N	N	–	–
$12_{0,12}$–$11_{0,11}$	263 748.625	82.3	25.6	9	Y	Y	Y	Y	Y	N	N	N	–	–
$12_{1,11}$–$11_{1,10}$	264 693.655	125.9	25.4	9	N	N	Y	Y	Y	N	N	N	–	–

Notes. [a]Y: Detected above $T_{mb} = 3\sigma$. Y*: Weakly detected (S/N ~ 2–3; see Section 4.1). N: undetected. B: detected but blended. —: not observed.

[b]Detected but with an anomalously high flux (maybe blended): removed from analysis.

[c]Blended with an unidentified feature: removed from analysis.

Blends: CH_3OH at 241.774 GHz

Table B3. L1544: Gaussian fits to the detected HNCO lines.

Transition	ν (MHz)	rms (mK)	$T_{\rm peak}$ (mK)	$V_{\rm lsr}$ (km s^{-1})	ΔV (km s^{-1})	$\int T_{\rm mb} {\rm d}V$ (mK km s^{-1})
$4_{0,4}$–$3_{0,3}$	87925.237	11.9	459 (2)	7.2 (1)	0.7 (2)	342 (9)
$5_{0,5}$–$4_{0,4}$	109905.996	4.8	601 (2)	7.6 (1)	0.7 (1)	448 (5)

Table B4. TMC-1: Gaussian fits to the detected HNCO lines.

Transition	ν (MHz)	rms (mK)	$T_{\rm peak}$ (mK)	$V_{\rm lsr}$ (km s^{-1})	ΔV (km s^{-1})	$\int T_{\rm mb} {\rm d}V$ (mK km s^{-1})
$5_{0,5}$–$4_{0,4}$	109 905.996	6.8	157 (8)	5.8 (1)	1.2 (1)	203 (11)
$6_{0,6}$–$5_{0,5}$	131 885.734	6.7	94 (7)	5.8 (1)	0.5 (3)	50 (5)
$7_{0,7}$–$6_{0,6}$	153 865.086	3.2	28 (3)	5.9 (1)	0.5 (4)	15 (2)

Table B5. B1: Gaussian fits to the detected HNCO lines.

Transition	ν (MHz)	rms (mK)	$T_{\rm peak}$ (mK)	$V_{\rm lsr}$ (km s^{-1})	ΔV (km s^{-1})	$\int T_{\rm mb} {\rm d}V$ (mK km s^{-1})
$4_{0,4}$–$3_{0,3}$	87 925.237	3.0	530 (12)	6.7 (1)	1.4 (1)	765 (5)
$5_{0,5}$–$4_{0,4}$	109 905.996	22.2	480 (6)	6.6 (1)	1.3 (1)	662 (32)
$6_{0,6}$–$5_{0,5}$	131 885.734	6.3	345 (7)	6.7 (1)	1.4 (1)	521 (8)
$7_{0,7}$–$6_{0,6}$	153 865.086	7.4	224 (6)	6.6 (1)	1.4 (1)	326 (10)

Table B6. L1527: Gaussian fits to the detected HNCO lines.

Transition	ν (MHz)	rms (mK)	$T_{\rm peak}$ (mK)	$V_{\rm lsr}$ (km s^{-1})	ΔV (km s^{-1})	$\int T_{\rm mb} {\rm d}V$ (mK km s^{-1})
$4_{0,4}$–$3_{0,3}$	87 925.237	2.3	145 (2)	5.9 (1)	1.3 (1)	198 (3)
$5_{0,5}$–$4_{0,4}$	109 905.996	7.9	135 (7)	5.9 (1)	1.2 (1)	175 (11)
$6_{0,6}$–$5_{0,5}$	131 885.734	6.7	138 (1)	5.9 (1)	0.8 (1)	115 (8)
$7_{0,7}$–$6_{0,6}$	153 865.086	8.0	63 (1)	5.8 (1)	0.7 (1)	47 (6)

Table B7. L1157mm: Gaussian fits to the detected HNCO lines.

Transition	ν (MHz)	rms (mK)	$T_{\rm peak}$ (mK)	$V_{\rm lsr}$ (km s^{-1})	ΔV (km s^{-1})	$\int T_{\rm mb} {\rm d}V$ (mK km s^{-1})
$4_{0,4}$–$3_{0,3}$	87 925.237	3.3	113 (7)	2.6 (1)	1.6 (1)	198 (7)
$5_{0,5}$–$4_{0,4}$	109 905.996	7.8	142 (5)	2.5 (1)	1.2 (1)	177 (13)
$6_{0,6}$–$5_{0,5}$	131 885.734	5.5	81 (3)	2.6 (1)	1.5 (1)	126 (11)
$7_{0,7}$–$6_{0,6}$	153 865.086	5.3	71 (1)	2.6 (1)	1.1 (1)	81 (8)

Table B8. IRAS 4A: Gaussian fits to the detected NH_2CHO and HNCO lines.

Transition	ν (MHz)	rms (mK)	$T_{\rm peak}$ (mK)	$V_{\rm lsr}$ (km s^{-1})	ΔV (km s^{-1})	$\int T_{\rm mb}{\rm d}V$ (mK km s^{-1})
NH_2CHO						
$5_{0,5}-4_{0,4}$	105 464.219	3.3	9.8 (1)	6.7 (4)	4.0 (13)	41 (11)
$5_{2,3}-4_{2,2}$	106 541.680	2.2	7.7 (17)	7.6 (3)	2.8 (9)	23 (5)
$7_{1,7}-6_{1,6}$	142 701.325	5.0	15 (4)	8.1 (3)	2.6 (5)	40 (8)
$8_{1,8}-7_{1,7}{}^{\rm w}$	162 958.657	38.2	14 (6)	8.5 (4)	2.9 (7)	44 (9)
$8_{0,8}-7_{0,7}{}^{\rm w}$	167 320.697	36.4	13 (4)	7.2 (4)	3.2 (7)	43 (10)
$10_{0,10}-9_{0,9}{}^{\rm w}$	207 679.189	55.3	19 (10)	6.6 (5)	3.3 (10)	66 (19)
$10_{2,9}-9_{2,8}$	211 328.960	7.1	31 (3)	6.7 (2)	2.4 (5)	82 (15)
HNCO						
$4_{0,4}-3_{0,3}$	87 925.237	3.1	195 (16)	7.2 (1)	2.2 (1)	458 (6)
$5_{0,5}-4_{0,4}$	109 905.749	8.0	198 (15)	7.1 (1)	2.3 (1)	495 (16)
$6_{0,6}-5_{0,5}$	131 885.734	5.9	203 (12)	7.0 (1)	2.5 (1)	545 (11)
$7_{0,7}-6_{0,6}$	153 865.086	6.8	168 (11)	7.1 (1)	2.2 (1)	395 (12)
$10_{0,10}-9_{0,9}$	219 798.274	9.0	88 (8)	6.8 (1)	3.3 (3)	307 (19)
$10_{1,9}-9_{1,8}$	220 584.751	6.8	37 (6)	6.5 (3)	2.8 (7)	111 (22)
$11_{1,11}-10_{1,10}$	240 875.727	7.2	23 (2)	6.6 (2)	1.7 (6)	42 (13)
$12_{1,12}-11_{1,11}$	262 769.477	8.9	44 (4)	6.6 (2)	3.8 (6)	177 (21)
$12_{0,12}-11_{0,11}$	263 748.625	12.9	54 (4)	6.5 (8)	3.9 (29)	230 (130)
$12_{1,11}-11_{1,10}$	264 693.655	9.1	26 (5)	6.3 (4)	3.7 (9)	103 (21)

Note. $^{\rm w}$ Transition weakly detected (see Table B1) but included in the analysis for completeness.

Table B9. I16293: Gaussian fits to the detected NH_2CHO and HNCO lines (intensity in $T^*_{\rm ant}$ units).

Transition	ν (MHz)	rms (mK)	$T_{\rm peak}$ (mK)	$V_{\rm lsr}$ (km s^{-1})	ΔV (km s^{-1})	$\int T_{\rm a}{\rm d}V$ (mK km s^{-1})
NH_2CHO						
$4_{0,4}-3_{0,3}$	84 542.330	5.3	17 (6)	3.2 (12)	6.7 (20)	120 (40)
$4_{1,3}-3_{1,2}$	87 848.873	2.6	12 (4)	2.6 (5)	3.8 (11)	50 (13)
$5_{1,5}-4_{1,4}$	102 064.267	3.3	16 (5)	2.0 (3)	2.4 (9)	42 (12)
$5_{0,5}-4_{0,4}$	105 464.219	5.3	20 (7)	5.1 (4)	3.0 (10)	64 (19)
$7_{6,2}-6_{6,1}{}^{\rm w}$	149 792.574	10.0	29 (10)	2.6 (4)	3.0 (7)	93 (22)
$8_{1,8}-7_{1,7}$	162 958.657	10.1	26 (10)	2.8 (4)	2.5 (13)	69 (27)
$8_{0,8}-7_{0,7}$	167 320.697	10.6	55 (11)	2.0 (2)	2.3 (5)	136 (24)
$8_{3,5}-7_{3,4}$	170 039.076	15.3	50 (80)	2.7 (17)	2.4 (46)	120 (170)
$10_{1,10}-9_{1,9}{}^{\rm w}$	203 335.761	6.8	19 (7)	0.5 (10)	6.7 (27)	135 (43)
$10_{2,8}-9_{2,7}$	215 687.009	5.5	30 (10)	1.0 (13)	5.5 (34)	175 (90)
$11_{2,10}-10_{2,9}$	232 273.646	4.6	23 (18)	1.5 (19)	5.0 (39)	120 (90)
$11_{2,9}-10_{2,8}$	237 896.684	8.2	45 (9)	2.8 (3)	3.1 (15)	148 (42)
HNCO						
$4_{0,4}-3_{0,3}$	87 925.237	3.2	162 (3)	4.0 (1)	3.9 (1)	671 (11)
$5_{1,5}-4_{1,4}$	109 495.996	5.4	38 (6)	2.0 (3)	4.5 (11)	182 (35)
$5_{0,5}-4_{0,4}$	109 905.749	5.9	254 (6)	3.9 (1)	3.2 (1)	853 (18)
$5_{1,4}-4_{1,3}$	110 298.089	5.4	16 (5)	5.4 (6)	5.4 (18)	90 (23)
$6_{1,6}-5_{1,5}$	131 394.230	5.4	39 (17)	2.5 (8)	5.2 (27)	217 (88)
$6_{0,6}-5_{0,5}$	131 885.734	7.3	263 (8)	3.9 (1)	3.0 (1)	825 (18)
$6_{1,5}-5_{1,4}$	132 356.701	6.9	39 (8)	3.6 (5)	5.3 (13)	218 (48)
$7_{1,7}-6_{1,6}$	153 291.935	9.5	73 (27)	5.1 (5)	3.0 (16)	230 (90)
$7_{0,7}-6_{0,6}$	153 865.086	12.3	224 (18)	3.9 (1)	4.0 (3)	950 (50)
$7_{1,6}-6_{1,5}$	154 414.765	11.1	57 (28)	2.7 (7)	3.4 (21)	200 (90)
$10_{1,10}-9_{1,9}$	218 981.009	6.2	103 (8)	2.8 (2)	6.0 (5)	664 (47)
$10_{0,10}-9_{0,9}$	219 798.274	4.4	260 (12)	3.3 (1)	5.7 (3)	1580 (60)
$10_{1,9}-9_{1,8}$	220 584.751	6.4	85 (10)	2.9 (3)	6.2 (7)	560 (50)
$11_{1,11}-10_{1,10}$	240 875.727	14.5	132 (16)	2.8 (3)	6.6 (9)	930 (100)
$12_{0,12}-11_{0,11}$	263 748.625	7.9	270 (70)	3.7 (6)	5.6 (15)	1640 (360)
$12_{1,11}-11_{1,10}$	264 693.655	6.9	119 (11)	3.4 (2)	6.6 (6)	840 (60)

Note. $^{\rm w}$ Transition weakly detected (see Table B1) but included in the analysis for completeness.

Table B10. SVS13A: Gaussian fits to the detected NH_2CHO and HNCO lines.

Transition	ν (MHz)	rms (mK)	T_{peak} (mK)	V_{lsr} (km s^{-1})	ΔV (km s^{-1})	$\int T_{mb}dV$ (mK km s^{-1})
			NH_2CHO			
$5_{0,5}$–$4_{0,4}$	105 464.219	3.9	16 (1)	8.1 (2)	1.8 (5)	14 (1)
$7_{1,7}$–$6_{1,6}$	142 701.325	6.4	28 (3)	8.6 (2)	2.2 (5)	22 (5)
$7_{3,4}$–$6_{3,3}$	148 709.018	7.1	26 (2)	7.1 (3)	2.2 (7)	22 (3)
$10_{2,9}$–$9_{2,8}$	211 328.960	7.3	62 (5)	7.5 (5)	4.4 (14)	31 (2)
$10_{3,8}$–$9_{3,7}$	212 572.837	7.2	43 (7)	8.4 (2)	2.7 (6)	29 (2)
$11_{4,8}$–$10_{4,7}$	233 734.724	6.6	26 (2)	6.9 (4)	3.0 (9)	23 (5)
$11_{4,7}$–$10_{4,6}$	233 745.613	7.5	26 (2)	8.2 (3)	1.5 (7)	26 (1)
$11_{3,9}$–$10_{3,8}$	233 896.577	6.6	49 (14)	8.2 (4)	2.9 (9)	20 (3)
$11_{2,9}$–$10_{2,8}$	237 896.684	6.9	48 (6)	8.1 (3)	4.3 (8)	28 (4)
$11_{1,10}$–$10_{1,9}$	239 951.800	8.1	66 (7)	7.6 (4)	3.4 (9)	23 (2)
$12_{3,10}$–$11_{3,9}$	255 225.651	5.6	45 (2)	8.8 (12)	3.3 (36)	24 (4)
$12_{1,11}$–$11_{1,10}$	261 327.450	8.7	26 (2)	8.4 (2)	4.6 (6)	38 (5)
$13_{1,13}$–$12_{1,12}$	263 542.236	7.6	54 (5)	7.7 (6)	4.4 (15)	32 (5)
			HNCO			
$4_{1,4}$–$3_{1,3}$	87 597.330	3.5	11 (3)	6.4 (4)	3.3 (8)	40 (9)
$4_{0,4}$–$3_{0,3}$	87 925.237	9.1	46 (4)	8.6 (2)	3.1 (6)	155 (23)
$4_{1,3}$–$3_{1,2}{}^{w}$	88 239.020	3.0	13 (3)	7.3 (4)	3.3 (20)	45 (17)
$5_{1,5}$–$4_{1,4}$	109 495.996	3.9	16 (1)	7.1 (2)	2.0 (5)	35 (8)
$5_{0,5}$–$4_{0,4}{}^{*}$	109 905.749	5.4	76 (5)	8.5 (1)	1.2 (1)	100 (8)
$5_{1,4}$–$4_{1,3}$	110 298.089	6.2	28 (4)	8.2 (3)	4.7 (8)	139 (19)
$6_{1,6}$–$5_{1,5}$	131 394.230	6.6	19 (3)	8.2 (4)	3.6 (8)	72 (15)
$6_{0,6}$–$5_{0,5}{}^{*}$	131 885.734	6.0	77 (10)	8.5 (1)	1.6 (3)	129 (15)
$7_{1,7}$–$6_{1,6}$	153 291.935	5.7	25 (2)	8.5 (5)	5.1 (13)	140 (30)
$7_{0,7}$–$6_{0,6}{}^{*}$	153 865.086	6.1	70 (6)	7.5 (1)	3.4 (5)	258 (19)
$7_{1,6}$–$6_{1,5}$	154 414.765	6.0	32 (3)	8.3 (6)	4.4 (15)	149 (40)
$10_{1,10}$–$9_{1,9}$	218 981.009	6.8	46 (3)	8.2 (2)	4.3 (4)	212 (15)
$10_{0,10}$–$9_{0,9}$	219 798.274	7.1	89 (4)	8.4 (1)	3.2 (2)	309 (16)
$10_{1,9}$–$9_{1,8}$	220 584.751	6.0	35 (3)	8.5 (4)	3.7 (9)	136 (27)
$11_{1,11}$–$10_{1,10}$	240 875.727	6.7	46 (4)	8.2 (5)	4.9 (17)	236 (66)
$11_{1,10}$–$10_{1,9}$	242 639.704	8.7	42 (5)	8.1 (3)	4.6 (6)	206 (24)
$12_{1,12}$–$11_{1,11}$	262 769.477	9.9	68 (4)	8.5 (2)	5.3 (5)	380 (32)
$12_{0,12}$–$11_{0,11}$	263 748.625	9.3	60 (5)	8.2 (4)	3.4 (9)	213 (48)
$12_{1,11}$–$11_{1,10}$	264 693.655	8.9	39 (4)	8.5 (3)	4.4 (6)	183 (23)

Notes. * Transition affected by emission at OFF position: lower limit point in the rotational diagram.

^{w} Transition weakly detected (see Table B1) but included in the analysis for completeness.

Table B11. Cep E: Gaussian fits to the detected NH_2CHO and HNCO lines.

Transition	ν (MHz)	rms (mK)	T_{peak} (mK)	V_{lsr} (km s^{-1})	ΔV (km s^{-1})	$\int T_{mb}dV$ (mK km s^{-1})
			NH_2CHO			
$4_{0,4}$–$3_{0,3}$	84 542.330	1.9	7.7 (1)	−11.5 (4)	2.8 (10)	23 (7)
$4_{2,2}$–$3_{2,1}$	85 093.272	1.3	4.3 (1)	−11.8 (3)	3.5 (7)	16 (3)
$4_{1,3}$–$3_{1,2}{}^{w}$	87 848.873	1.2	6.3 (1)	−10.5 (2)	2.6 (5)	17 (3)
$5_{1,5}$–$4_{1,4}$	102 064.267	1.6	7.6 (1)	−10.6 (2)	1.7 (5)	13 (3)
$5_{0,5}$–$4_{0,4}$	105 464.219	2.1	4.1 (1)	−10.6 (6)	2.9 (11)	13 (4)
			HNCO			
$4_{0,4}$–$3_{0,3}$	87 925.237	1.4	90 (4)	−11.1 (1)	1.9 (1)	179 (3)
$5_{0,5}$–$4_{0,4}$	109 905.749	2.8	104 (12)	−11.1 (1)	2.4 (1)	262 (6)
$6_{0,6}$–$5_{0,5}$	131 885.734	7.8	128 (9)	−11.1 (1)	2.2 (3)	299 (23)
$10_{0,10}$–$9_{0,9}$	219 798.274	7.5	45 (10)	−10.1 (73)	8.0 (80)	380 (65)
$12_{0,12}$–$11_{0,11}$	263 748.625	6.0	38 (8)	−10.2 (5)	5.6 (14)	226 (45)

Note. ^{w} Transition weakly detected (see Table B1) but included in the analysis for completeness.

Table B12. OMC-2 FIR 4: Gaussian fits to the detected NH_2CHO and HNCO lines.

Transition	ν (MHz)	rms (mK)	T_{peak} (mK)	V_{lsr} (km s^{-1})	ΔV (km s^{-1})	$\int T_{\mathrm{mb}} \mathrm{d}V$ (mK km s^{-1})
			NH_2CHO			
$4_{0,4}$–$3_{0,3}$	84 542.330	2.8	15 (2)	10.8 (2)	2.2 (4)	35 (5)
$4_{1,3}$–$3_{1,2}$	87 848.873	2.8	9 (2)	11.0 (4)	3.6 (6)	37 (7)
$5_{1,5}$–$4_{1,4}$	102 064.267	3.5	15 (1)	11.0 (2)	2.9 (5)	46 (6)
$5_{0,5}$–$4_{0,4}$	105 464.219	4.7	16 (1)	11.5 (4)	3.7 (10)	64 (15)
$5_{2,4}$–$4_{2,3}$	105 972.599	4.6	15 (5)	11.3 (2)	1.7 (5)	28 (8)
$6_{1,5}$–$5_{1,4}$	131 617.902	5.6	29 (3)	11.2 (2)	3.8 (6)	115 (13)
$7_{1,7}$–$6_{1,6}$	142 701.325	6.4	28 (3)	11.5 (2)	3.1 (7)	91 (14)
$7_{3,4}$–$6_{3,3}$	148 709.018	5.6	26 (2)	11.5 (2)	1.8 (5)	51 (10)
$7_{1,6}$–$6_{1,5}$	153 432.176	8.2	40 (3)	11.8 (3)	2.7 (10)	114 (31)
$10_{1,10}$–$9_{1,9}$	203 335.761	10.8	52 (4)	11.3 (2)	2.8 (5)	156 (20)
$10_{0,10}$–$9_{0,9}$	207 679.189	8.8	49 (3)	11.6 (1)	1.8 (4)	97 (14)
$10_{3,8}$–$9_{3,7}$	212 572.837	12.7	43 (7)	11.7 (3)	2.9 (6)	131 (23)
$11_{1,11}$–$10_{1,10}$	223 452.512	12.6	44 (6)	11.7 (5)	3.0 (12)	142 (48)
$11_{0,11}$–$10_{0,10}$	227 605.658	14.5	61 (10)	11.9 (3)	3.7 (7)	237 (33)
$11_{3,9}$–$10_{3,8}$	233 896.577	16.9	49 (14)	11.6 (3)	2.9 (10)	151 (36)
$11_{2,9}$–$10_{2,8}$	237 896.684	10.1	48 (6)	11.4 (2)	3.7 (6)	186 (23)
$11_{1,10}$–$10_{1,9}$	239 951.800	10.5	66 (7)	11.5 (1)	2.5 (4)	175 (21)
$12_{2,11}$–$11_{2,10}$	253 165.793	12.4	44 (9)	11.2 (3)	3.2 (7)	152 (27)
$12_{4,9}$–$11_{4,8}{}^{\mathrm{w}}$	255 058.533	12.5	39 (12)	11.6 (2)	1.9 (4)	80 (17)
$12_{3,10}$–$11_{3,9}$	255 225.651	11.4	45 (2)	11.5 (4)	1.6 (9)	74 (4)
$12_{3,9}$–$11_{3,8}$	255 871.830	11.8	41 (7)	11.8 (2)	2.7 (5)	119 (19)
			HNCO			
$4_{0,4}$–$3_{0,3}$	87 925.237	2.8	128 (13)	11.2 (1)	2.5 (1)	344 (6)
$4_{1,3}$–$3_{1,2}{}^{\mathrm{w}}$	88 239.020	2.3	9 (2)	12.7 (3)	3.1 (6)	31 (5)
$5_{0,5}$–$4_{0,4}$	109 905.749	6.9	224 (22)	11.4 (1)	2.1 (1)	512 (14)
$5_{1,4}$–$4_{1,3}{}^{\mathrm{w}}$	110 298.089	6.2	18 (5)	12.8 (2)	1.4 (5)	26 (7)
$6_{0,6}$–$5_{0,5}$	131 885.734	4.7	267 (27)	11.2 (1)	2.7 (1)	775 (11)
$7_{0,7}$–$6_{0,6}$	153 865.086	8.8	304 (38)	11.2 (1)	3.0 (4)	962 (89)
$10_{0,10}$–$9_{0,9}$	219 798.274	9.2	343 (28)	11.4 (1)	2.5 (1)	918 (17)
$10_{1,9}$–$9_{1,8}$	220 584.751	11.0	36 (1)	11.7 (4)	2.1 (13)	79 (35)
$12_{0,12}$–$11_{0,11}$	263 748.625	5.1	202 (9)	11.9 (3)	3.0 (5)	648 (24)

Note. $^{\mathrm{w}}$ Transition weakly detected (see Table B1) but included in the analysis for completeness.

APPENDIX C: FIGURES

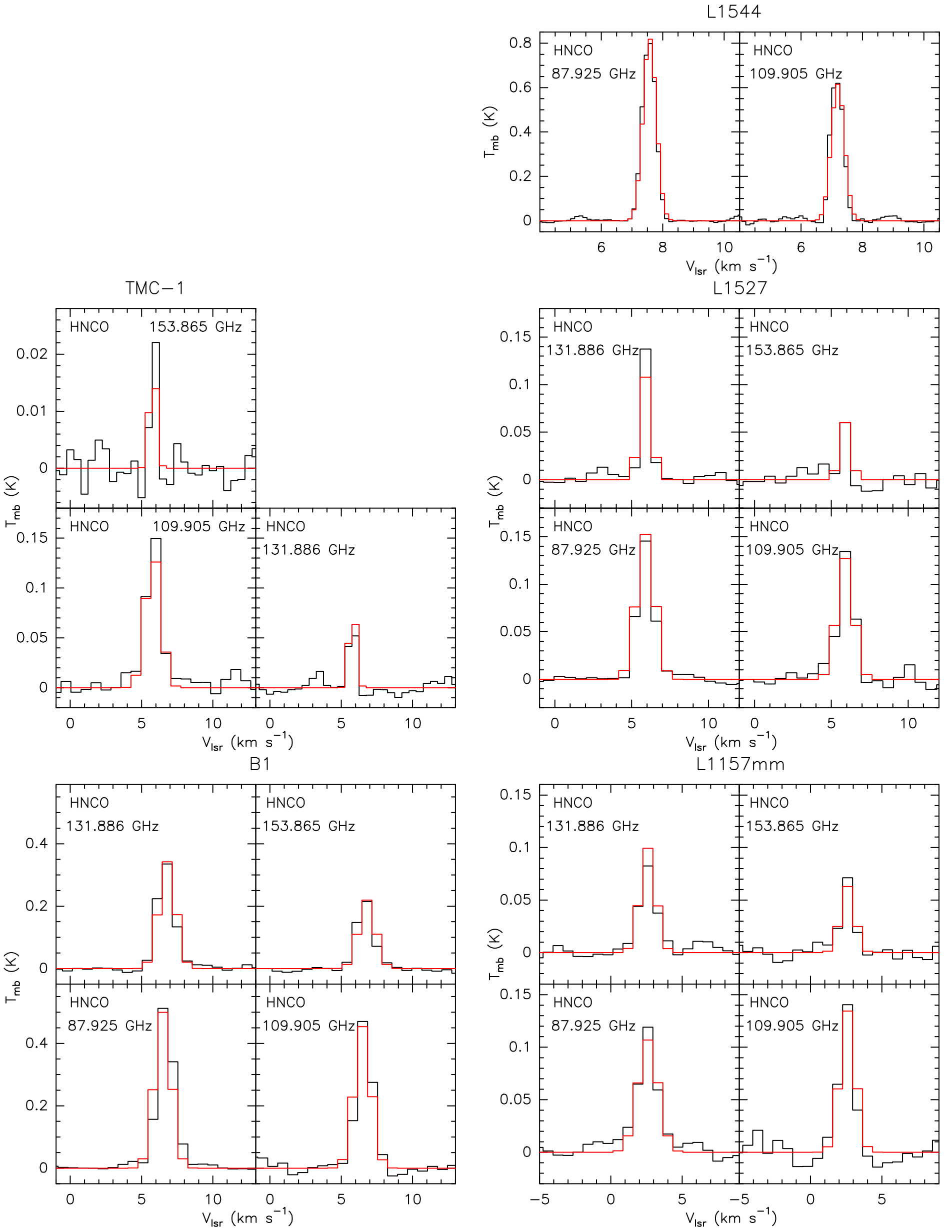

Figure C1. HNCO observed spectral lines (black) in L1544, TMC-1, B1, L1527, and L1157mm, and the spectra predicted by best-fitting LTE model (red).

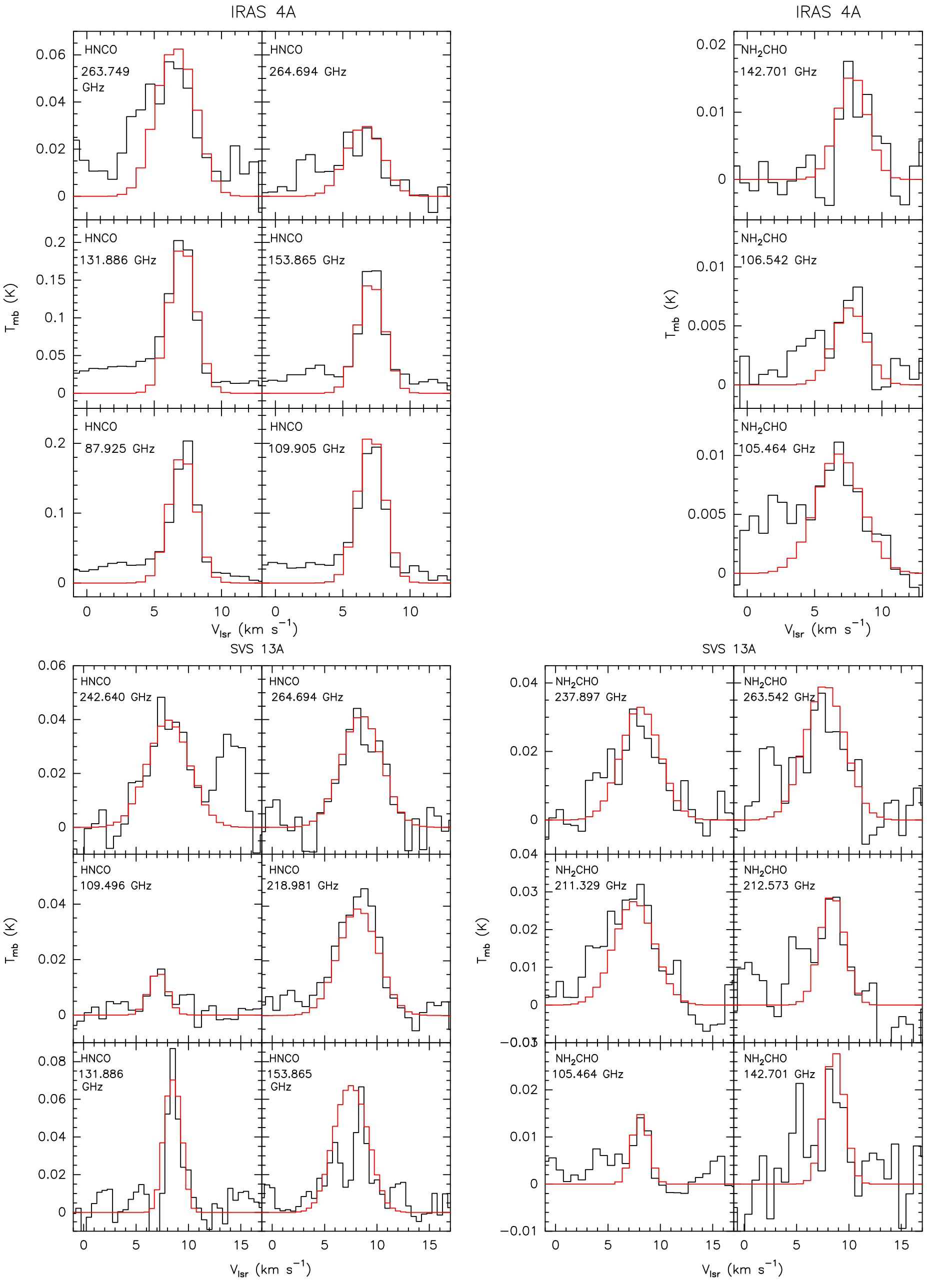

Figure C2. Sample of HNCO (left) and NH_2CHO (right) observed spectral lines (black) in IRAS 4A and SVS13A (compact solution), and the spectra predicted by best-fitting LTE model (red).

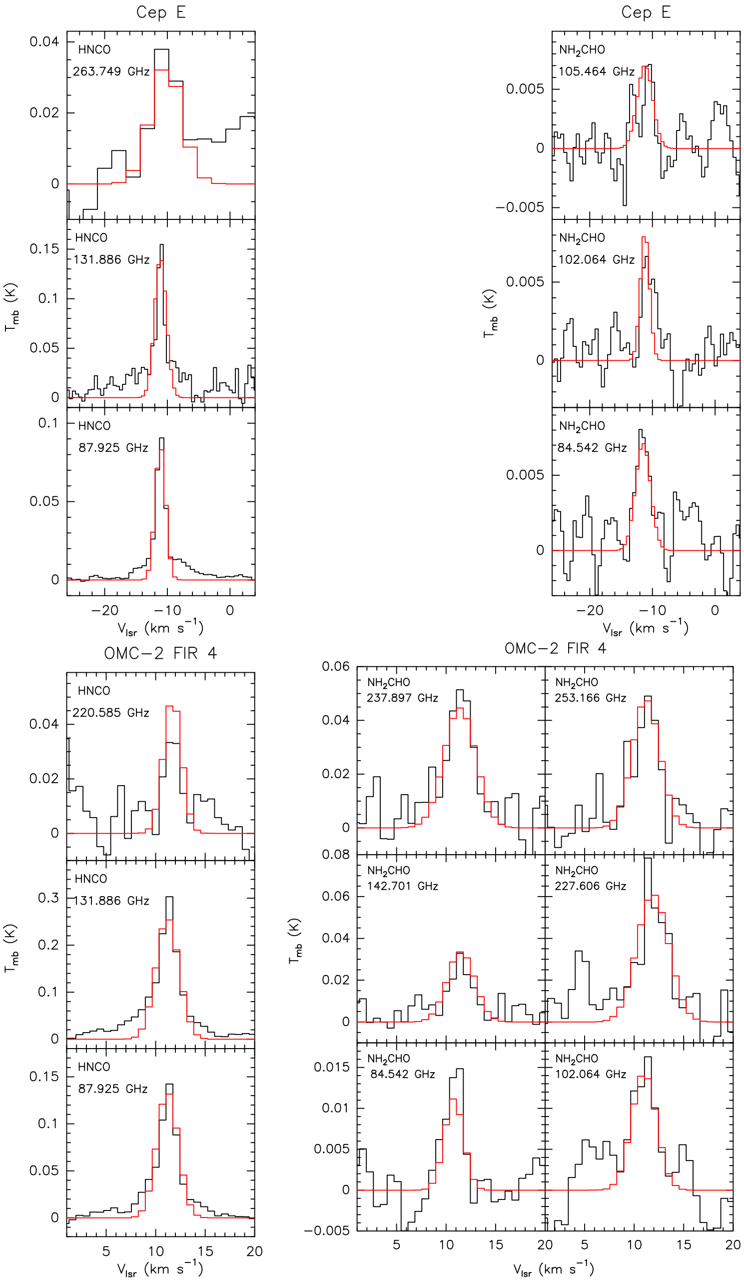

Figure C3. Sample of HNCO (left) and NH_2CHO (right) observed spectral lines (black) in Cep E and OMC-2 FIR 4 (extended solutions), and the spectra predicted by best-fitting LTE model (red).

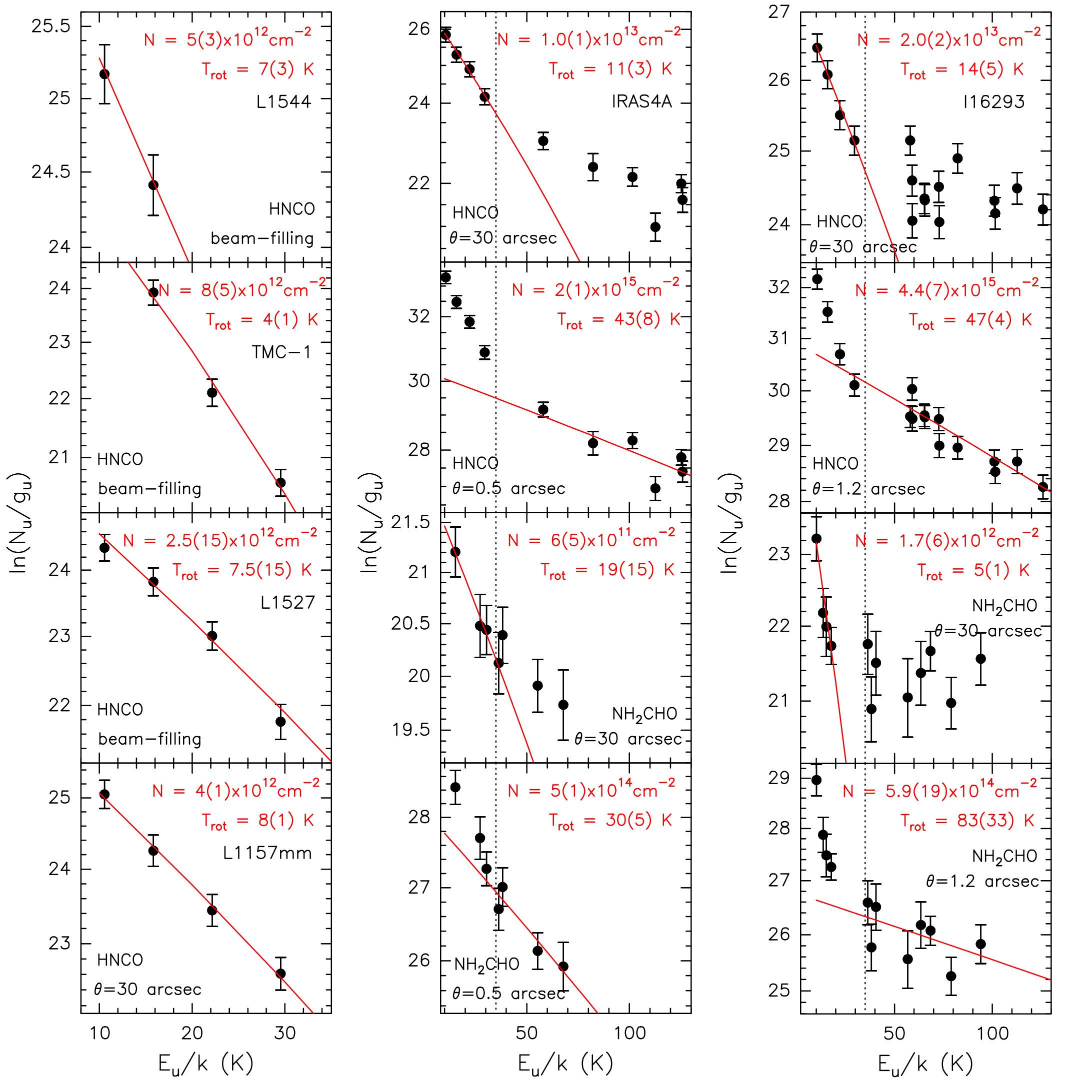

Figure C4. Rotational diagrams for L1544, TMC-1, L1527, and L1157mm (left), IRAS 4A (middle), and I16293 (right). Data points are depicted in black. The red lines correspond to the best fit to the data points. The dashed vertical lines in the middle and right panels indicate the upper-level energy (35 K) at which the division of the two-component fitting was made.

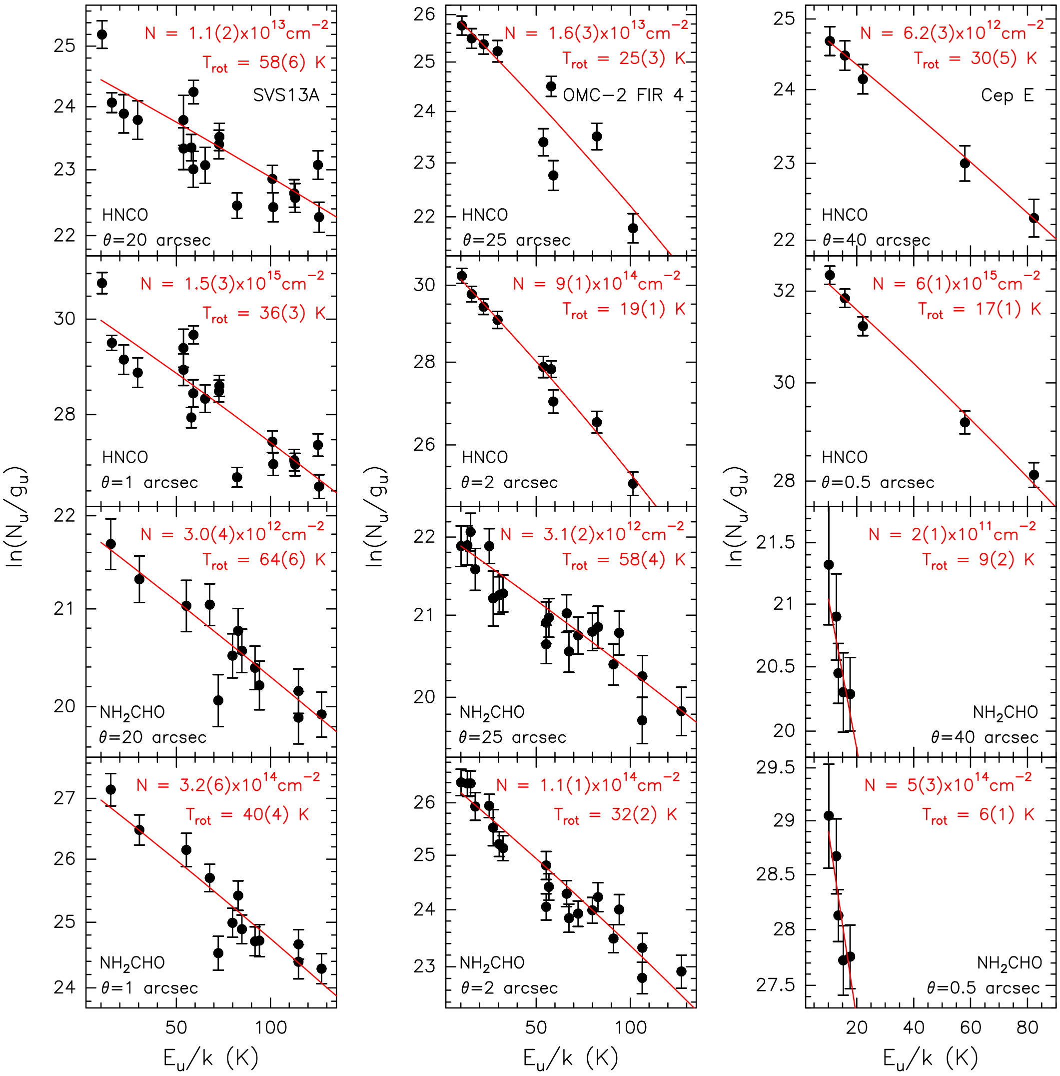

Figure C5. Rotational diagrams for SVS13A (left), OMC-2 FIR 4 (middle), and Cep E (right). Data points are depicted in black. The red lines correspond to the best fit to the data points.

This paper has been typeset from a TEX/LATEX file prepared by the author.

Bibliography

Adams, F. C. & Shu, F. H. 1986, ApJ, 308, 836

Adande, G., Woolf, N., & Ziurys, L. 2011, Astrobiology, 13, 439

Aladro, R., Martín-Pintado, J., Martín, S., Mauersberger, R., & Bayet, E. 2011, A&A, 525, A89

Andre, P. & Montmerle, T. 1994, ApJ, 420, 837

Anglada, G. 1995, in Revista Mexicana de Astronomia y Astrofisica Conference Series, Vol. 1, Revista Mexicana de Astronomia y Astrofisica Conference Series, ed. S. Lizano & J. M. Torrelles, 67

Arce, H. G., Shepherd, D., Gueth, F., et al. 2007, Protostars and Planets V, 245

Asplund, M., Grevesse, N., Sauval, A. J., & Scott, P. 2009, ARA&A, 47, 481

Bachiller, R. & Pérez Gutiérrez, M. 1997, ApJ, 487, L93

Bacmann, A., Caux, E., Hily-Blant, P., et al. 2010, A&A, 521, L42

Bacmann, A., Taquet, V., Faure, A., Kahane, C., & Ceccarelli, C. 2012, A&A, 541, L12

Ball, J. A., Gottlieb, C. A., Lilley, A. E., & Radford, H. E. 1971, IAUC, 2350, 1

Bally, J., Langer, W. D., Stark, A. A., & Wilson, R. W. 1987, ApJ, 312, L45

Bell, M. B., Feldman, P. A., Travers, M. J., et al. 1997, ApJ, 483, L61

Ben Abdallah, D., Najar, F., Jaidane, N., Dumouchel, F., & Lique, F. 2012, MNRAS, 419, 2441

Bisschop, S. E., Jørgensen, J. K., van Dishoeck, E. F., & de Wachter, E. B. M. 2007, A&A, 465, 913

Blake, G. A., Sutton, E. C., Masson, C. R., & Phillips, T. G. 1987, ApJ, 315, 621

Blake, G. A., van Dishoeck, E. F., Jansen, D. J., Groesbeck, T. D., & Mundy, L. G. 1994, ApJ, 428, 680

Bockelée-Morvan, D., Lis, D. C., Wink, J. E., et al. 2000, A&A, 353, 1101

Bodenheimer, P. 1995, ARA&A, 33, 199

Bottinelli, S., Ceccarelli, C., & Neri, R. e. a. 2004, ApJ, 617, L69

Brack, A. 1998, The Molecular Origins of Life: Assembling Pieces of the Puzzle (Cambridge University Press)

Brouillet, N., Despois, D., Baudry, A., et al. 2013, A&A, 550, A46

Brown, R. D., Crofts, J. G., Godfrey, P. D., et al. 1975, ApJ, 197, L29

Carrasco-González, C., Anglada, G., Rodríguez, L. F., Torrelles, J. M., & Osorio, M. 2008, AJ, 136, 2238

Caselli, P. & Ceccarelli, C. 2012, A&ARv, 20, 56

Caselli, P., Hasegawa, T. I., & Herbst, E. 1993, ApJ, 408, 548

Caselli, P., Walmsley, C. M., Terzieva, R., & Herbst, E. 1998, ApJ, 499, 234

Castets, A. & Langer, W. D. 1995, A&A, 294, 835

Caux, E., Kahane, C., Castets, A., et al. 2011, A&A, 532, A23

Cazaux, S., Tielens, A. G. G. M., Ceccarelli, C., et al. 2003, ApJ, 593, L51

Ceccarelli, C. 2007, in Molecules in Space and Laboratory, 1

Ceccarelli, C., Caselli, P., Bockelée-Morvan, D., et al. 2014a, Protostars and Planets VI, 859

Ceccarelli, C., Caselli, P., Herbst, E., Tielens, A. G. G. M., & Caux, E. 2007, Protostars and Planets V, 47

Ceccarelli, C., Castets, A., Caux, E., et al. 2000a, A&A, 355, 1129

Ceccarelli, C., Castets, A., Loinard, L., Caux, E., & Tielens, A. G. G. M. 1998a, A&A, 338, L43

Ceccarelli, C., Caux, E., White, G. J., et al. 1998b, A&A, 331, 372

Ceccarelli, C., Dominik, C., López-Sepulcre, A., et al. 2014b, ApJ, 790, L1

Ceccarelli, C., Hollenbach, D. J., & Tielens, A. G. G. M. 1996, ApJ, 471, 400

Ceccarelli, C., Loinard, L., Castets, A., Tielens, A. G. G. M., & Caux, E. 2000b, A&A, 357, L9

Ceccarelli, C., Loinard, L., Castets, A., et al. 2001, A&A, 372, 998

Ceccarelli, C., Maret, S., Tielens, A. G. G. M., Castets, A., & Caux, E. 2003a, A&A, 410, 587

Ceccarelli, C., Maret, S., Tielens, A. G. G. M., Castets, A., & Caux, E. 2003b, A&A, 410, 587

Cernicharo, J., Marcelino, N., Roueff, E., et al. 2012, ApJ, 759, L43

Chandler, C. J., Brogan, C. L., Shirley, Y. L., & Loinard, L. 2005, ApJ, 632, 371

Charnley, S. B., Tielens, A. G. G. M., & Millar, T. J. 1992, ApJ, 399, L71

Chen, X., Launhardt, R., & Henning, T. 2009, ApJ, 691, 1729

Cheung, A. C., Rank, D. M., Townes, C. H., Thornton, D. D., & Welch, W. J. 1968, Physical Review Letters, 21, 1701

Chini, R., Ward-Thompson, D., Kirk, J. M., et al. 2001, A&A, 369, 155

Clarke, D. W. & Ferris, J. P. 1995, Icarus, 115, 119

Collings, M. P., Anderson, M. A., Chen, R., et al. 2004, MNRAS, 354, 1133

Cordiner, M. A., Charnley, S. B., Wirström, E. S., & Smith, R. G. 2012, ApJ, 744, 131

Correia, J. C., Griffin, M., & Saraceno, P. 2004, A&A, 418, 607

Coutens, A., Jørgensen, J. K., van der Wiel, M. H. D., et al. 2016, A&A, 590, L6

Coutens, A., Vastel, C., Cabrit, S., et al. 2013a, A&A, 560, A39

Coutens, A., Vastel, C., Caux, E., et al. 2012, A&A, 539, A132

Coutens, A., Vastel, C., Cazaux, S., et al. 2013b, A&A, 553, A75

Crapsi, A., Caselli, P., Walmsley, C. M., et al. 2005, ApJ, 619, 379

Crimier, N., Ceccarelli, C., Alonso-Albi, T., et al. 2010a, A&A, 516, A102

Crimier, N., Ceccarelli, C., Lefloch, B., & Faure, A. 2009, A&A, 506, 1229

Crimier, N., Ceccarelli, C., Maret, S., et al. 2010b, A&A, 519, A65

Daniel, F., Gérin, M., Roueff, E., et al. 2013, A&A, 560, A3

Doty, S. D., Schöier, F. L., & van Dishoeck, E. F. 2004, A&A, 418, 1021

Douglas, A. E. & Herzberg, G. 1941, ApJ, 94, 381

Elias, J. H. 1978, ApJ, 224, 857

Esplugues, G. B., Cernicharo, J., Viti, S., et al. 2013, A&A, 559, A51

Evans, II, N. J., Rawlings, J. M. C., Shirley, Y. L., & Mundy, L. G. 2001, ApJ, 557, 193

Faure, A., Lique, F., & Wiesenfeld, L. 2016, MNRAS, 460, 2103

Fontani, F., Codella, C., Ceccarelli, C., et al. 2014, ApJ, 788, L43

Friesen, R. K., Medeiros, L., Schnee, S., et al. 2013, MNRAS, 436, 1513

Furlan, E., Megeath, S. T., Osorio, M., et al. 2014, ApJ, 786, 26

García-Rojas, J. & Esteban, C. 2007, ApJ, 670, 457

Garrod, R. T., Vasyunin, A. I., Semenov, D. A., Wiebe, D. S., & Henning, T. 2009, ApJ, 700, L43

Garrod, R. T., Widicus Weaver, S. L., & Herbst, E. 2008, ApJ, 682, 283

Gatley, I., Becklin, E. E., Mattews, K., et al. 1974, ApJ, 191, L121

Geppert, W. D., Vigren, E., Hamberg, M., et al. 2007, in European Planetary Science Congress 2007, 613

Gibb, E., Nummelin, A., Irvine, W. M., Whittet, D. C. B., & Bergman, P. 2000, ApJ, 545, 309

Girart, J. M., Estalella, R., Palau, A., Torrelles, J. M., & Rao, R. 2014, ApJ, 780, L11

Goesmann, F., Rosenbauer, H., Bredehöft, J. H., et al. 2015, Science, 349

Goumans, T. P. M., Catlow, C. R. A., & Brown, W. A. 2008, The Journal of Chemical Physics, 128,

Green, S. 1986, ApJ, 309, 331

Guarnieri, A. & Huckauf, A. 2003, Naturforsch, 58, 275

Halfen, D. T., Ilyushin, V., & Ziurys, L. M. 2011, ApJ, 743, 60

Hasegawa, T. I. & Herbst, E. 1993, MNRAS, 263, 589

Herbst, E. & van Dishoeck, E. F. 2009, A&ARv, 47, 427

Hily-Blant, P., Maret, S., Bacmann, A., et al. 2010, A&A, 521, L52

Hirano, N., Kamazaki, T., Mikami, H., Ohashi, N., & Umemoto, T. 1999, in Star Formation 1999, ed. T. Nakamoto, 181–182

Hirota, T., Bushimata, T., Choi, Y. K., et al. 2007, PASJ, 59, 897

Hirota, T., Bushimata, T., Choi, Y. K., et al. 2008, PASJ, 60, 37

Horn, A., Møllendal, H., Sekiguchi, O., et al. 2004, ApJ, 611, 605

Ikeda, M., Ohishi, M., & Nummelin, A. e. a. 2001, ApJ, 560, 792

Jaber, A. A., Ceccarelli, C., Kahane, C., & Caux, E. 2014, ApJ, 791, 29

Jefferts, K. B., Penzias, A. A., & Wilson, R. W. 1973, ApJ, 179, L57

Jones, B. M., Bennett, C. J., & Kaiser, R. I. 2011, ApJ, 734, 78

Jørgensen, J. K., Bourke, T. L., Nguyen Luong, Q., & Takakuwa, S. 2011, A&A, 534, A100

Jørgensen, J. K., Favre, C., Bisschop, S. E., et al. 2012, ApJ, 757, L4

Jørgensen, J. K., Johnstone, D., van Dishoeck, E. F., & Doty, S. D. 2006, A&A, 449, 609

Jørgensen, J. K., Lahuis, F., Schöier, F. L., et al. 2005, ApJ, 631, L77

Jørgensen, J. K., Schöier, F. L., & van Dishoeck, E. F. 2002, A&A, 389, 908

Jørgensen, J. K., Schöier, F. L., & van Dishoeck, E. F. 2004, A&A, 416, 603

Jørgensen, J. K., van der Wiel, M. H. D., Coutens, A., et al. 2016, ArXiv e-prints

Kahane, C., Ceccarelli, C., Faure, A., & Caux, E. 2013, ApJ, 763, L38

Kama, M. 2013, PhD thesis, University of Amsterdam

Kama, M., Dominik, C., Maret, S., et al. 2010, A&A, 521, L39

Kama, M., López-Sepulcre, A., Dominik, C., et al. 2013, A&A, 556, A57

Karska, A., Herczeg, G. J., van Dishoeck, E. F., et al. 2013, A&A, 552, A141

Kleiner, I., Lovas, F. J., & Godefroid, M. 1996, Journal of Physical and Chemical Reference Data, 25, 1113

Kristensen, L. E., Klaassen, P. D., Mottram, J. C., Schmalzl, M., & Hogerheijde, M. R. 2013, A&A, 549, L6

Kristensen, L. E., van Dishoeck, E. F., Bergin, E. A., et al. 2012, A&A, 542, A8

Lada, C. J. & Wilking, B. A. 1984, ApJ, 287, 610

Lefloch, B. & Bachiller, R. 2015, in Highlights of Spanish Astrophysics VIII, ed. A. J. Cenarro, F. Figueras, C. Hernández-Monteagudo, J. Trujillo Bueno, & L. Valdivielso, 1–6

Lefloch, B., Castets, A., Cernicharo, J., Langer, W. D., & Zylka, R. 1998, A&A, 334, 269

Linsky, J. L., Draine, B. T., Moos, H. W., et al. 2006, ApJ, 647, 1106

Lis, D. C., Roueff, E., Gerin, M., et al. 2002, ApJ, 571, L55

Loinard, L., Castets, A., Ceccarelli, C., et al. 2000, A&A, 359, 1169

Loinard, L., Torres, R. M., Mioduszewski, A. J., & Rodríguez, L. F. 2008, ApJ, 675, L29

Loinard, L., Zapata, L. A., Rodríguez, L. F., et al. 2013, MNRAS, 430, L10

Loison, J.-C., Wakelam, V., Hickson, K. M., Bergeat, A., & Mereau, R. 2014, MNRAS, 437, 930

Loomis, R. A., Shingledecker, C. N., Langston, G., et al. 2016, mnras, 463, 4175

Looney, L. W., Mundy, L. G., & Welch, W. J. 2000, ApJ, 529, 477

López-Sepulcre, A., Jaber, A. A., Mendoza, E., et al. 2015, MNRAS, 449, 2438

López-Sepulcre, A., Taquet, V., Sánchez-Monge, Á., et al. 2013, A&A, 556, A62

Lunine. 2009, EPJ Web of Conferences, 1, 267

Machida, M. N., Inutsuka, S.-i., & Matsumoto, T. 2008, ApJ, 676, 1088

Maeda, A., De Lucia, F. C., & Herbst, E. 2008, Journal of Molecular Spectroscopy, 251, 293

Maezawa, H., Ikeda, M., Ito, T., et al. 1999, ApJ, 524, L129

Majumdar, L., Gratier, P., Vidal, T., et al. 2016, MNRAS, 458, 1859

Manoj, P., Watson, D. M., Neufeld, D. A., et al. 2013, ApJ, 763, 83

Marcelino, N., Cernicharo, J., Roueff, E., Gerin, M., & Mauersberger, R. 2005, ApJ, 620, 308

Marcelino, N., Cernicharo, J., Tercero, B., & Roueff, E. 2009, ApJ, 690, L27

Marenich, A. & Boggs, J. 2003, The Journal of Chemical Physics, 107, 2343

Maret, S., Ceccarelli, C., Caux, E., Tielens, A. G. G. M., & Castets, A. 2002, A&A, 395, 573

Marr, J. M., Wright, M. C. H., & Backer, D. C. 1993, ApJ, 411, 667

McElroy, D., Walsh, C., Markwick, A. J., et al. 2013, A&A, 550, A36

McKellar, A. 1940, PASP, 52, 187

Mendoza, E., Lefloch, B., López-Sepulcre, A., et al. 2014, MNRAS, 445, 151

Menten, K. M., Reid, M. J., Forbrich, J., & Brunthaler, A. 2007, A&A, 474, 515

Miettinen, O. 2014, A&A, 562, A3

Millar, T. J., Herbst, E., & Charnley, S. B. 1991, ApJ, 369, 147

Mizuno, A., Fukui, Y., Iwata, T., Nozawa, S., & Takano, T. 1990, ApJ, 356, 184

Müller, H. S. P., Schlöder, F., Stutzki, J., & Winnewisser, G. 2005, Journal of Molecular Structure, 742, 215

Mumma, M. J. & Charnley, S. B. 2011, A&ARv, 49, 471

Mundy, L. G., Wootten, A., Wilking, B. A., Blake, G. A., & Sargent, A. I. 1992, ApJ, 385, 306

Neustock, W., Guarnieri, A., & G., D. 1990, Naturforsch, 45, 702

new scientistwebsite. 2016, , `https://www.newscientist.com`, accessed: 2016-06-30

Nummelin, A., Bergman, P., Hjalmarson, Å., et al. 2000, ApJS, 128, 213

Öberg, K. I., Bottinelli, S., Jørgensen, J. K., & van Dishoeck, E. F. 2010, ApJ, 716, 825

Oya, Y., Sakai, N., López-Sepulcre, A., et al. 2016, apj, 824, 88

Parise, B., Bergman, P., & Menten, K. 2014, Faraday Discussions, 168, 349

Parise, B., Castets, A., Herbst, E., et al. 2004, A&A, 416, 159

Parise, B., Ceccarelli, C., & Maret, S. 2005, A&A, 441, 171

Parise, B., Du, F., Liu, F.-C., et al. 2012, A&A, 542, L5

Pickett, H. M., Poynter, R. L., Cohen, E. A., et al. 1998, JQSRT, 60, 883

Pineda, J. E., Maury, A. J., Fuller, G. A., et al. 2012, A&A, 544, L7

Pirim, C., Krim, L., & Laffon, C. 2010, The Journal of Chemical Physics, 114, 3320

Quan, D. & Herbst, E. 2007, A&A, 474, 521

Raunier, S., Chiavassa, T., Duvernay, F., et al. 2004, A&A, 416, 165

Reboussin, L., Wakelam, V., Guilloteau, S., & Hersant, F. 2014, MNRAS, 440, 3557

Redondo, P., Barrientos, C., & Largo, A. 2014, ApJ, 780, 181

Reipurth, B., Rodríguez, L. F., & Chini, R. 1999, AJ, 118, 983

Requena-Torres, M. A., Martin-Pintado, J., Martin, S., & Amo-Baladron, A. 2007, ATNF Proposal, 939

Requena-Torres, M. A., Martín-Pintado, J., Martín, S., & Morris, M. R. 2008, ApJ, 672, 352

Requena-Torres, M. A., Martín-Pintado, J., Rodríguez-Franco, A., et al. 2006, A&A, 455, 971

Ruaud, M., Loison, J. C., Hickson, K. M., et al. 2015, MNRAS, 447, 4004

Rubin, R. H., Swenson, Jr., G. W., Benson, R. C., Tigelaar, H. L., & Flygare, W. H. 1971, ApJ, 169, L39

Sakai, N., Sakai, T., Hirota, T., & Yamamoto, S. 2008, ApJ, 672, 371

Saladino, R., Botta, G., Pino, S., Costanzo, G., & Di Mauro, E. 2012, Chem. Soc. Rev., 41, 5526

Schöier, F. L., Jørgensen, J. K., van Dishoeck, E. F., & Blake, G. A. 2002, A&A, 390, 1001

Schöier, F. L., Jørgensen, J. K., van Dishoeck, E. F., & Blake, G. A. 2004, A&A, 418, 185

Schöier, F. L., van der Tak, F. F. S., van Dishoeck, E. F., & Black, J. H. 2005, A&A, 432, 369

Shimajiri, Y., Sakai, T., Kitamura, Y., et al. 2015, ApJS, 221, 31

Shimajiri, Y., Takahashi, S., Takakuwa, S., Saito, M., & Kawabe, R. 2008, ApJ, 683, 255

Shirley, Y. L., Evans, II, N. J., Rawlings, J. M. C., & Gregersen, E. M. 2000, ApJS, 131, 249

Shu, F. H. 1977, ApJ, 214, 488

Snell, R. L., Schloerb, F. P., Young, J. S., Hjalmarson, A., & Friberg, P. 1981, ApJ, 244, 45

Solomon, P. M., Jefferts, K. B., Penzias, A. A., & Wilson, R. W. 1971, ApJ, 168, L107

Stark, R., Sandell, G., Beck, S. C., et al. 2004, ApJ, 608, 341

Suzuki, H., Yamamoto, S., Ohishi, M., et al. 1992, ApJ, 392, 551

Swings, P. & Rosenfeld, L. 1937, ApJ, 86, 483

Taquet, V., Ceccarelli, C., & Kahane, C. 2012, A&A, 538, A42

Taquet, V., López-Sepulcre, A., Ceccarelli, C., et al. 2015, ApJ, 804, 81

Thronson, Jr., H. A., Harper, D. A., Keene, J., et al. 1978, AJ, 83, 492

Tielens, A. 2005, The Physics and Chemistry of the Interstellar Medium (Cambridge University Press)

Tielens, A. G. G. M. & Hagen, W. 1982, A&A, 114, 245

Tóth, L. V., Haas, M., Lemke, D., Mattila, K., & Onishi, T. 2004, A&A, 420, 533

Turner, B. E. 1990, ApJ, 362, L29

van Dishoeck, E. F., Blake, G. A., Draine, B. T., & Lunine, J. I. 1993, in Protostars and Planets III, ed. E. H. Levy & J. I. Lunine, 163–241

van Dishoeck, E. F., Blake, G. A., Jansen, D. J., & Groesbeck, T. D. 1995, ApJ, 447, 760

Vastel, C., Ceccarelli, C., Lefloch, B., & Bachiller, R. 2014, apjl, 795, L2

Vasyunin, A. I. & Herbst, E. 2013, ApJ, 769, 34

Viti, S., Collings, M. P., Dever, J. W., McCoustra, M. R. S., & Williams, D. A. 2004, MNRAS, 354, 1141

Wakelam, V., Loison, J.-C., Herbst, E., et al. 2015, apjs, 217, 20

Walker, C. K., Lada, C. J., Young, E. T., Maloney, P. R., & Wilking, B. A. 1986, ApJ, 309, L47

Watanabe, N. & Kouchi, A. 2002, ApJ, 571, L173

Wernli, M., Wiesenfeld, L., Faure, A., & Valiron, P. 2007, A&A, 464, 1147

Winstanley, N. & Nejad, L. A. M. 1996, Ap&SS, 240, 13

Woon, D. E. 2002, ApJ, 571, L177

Wootten, A. 1989, ApJ, 337, 858

Yamaguchi, T., Takano, S., Watanabe, Y., et al. 2012, PASJ, 64

Zapata, L. A., Loinard, L., Rodríguez, L. F., et al. 2013, ApJ, 764, L14